Università degli Studi di Ferrara

DOTTORATO DI RICERCA IN FISICA

CICLO XXVII

COORDINATORE Prof. Vincenzo Guidi

PHYSICS AND TECHNOLOGY OF THE SPES CHARGE BREEDER

Settore Scientifico Disciplinare FIS/04

Dottorando

Dott. Galatà Alessio

Tutori

Prof. Fiorentini Giovanni
Dott. Ing. Celona Luigi

Anni 2012/2014

Acknowledgement

This thesis has been a very exciting experience: I consider myself lucky for having had the possibility to deal with such a "full-of-physics" device, the ECR-based charge breeder, from different points of view: the main one has been the theoretical-numerical approach, but also the experimental and technological aspects strongly enriched my professional experience. For all this my sincere gratitude goes to my Director, Prof. Giovanni Fiorentini, the first one who, after many years, agreed and encouraged me to undertake this trip, even if I was not exactly a "just graduated" student.
My deepest gratitude goes to my external tutor and "older brother" Dr. Eng. Luigi Celona: since the beginning of my activity he has been a point of reference, and I appreciate the efforts spent in supervising me, especially for a full-of-commitments researcher as he is. I'm grateful also to my friend Dr. David Mascali from LNS, whose professionalism and knowledge of plasma physics have been determinant for the success in developing the numerical code. I wish to thank also the colleague Dr. Lorenzo Neri from LNS, for his help in debugging the code and, in general, for his "critical" approach to my work that revealed to be very stimulating for me.
I want to say thank you also to the international colleagues of the EMILIE collaboration, for the intense experimental activity carried out in the past three years: among them I would like to mention Thierry Lamy and Julien Angot from LPSC, with whom I have been collaborating for the delivery of the SPES-CB at LNL; Hannu Koivisto and Olli Tarvainen from JYFL, internationally recognized experts in ECR plasma physics; Pierre Delahaye from GANIL, the first person I interacted with, before starting the experience within EMILIE.
Of course without the Laboratory, and in particular my participation to the SPES project, I surely wouldn't have had the possibility to do what I did: for this I would like to thank the project leader, Dr. Gianfranco Prete, and two colleagues of mine who helped me a lot in making technological choices for the SPES-CB: Dr. Carlo Roncolato and Eng. Jesus Vasquez.
Finally, to my wife: a thought well-suited for PhD in Physics....we are and will be entangled!

Contents

Introduction

Starting from the experiments performed in the 80's at CRC Louvain-La-Neuve, the interest in post accelerated radioactive ion beams (RIBs) has been growing constantly, due to their better optical quality compared to beams produced through fragmentations. This led to the construction of different facilities all over the world, like ATLAS at ANL with the CARIBU project (US), TRIUMF (Canada), SPIRAL (France), TRIAC (Japan, not operational any more) and ISOLDE at CERN. The main goal of those facilities is to provide an accelerator system to perform forefront research in nuclear physics by studying nuclei far from stability. The European road map is now going through the development of second generation facilities pointing to EURISOL: presently three main projects are ongoing in different Laboratories, HIE-ISOLDE at CERN, SPIRAL2 at GANIL and SPES at Laboratori Nazionali di Legnaro (INFN-LNL); this last project is the framework of the work of this thesis.

Radioactive ion beams will be produced at SPES with the Isotope Separation On Line (ISOL) technique: a primary proton beam will induce fissions by striking on an especially designed uranium carbide (UC_x) target. Radioactive species will effuse towards an ion source, directly connected to the target, and will be extracted as a singly charged radioactive ion beam: desired characteristics of the ion source are the highest possible ionization efficiency and good beam quality. The combination of the previously mentioned parts is usually called Target-Ion Source system (TIS). Considering all the possible masses to be produced at SPES, three ionization mechanisms will be employed: surface ionization, laser ionization and plasma ionization. The extracted beam will consist of the desired radioactive ions and other isobars, those also created and ionized inside the TIS: the ions of interest will be selected by means of an High Resolution Mass Spectrometer (HRMS) with a resolving power $\Delta M/M \sim 1/20000$; prior to the injection into the HRMS, the beam will pass through a Radio Frequency Quadrupole (RFQ) cooler, in order to decrease the beam emittance and allow reaching the desired resolution.

Post-acceleration of RIBs at high energies (E≥10*A MeV) is expected at SPES by employing a newly designed normal conducting Radio Frequency Quadrupole (RFQ) accelerator, working as injector for the superconducting linac ALPI: anyway, the low charge of the cleaned 1+ beam coming from the TIS and the following selection is not suited for reaching such performances; this is true not only in the particular case of SPES but for any facility aiming at keeping reasonable the costs of the

post-accelerator. To overcome this difficulty it is necessary to implement a further device, able to accept the radioactive 1+ beam, increase its charge state and extract it efficiently and rapidly as a highly charged q+ beam: this task is carried out by the so called "Charge Breeder" (CB). In the past years mainly two techniques have been developed, both consisting in adapting ions sources for stable beams to the charge breeding process: this has been done with the Electron Beam Ion Sources (EBIS) and the Electron Cyclotron Resonance Ion Sources (ECRIS); both techniques were compared in view of the performances expected for EURISOL and were found to be complementary. In particular, the ECR-based technique is the one chosen for SPES: the facility will employ an upgraded version of the model denominated PHOENIX developed by the French Institution Laboratoire de Physique et de Cosmologie (LPSC) of Grenoble. Characteristics of this technique are the reliability, the high acceptance in terms of injected current and emittance, the possibility to produce both continuous and pulsed beams and the high charge states produced.
Since the first experiments carried out in the 90's by the team of Prof. Geller in Grenoble, the performances of such technique have seen a rapid increase to reach recently a slow saturation: as in the case of the ECR sources, to overcome the limits a deeper understanding of the physics behind this process is necessary and the work of this thesis goes exactly in this direction. During my PhD I had in fact the opportunity to participate as deputy coordinator to the European project Enhanced Multi-Ionization of short-Lived Isotopes at EURISOL (EMILIE) aiming at improving the performances of the ECR-based charge breeder PHOENIX. The main part of this PhD thesis was carried out in this context: after a theoretical analysis of the base mechanisms involved in this technique, a Matlab code was written to simulate the capture of a 1+ beam by the plasma of the PHOENIX charge breeder. As will be clearer in the course of this thesis, the knowledge of this device has been enriched by a fruitful experimental activity performed in the last three years on the LPSC test bench within EMILIE. Its first aim was mainly the improvement of the performances of PHOENIX by applying different well known "tricks" of ECR ion sources but, very surprisingly, it revealed to be a very useful way to build a physically reasonable picture of the charge breeding process. Finally, part of the work done during this PhD contributed to the future installation and operation of the SPES-Charge Breeder (SPES-CB), through the suggestion and the choice of different adopted technical solutions.
This thesis starts with a first general chapter describing briefly the main reasons for the interest in RIBs, mentioning also further applications like in solid state physics or medicine. The second chapter is dedicated to the SPES project: after the description of its organization and its scientific context, the various parts of the facility are analysed more in detail, starting from the TIS and ending with the expected performances of the post-accelerated radioactive beams. The main techniques for charge breeding are described and compared in chapter three, underlining the reasons for the particular choice adopted for SPES. After those three introductory chapters we arrive at the most important part of the thesis, from chapter four to six: in

chapter four all the physical mechanism involved in the functioning of a charge breeder are described. It starts with the single particles dynamics and the description of the processes responsible for ions creation and destruction; the peculiarity of the electromagnetic propagation in a magnetized plasma is treated, to go then to the fluid approach and the description of diffusion mechanisms typical of ECR ion sources. The confinement of charged particles inside the plasma is also discussed and mention is done on ion beam formation. The final section of this chapter is dedicated to the description of the peculiarity of an ECR-based charge breeder, that is the interaction of an ion beam with a plasma: the equations describing the dynamics of the process are derived, emphasising the ones that will be implemented in the numerical simulations. Chapter five is dedicated to the SPES-CB: first, a description of the mains components of this device and its beam line is given, underlining the proposed and adopted technical improvements; then, the experimental results obtained within the EMILIE project are described, focusing on those used to benchmark the numerical simulations. This last aspect is the most important part of this thesis and is deeply described in chapter 6: it starts with general considerations about the usefulness of a numerical approach, the domain of the simulation and all the times involved in the calculation. The correct implementation of the process is verified first by an extremely simplified model of the plasma; then, the injection of a Rb^{1+} beam inside the PHOENIX charge breeder is simulated by implementing plasma models of increasing accuracy, to get finally a physically reasonable picture of the charge breeding process. As will be seen, the results obtained at each level of accuracy very well agree with the theoretical predictions: in particular, the final model is able to reproduce, for particular simulated plasma parameters, the experimental results on the anomalous Rb^{1+} efficiencies obtained at LPSC within the EMILIE project. The thesis ends with a summary and perspectives.

Chapter 1

The Facilities for Radioactive Ion Beams Production

1.1 Why Radioactive Ion Beams (RIBs)?

Most of our present knowledge of nuclear properties has been gained by studying nuclei near the valley of beta stability or on the neutron-deficient side with respect to the two variables excitation energy and spin [1]. Very asymmetric combinations of protons and neutrons are expected to reveal new aspects of nuclear structure: up to now, the most severe constraint on our ability to advance the understanding of nuclear physics has been the fact that in any nuclear reaction both the beam and target species were stable.

The most critical ingredients in determining the properties of a nucleus are the overall number of nucleons A and the ratio N/Z of neutrons to protons: it is the extremes that will be opened up for study with high energy radioactive beams. As neutrons are successively added to a nucleus on the stability line, the binding energy of the last neutron decreases steadily until it vanishes and the nucleus decays by neutron emission: the position in the nuclear chart where this takes place defines the neutron drip line. Owing to the absence of electrical repulsion between neutrons, it lies much farther away from the valley of stability than the one for protons, even if its location is known only for nuclei with mass up to around 30 (see figure 1.1).

The main goal of the facilities dedicated to the production of radioactive ion beams is to provide an accelerator system to perform forefront research in nuclear physics by studying nuclei far from stability. The interest in the study of nuclei with large neutron excess is not only focused on the location of the drip line but also on the investigation of the density dependence of the effective interaction between the nucleons for exotic N/Z ratios. In fact, changes of the nuclear density and size in nuclei with increasing N/Z ratios are expected to lead to different nuclear symmetries and new excitation modes.

The study of nuclear structure is not the only application of radioactive ion beams: RIBs can be extremely useful also in other fields such as nuclear astrophysics, solid-

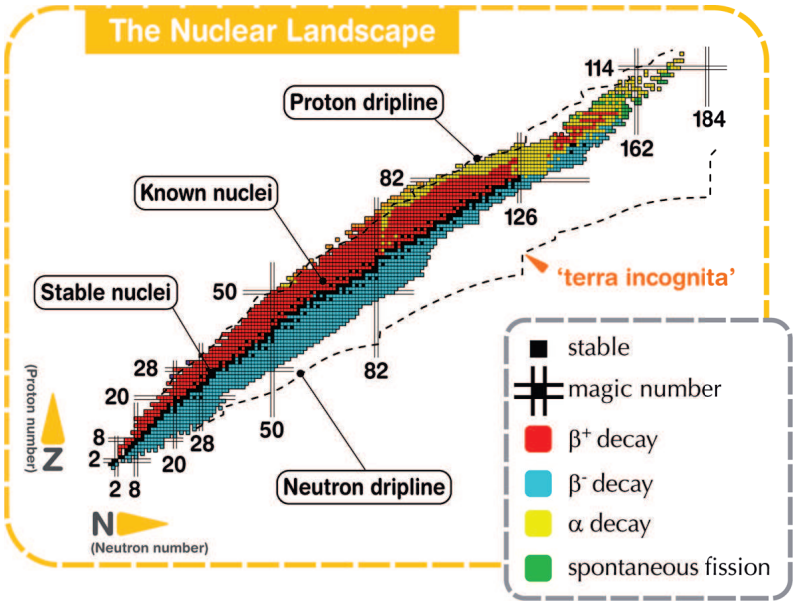

Figure 1.1: Chart of nuclide.

state physics and nuclear medicine. In the following some particular applications are briefly described.

- **Nuclear Astrophysics**. Nuclear astrophysics plays a fundamental role in understanding the structure and composition of the Universe and its constituents. Stars produce energy through nuclear reactions between stable and unstable nuclei: these processes can last for billions of years or be explosive involving a time-scale of seconds. To model some steps of these processes, nuclear astrophysics must rely on a number of specific characteristics of exotic nuclei: when available, the experimental informations can help in avoiding the used of extrapolated nuclear models or testing the applicability of the current ones.

- **Solid State Physics**. Radioactive ion beams can be used as a powerful diagnostic tool to furnish detailed information on the environment in which they are implanted: an important application is represented by the Emission Channelling technique, used to study the structure and properties of impurity-defect complexes in solids, particularly in semiconductor. As shown in figure 1.2, it can be described as the movement of a charged particles through a single crystal, emitted by α or β decay of the radioactive ions previously implanted into the crystal and registered by a 2-dimensional position sensitive detector. The working principle of this technique is based on the angle dependence of the intensity of the emitted radiation as a function of the orientation of the host crystal: from the measured anisotropic intensity distributions the lattice sites of the emitting radioactive ions can be determined with a great accuracy. This kind of technique can be very useful to study diffusion phenomena and doping in semiconductors.

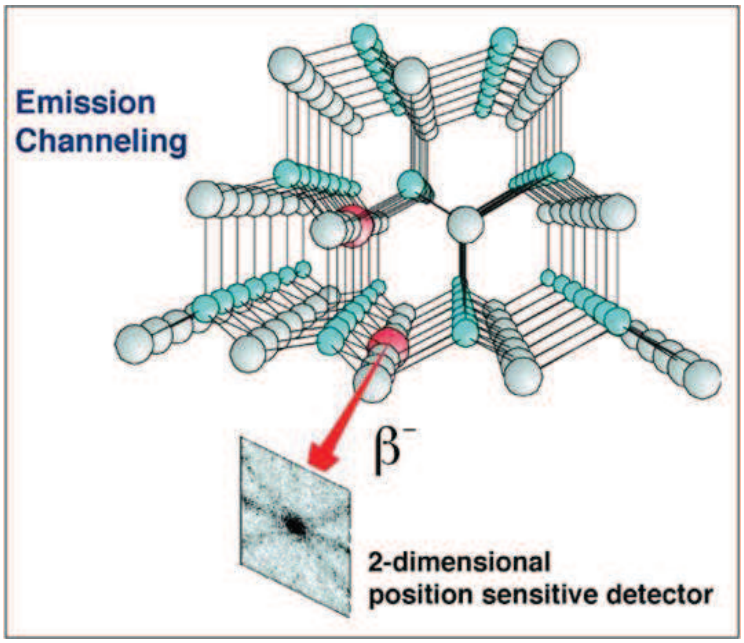

Figure 1.2: The Emission Channelling technique.

- **Nuclear Medicine**. Since the early days of nuclear physics, it was realized that nuclear radiation could be used in medicine for diagnostic and therapy operations: nuclear medicine is a branch of medicine that exploits radioactive decay in the diagnosis and treatment of disease. An important application of radioactive ion beams in nuclear medicine is the production of radioactive isotopes (or radionuclide) to be used for Positron Emission Tomography (PET). Radionuclide used for PET are typically isotopes with short half lives such as ^{11}C ($t_{1/2}$ ~20 min), ^{13}N ($t_{1/2}$ ~10 min), ^{15}O ($t_{1/2}$ ~2 min), and ^{18}F ($t_{1/2}$ ~110 min). The radionuclide are incorporated either into compounds normally used by the body (glucose , water, ammonia) or into molecules involved in the functional process of interest: incorporated radionuclide emit a positron that after travelling up to a few millimetres annihilates with an electron, producing two or more gamma ray photons moving in opposite directions. The photons are recorded by a scintillator coupled to a photomultiplier tubes or silicon avalanche photodiodes (Si APD): the produced signals are then opportunely elaborated to reconstruct a digital image of the zone of interest. One of the main applications of PET is surely in clinical oncology: because of the short half lives of most radioactive isotopes, the radiotracers (tracers containing radioactive isotopes) must be produced using a cyclotron and a radiochemistry laboratory that are in close proximity to the PET imaging facility.

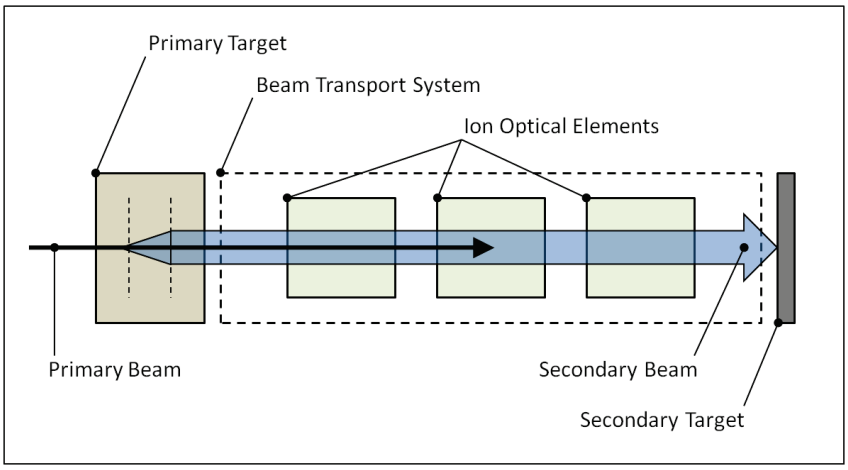

Figure 1.3: Schematic representation of the in-flight separation technique.

1.2 RIBs production

The techniques nowadays used for the production of radioactive ion beams are basically two: the in-flight separation technique and the isotope separation online (ISOL) technique. Both methods face with common difficulties like the very low production cross section and life times of radioactive species and the high percentage of unwanted contaminants. In both cases the radioactive ions of interest are transported away from the place where they are produced, in order to explore their nuclear properties or purify and prepare the beam for post-acceleration.

In the in-flight separation technique [2] is schematically described in figure 1.3: a primary heavy ions beam of several tens of MeV per nucleon is fragmented in a "primary" target, producing particles that, following electromagnetic selection, are directly used for experiments. The challenge for the beam transport system is to provide an efficient mechanism for suppressing the intense primary beam transmitted through the primary target while efficiently transporting the secondary beam. An example of the application of such a technique is the production of ^{17}F through the reaction $d(^{16}O,^{17}F)n$. The in-flight separation technique is able to provide isotopes close to stability without limitations due to lifetimes or chemical properties; it allows also for an easy variation of the energy of the reaction products within a certain range and can be implemented in existing heavy-ion accelerators. On the other hand, the main disadvantages are the low beam quality and the low number of ion species that can be produced.

With the ISOL technique [3] the radioactive isotopes are produced in a target, bombarded by a high energy primary beam, and thermalized in a catcher consisting of solid, liquid or gas material; the target and the catcher are often the same object. The radioactive isotopes are transported from the target/catcher to the a source where they are ionized one time; then, they can be extracted, selected using a dipole magnet and transported for further ionization and subsequent acceleration to the

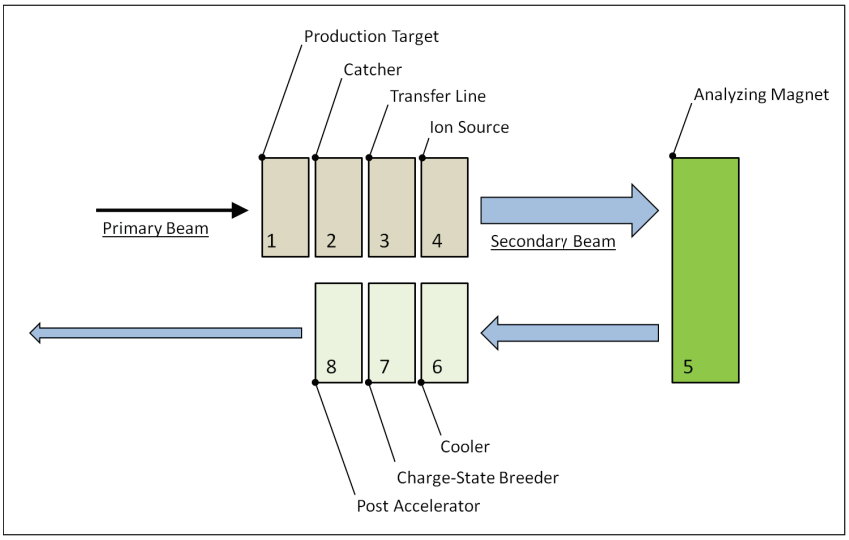

Figure 1.4: Schematic representation of an ISOL facility.

required energy. The whole production sequence must be:

- **efficient** to avoid losses of the few precious nuclei.
- **fast** if the species of interest are short lived exotic nuclei.
- **selective**, that is able to separate with efficacy wanted from unwanted (generally stable) species. The source of unwanted species is always the reaction itself or the materials constituting the Target-Ion-Source system.

Another important characteristic is the production rate, that depends on the delivered intensity, for a given target's material or type and the energy of the primary beam. The basic ingredients of an ISOL facility are presented in figure 1.4: production, thermalization, ionization, extraction, mass separation, cooling, charge-state breeding and post-acceleration; a delay time can also be defined as the average time the radioactive atoms spend from the moment of production to the moment of arrival at the experimental position. We will come back to the description of the above mentioned ingredients later in this thesis. It is now important to introduce some general notions about the functioning of an ISOL facility: the intensity I_{prod} of the reaction products synthesized in the target is calculated using the following equation

$$I_{prod} = \sigma N_{target} I_{beam} \tag{1.1}$$

where, σ is the cross-section of production of a desired radionuclide, N_{target} is the number of target atoms per unit surface area and I_{beam} is the primary beam intensity. Since the cross section is energy dependent and the primary beam looses energy while passing through the target, the intensity has to be calculated by integrating over the target thickness taking into account the energy loss of the beam. The final intensity I of the secondary beam will be reduced respect to I_{prod} as follows:

$$I = \epsilon I_{prod} = \epsilon \ \sigma \ N_{target} \ I_{beam} \tag{1.2}$$

with ϵ being the efficiency of the whole facility: such quantity takes into account the efficiency of all the various parts of the facility and can be expressed as

$$\epsilon = \epsilon_{delay}\ \epsilon_{1+}\ \epsilon_{line}\ \epsilon_{cool}\ \epsilon_{breed}\ \epsilon_{post-acc} \tag{1.3}$$

where,

- ϵ_{delay} is the probability of survival against radioactive decay during the time needed to extract the ion from the target-ion source system
- ϵ_{1+} is the ionization efficiency
- ϵ_{line} is the efficiency of mass analysis and transport to the experimental set-up
- $\epsilon_{cool}$is the cooling and bunching efficiency
- ϵ_{breed} is the charge-state breeding efficiency
- $\epsilon_{post-acc}$ is the efficiency of the post-accelerator.

The time associated to ϵ_{delay} is often called **release time** since in case of solid and liquid catcher systems it is determined by the diffusion from the target/catcher material and the effusion to the ion source exit hole.

Chapter 2

The SPES Project

2.1 Introduction

SPES (Selective Production of Exotic Species) [4] is a INFN project supported by two Italian national laboratories, Laboratori Nazionali di Legnaro (LNL, Legnaro PD) and Laboratori Nazionali del Sud (LNS, Catania), and is currently under way at LNL. The main goal of the project is the development of a facility for neutron-rich exotic beams production to perform forefront research in nuclear structure, reaction dynamics and interdisciplinary fields like medical, biological and material sciences. As symbolically described in figure 2.1 by means of a four-leaved clover, the SPES project is articulated in four phase: α, β, γ and δ.
SPES-α foresees the acquisition, installation and commissioning of a high performance cyclotron with high output current ($\sim$0.7 mA) and high energy (up to 70 MeV), together with the related infrastructure for the accelerator and experimental stations. The cyclotron will be provided with two exit ports: one of the two beams will be dedicated to the nuclear physics facility (producing neutron-rich ions by collisions of protons onto a UC_x target); the second will be dedicated to applied physics. SPES-α was fully financed by INFN and is presently under construction in Legnaro.

Figure 2.1: Symbolic representation of the four phases of the SPES project.

Within SPES-β neutron-rich exotic species will be accelerated and delivered against suitable targets. In the collisions, new extremely neutron-rich nuclei will be produced, which are similar to those generated in advanced stellar stages and are not present on Earth due to their short lifetime. The investigation on such systems is a new frontier of physics, for extending our knowledge of nuclei at extreme conditions and for providing basic information in the study of stellar evolution. SPES-β has been approved and partially funded by the Italian Government within the Premium-Projects 2011; funds from INFN will will ensure its completion.
SPES-γ [5] concerns the production of radionuclide of medical interest by using the SPES-α cyclotron: the goal is the production of innovative radiopharmaceutical (e.g. those based on ^{82}Sr/^{82}Rb and ^{68}Ga/^{68}Ge) as well as the production of conventional radionuclide with new accelerator-based approaches. In this respect the metastable state of Technetium-99 (Tc99-m) is of particular interest. This phase of the SPES project, which has been approved by MIUR within the Premium-Projects 2012, is the result of a collaboration between INFN, CNR, Italian Universities and a private partner.
Finally, SPES-δ [6] foresees the development of an intense neutron source, from the cyclotron and/or from a high intensity linear accelerator based on radio-frequency quadrupole (RFQ) technology. Applications of the neutron source range from nuclear astrophysics to test of electronics in space, characterization of nuclear waste or experimental tumour treatments. For the development of this approach, an agreement has been signed by SOGIN, University of Pavia and INFN and the project MUNES (MUltidisciplinary NEutron Source) has been funded by the Italian Government within the Premium-Project 2011.
The work described in this thesis deals with the phase β of the SPES project so only this one will be considered in the following sections and chapters and will be conventionally termed as SPES.

2.2 Overview of the project

SPES will be an Isotope Separation On Line (ISOL) facility based on a commercial 70 MeV Cyclotron produced by the BEST Theratronics company [7] as proton driver. The cyclotron is designed to provide a beam intensity up to 750 μA with variable energy ranging between 30 and 70 MeV. The proton beam will hit a direct multi-foil uranium carbide (UC_x) target in order to obtain the desired number of 10^{13} fissions/s [8]. Different Target-Ionization Sources systems (TIS) are under development at LNL in order to optimize the extraction efficiency of the radioactive ions produced and to minimize the beam contaminants [9].
A first discrimination of the exotic beams will be performed just at the exit of the TIS system by means of a Wien Filter and a 90° dipole magnet (mass resolving power $\Delta M/M \simeq 1/200$). The beam will then pass through a Beam Cooler stage [10], to lower its emittance, and then into the High Resolution Mass Spectrometer (HRMS) [11] with a mass resolving power of $\Delta M/M \simeq 1/20000$ that will allow cleaning of

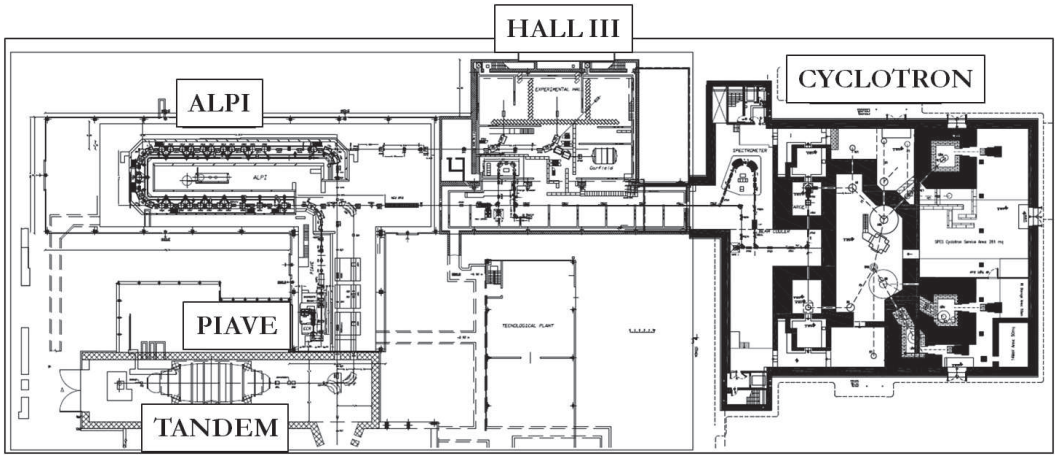

Figure 2.2: Overall layout of the SPES facility: the Cyclotron building housing the driver and the production target halls, together with the area dedicated to future applications are shown on the right part. In the middle the third experimental hall, where the charge breeder will be installed. On the left the accelerator complex in operation at LNL.

the desired radioactive ions from the isobars contaminant. The beam will then be transported towards the Charge Breeder [12] where its charge state will increase from 1+ to q+ allowing post-acceleration at high energy. After the Charge Breeder the highly charged radioactive beam will be analysed by means a Medium Resolution Mass Spectrometer MRMS ($\Delta(A/q)/A/q \simeq 1/1000$) in order to clean it up from the possible contaminants deriving from the breeding stadium. Finally, a new normal conductive RFQ injector [13], especially designed for SPES, and the superconducting linac ALPI will post-accelerate radioactive ions for nuclear physics experiments [14]. An overall cross section of the SPES layout is shown in figure 2.2.

The project is articulated in Work Packages (WPs) one of which, indicated with the letter "B" (WPB), is dedicated to the realization of the facility: it is divided in eleven Work Unit (WU), four covering some generals issues while seven directly related to the study, design and/or construction of parts of the facility. Table 2.1 gives an overview of the objectives of the WPB: each Work Unit is in turn subdivided into Sub-Unit: in particular the B9.3, denominated "Charge Breeder", is in charge of the design, construction and commissioning of the homonymous device, object of this PhD thesis. This work is being presently carried out in collaboration with the Laboratoire de Physique Subatomique et de Cosmologie (LPSC) of Grenoble. The activity, collocated in the framework of the LEA-Colliga between INFN and the French laboratory Grand Accéléraeur National d'Ion Lourds (GANIL), started in 2010 with a collaboration between LNL and LPSC for experimental activity on the charge breeder denominated PHOENIX [15], operating at Grenoble. It then proceeded in the following years in a more European context with the participation to the NuPNET project Enhanced Multi-Ionization of short-Lived Isotopes at EURISOL (EMILIE) [16], approved in 2011 and started in January 2012. The collaboration let, in June 2014, to the signature of a research collaboration agreement between INFN

Table 2.1: Description of the Work Packages "B" of the SPES project.

Unit	Objectives
B1: Scientific Support	Is the interface with future users and provide nuclear data and exotic beam identification tools.
B2: Radiation Protection and Safety	Gives the rules for all the aspects concerning conventional and radiation protection safety.
B3: Infrastructures	Follows the construction of the new building and plant installations and also the adaptation of the existing ones to the needs of the project
B4: Controls	Designs and manages all the hardware and software to control the various devices of the facility as the various signals for the safety system.
B5: Cyclotron	Follows the Cyclotron's construction and validates its acceptance tests together with the beam line up to the target.
B6: Exotic Beams	Is in charge of the construction and first operation of the Target-Ion Source system (TIS).
B7: Beam Transport and Selection	Is in charge of the beam dynamics and also of the design of the beam lines from the TIS to the charge breeder. Takes care also of beam diagnostic tools.
B8: RFQ	Chairs the design, construction and commissioning of the new RFQ injector for SPES.
B9: RNB-Accelerator	Is in charge of the Charge Breeder and its beam line until the completion of the commissioning phase. It is in charge also of all the modifications and upgrades of the ALPI booster.
B10: Mechanical and Engineering	Coordinates the mechanical design, drawings and construction of some components of the facility. Will follow-up the installation phase.
B11: Vacuum System	Is in charge of the design and purchase of the vacuum and gas recovery system for the beam lines. It will be also consultant for the vacuum systems of the various devices composing the facility.

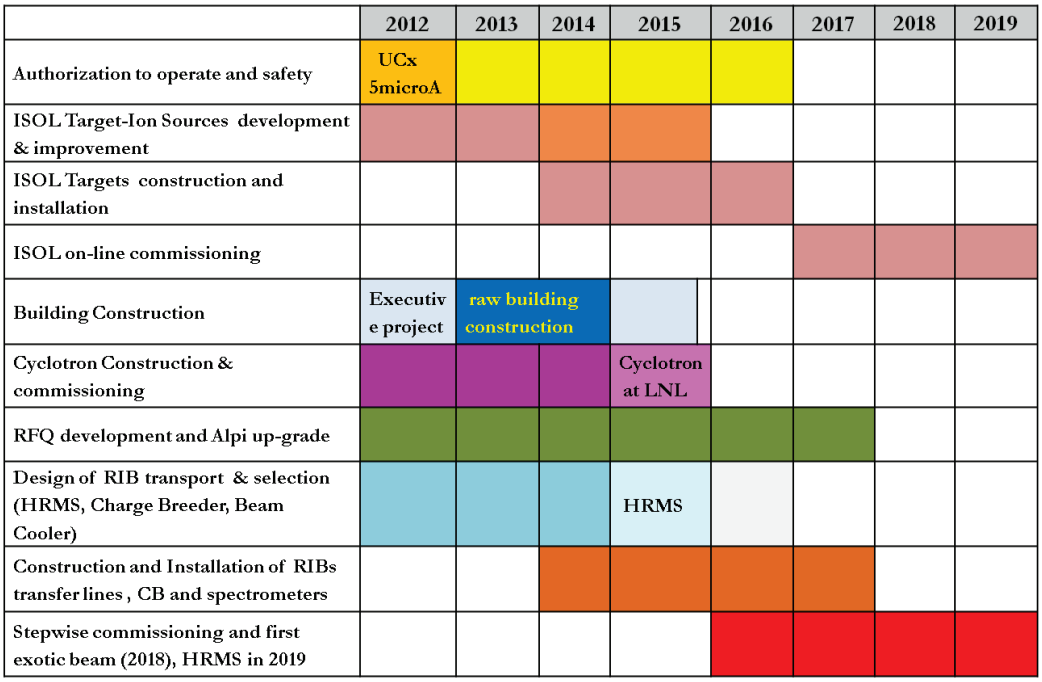

Figure 2.3: Overall planning of the SPES project.

and the French Institution CNRS for the delivery to SPES of an improved version of the French charge breeder from LPSC. The subject of this thesis is related to the activity performed in this framework between 2012 and 2014 and will be deeply described in dedicated chapters. Unfortunately the commissioning of the SPES-CB will be performed after the completion of this thesis, starting from March 2015. To properly conclude this section, figure 2.3 shows the general planning of the project from which it comes out that the first exotic beams are expected not before 2018.

2.3 Scientific context and physics case

The European road map for nuclear physics with RIBs goes through the development of second generation ISOL facilities pointing to EURISOL [17]: presently three facilities are under construction in Europe, HIE-ISOLDE [18], SPIRAL2 [19] and SPES. The common goal is to offer to the European and International Nuclear Physics community up-to-date neutron rich exotic beams and to improve the ISOL technology toward EURISOL. Expected performances for the new facilities are:

- **up to 10^{13} fission per second** and more in the production target.
- **post-acceleration** of the exotic beams at energies of **10*A MeV** and more to address nuclear physics questions through a wide range of reaction mechanisms.
- **improvement of selection** capabilities of the beam handling systems producing more pure exotic beams.

Within the Seventh Framework Programme (FP7) of the European Community a strong collaboration is going on, coordinated by Nupecc and funded by the ENSAR project. All the major nuclear physics European institutions are involved in order to carry out research at the forefront of fundamental nuclear science. In the framework of this collaboration up-to-date detectors are proposed for experiments, reshaping actual LNL detectors, like the PRISMA [20] spectrometer, exploiting new set-up, as the GALILEO [21] gamma array under construction, or performing campaign of measurements with complex detectors under construction among European collaborations (AGATA [22], NEDA [23], PARIS [24] and FAZIA [25]). The interest for SPES is demonstrated by the numerous letters of intent received: The most requested beam revealed to be the ^{132}Sn with the aim to study the shell evolution around the double magic numbers Z=50, N=82.

To understand the properties of a nucleus, apart from establishing the interaction between its components, it is necessary to determine the arrangement of the nucleons, that is its structure. Presently our knowledge about the structure of nuclei is mostly limited to nuclei close to the valley of stability or nuclei with a deficiency of neutrons: only recently the availability of beams of unstable ions has given access to unexplored regions of the nuclear chart, especially on the neutron-rich side. Starting from a nucleus on the stability line and adding successively neutrons, one observes that the binding energy of the last neutron decreases steadily until it vanishes and the nucleus decays by neutron emission. The position in the nuclear chart where this happens defines the neutron drip line: it lies much farther away from the valley of stability than the corresponding one associated with protons, owing to the absence of electrical repulsion between neutrons. The location of the neutron drip line is largely unknown as experimental data are available only for nuclei with mass up to around 30. The interest in the study of nuclei with large neutron excess is not only focused on the location of the drip line but also on the investigation of the density dependence of the effective interaction between the nucleons for exotic N/Z ratios. In fact, changes of the nuclear density and size in nuclei with increasing N/Z ratios are expected to lead to different nuclear symmetries and new excitation modes. While in the case of some very light nuclei a halo structure has been identified, for heavier nuclei the formation of a neutron skin has been predicted. Presently, neither the thickness nor the detailed properties of the neutron skin of exotic nuclei are known: this information is needed to enable a quantitative description of compact systems like neutron stars, where exotic nuclei forming a Coulomb lattice are immersed in a sea of free neutrons, a system which is expected to display the properties of both finite and infinite (nuclear matter) objects. At the energy of SPES it will be possible to address important questions related to the study of neutron-rich matter: with the high intensity beams delivered by SPES, a challenging and broader range of studies in nuclear spectroscopy and reaction mechanism will be performed. Effects of how the pairing interaction is modified in the nuclear medium will receive significant inputs by measurements of multi-nucleon transfer reactions to specific nuclear states. Effects of rotational damping in the decay of high energy levels, for instance the

dynamical dipole emission, will be studied by changing the N/Z of projectile and target. Neutron rich nuclei will be used to investigate the tunnelling process in sub-barrier fusion reactions in presence of very positive Q-values, an issue interesting also for astrophysics.

2.4 Description of the Facility

After giving an overview of the project and its scientific context, in this section the facility will be described in more details. On the basis of the organization in Work Unit, the facility can be divided into four "macro-parts": the driver, the so called Target-Ion-Source system, the Beam Selection and Transport and the Post-Acceleration. The four macro-parts parts are described in the following subsections.

2.4.1 The proton driver

As a driver for the SPES project a cyclotron accelerator [26] delivering proton beams was chosen: from the point of view of the acceleration, it consists in a circular vacuum chamber immersed in a high vertical magnetic field. Low energy ions are injected from the central region with a velocity orthogonal to the external magnetic field so that they start moving on circular orbits due to the Lorentz force. In the first versions, the vacuum chamber was usually divided into two identical parts, called "Dee", separated by a gap: an RF system synchronized with the particle motion accelerates it when crosses the gap between the Dees, increasing its energy. This energy increase causes the radius of the particle's orbit to grow till a maximum (connected to the dimension of the machine), at which the particle is extracted by means of an electric field or a stripping process. The SPES driver will be a room temperature cyclotron able to deliver two simultaneous proton beams for a total of 750 μA, with a variable energy between 30 and 70 MeV [27]; the cyclotron is at present going to be shipped at LNL by the BEST Cyclotron System (BCSI) company and is expected to be installed at LNL in middle 2015. This machine is a four straight sectors one (see figure 2.4), accelerating H^- ions that are extracted by the stripping process to get the desired proton beams; the main advantage of the H^- acceleration is the possibility to extract simultaneously two proton beams by sharing the total current available. The accelerated ions are produced by a multi-cusp ion source: 10 mA of H^- will be extracted at 40 kV, focused by two solenoids and three quadrupole magnet, bunched and then vertically injected into the cyclotron with an expected normalized emittance of 0.605 π*mm*mrad. Figure 2.5 shows a picture of the cyclotron and its beam lines.
Within SPES a new building is under construction at LNL to house the new accelerator and its applications: this building will be a three levels structure with an underground lower level, hosting the cyclotron and the target caves. The area will be heavily shielded according to the expected production of gamma and neutrons in the target points and beam losses along the transport lines. During the operation neutrons

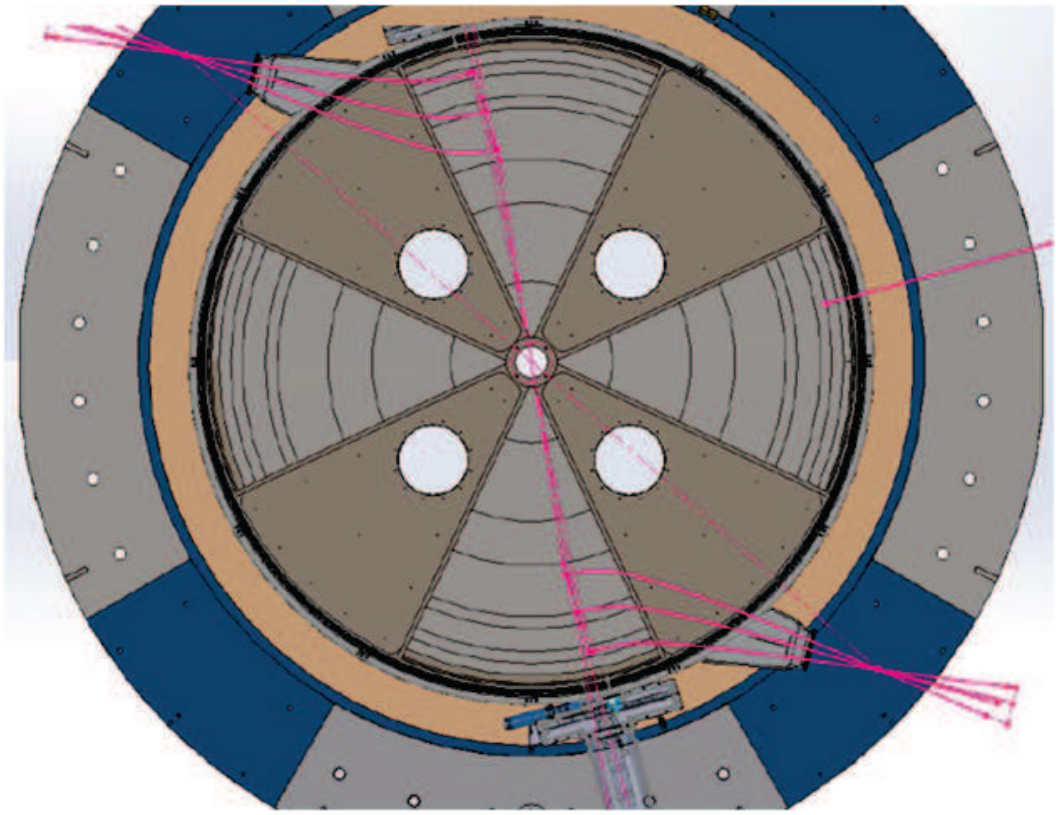

Figure 2.4: View of the 4 sectors vacuum chamber of the SPES cyclotron.

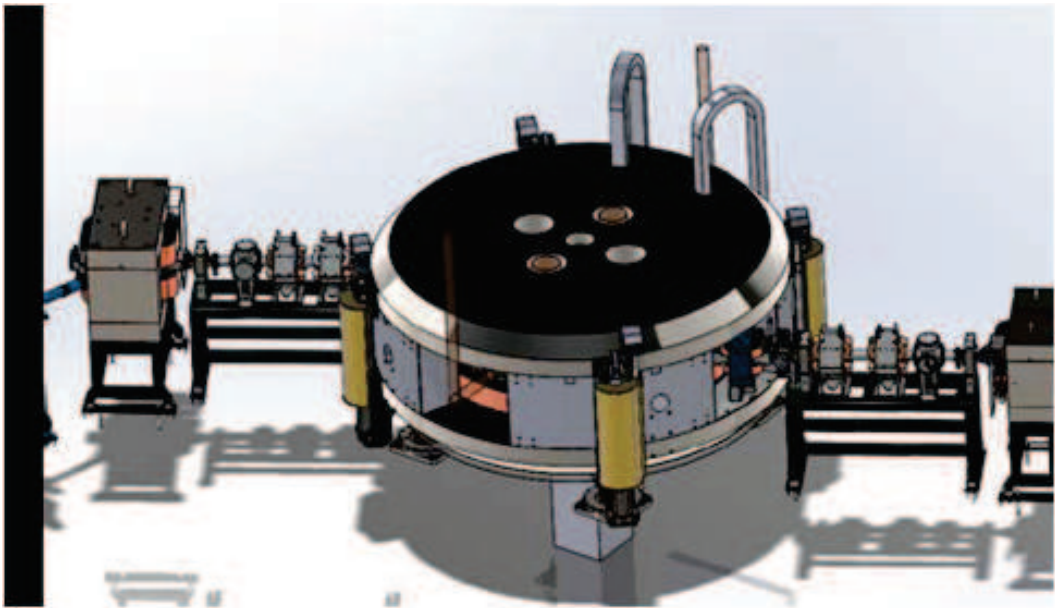

Figure 2.5: The SPES cyclotron and its beam lines.

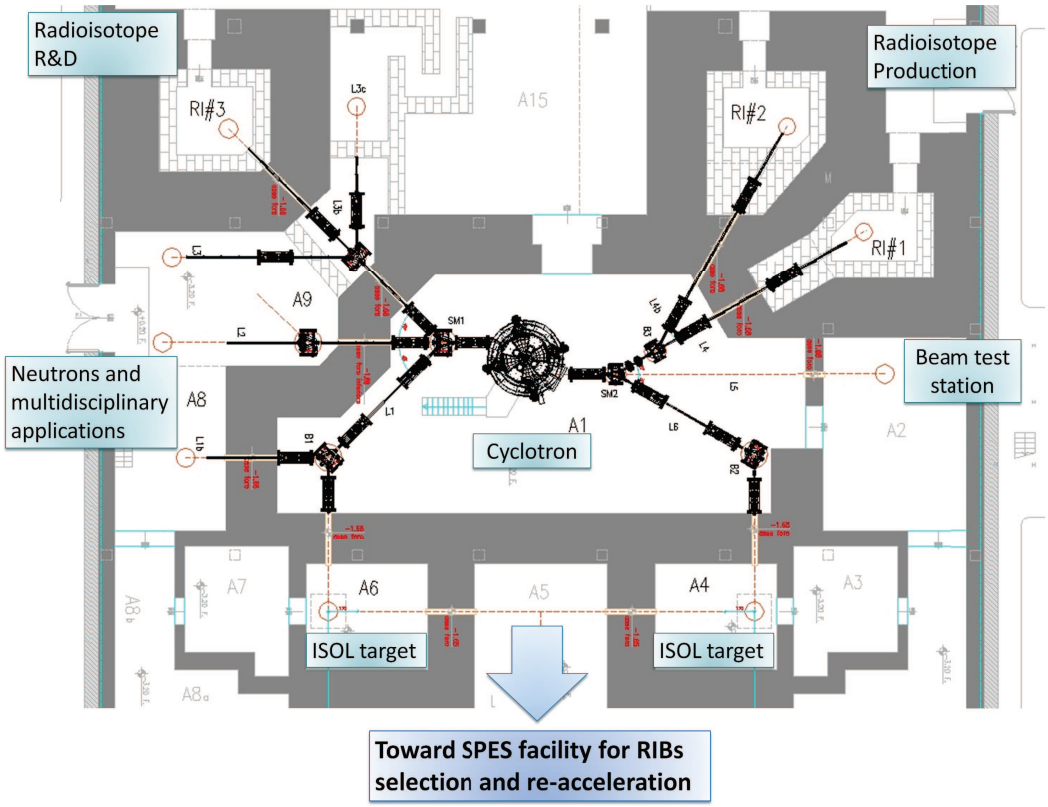

Figure 2.6: Sketch of the new building at the cyclotron level. All the possible applications of the proton beam are indicated.

will produce the activation of the air: to prevent the escape of radioactivity, the pressure in the cyclotron cave will be kept lower than atmospheric by a dedicated ventilation system. Figure 2.6 shows a sketch of the the new building at the cyclotron level together with the experimental halls that will use the proton beam for different applications.

2.4.2 The Target-Ion Source System (TIS)

The interaction of the proton beam with the Uranium Carbide target (UC_2+2C, namely UC_x) will produce fission fragments with masses ranging from A=60 to A=160, among which the neutron-rich isotopes of interest [28]. The proposed target represents an innovation of the one adopted at ISOLDE: it is composed of 7 UC_x disks (diameter and thickness respectively of 40 and 1.3 mm), appropriately spaced in the axial direction in order to dissipate by radiation the average power of 8 kW due to the proton beam. The target is contained in a graphite box housed inside a tubular tungsten ohmic heater, making up for the thermal losses due to heat exchange by radiation.

The isotopes produced will diffuse from the crystal lattice to the grain boundary and to the surface of the target disks and effuse towards an ion source directly

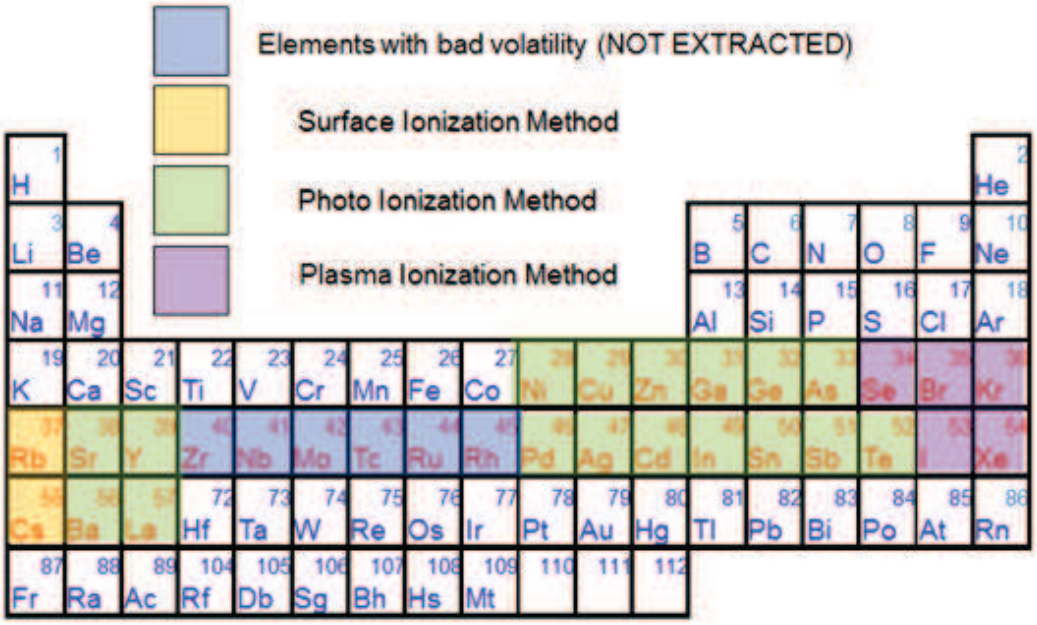

Figure 2.7: The SPES fission isotopes produced by the three main ionization schemes considered.

connected with the production target, where they will become singly charges ions. Figure 2.7 shows the fission isotopes that will be produced at SPES: as can be seen, the refractory elements (Zr, Nb, Mo, Tc, Ru, Rh) have a too low vapour pressure at the operating temperature of the target and will not escape from it. The remaining elements can be classified taking as a reference their first ionization potential and consequently choosing the most appropriate ionization mechanism: figure 2.8 shows the three available at SPES. They will be implemented by means of three ion sources: a surface ionization source (SIS) [29], a laser ion source (LIS) [30] and a plasma ion source (PIS) [31]. The three ion sources, at present under development at LNL on the basis of the ones used at CERN, have in common the external part but differs for the vacuum chamber where the ionization takes place.

The surface ionization source can provide mainly singly charged alkali metal and alkaline earth metal ion beams, and in general is applied to elements with ionization potential lower than 6 eV (in particular for Rb and Cs, but also for Sr and Ba). This technique is quite selective and can allow to reach high values of the ionization efficiency (up to 60%), defined as the number or radioactive species extracted as 1+ ions divided by the number of radioactive species that arrive at the ion source. Metallic elements indicated in green in figure 2.7, being characterized by a first ionization potential between 6 and 10 eV, are expected to be ionized by the laser ion source: basically it consists in the surface ionization source adapted to accept a laser beam injected from the extraction hole. The laser ionization technique is surely the most selective one but possible contaminants can anyway be produced due to the always present surface ionization mechanism. The electron impact ionization

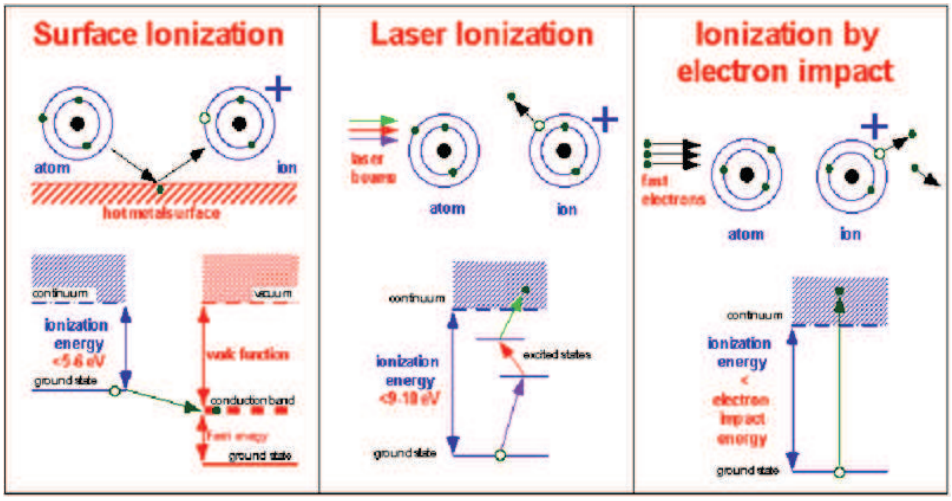

Figure 2.8: The three different schemes for the +1 isotope ionization.

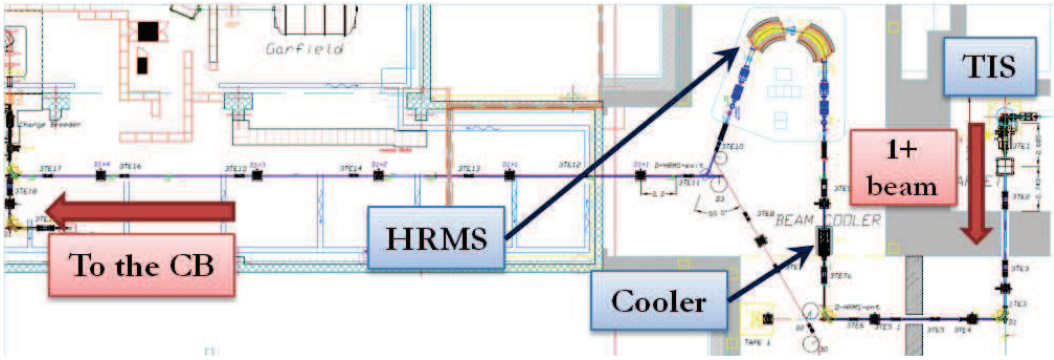

Figure 2.9: The beam line from the TIS to the post-acceleration stage: the Cooler and the HRMS will be described in a following subsection.

mechanism is indicated for the noble gases (Kr and Xe), the halogens (Br and I), and for Se: all these elements are characterized by an ionization potential higher than 10 eV. This ionization technique is not selective, but can reach quite high ionization efficiency (up to 40% in the case of Xe).
From the point of view of the beam quality, the plasma ion source is the one showing the worst characteristics. Its rms emittance is 2-3 times higher than the other two sources. Measurement performed at LNL with Argon at 25 kV of extraction voltage showed an rms value of of 12 π*mm*mrad without target out-gassing and fission products. A 2 times higher value can be expected for online operation.

2.4.3 Beam selection and transport

This part of the facility is in charge of the purification and transport of the radioactive beam from the TIS to the post-acceleration stage: an overview of the beam line is shown in figure 2.9. The singly charged radioactive ions will be extracted from the ion sources at a maximum energy of 40 keV: a first rough mass selection will be done

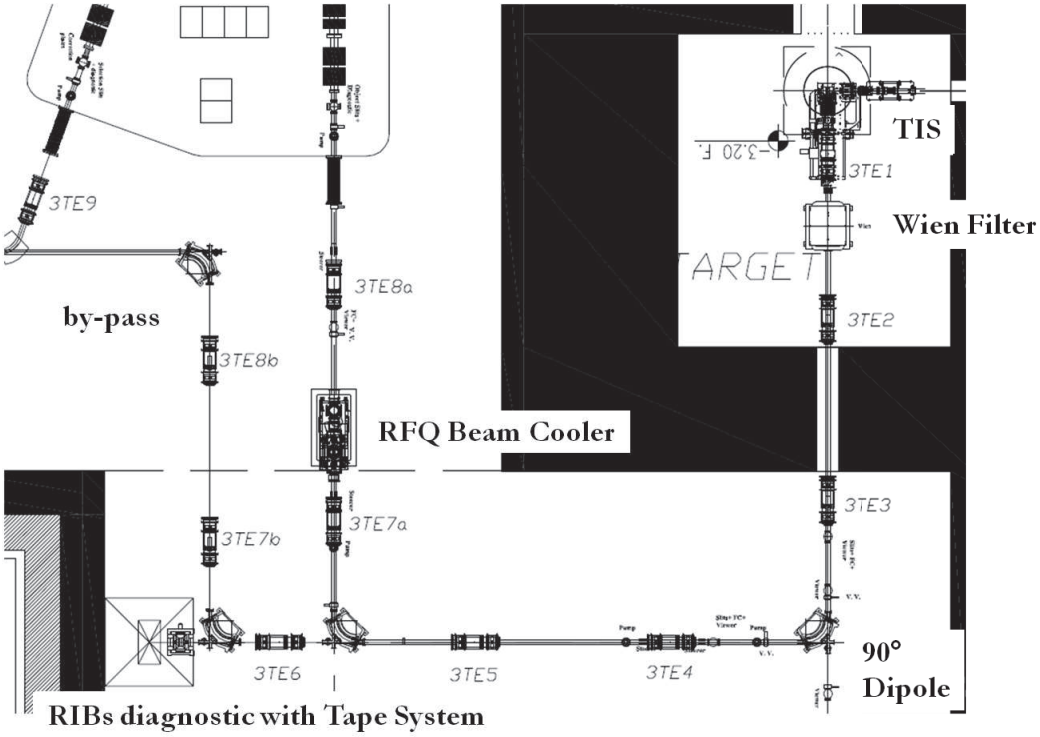

Figure 2.10: Detail of the part of the beam line where the first selection takes place; the layout of the High Resolution Mass Spectrometer refers to a previous design.

by mean of a Wien filter with $\Delta M/M \sim 1/100$ (mounted inside the bunker) and a 90° dipole with $\Delta M/M \sim 1/200$ (outside the bunker, see details in figure 2.10), allowing to stop inside the bunker almost the 90% of the radioactive contaminants coming out from the ion source. The main focusing elements of the beam transport line are electrostatic quadrupoles while the bending elements is mass independent for a given extraction voltage.

After the first selection, the radioactive beam of interest is still contaminated by the isobars created inside the target and extracted at the same time: to remove this contaminants an High Resolution Mass Spectrometer (HRMS)[32] with a resolving power of 1/20000 will be implemented. This spectrometer (see figure 2.11) is a scaled version of the one designed for CARIBU at Argonne National Laboratories [33]: it will consist in two 90° bending dipoles with a radius of 2.6 m, four quadrupoles, two hexapoles and one multipolar corrector (up to); to increase the beam energy and so the resolution the HRMS will be placed on a high voltage platform with a maximum voltage of -220 kV. The HRMS is still in a design phase: in the very first phase of the project a "by-pass" line will be used to deliver the beams to the post-acceleration as indicated in figure 2.10.

To help in reaching the desired resolution with the HRMS, the 1+ beam will be first injected into a buffer gas-filled Radio Frequency Quadrupoles (RFQ) cooler [10,34] to lower the transversal emittance. In those devices the temperature of the

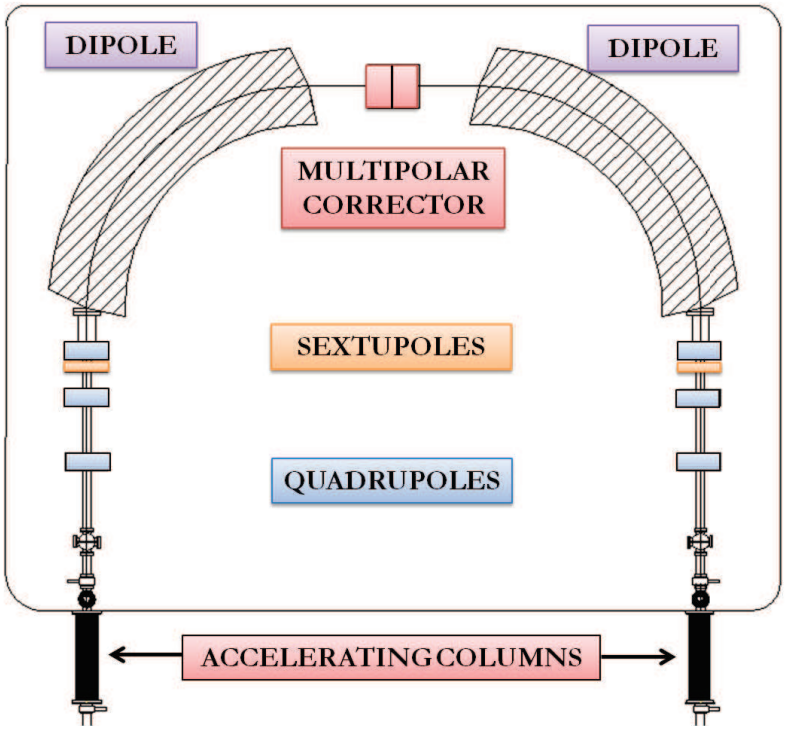

Figure 2.11: Sketch of the High Resolution Mass Spectrometer (HRMS) based on a design from the CARIBU project at ANL.

ion beams is reduced via successive collisions with the atoms of a buffer gas; an RF voltage with amplitude V and frequency ω_{RF} is applied to the rods of a quadrupole in phase opposition: the motion of the ions is then governed by the so-called Mathieu parameter Q [35]

$$Q = \frac{4qV}{mr_0\omega_{RF}} \tag{2.1}$$

where q is the charge and m the mass of the ion, and r_0 is one half of the distance between two opposite rods. The best condition for an efficient ions thermalization is $0 < q < 0.5$. This device is composed by 3 main sections: the deceleration system, which provides the reduction of the energy of the incoming beam from the nominal energy to some hundreds of eV; the main body of the cooler where the beam is confined by the RF field and cooled by collisions with a buffer gas (usually helium) at a pressure from 0.5 to 3 Pa; finally the extraction part where the beam comes out at the same energy as the injection but with a lower emittance. In the cooling phase ions are dragged to the exit by a longitudinal component of the electric field provided by DC potentials applied to the successive RFQ segments. The preliminary design of the device started in 2011 in the framework of the REGATA experiment approved by the V scientific committee of INFN and prosecuted within the COOLBEAM experiment [34]; a picture of the designed device can be seen in figure 2.12. Both the HRMS and the Beam Cooler will be installed in the same building housing the cyclortron.

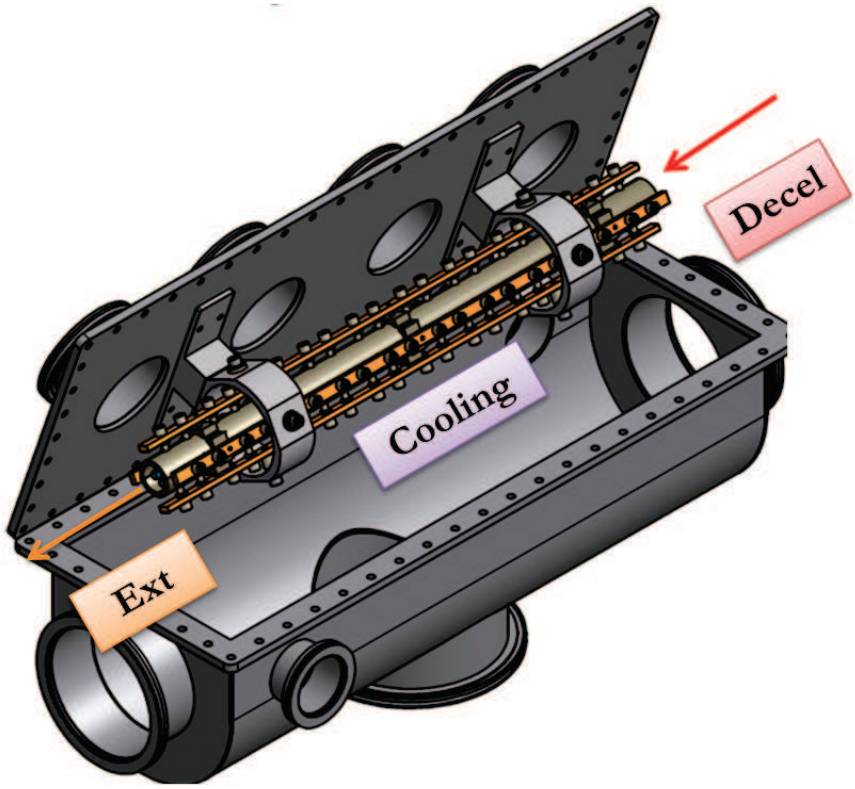

Figure 2.12: Layout of the quadrupole structure under construction at LNL.

2.4.4 The post-acceleration

After passing through the HRMS the radioactive beam will be cleaned from contaminants and will be ready for post-acceleration: anyway, a charge state 1+ is too low to reach a final energy around 10*A MeV keeping the overall dimensions and costs of the accelerator on a reasonable level. For this reason a further device has to be implemented, able to accept a 1+ beam, multiply its charge state and extract it as a q+ beam: this work is done by the so called "Charge Breeder" (CB). An ECRIS type CB was chosen for the SPES project: it was developed on the basis of the PHOENIX booster [36,15] and is presently being installed at LPSC (Grenoble) for the acceptance test. This device is the object of this thesis and will be deeply described in the following chapters.
The highly charged ions extracted from the charge breeder are expected to have a mass-to-charge ratio A/q between 4 and 7 and a maximum energy of 40*q keV: they will be injected into an especially designed Medium Resolution Mass Spectrometer (MRMS) [32] with a resolving power of $\Delta(A/q)/A/q \simeq 1/1000$: this in order to remove possible contaminants introduced by the breeding stage (see chapter 5 for more details). Both the charge breeder and MRMS will be installed inside the existing III experimental hall. The beam will be transported through a magnetic beam line and injected into the first acceleration stage consisting in a CW Radio Frequency Quadrupole (RFQ) especially designed for SPES [13]. The new injector, working at

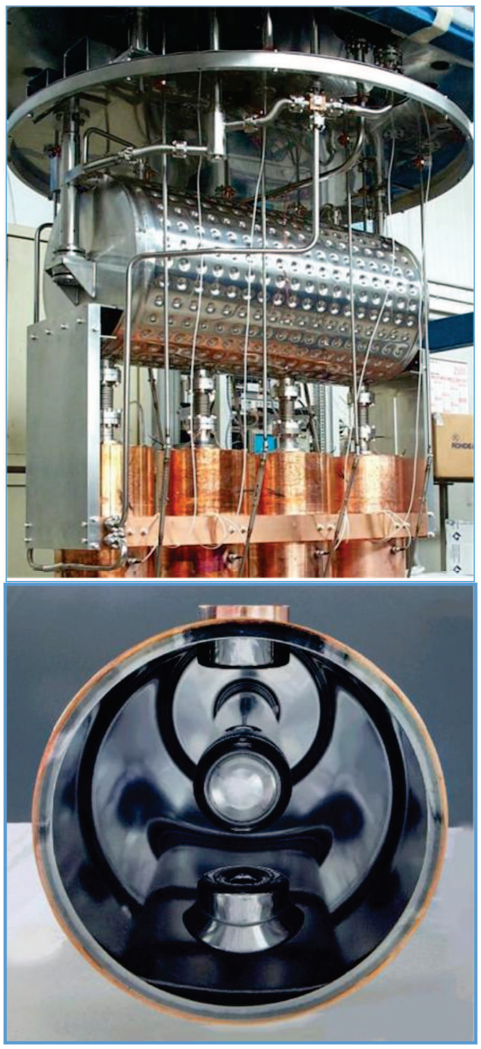

Figure 2.13: Accelerating cavities for ALPI: picture of the internal part of a cryostat housing 4 cavities (top); detail of a superconducting cavities (bottom).

80 MHz, has an injection energy of 5.7*A keV and an extraction energy of 727*A keV; it will be installed in the existing "area 2" of the accelerator building. Finally the beam will be injected into the superconducting linac ALPI [37]: this accelerator, working at LNL since 90's, is a modular superconducting machine consisting in 17 cryostats, each housing four quarter wave resonator: a detail of the cryostat and the cavity is shown in figure 2.13. Particles are accelerated two times per cavity by electric fields with amplitudes from 3 to 5 MV/m. The linac can be divided into three section depending on the value of $\beta = v_{beam}/c$: the low-β section working at 80 MHz and the medium and high-β sections working at 160 MHz. In the framework of the SPES project an upgrade of ALPI was proposed in order to make it suitable to accelerate even heavy ions at more than 10*A MeV with a very high transmission. In particular, a cryostat will be added to the low-β section and the accelerating fields of its cavities will be increased to 5 MV/m; a further cryostat will be also added at

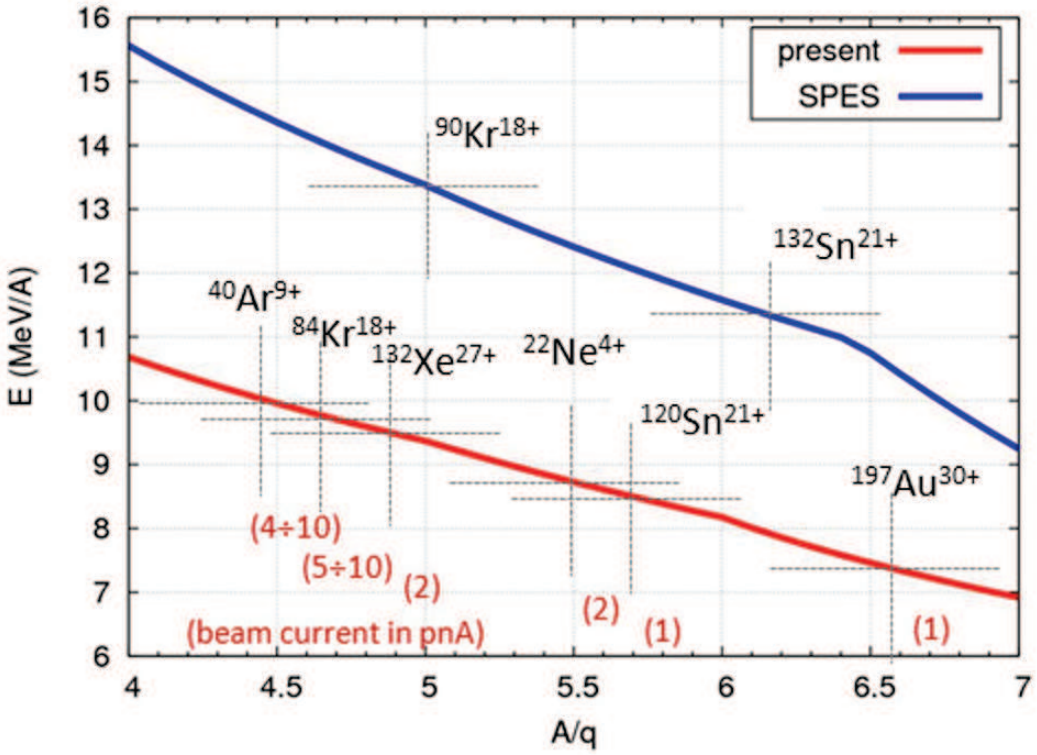

Figure 2.14: Comparison between the current performances in terms of final energy at the end of ALPI and the one expected after the upgrade planned for SPES.

the end of the acceleration. To improve the transmission of the high energy beams expected for SPES, the gradients of the magnetic triplets used to transport the beam will be increased from 20 T/m to 25 T/m. Figure 2.14 shows a comparison between the actual performances of the positive ions accelerator complex at LNL and the ones expected for SPES: it can be seen that the energy will be higher than 10*A MeV for the most of the A/q ratios of interest. It has to be pointed out that the actual performances are obtained with the linac ALPI fed by the superconducting RFQ PIAVE [38].

An R&D on low-intensity beam diagnostics, required from the target-ion-source system to the final experimental stations after ALPI, is going on at LNL too. The ideal situation would be to have the same diagnostic box able to handle both the low-intensities expected for the radioactive beams and the high-intensities of the stable beams used to set the facility. For the current monitors a lot of efforts are devoted to develop electronics with a very low signal-to.noise ratio in order to measure down to 10 fA; below this value, a counting technique is the only choice to verify the beam current. To help in transporting the beam during acceleration, beam position and profile monitors based essentially on micro-channel plates (MCP) put directly online are under test at LNL; in specific points of the beam line tape stations for radioactive ions identification and counting will be mounted [39,40].

Chapter 3

The Charge Breeding Techniques

3.1 Introduction

This chapter will deal with the description of the different charge breeding techniques adopted nowadays. The charge breeder is a fundamental device of an ISOL facility that accepts an incoming 1^+ beam, multiplies its charge and gives as output a q^+ extracted beam, allowing post-acceleration of radioactive ions; its performances determine the yield of a given accelerator complex in terms of intensity and attainable final energy. Different techniques have been developed so far but, whatever the particular one applied, any charge breeder has to fulfil some basic requirements:

- If I_{1^+} is the current of a given element injected into the charge breeder and I_{q^+} is the current extracted on a given charge state, the **efficiency** defined as $\eta_q = I_{q^+}/q^+ I_{1^+}$ has to be as **high** as possible for all the masses of interest. Its dependence on the amount of particles injected or the injected beam characteristics (that is, current and emittance of the 1+ beam) should be low. This aspect directly influences the intensity delivered to the experiments.

- The output charge states have to be as **high** as possible: the final energy attainable from a linac is in fact directly proportional to the ratio **A/q** of the accelerated beam. This is even more evident for Cyclotrons whose final energy depends on the square of this ratio.

- The **charge breeding time** τ_{cb}, that is the time necessary to further ionize 1^+ ions and let them be available as a q^+ beam, has to be **short** in order to avoid decay losses of the radioactive ions.

- The **contamination** due to the charge breeding process should be **limited**.

Other requirements, in common with all the ion sources but even more important for an ISOL facilities, are a good quality of the extracted beam and a high reliability; considering also that usually the intensities of the radioactive beams are so low to not allow a real tuning, a charge breeder has to be easy to operate, giving reproducible performances. In the following sections the three techniques historically used for

charge breeding will be described: the first, the stripping technique, consists in using a passive device to further ionize an ion beam striking on it; the other two consist in adapting ion sources for stable beams to operate as a charge breeder: this is done using Electron Beam Ion Sources (EBIS) [41] or Electron Cyclotron Resonance Ion Sources (ECRIS) [42].

3.2 Stripping

This technique is presently not used with radioactive beams so it will be just mentioned for the sake of completeness; on the contrary, it is routinely employed to strip stable ions inside electrostatic accelerators like a Tandem or all along the beam lines of a superconducting linac. This technique consists in letting an ion beam impinges on a foil made of a light element, usually carbon: if the incident velocity is high enough (E $\geq$ 500*A keV), primary ions loose electrons due to the interaction with the target atoms and the outgoing beam shows a higher average charge. Such quantity can be predicted by means of the following formula obtained through a least-square fits on 850 experimental data points by G. Schiwietz and P.L. Grande [43]:

$$q_{mean} = Z_p \frac{12x + x^4}{0.07/x + 6 + 0.3x^{0.5} + 10.37x + x^4} \tag{3.1}$$

with

$$x = \left(\frac{v_p/v_0 Z_p^{-0.52} Z_t^{-0.019 Z_p^{-0.52} \frac{v_p}{v_0}}}{1.68} \right)^{1+1.8/Z_p} \tag{3.2}$$

In the previous formulas v_0 is the Bohr velocity (v_0 = 2.19x10^6 m/s), v_p is the projectile velocity, Z_p is the projectile nuclear charge and Z_t is the target nuclear charge. In the case of carbon foils an handy formula allows to estimate also the width of the charge state distribution supposing it to be Gaussian (not valid for very low projectile's nuclear charge or very high average charge):

$$\sigma = 0.5 \sqrt{q_{mean} \left(1 - \left(\frac{q_{mean}}{Z_{proj}} \right)^{1.67} \right)} \qquad for \qquad Z_{proj} < 54$$

$$\sigma = \sqrt{q_{mean} \left(0.07535 + 0.19 \left(\frac{q_{mean}}{Z_{proj}} \right) - 0.2657 \left(\frac{q_{mean}}{Z_{prof}} \right)^2 \right)} \qquad for \qquad Z_{proj} \geq 54. \tag{3.3}$$

About the characteristics of the foil, it was found that it exists an "equilibrium" thickness defined as the value above which the charge state distribution of the outgoing beam does not change further: this value is about two times x_{66} where $x_{66} = 2.43 \cdot W_p^{1.47}$, where W_p is the projectile energy per nucleon [44]. The stripping by carbon foil is very fast and simple: anyway, a pre-acceleration is needed in order

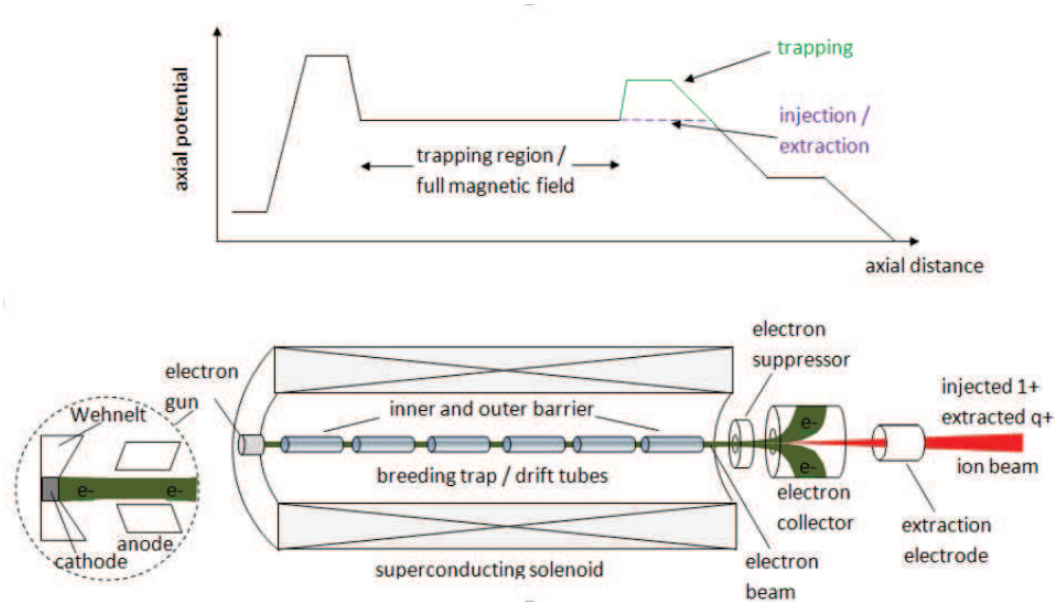

Figure 3.1: Schematic view of an EBIS source (lower part) together with the distribution of the trapping electrostatic potential (upper part).

the incoming beam to reach an energy high enough for the relations given above to be valid. More, the efficiency on a given charge state is very high for lights elements but tends to decrease as the nuclear charge of the incoming beam increases, due to the broader charge state distribution; in this last case the lifetime of the foil becomes another issue. For lower energy beam (E∼5-25*A keV) the gas stripping technique can be used but the charge increase is so small to not allow post acceleration to high energies unless for very light elements.

3.3 The EBIS-based Charge Breeder

EBIS sources [41]are able to produce very high charge states of heavy elements: they consist in a strong axial magnetic field (from 2 up to 8 T), created by a long solenoid, and of an axial electrostatic potential generated by cylindrical electrodes. An electrons gun produces an intense beam, focused by the magnetic field, that generates ionizations to very high charge states. The injected singly charged ions are guided towards the center by the magnetic field lines, radially trapped by the electron beam space charge and axially confined by the electrostatic trap: a schematic view of an EBIS charge breeder [45] is shown in figure 3.1.
They key parameters of this device are:

- The **electron beam** characteristics, defined through the total current I_e, the current density j_e and the beam energy E_e. This last parameter mainly determines the maximum reachable charge state, affecting the cross-section for electron-impact ionization. The role of I_e and j_e can be guessed but will be

clear below.

- The **magnetic field**, which compresses the electron beam of current I_e to the required current density j_e. Stronger magnetic field leads to a shorter breeding time, but also a smaller transverse trapping acceptance due to the reduced beam radius.

- The design of the **trapping region**, especially the trap length L, that affects the charge capacity.

In such devices the time necessary to reach a given charge state q^+ (equivalent to the charge breeding time τ_{cb}) is given by the relation:

$$\bar{\tau_q} = \sum_{i=1}^{q-1} \bar{\tau}_{i\to i+1} = \frac{1}{j_e} \sum_{i=1}^{q-1} \frac{e}{\sigma_{i\to i+1}} \tag{3.4}$$

where $\sigma_{i\to 1+1}$ is the cross-section for stepwise ionization and j_e is the electron current density. Supposing that the electron energy E_e is chosen so as to maximize the ionization cross section for a given charge state ($E \sim 2.7 \cdot I_p^q$ with I_p^q the ionization potential of the desired charge state q+), it is clear that the charge breeding time can be made shorter acting on the electron current density. This can be accomplished either by increasing the electron current or by increasing the focusing magnetic field. The charge capacity of a trap can be readily calculated through the formula

$$Q = 3.32 \cdot 10^{11} \times f \times L \times I_e / \sqrt{E_e} \tag{3.5}$$

where Q is the maximum number of positive charges that can be trapped, f is the actual electron beam compensation factor (attainable values are between 0.5 and 0.7), L is in m, I_e in A and E_e in keV. From the point of view on the injection, the 1+ beam emittance should be low in order to match the limited spatial acceptance of this device. The extracted beam is intrinsically pulsed as ions are usually injected and extracted through a unique opening by lowering the electrostatic barrier (see figure 3.1): for this reason the EBIS requires a preparation stage, for example with a Penning trap like at REX-ISOLDE [46], to accumulate, cool and bunch the singly charged ions to be injected. Such a trap has usually an efficiency around 50% and this value has to be taken into account while comparing the overall performances of different charge breeders. Considering also that the cooling time by the trap is of the same order of magnitude of the breeding time the overall preparation time of a charge bred radioactive beam with an EBIS is actually twice its breeding time. The spectrum extracted from this device reveals a very low level of stable background level, obtaining a very clean beam; a drawback of this technique is the high energy spread of the extracted beam (Tens*q eV).
REXEBIS at ISOLDE, CERN has been the first charge breeder routinely delivering beams to a post-accelerator facility [47]: it is useful to make a numerical example about the capacity of such device, using the parameters showed in table 3.1. By

Table 3.1: Characteristics of REXEBIS at ISOLDE.

B-field	2T
Electron beam	Cathode LaB6 $j_{cathode} < 20$ A/cm^2 $j_{trap}/j_{cathode} \sim 10$; $j_e = j_{trap} < 200$ A/cm^2 $I_e = 460$ mA (normal operation 200 mA) $E_e = 3.5 - 6$ keV
Trap	3 drift tubes L=200 to 800 mm Capacity 5x10^{10} positive charges
Acceptance	11 π*mm*mrad (95% geometrical) for 60 keV estimates for $A \simeq 30$
Emittance out	15-20 π*mm*mrad (95% geometrical) for 20*q keV measured with a non-separated beam
Max. energy spread	50*q eV (estimated)
Vacuum	$10^{-10} - 10^{11}$ $mbar$ 10^{-7} $mbar$ without plasma
Pulse length	FWHM 40 to 300 μs

putting the numbers in the equation 3.5 we obtain a capacity of $3 \cdot 10^{10}$ charges: if we want those charges to be composed by ^{132}Sn ions with the 20% on the charge state $^{132}Sn^{34+}$, then the number of ions per pulse should be $3 \cdot 10^{10}/34 * 0.2 = 2 \cdot 10^8$ ions/pulse. The actual ion throughput (ions/s) is obtained by dividing this last number by the charge breeding time.

3.4 The ECRIS-based Charge Breeder

ECR ion sources [42] are very common device to produce intense beams of highly charged ions for nuclear physics experiments. In such devices microwaves are injected inside a vacuum cavity (that works as a resonant cavity) surrounded by a particular magnetic configuration called "B-minim structure". This configuration is obtained by superimposing the (axial) field generated by two or three coils and the (radial) field generated by a hexapole: the result is a magnetic field growing from the center of the chamber towards its periphery, giving to the plasma the typical triangular shape as shown in figure 3.2. The magnetic field helps in confining the plasma created by the so called Electron Cyclotron Resonance (ECR) between the injected microwaves of given frequency ν_{MW} and the cyclotron motion of free electrons inside the magnetic field with an angular frequency $\nu_c = eB/2\pi m_e$: this process leads to the creation of high energy electrons that produces high charge states through stepwise ionizations. Those electrons are also responsible for the creation of a negative potential dip at the center of the plasma that further improves the confinement of the ions. To transform

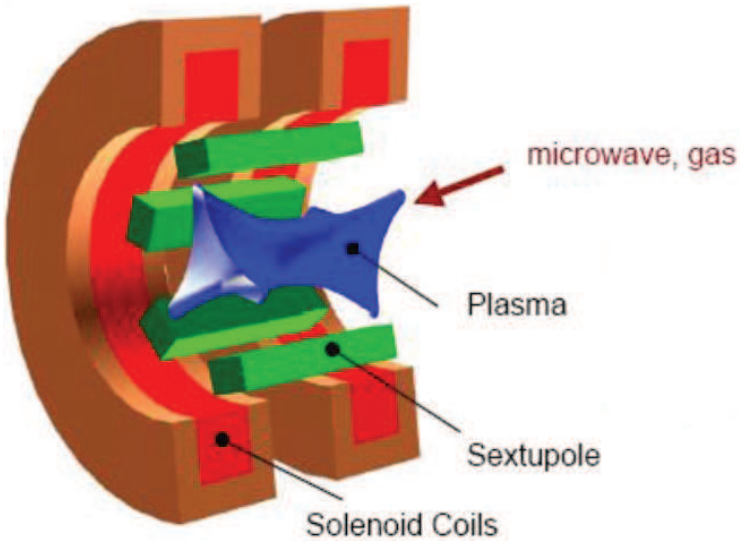

Figure 3.2: Sketch of a B-minimum structure obtained by superimposing the fields generated by two coils (red) and an hexapole (green).

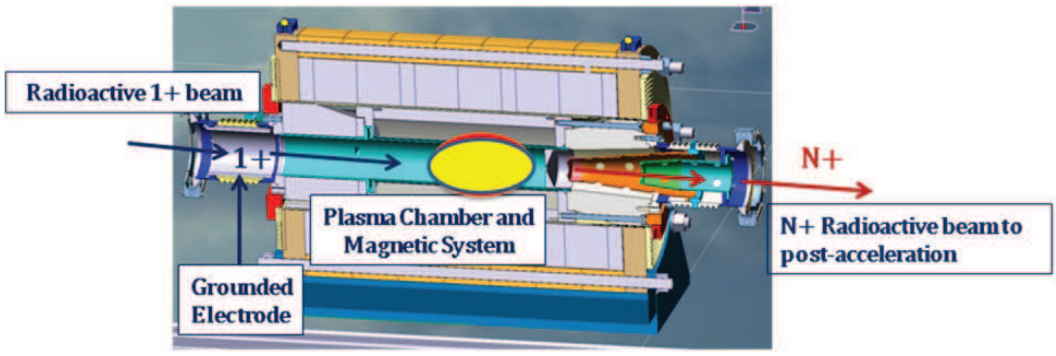

Figure 3.3: Schematic view of the injection of a 1+ beam inside the PHOENIX charge breeder.

these device into a charge breeder, usually the injection part is modified so as to accept the incoming 1+ beam, leaving basically free space, as shown in figure 3.3, or by mounting a grounded tube going inside the source as close as possible to the plasma; the charge bred beam is extracted from the opposite side allowing this device a continuous or pulsed injection and extraction.

A particular model, called the PHOENIX charge breeder designed by LPSC [48], was chosen for the SPES project and is the object of this thesis: for this reason the base mechanisms of an ECRIS-based charge breeder will be extensively described in the following chapters, underlining its peculiarities with respect to the homonymous ions source and focusing the attention on the SPES model. Some characteristics of the PHOENIX charge breeder are given in table 3.2: in the present section only a general description of an ECRIS-based charge breeder will be given, sufficient to compare it with the previous techniques.

Table 3.2: Characteristics of the PHOENIX charge breeder.

Microwave Frequency	14.5 GHz Max power 1 kW
Magnetic confinement	B_minimum Structure 3 axial coils and a permanent magnet hexapole $B_{inj} = 1.5\ T$; $B_{ecr} = 0.52\ T$; $B_{min} = 0.5\ T$; $B_{ext} = 1\ T$; $B_{rad} = 1.35\ T$
Available A/q	<7
Plasma chamber	$\sim 1\ l$ volume stainless steel
Acceptance	55 π*mm*mrad at 20 keV (90%)
Emittance out	$<$ 80 π*mm*mrad at 20*q keV (90%)
Energy spread	$\sim$ 15 eV
Vacuum	some $10^{-7}\ mbar$ in the injection and extraction region $< 10^{-7}\ mbar$ without plasma
Support gas injection	usually O_2 at $5 \cdot 10^{-5} mbar \cdot l/s$

In ECRIS charge breeders [45] the 1^+ radioactive beam is stopped and captured by Coulomb collisions with plasma ions: once inside the plasma, radioactive ions are further ionized by electron impact and then extracted as q^+ beam. In these devices, the charge breeding τ_{cb} is defined as the time between the injection of the 1^+ beam and the q^+ extracted current reaching the 90% of its maximum: it was observed experimentally that this time can be estimated through the empirical relation $\tau_{cb}(q^+) \sim 5 \div 10$ ms*q. These charge breeders are able to handle very intense injected beams without compromising the breeding efficiency: the global capture is quite high, usually around 50% for metallic 1+ beams and up to 80% for gaseous ones. This difference is due to the fact that gaseous ions benefit from wall recycling and have more chances to be ionized; unfortunately this high global efficiency is spanned over a broad charge states distribution. The quality of the extracted beam in terms of emittance is determined by the magnetic field intensity (supposing an optimized extraction system), while the energy spread (usually difficult to be measured) is estimated to be around 15 eV. If the incoming 1^+ beam has an energy $E = eV_{1^+}$, to have a proper injection into the charge breeder its potential should be $V_{CB} = V_{1^+} - \Delta V$, where the $e\Delta V$ is necessary energy for the injected ions to overcome the plasma potential barrier and to be stopped and captured close to the center of the plasma. As will be clear later in this thesis, the regulation of this ΔV is a very important parameter determining the efficiency of the charge breeder. The experience gained in the last years showed also an high sensitivity of the breeding performances to the base vacuum of the charge breeder [49].

Unfortunately, a drawback of this device is the presence of a stable background due to the use of support gas and the emission of neutrals by the parts exposed to the

plasma: this could contaminate or even hide the peaks of the radioactive ions. As will be mentioned in the chapter dedicated to the SPES charge breeder, this problem can be limited by two means: on one hand, by paying attention to the treatment of all the surfaces exposed to vacuum, as demonstrated at KEK [50]; on the other hand, by adopting a q^+ spectrometer with a high resolving power ($\Delta(A/q)/(A/q) \sim 1/1000$), as in the case of SPES.
The first application of an ECRIS source to the charge breeding was done in the late 90's with a model called MINIMAFIOS, thanks the pioneering work performed by Prof. Geller's group for the PIAFE project [51, 52]. The PHOENIX model was then designed and tested [53] in order to improve the obtained performances: in particular, on-line results were obtained with this charge breeder at ISOLDE [54]. The first post-accelerated beams were produced at KEK for the TRIAC facility [55]. Presently ECRIS charge breeders are operational at TRIUMF [56] and ANL [57].

3.5 The choice for SPES

The choice of a particular technique to charge bred RIBs for post-acceleration influences the entire facility in terms of attainable final energy and intensity: in this section the reasons that led to the particular choice for SPES will be justified by means of a comparison between the two techniques.
Among the two, the EBIS charge breeder itself is surely the most performing in terms of charge states obtained, efficiencies and charge breeding time: the necessity of a trap to cool the beam actually doubles the charge breeding time (up to 400 ms) and halves the efficiency. On the other hand, the performances of the past years obtained with the ECRIS charge breeder installed at Argonne National Laboratories considerably reduced the gap in terms of the extracted charge states [57]. Considering the case of SPES and its post-accelerator, if one aims at accelerating ^{132}Sn to 10*A MeV or more it is necessary to produce an ion with A/q=6.5 or lower: this translates in a charge state of at least 20^+, absolutely producible by using both techniques. This means that potentially **the outputs of both techniques in terms of charge states are suited for the scope of the SPES- project**. Another consideration to be done regards the expected intensity of the radioactive ions to be charge bred: as described above this could be a serious limitation in case of an EBIS-charge breeder. Simulation of the production target with MCNPX [58] revealed that one of the most intense beam foreseen for SPES will be ^{135}I with an expected intensity at the input of the charge breeder of ~ 6.5 nA ($\sim 4 \cdot 10^{10}$ ions/s). Such an intensity is absolutely manageable by an ECRIS charge breeder (able to handle even μA of injected current) but, for example, exceeds the trap capacity calculated in a section 3.3 for REXEBIS, even without considering further ionizations. To manage this intensity a more complex version should be designed, with higher complexity of the installation and realization costs as a consequence. It can be deduced that **the ECR-based charge breeder is better suited for the high intensities expected for SPES**.
A further aspect to be taken into account regards the operation, in connection with

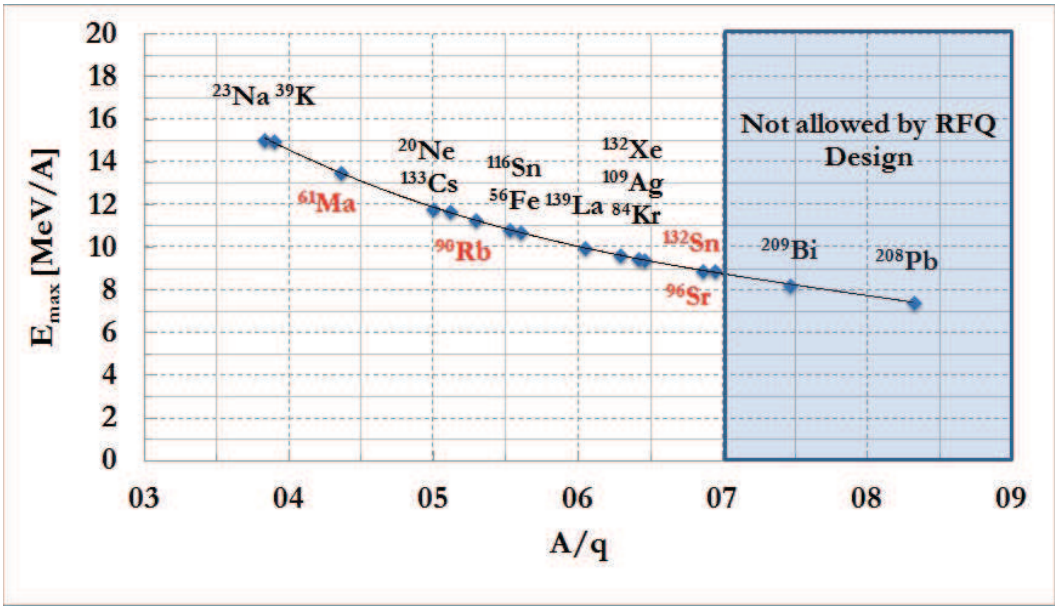

Figure 3.4: Final energies attainable at SPES as a function of the A/q ratio for stable and radioactive species (in red). Values above 7 are not suited for the acceleration with the SPES-RFQ.

radiation protection issues. None of the two techniques has a 100% of extraction efficiency: this means that parts of the radioactive ions will be deposited inside the charge breeder. This could cause problems in case of an intervention for maintenance due to the radioactivity induced by the losses. As described above, a typical characteristic of ECR ion sources is its reliability, allowing the possibility to perform just routine maintenance; accordingly, for this device this last point has a marginal impact. The simple geometry of the plasma chamber (basically a cylinder) allows also the possibility to use a hot liner (as in the case of stable metallic beams production) that could limit the contamination and make considerably easier the eventual substitution of the contaminated parts. The situation with an EBIS is definitively more complicated: it is widely known, in fact, that devices mounting the electron guns are more often subject to unexpected maintenance due to its failure; moreover EBIS cannot be equipped with an hot liner leading to a much more diffuse contamination of the device. In synthesis, **with an ECR-based charge breeder the risks of unexpected maintenances are reduced**. The last but not the least aspect is connected to the fact that LNL has a long time experience in ECR sources but not on EBIS ones.

The considerations given above are summarized in table 3.3: it clearly comes out that **the ECRIS-based charge breeder is the best choice to reliably charge breed the radioactive ions expected for SPES**.

Table 3.3: Comparison between EBIS and ECRIS charge breeders.

	EBIS	ECRIS
Global Efficiency	50% with the trap	up to 80% for gases
Charge States	High	From medium to high
Output ion beam quality	Clean device	Dirty device (can be overcome)
rms-emit	$< 20\ \pi mm\ mrad$	$< 20\ \pi mm\ mrad$
1^+ beam acceptance	Limited in intensity and emittance	No real limitations
Operation	Pulsed (CW)	CW and pulsed
Maintenance	Electron gun	Basically no parts to be replaced
Costs	Installation complicated and expensive	Simpler and cheaper installation
Possible upgrades	Substitution of main parts	Profit from ECR sources developments

Chapter 4

The Physics of an ECR-based Charge Breeder

4.1 Introduction

The previous chapters gave the useful information to properly set the area of interest of this thesis. We are now going to deal with the part of the work connected to the investigation of the physical processes involved in the functioning of an ECR-based charge breeder. As previously described, it is basically an ion source modified to accept an incoming 1+ beam: for this reason the most of those processes are shared with the homonymous device. The different nature of the injected particles (1+ ions instead of neutral) and the following interactions are the peculiarities of the charge breeder.

The Electron Cyclotron Resonance Ion Sources (ECRIS) [42] are nowadays the most effective devices that can feed the particle accelerators in a continuous and reliable way, providing high current beams of low and medium charge state ions and lower, but still important, beam current for highly charged ions. In such sources a plasma is generated inside a high vacuum chamber and confined by means of a particular magnetic configuration called "B-minimum" structure. It is generated by the superposition of a hexapolar field (generating a radially varying field) and a mirror trap, that is a set of two or three coils (generating the axial field); the field obtained has the characteristic of growing from the center towards the periphery of the plasma chamber.

The plasma is generated and sustained by microwaves (usually between 14 and 28 GHz) through a resonant interaction, called Electron Cyclotron Resonance, between a wave of frequency ν_{MW} and the cyclotron motion of the electrons in the magnetic field at an angular frequency ω_c: the condition for the resonance to take place is that $\nu_{MW} = \omega_c/2\pi$; considering the topology of the magnetic field, this condition is met on a closed "egg-shaped" surface, usually called ECR-resonance surface. Being the plasma an anisotropic medium for wave propagation, the outcome of the resonant interaction depends on various parameters like the microwave frequency,

the propagation with respect to the magnetic field and the plasma density. Energetic electrons generated by the ECR resonance are able to create highly charged ions through stepwise ionizations: as a consequence, the higher the desired charge states q+ the higher has to be the time spent by the ion inside the plasma. As will be clearer later in this chapter, ions confinement is ensured by both magnetic and electrostatic forces.
The development of ECRIS during last twenty years has been driven by the improvement of the minimum-B magnetic trap, according to the High B mode concept proposed in 1990 [59]. In particular, the need to achieve higher currents of highly charged ions pushed the development of ECRIS towards the use of higher power and higher microwave frequency generators that require higher confining magnetic field, according to the Geller's scaling laws [60]. A classification in terms of ECRIS' generation is commonly accepted according to the typical operational frequency: the very first sources operated usually below 10 GHz and were characterized by a very high power consumption and a poor vacuum, leading to a low average extracted charge. The second generation ECRIS, still nowadays used, are operated at 14-18 GHz in high vacuum condition, with an improvement of the extracted charge state distribution (charge states between 8 and 14 for Ar). Third generation ECRIS work at 28 GHz or more, giving for example charge states between 14 and 18 for Ar: sources of this kind operates in international laboratories like LBNL [61]; more or less in the middle of the last two generations is placed the superconducting source SERSE, into operation at INFN-LNS since the 90's [62].
The following sections will describe all the physical mechanisms involved in the functioning of an ECR-based charge breeder.

4.2 Charged particles motion in electric and magnetic fields

Plasma particles are generated and confined in a magnetic field so it is important to start this theoretical description with the motion of a single particle under the influence of electric and magnetic forces. Generally, the equation of motion of a particle of mass m and charge q moving in a region where a magnetic field $\mathbf{B}$, an electric field $\mathbf{E}$ and a generic force $\mathbf{F}$ are present can be written:

$$m\frac{d\mathbf{v}}{dt} = q\left(\mathbf{v}\times\mathbf{B}+\mathbf{E}\right)+\mathbf{F} \tag{4.1}$$

It can be seen that the general solutions of this equation, represented by the vector position $\mathbf{r}(t)$, can assume a periodic behaviour, in particular with three types of periodicity:

- **Cyclotron motion**: the particle will rotate in a plane perpendicular to the magnetic field.

- **Mirror reflection**: the particle will move back and forth along a magnetic field line.
- **Drift motion**: the particle will move on a closed surface described by a number of magnetic field lines.

The first motion is the one with the highest frequency; the second is orders of magnitude slower: each magnetic configuration where this last motion happens is said **magnetic trap** and, as we will see later in this chapter, the process is termed magnetic trapping. Finally, the drift motion is orders of magnitude slower than the reflection.
In analysing the cyclotron motion the guiding centre approximation can be used, where the guiding centre is the centre of the circle described by the particle motion: the radius of this circle is called Larmor radius $\mathbf{r}_c$ while the period of the motion is called cyclotron period τ_c. The particle position can then be expressed through the vector position $\mathbf{R}_c$, the Larmor radius vector $\mathbf{r}_c$ and a phase ϕ. The instantaneous velocity $\mathbf{v}_G$ of the guiding centre can be decomposed with respect to the magnetic field direction as:

$$\mathbf{v}_G = \mathbf{v}_{G\parallel} + \mathbf{v}_{G\perp} \tag{4.2}$$

where the first component coincides with the particle velocity along the magnetic field

$$\mathbf{v}_{G\parallel} = \mathbf{v}_{\parallel} \tag{4.3}$$

while the second differs from the orthogonal one $\mathbf{v}_{\perp}$. The component $\mathbf{v}_{\perp}$ is usually termed "drift velocity" $\mathbf{v}_D$ because represents the motion of the guiding centre across the magnetic field lines. Special conditions of externally applied forces and magnetic field geometry will be discussed in the following subsections.

4.2.1 Uniform E and B fields

Let's start with a uniform magnetic field and the electric field $\mathbf{E} = \mathbf{F} = 0$. A charged particle has in this case a simple cyclotron motion and equation 4.1 become:

$$m\frac{d\mathbf{v}}{dt} = q\mathbf{v} \times \mathbf{B} \tag{4.4}$$

Supposing the magnetic field $\mathbf{B}$ to be in z direction ($\mathbf{B} = B\hat{\mathbf{z}}$) we obtain the equations:

$$\begin{aligned} m\dot{v}_x = qBv_y \qquad m\dot{v}_y = -qBv_x \qquad m\dot{v}_z = 0 \\ \ddot{v}_x = \frac{qB}{m}\dot{v}_y = -\left(\frac{qB}{m}^2\right)v_x \\ \ddot{v}_y = \frac{qB}{m}\dot{v}_x = -\left(\frac{qB}{m}^2\right)v_y \end{aligned} \tag{4.5}$$

that describe a simple harmonic oscillator at the cyclotron frequency:

$$\omega_c \equiv \frac{|q|B}{m} \tag{4.6}$$

The solution to equation 4.5 is a circular motion about the guiding center in a plane perpendicular to the magnetic field: the radius of this gyromotion, that is the Larmor radius r_c, is given by the relation

$$r_c \equiv \frac{v_\perp}{\omega_c} = \frac{m v_\perp}{|q|B} \tag{4.7}$$

being $v_\perp$ the component of the particle's velocity perpendicular to the magnetic field. Two handy formulas allow a fast calculation of this parameter for ions with mass number A and charge q and electrons:

$$\begin{aligned} r_c^+ &\approx 1.5 * 10^{-4} \frac{\sqrt{W_\perp A}}{qB} \qquad [\text{m}] \\ r_c^- &\approx 3.8 * 10^{-6} \frac{\sqrt{W_\perp}}{B} \qquad [\text{m}] \end{aligned} \tag{4.8}$$

being $W_\perp$ the energy corresponding to the motion perpendicular to $\mathbf{B}$. The direction of gyration is always such that the magnetic field generated by the charged particle is opposite to the externally imposed field: plasma particles therefore tend to reduce the magnetic field and so plasmas can be classified as diamagnetic.
Let's now add to the magnetic field an electric field $\mathbf{E}$ and suppose it lies in the $x-z$ plane so that $E_y = 0$. Equation 4.1 becomes:

$$m\frac{d\mathbf{v}}{dt} = q\left(\mathbf{E} + \mathbf{v} \times \mathbf{B}\right) \tag{4.9}$$

The z component of this equation will lead to the normal acceleration of the charged particle under the component E_z electric field along a magnetic field line. The other two components will lead to the usual gyromotion with angular frequency ω_c about the magnetic field line to which is superimposed a drift motion of the guiding centre with a velocity $\mathbf{v}_{gc}$ (in the negative y direction for $E_x > 0$, see figure 4.1) given by:

$$\mathbf{v}_{gc} = \frac{\mathbf{E} \times \mathbf{B}}{B^2} \equiv \mathbf{v}_E \tag{4.10}$$

As we see from the above formula, this drift is perpendicular to both electric and magnetic fields and is independent of q, m, and $v_\perp$: the formula can be generalized to a generic force $\mathbf{F}$ by replacing $\mathbf{E}$ with $\mathbf{F}/q$ in the equation of motion. In the case of the gravitational force $\mathbf{F} = m\mathbf{g}$, we obtain the drift velocity:

$$\mathbf{v}_g = \frac{m}{q}\frac{\mathbf{g} \times \mathbf{B}}{B^2} \tag{4.11}$$

It can be noted that in this case ions and electrons drift in opposite directions so the motion leads to a net current density in the plasma given by:

$$\mathbf{j} = n\left(M_i + m\right)\frac{\mathbf{g} \times \mathbf{B}}{B^2} \tag{4.12}$$

being M_i the ion mass. Anyway, the magnitude of this drift is usually negligible.

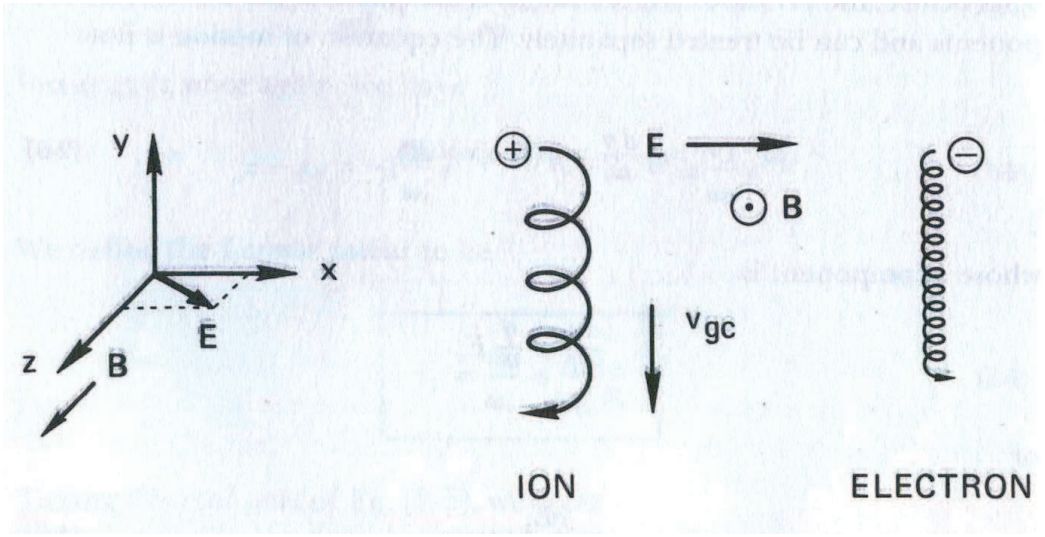

Figure 4.1: Particle drifts in crossed **E** and **B** fields.

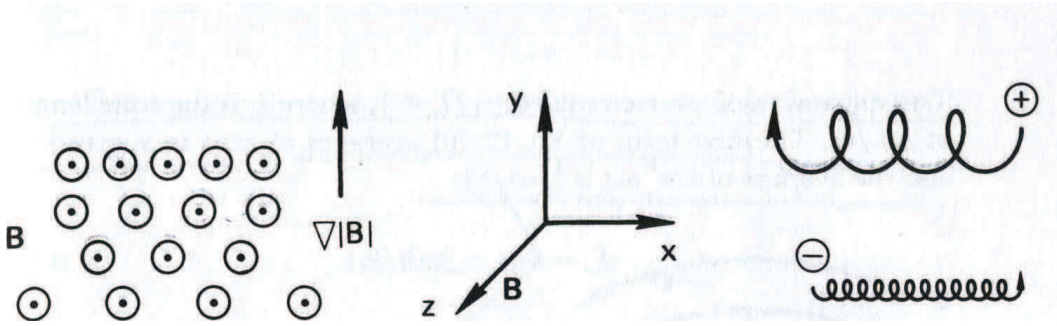

Figure 4.2: Drift of a particle in a non uniform magnetic field.

4.2.2 Non uniform B

The more real case of a non uniform magnetic field will be treated in this subsection, considering the following two important cases,

- **gradB Drift.**

  Consider now a magnetic field only in $\hat{\mathbf{z}}$ direction that increases in intensity in $\hat{\mathbf{y}}$ direction as shown in figure 4.2: the gradient in $|B|$ causes the Larmor radius to be larger at the bottom of the orbit than at the top, leading to a drift, in opposite direction for ions and electrons, perpendicular to both **B** and $gradB$. By supposing that the scale of inhomogeneity of the magnetic field is big compared to the Larmor radius r_c ($|\nabla B/B| \ll 1/r_c$), if we average the Lorentz force $\mathbf{F} = q\mathbf{v} \times \mathbf{B}$ over a gyration we obtain that the average of F_x is zero since the particle spends as much time moving up as down. The average of F_y can be obtained by a Taylor expansion of the field **B** about the point

$x_0 = y_0 = 0$:

$$\begin{aligned} \mathbf{B} &= \mathbf{B}_0 + (\mathbf{r} \cdot \boldsymbol{\nabla}) + \dots \\ B_z &= B_0 + y\,(\partial B/\partial y) + \dots \end{aligned} \tag{4.13}$$

The average of F_y then becomes:

$$\bar{F}_y = \mp q v_\perp r_c \frac{1}{2}\left(\frac{\partial B}{\partial y}\right) \tag{4.14}$$

and the guiding centre drift velocity is, generalizing the result:

$$\mathbf{v}_{\boldsymbol{\nabla} B} = \pm \frac{1}{2} v_\perp r_c \frac{\mathbf{B} \times \boldsymbol{\nabla} B}{B^2} \tag{4.15}$$

It is important to note that the sign stands for the sign of the charge so this kind of drift causes a current transverse to $\mathbf{B}$.

- **Curvature Drift**.

  Suppose a magnetic field with the line of force curved with constant radius $\mathbf{R}_c$ and take $|B|$ to be constant (figure 4.3). Such a filed does not obey Maxwell's equations in vacuum so in practice the gradB drift will always be added to the effect derived here. A guiding centre drift arises from the centrifugal force felt by the particles as they move along the field lines. If we denote with $v_\parallel^2$ the average square of the component of the random velocity along $\mathbf{B}$ the average centrifugal force is:

$$\mathbf{F}_{cf} = \frac{m v_\parallel^2}{\mathbf{R}_c} \hat{\mathbf{r}} \tag{4.16}$$

  This gives rise to a drift, called curvature drift, given by the equation:

$$\mathbf{v}_R = \frac{1}{q} \frac{\mathbf{F}_{cf} \times \mathbf{B}}{R_c} \tag{4.17}$$

  We must now compute the gradB drift that accompanies this last one when the decrease of $|B|$ with radius is taken into account. In vacuum we have $\boldsymbol{\nabla} \times \mathbf{B} = 0$: in the cylindrical coordinates shown in figure 4.3 it has only a z component, since $\mathbf{B}$ has only the $\hat{\boldsymbol{\theta}}$ component and $\boldsymbol{\nabla}\mathbf{B}$ has only $\hat{\mathbf{r}}$ component. We then have:

$$(\nabla \times B)_z = \frac{1}{r}\frac{\partial}{\partial r}(r B_\theta) \qquad B_\theta \propto \frac{1}{r} \tag{4.18}$$

  By using equation 4.15 we obtain:

$$\mathbf{v}_{\boldsymbol{\nabla} B} = \frac{m}{2q} v_\perp^2 \frac{\mathbf{R}_c \times \mathbf{B}}{R_c^2 B^2} \tag{4.19}$$

  that summed to the previous drift gives:

$$\mathbf{v}_{\boldsymbol{\nabla} B} + \mathbf{v}_R = \frac{m}{q} \frac{\mathbf{R}_c \times \mathbf{B}}{R_c^2 B^2} \left(v_\parallel^2 + \frac{1}{2} v_\perp^2\right) \tag{4.20}$$

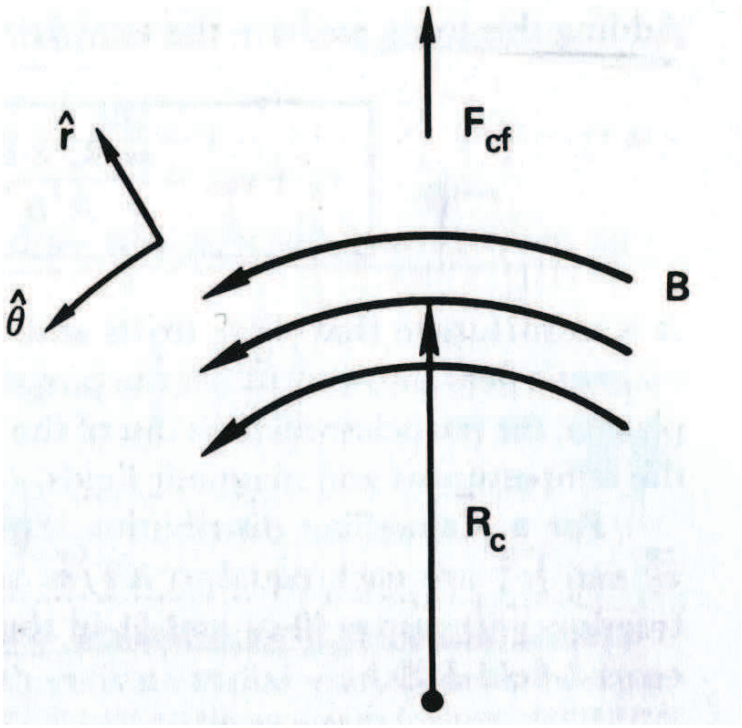

Figure 4.3: A curved magnetic field that generates a centrifugal force on the particle.

As for the previous drifts, this leads to a net current into the plasma: if the particles have a Maxwellian velocities distribution with an rms speed v_{th} equation 4.20 simplifies as:

$$\bar{\mathbf{v}}_{R+\nabla B} = \pm\frac{v_{th}^2}{\mathbf{R}_c\omega_c}\hat{\mathbf{y}} = \pm\frac{\bar{r_c}}{\mathbf{R}_c}v_{th}\hat{\mathbf{y}} \tag{4.21}$$

4.2.3 Magnetic mirror and particle trapping

We are now able to treat the motion of a charged particle in a magnetic trap: consider a magnetic field which is pointed primarily in the z direction and whose magnitude varies in the z direction, with $B_\theta = 0$ and $\partial/\partial\theta = 0$. Since the lines of force converge and diverge, to satisfy the equation $\boldsymbol{\nabla}\cdot\mathbf{B} = 0$ a component B_r has to be present (see figure 4.4): it can be demonstrated that it takes the form

$$B_r = -\frac{1}{2}r^2\left(\frac{\partial B_z}{\partial z}\right)_{r=0} \tag{4.22}$$

The variation of $|B|$ with r causes a gradB drift of the guiding centres about the axis of symmetry, but there is no radial gradB drift because $\partial B/\partial\theta = 0$: the components of the Lorentz force are

$$\begin{aligned} F_r &= qv_\theta B_z \\ F_\theta &= q\left(-v_r B_z + v_z B_r\right) \\ F_z &= -qv_\theta B_r \end{aligned} \tag{4.23}$$

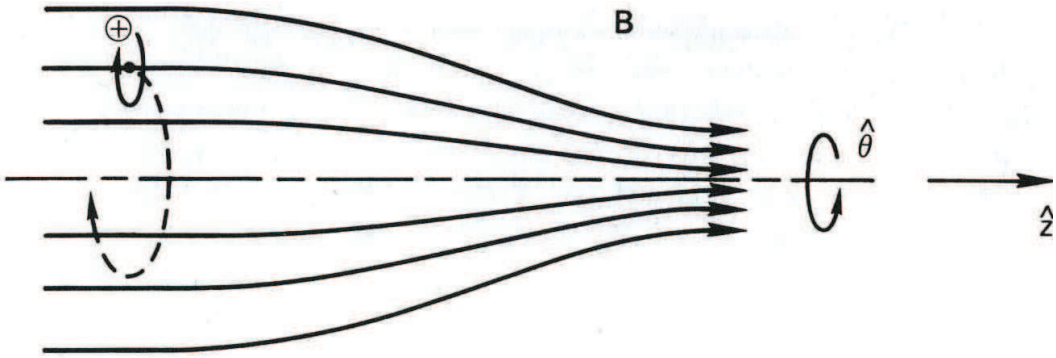

Figure 4.4: Drift of a particle in a magnetic mirror field.

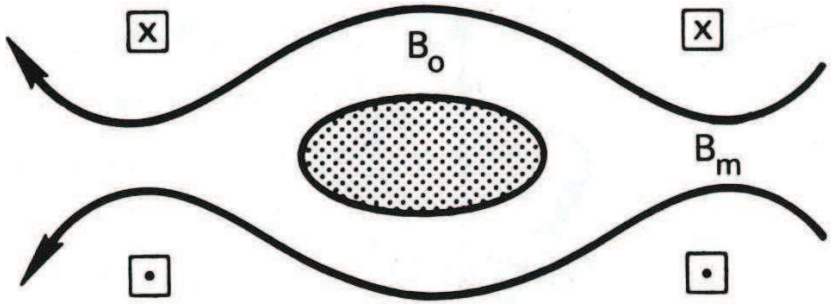

Figure 4.5: A plasma trapped between magnetic mirrors.

The first equation and the first term in the second equation give rise to the usual Larmor motion. The second term in the second equation vanishes on axis; when it does not vanish, this azimuthal force causes a drift in the radial direction: this drift basically makes the guiding centres follow the lines of force. By using equation 4.22 the equation for F_z becomes: where $\mu \equiv mv_\perp^2/2B$ is the *magnetic moment*. As the particle moves into the regions of stronger or weaker **B**, its Larmor radius changes but it can be demonstrated that μ remains constant: for this reason it is called the first adiabatic invariant. The invariance of μ is the basis for the confinement scheme of the magnetic mirrors: as a particle moves from a weak-field region to a strong-field region it sees an increasing **B** and its $v_\perp$ must increase in order to keep μ constant. Since the magnetic field cannot change the total energy of the particle, the component $v_\parallel$ must in turn decrease or eventually become zero: in this case the particle is reflected back to the weak-field region by the force $\mathbf{F}_\parallel$. An example of such a magnetic configuration is given by a pair of coils creating two magnetic mirrors for plasma trapping as shown in figure 4.5.

A trapping is not perfect however: for example, a particle with $v_\perp = 0$ will have no magnetic moment and will not feel any force along **B**. A particle with small $v_\perp/v_\parallel$ at the mid-plane ($B = B_0$) will also escape if the maximum field B_m is not large enough: so, it is interesting to know which particles will escape from a given trap. A particle with $v_\perp = v_{\perp 0}$ and $v_\parallel = v_{\parallel 0}$ at the mid-plane will have $v_\perp = v'_\perp$ and $v_\parallel = 0$

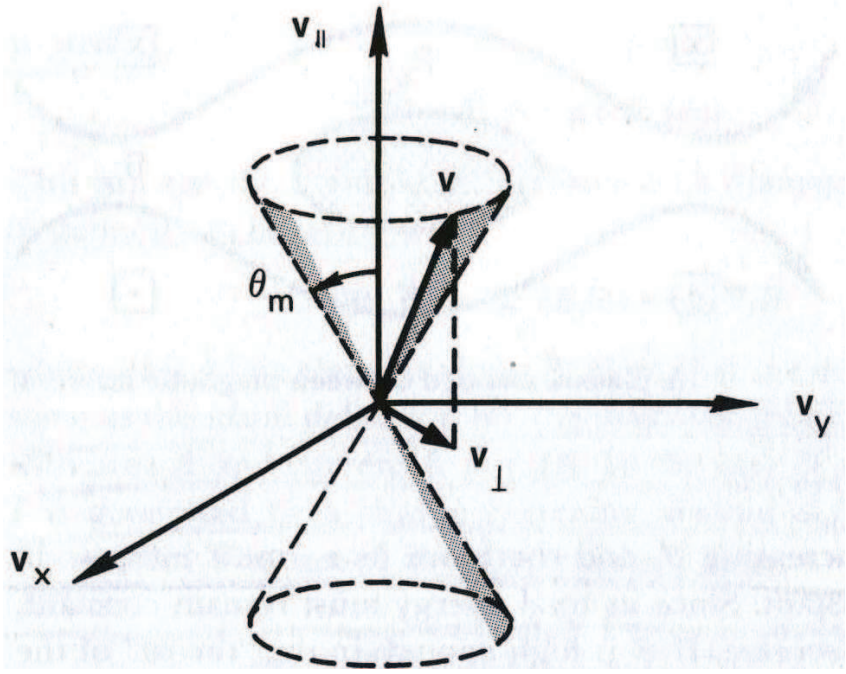

Figure 4.6: The loss cone in velocity space.

at its turning point. If B' is the field there, then the invariance of μ yields:

$$\frac{1}{2}\frac{mv_{\perp 0}^2}{B_0} = \frac{1}{2}\frac{mv\prime_{\perp}^2}{B'} \tag{4.24}$$

Conservation of energy requires:

$$v\prime_{\perp}^2 = v_{\perp 0}^2 + v_{\parallel 0}^2 \equiv v_0^2 \tag{4.25}$$

so combining the last two equations we get

$$\frac{B_0}{B\prime} = \frac{v_{\perp 0}^2}{v\prime_{\perp}^2} = \frac{v_{\perp 0}^2}{v_0^2} \equiv \sin^2\theta \tag{4.26}$$

where θ is the pitch angle of the orbit in the weak-field region. Particles with smaller θ will mirror in regions of higher B: if θ is too small, B' exceeds B_m and the particle does not mirror at all. Replacing B' by B_m in equation 4.26 we see that the smallest θ for a confined particle is:

$$\sin^2\theta = B_0/B_m \equiv 1/R_m \tag{4.27}$$

where R_m is called the **mirror ratio**. Equation 4.27 defines the boundary of a region in velocity space in the shape of a cone, called the loss cone, as shown in figure 4.6: particles lying within the loss cone are not confined, leading to an anisotropy of the mirror-confined plasmas. Note that the loss cone is independent of q and m: without collisions, both ions and electrons are equally well confined. When collisions occur,

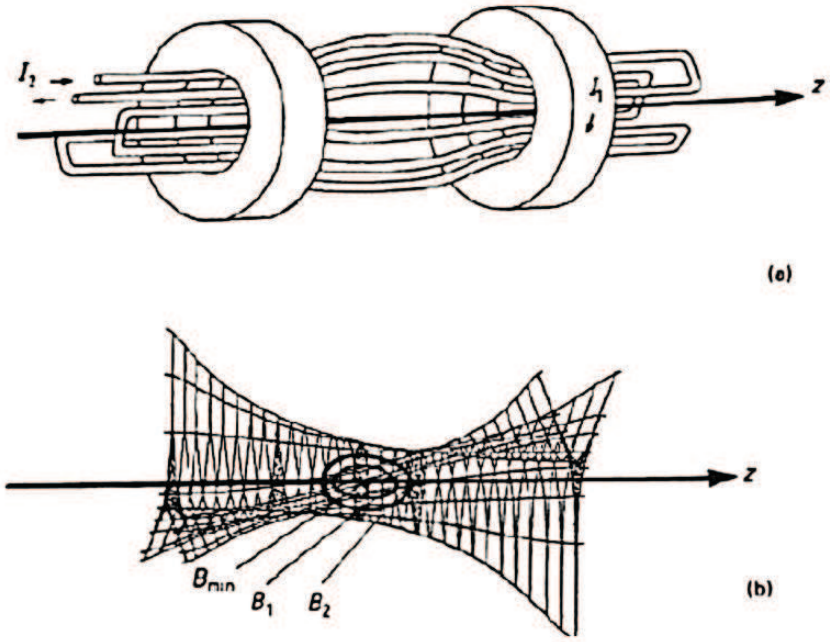

Figure 4.7: Magnetic system (a) and magnetic field structure obtained by the superposition of the field produced by two solenoids and an hexapole (b).

particles are lost when they change their pitch angle in and are scattered into the loss cone. Generally, as we will see later, electrons are lost more easily because they have a higher collision frequency.

In 1962 Ioffe [63] first reported on plasma-confinement experiments in a magnetic field configuration that had the desirable feature that the magnetic field increased in every direction away from the plasma boundary, and that did not have the undesirable feature of a region where the magnetic field went to zero inside the plasma (as in the case of cusp configurations). Such a configuration is exactly the previously mentioned B-minimum structure: it can also be thought as a multi-mirror device, where the particle is reflected in many points travelling along the field lines. Figure 4.7 shows schematically the structure of the B-minimum configuration: note that the geometrical locus where B is constant is an egg-shaped surface.

4.3 The so called "Spitzer" collisions

In this section an important collective mechanism of plasma physics will be treated, responsible of electron losses inside an ECR-plasma and at the basis of the charge breeding process. Leaving the more detailed description at the end of the chapter, some basic equations will be here presented, useful to properly understand particles confinement.

The long range encounters or distant collisions represent the multiple interactions of a single particles with many others particles such that the net effect is to give a

large-angle (about 90°) scattering. In principle, these long range Coulomb forces can extend over the whole of the plasma: however, in order to make possible the calculation of the cross section, it is necessary to choose a distance, identified with the *Debye distance*, within which interactions of a charged particle with other charged particles may be supposed to occur. Beyond, the plasma may be regarded as being electrically neutral so that the particle under consideration is not affected by Coulomb forces. This kind of collisions are termed "Spitzer" from the name of the scientist who first analysed this process and its influence on the plasma particles dynamics: he promoted the idea that in strongly ionized plasma, as the one in ECR ion sources, the cumulative deflections due to small-angle scattering are actually larger than those due to single large-angle scatterings [64]. The cumulative small-angle scatterings resulting finally in a 90° deflection are then supposed to be the most active scattering mechanism inside the plasma: this of course is true if turbulences are not considered. It can be demonstrated that the mean free path for a 90° deflection of a particle of mass M, charge z_1 and velocity v scattered by particles of density n and charge z_2 can be expressed by the relation (in CGS):

$$\lambda_{90^\circ} = \left[8\pi n \left(\frac{z_1 z_2 e^2}{M v^2} \right)^2 ln \left(\frac{\lambda_D}{b_{min}} \right) \right]^{-1} \tag{4.28}$$

where λ_D is the so called *Debye length* [65]. Now an effective cross section for a 90° deflection by means of multiple collisions can be defined in the usual manner:

$$\lambda_{90^\circ} = \frac{1}{n\sigma_{90^\circ}} \tag{4.29}$$

$$\sigma_{90^\circ} = 8\pi \left(\frac{z_1 z_2 e^2}{M v^2} \right)^2 ln \left(\frac{\lambda_D}{b_{min}} \right) \tag{4.30}$$

with $b_{min} = 2e^2/Mv^2$. For most ECRIS plasmas $ln(\lambda_D/b_{min})$ has a value between 10 and 20 (usually around 15) and is almost insensitive to the plasma parameters: it is called the Coulomb logarithm and is often expressed by $ln\Lambda$.
The quantity λ_{90° is a measure of the penetration required for a multiple scattering through an angle of 90° while σ_{90° is a useful quantity in comparing the effect of Coulomb scattering and other collisions. From the cross-section and the mean free path it is possible to derive the time required for the 90° deflection in the Centre of Mass (CM) system through the relation: we can write

$$\nu_{90^\circ}^{-1} \equiv \tau_{90^\circ} \equiv \lambda_{90^\circ}/v' \tag{4.31}$$

where $v\prime = v_1 - v_2$ is the relative velocity. For e-e and e-i collisions the deflection in the laboratory system is comparable to the deflection in the centre of mass and we have also that $\nu_{90^\circ}^{ee} \sim \nu_{90^\circ}^{ei}$ and $\tau_{90^\circ}^{ee} \sim \tau_{90^\circ}^{ei}$. The following are good handy formulas for the calculation of the various possible collision frequencies for particles in thermal

equilibrium:

$$\begin{aligned}
\nu_{90^\circ}^{ee} &= \frac{5\times10^{-6}\ n}{KT_e^{\frac{3}{2}}} ln\Lambda \\
\nu_{90^\circ}^{ei} &\sim \frac{2\times10^{-6}\ zn}{KT_e^{\frac{3}{2}}} ln\Lambda \\
\nu_{90^\circ}^{ii} &\sim z^4 \frac{m_e}{m_i}^{1/2} \frac{KT_e}{KT_i}^{3/2} \nu_{90^\circ}^{ee}
\end{aligned} \tag{4.32}$$

where n is in cm^{-3} while KT_e and KT_i are in eV. From conservation of energy and momentum the change in particle's energy following a 90° collision can be approximated as:

$$\frac{\Delta E}{E_0} \approx \frac{m_1 m_2}{(m_1+m_2)^2} \tag{4.33}$$

where E_0 is the initial energy. It can be noted that like-particle collisions result in the transfer of about half of the initial energy in a 90° deflection time, while for e-i collisions the fractional energy transfer in a 90° deflection is only about m_e/m_i. Thus, the characteristic times for energy transfer τ_m are related to the 90° deflection time by the relations:

$$\begin{aligned}
\tau_m^{ee} &\sim \tau_{90^\circ}^{ee} \sim \tau_{90^\circ}^{ei} \\
\tau_m^{ii} &\sim \tau_{90^\circ}^{ii} \sim \left(\frac{m_i}{m_e}\right)^{1/2} \tau_{90^\circ}^{ei} \\
\tau_m^{ei} &\sim \tau_m^{ie} \sim \frac{m_i}{m_e} \tau_{90^\circ}^{ei}
\end{aligned} \tag{4.34}$$

The above formulas are valid for cold plasma ($Z = 1$ and $KT_e \approx KT_i$): for ECR plasmas, being $KT_e \neq KT_i$, one has to take into account the values of z and the ratio $(KT_e/KT_i)^{3/2}$ in the Spitzer times for 90° deflection. We see that electron momentum transfer time equals the Spitzer time, so electron heating (energy equipartition) through Spitzer e-e collisions seems much easier and faster than ion heating through e-i collisions ($\tau_m^{ei} \gg \tau_{90^\circ}^{ei}$). A number of important conclusions follow immediately: first of all, electrons in an ECRIS plasma exchange energy with each other and can reach an equilibrium distribution on a rather short time scale. Considering the characteristic times in usual ECRIS plasma, we note that ν_{ee} and ν_{ei} are much smaller than ω_c and the microwave frequency ν_{MW}: for this reason they do not impede the electron gyromotion, giving to the ECR plasmas the term "collisionless". More, electron transfer energy to ions or vice versa on a time scale that is (m_i/m_e) times longer than the time required for electrons to equilibrate with themselves.
Let's give some numerical examples. In an ECRIS plasma with a density of $10^{11} cm^{-3}$ and $T_e = 10\ eV$ ν_{ee} lies in the range $10^5 - 10^6 s^{-1}$ so electron thermal equilibrium is reached on a very short scale. Ions would be heated by the same electrons on a time scale of about milliseconds: if their lifetime is shorter they will never be heated by e-i collisions and will remain cold. On the other hand, for $T_e = 1\ keV$ ν_{ee} lies in

the range of milliseconds: only if electron lifetime could match these values it would be possible to obtain an electron thermalization through e-e collisions. This is the reason why in ECRIS plasma we can find hot electrons mixed with cold ions: the collision frequency of the former particles is so low that their confinement is possible. Finally, the i-i collision rate can become the main scattering agent for these particles because the temperature is very low and $\nu_{90^\circ}^{ii}$ is proportional to $KT_i^{3/2}$ and to $z_1 z_2$ [64].

4.3.1 Ion confinement in ECR Plasmas

In order to estimate the ions confinement times in ECR plasma it is necessary to determine first its "working regime": this is done by comparing the collision time τ_{coll} with the estimated confinement time due to the magnetic trap τ_{mag}. This last parameter is given by the formula:

$$\tau_{mag} = \frac{Rl_p}{\langle v_i \rangle} \tag{4.35}$$

where R is the mirror ration, l_p is the plasma length and $\langle v_i \rangle = \sqrt{KT_i/M}$ is the one dimensional thermal velocity. As can be seen, such confinement time does not depend on any plasma parameter except for the ion temperature and is the same for all charge states: it can be deduced that the lower the ion temperature, the higher would be the confinement time. In those condition for which $\tau_{coll} \gg \tau_{mag}$ the plasma is said to be in an **uncollisional** regime: in this case the ion dynamics is completely determined by the magnetic field; this condition is hardly applicable to ECR-plasma except for the rarefied halo or for very low densities. When the contribution of collisions increase the plasma goes to a **weakly collisional** regime: this transition takes place inside the plasma for moderate densities. Such regime is characterized by $\tau_{coll} \leq \tau_{mag}$: the ion dynamics in this case is influenced by the well known negative potential dip $\Delta\phi$ present inside the ECR plasma. The origin of this effect is still controversial but from the beginning it has been attributed to the hot electrons component that is weakly collisional and better confined. This population forms a negative cloud at the center of the plasma superimposed to the positive plasma potential profile: a picture of this effect is shown in figure 4.8. It is difficult to determine the exact value of such negative contribution but it has been estimated to be in the order of the ion temperature KT_i. The confinement time in this case is further increased and can be expressed by the relation:

$$\tau_{conf} \simeq \tau_{mag} \exp \frac{Z\Delta\phi}{KT_i} \tag{4.36}$$

with $Z = qe$ the ion charge ion state. Contrary to before, now a dependence on the ion charge state appears, letting the potential dip be more effective for highly charged ions.
Finally, when $\tau_{coll} \ll \tau_{mag}$ the plasma is said to be in a **fully collisional** regime [66]: this condition applies to the dense plasma core where collisions become the

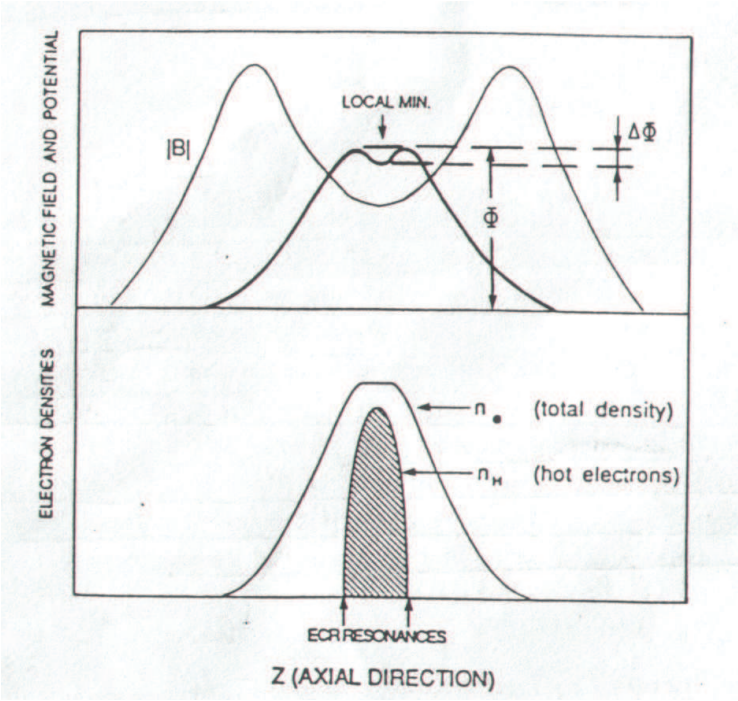

Figure 4.8: Axial plasma potential profile with the potential dip (upper part) and plasma electrons distribution (lower part).

dominant process. Following Spitzer, the collision frequency of an ion with all the possible species present in the plasma can be expressed by the relation (in eV, s^{-1} and cm^{-3} units):

$$\nu_{ij} = \frac{1}{\tau_{coll}} \simeq \frac{6.8 \times 10^{-8} \ln \Lambda_{ij}}{KT_i^{3/2}} \frac{q^2}{A_i} n_e \sum_j \sqrt{A_j} \langle z \rangle_j \tag{4.37}$$

where q is the charge state of the ion with mass number A_i, $\langle z \rangle$ is the average charge of the plasma and the subscripts i and j refer to the different plasma species. In this condition the confinement time τ_{conf} can be estimated as follows. In a time equal to the confinement time the ions moves over the characteristic plasma dimension l_p while undergoing a number of collisions $N = \tau_{conf}/\tau_{ij}$. Following statistics it can be written:

$$l_p \simeq \sqrt{N}\lambda = \sqrt{\tau_{conf}\nu_{ij}} \frac{\langle v^2 \rangle_i}{\nu_{ij}^2} \tag{4.38}$$

where λ is the mean free path. From the previous equation the confinement time of an ion of the specie i with charge q can be expressed by the relation (in eV, s^{-1} and cm^{-3} units):

$$\tau_i^q \simeq 7.1 \times 10^{-20} l_p^2 \ln \Lambda_{ij} \frac{q^2}{KT_i^{5/2}} n_e \sum_j \sqrt{A_j} \langle z \rangle_j \tag{4.39}$$

It can be noted the critical dependence on the ion temperature and charge state: confinement times estimated with this formula give values up to hundreds of ms,

depending on the particular ion and plasma characteristics. As will be described in chapter 6, recent studies performed at INFN-LNS brought into question the evaluation of the ion confinement time in a collisional regime, leading to the formulation of a more complete interpretation of the process [67].

4.4 Binary Collisions

4.4.1 Ionizing collisions

Generally, the ionization processes show a threshold behaviour with respect to the electron energy E_e: if the ionization potential to obtain a given charge state z is $P_i(z-1)$, it must be $E_e \geq P_i(z-1)$ for a given ionization to occur. The process of single ionization can be described as follows:

$$e + X^{(z-1)+} \Longrightarrow X^{z+} + 2e$$

The rate of ionization of an ion from charge $z-1$ to charge z by electrons with energy E_e is in general expressed as:

$$\nu^{ion}_{z-1\to z}(E_e) = \sigma^{ion}_{z}(E_e) v(E_e) n_e(E_e) \tag{4.40}$$

where all the quantities are a function of energy. If a Maxwell-Boltzmann distribution with a temperature KT_e is supposed for the electrons, then the above formula can be averaged by writing:

$$\nu^{ion}_{z-1\to z} = \int \sigma^{ion}_{z-1\to z}(E_e) v(E_e) n_e \frac{2}{\sqrt{\pi}} \left(\frac{E_e^{1/2}}{KT_e^{3/2}} e^{-E_e/KT_e} \right) dE_e \tag{4.41}$$

The most reliable expression for the ionization cross section is a semiempirical formula obtained by Lotz [68, 69] which, in the most general form, can be written as:

$$\sigma^{ion}_{z-1\to z} = \sum_{j=1}^{N} \frac{a_{ij} q_{ij}}{T_e^{3/2}} \ln \frac{E_e}{P_{ij}} \{1 - b_{ij} \exp[-c_{ij}(E_e/P_{ij} - 1)]\} \tag{4.42}$$

In the previous equation, P_{i1} is the ionization potential of the outer shell, P_{i2} the one of the first inner subshell and so on; q_{ij} is the number of electrons in a given shell, while a_{ij}, b_{ij} and c_{ij} are typical parameters of the fit.
The transition from charge states z_1 to another charge state z_2, through a given ionization channel x, takes a time on average:

$$\tau^{(x)}_{z_1 z_2} = \left[n_e \sigma^{(x)}_{z_1 z_2}(v_e) v_e \right]^{-1} \tag{4.43}$$

Being the cross section velocity dependent, the above formula has to be averaged over the electrons distribution: consequently, the average ionization time becomes a

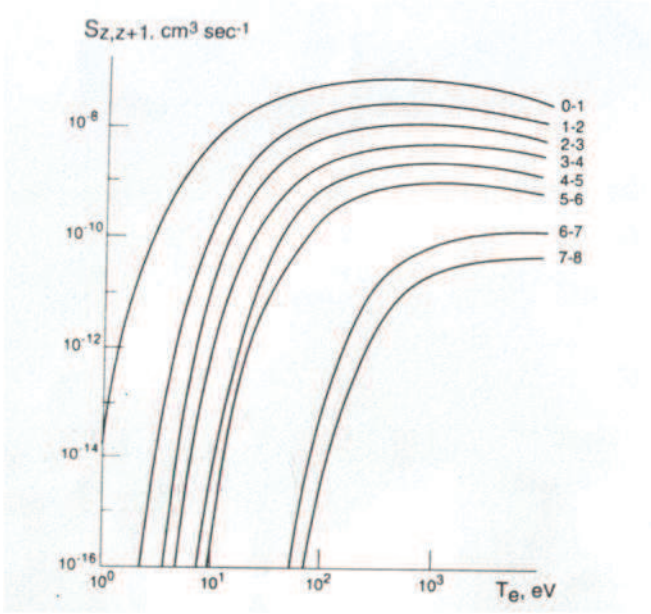

Figure 4.9: Oxygen ionization coefficient as a function of electron temperature.

function of electron density and energy and can be expressed through the ionization coefficient

$$\begin{cases} \tau_{z_1 z_2}^{(x)} = \left[n_e S_{z_1 z_2}^{(x)}(KT_e) \right]^{-1} \\ S_{z_1 z_2}^{(x)} = \langle \sigma_{z_1 z_2}^{(x)}(v_e) v_e \rangle \end{cases} \tag{4.44}$$

If the ion confinement time τ_i is such that $\tau_i \geq \tau_{z_1 z_2}^{(x)}$ then the transition $z_1 \rightarrow z_2$ can take place: from equation 4.44 this condition can be expressed as

$$n_e \tau_i \geq \left[S_{z_1 z_2}^{(x)}(KT_e) \right]^{-1} \tag{4.45}$$

known **multiply charged ions criterion**. In case of stepwise ionizations, as in ECRIS plasmas, we have to substitute in the above formula (x) with (i) and z_1 and z_2 with z and $z+1$: by approximating the Lotz formula the ionization coefficient becomes a function of electron temperature

$$S_{z,z+1}(T_e) \approx 3 \cdot 10^{-6} K T_e^{-\frac{3}{2}} \sum_{j=1}^{N} \frac{q_j}{R_j} [e_i(-R_j)] \tag{4.46}$$

where j is the number of sub shells in the inner shell, $R_j = P_j / T_e$ is the ratio between the binding energy of the j-th sub shell and the electron temperature, e_i is an integral exponential function, q_j is the number of equivalent electrons in the j-th sub shell and N in number of sub shells in the outer shell. Figure 4.9 shows the ionization coefficient as a function of electron temperature for oxygen: it can be noted that an optimum electron energy KT_e^{opt} exists that increases with the charge state z.

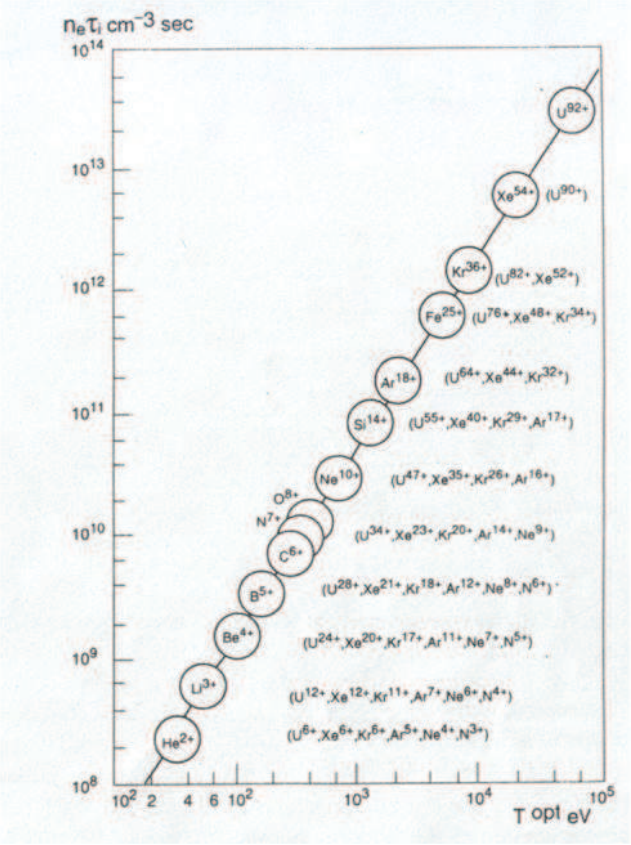

Figure 4.10: Golovanivsky's diagram.

When this charge state is within a distribution, the optimum electron energy can be expressed as:

$$KT_e^{opt} \approx 5P_i(z) \tag{4.47}$$

where $P_i(z)$ is the ionization energy of the given charge state. This value for KT_e corresponds to $R_j = 0.2$: by substituting it in equation 4.46 and using equation 4.45 we obtain the **criterion for multiply charge ion formation** by step-by-step ionizations as a minimum value for the product $n_e\tau_i$:

$$\xi n_e\tau_i \geq 5 \cdot 10^4 (T_e^{opt})^{3/2} \tag{4.48}$$

where $\xi = \sum_{j=1}^{N} q_j$ is the total number of electrons in the outer shell. The quantity $n_e\tau_i$ is a really important parameter for the performances of an ECR source (together with electron temperature KT_e) and is called **Quality Factor**. Figure 4.10 shows the so called Golovanivsky's diagram [70]: it basically estimates the necessary values for the quality factor and the electron energy for an ECR source to have certain performances.

4.4.2 Recombination and charge exchange processes

The most important mechanisms that lower the average charge state in ECR plasma are the capture of a free electron by a multiply charged ion and the charge exchange with a neutral atom. The coefficient of the first process has been given by MacWhriter [71]:

$$\alpha_r = \alpha_{z+1,z} \simeq 5.2 \cdot 10^{-14} \left(\frac{l}{\Lambda}\right)^{1/2} z \left(0.43 + \frac{1}{2}\ln\frac{l}{\Lambda} + 0.47\Lambda^{1/2}\right) \tag{4.49}$$

with $\Lambda = KT_e/P_i(z)$. Such a process is probable for collisions of ions with very slow electron: it becomes important when the relative velocity during the collision is such that $v \ll v_0\sqrt{z}$, where $v_0 = 2.2 \cdot 10^{-8}$ cm/s is the orbital speed of electrons in the hydrogen atom and z is the charge after the collision. Within the range $v/v_0 \approx z^{1/2}$, ionization and recombination cross sections are of the same order of magnitude. For $v/v_0 \gg z^{1/2}$ the ionization becomes more probable.
The charge exchange process consists in a collision between a positive ion and a neutral atom: both particles form a molecular ion (metastable state) that split up into two particles following the scheme:

$$A^{z+} + B \Longrightarrow (AB)^{z+} \longrightarrow A^{(z-1)+} + B^{+}$$

For the cross-section, expressed in cm^2, an approximation due to Muller and Salzborn exists [72]:

$$\alpha_{rec} = 1.43 \cdot 10^{-12} z^{1.17} P_0^{-2.76} \tag{4.50}$$

where P_0 is the ionization potential of the neutral atom. The formula above foresees ions and neutral of the same species.
For typical neutral particles density in ECR sources, the time for charge exchange τ_{exc} limits the lifetime of a cold ion at the charge stare z: it is necessary to point out that this coincides with the lifetime of a given charge state, different from the lifetime of an ion inside the plasma. A rate can be estimated as:

$$\begin{cases} \tau_{z\to z-1} = (n_0 v_i \sigma_{exc}) \approx 5 \cdot 10^8 \frac{\sqrt{A}}{z n_0} \\ \\ KT_i \approx 1eV \Longrightarrow vi \approx \frac{10^8}{\sqrt{A}} \frac{\text{cm}}{\text{s}} \end{cases} \tag{4.51}$$

where n_0 is the neutral particle density in cm^{-3} and A is the atomic mass number. For a given electron density, τ_{exc} has to be higher than the ionization time for a given charge state z to be present inside the plasma. This last condition, together with relation 4.51, gives an upper limit to the neutral particle density (for a given electron density) to obtain a given charge states:

$$\frac{n_0}{n_e} \leq 7 \cdot 10^3 \xi (T_e)^{-\frac{3}{2}} A^{\frac{1}{2}} z^{-1} \tag{4.52}$$

4.5 Waves in plasma and electron heating

4.5.1 Propagation of EM waves inside a magnetoplasma

The wave propagation in plasmas is a quite complex topic, as it involves many aspects of the plasma physics and the mathematical approach is not so easy: it is determined by the plasma's dielectric properties, which in turns depend on the steady state values of magnetic and electric fields. Plasma may be both inhomogeneous and anisotropic when immersed in a magnetic field: this is exactly what happens for ECR plasmas and this condition further complicates its dielectric properties.
When a magnetostatic field is applied to the plasma the dielectric constant will transform in a tensor ($\bar{\bar{\epsilon}}$) and the field propagation will depend on the direction of the wave injection into the plasma with respect to the magnetic field. The tensor can be determined in the so called cold plasma approximation and in the high frequency limit (neglecting the ions response to the electromagnetic field because of their high inertia) by means of the single particle approach. It can be demonstrated that the wave vector **k** depends on the angle formed by the incoming wave with the magnetic field direction; in addition, for a given angle two different constants of propagation exist for the wave [73]:

$$k'_\theta = \frac{\omega}{c}\left[1 - \frac{X(1+\imath Z - X)}{(1+\imath Z)(1+\imath Z - X) - \frac{1}{2}Y_T^2 + \sqrt{\frac{1}{4}Y_T^4 + Y_L^2}(1+\imath Z - X)^2}\right]^{1/2} \tag{4.53}$$

$$k''_\theta = \frac{\omega}{c}\left[1 - \frac{X(1+\imath Z - X)}{(1+\imath Z)(1+\imath Z - X) - \frac{1}{2}Y_T^2 - \sqrt{\frac{1}{4}Y_T^4 + Y_L^2}(1+\imath Z - X)^2}\right]^{1/2} \tag{4.54}$$

In the above formulas $X = (\omega_p/\omega)^2$, $Y = (-\omega_c/\omega)$, $Z = (\omega_{eff}/\omega)$,$Y_T = Y\sin\theta$ and $Y_L = Y\cos\theta$, with ω the wave frequency, ω_c the cyclotron frequency, ω_p is the plasma frequency and ω_{eff} the collision frequency. Neglecting the collisions, for a incidence angle of 0° we obtain

$$k'_0 = \frac{\omega}{c}\sqrt{1 - \frac{X}{1+Y}} = \frac{\omega}{c}\sqrt{1 - \frac{\omega_p^2}{\omega(\omega - \omega_c)}} \tag{4.55}$$

$$k''_0 = \frac{\omega}{c}\sqrt{1 - \frac{X}{1-Y}} = \frac{\omega}{c}\sqrt{1 - \frac{\omega_p^2}{\omega(\omega + \omega_c)}} \tag{4.56}$$

while for 90° we obtain

$$k'_{\frac{\pi}{2}} = \frac{\omega}{c}\sqrt{1 - X} = \frac{\omega}{c}\sqrt{1 - \frac{\omega_p^2}{\omega^2}} \tag{4.57}$$

$$k''_{\frac{\pi}{2}} = \frac{\omega}{c}\sqrt{1 - \frac{\frac{\omega_p^2}{\omega^2}}{1 - \frac{\omega_g^2}{(\omega^2 - \omega_p^2)}}} \tag{4.58}$$

As a function of X, k'_θ is more similar to a wave propagating in an isotropic plasma and for this reason the wave associated is termed **ordinary wave**; on the other hand, the wave with k''_θ is termed **extraordinary wave**. Considering the two extreme conditions (0° and 90°) we actually have four waves: usually the ones propagating along the magnetic field are named **R** and **L**, due to their circular polarization; the waves propagating in a direction perpendicular are named O and X, according to the orientation of the wave electric field with respect to the magnetostatic field direction. The O-mode is characterized by $\mathbf{k} \perp \mathbf{B}_0$ and $\mathbf{E} \parallel \mathbf{B}_0$; If $\mathbf{E} \perp \mathbf{B}_0$ the wave is the X mode.
Let us consider now the possible cut-off and resonances for the waves described above: for the R waves, the refraction index c^2k^2/ω^2 becomes infinite at $\omega = \omega_c$, leading to the condition for the Electron Cyclotron Resonance to take place. The X mode has a resonance at the **upper hybrid frequency** defined as:

$$\omega^2 = \omega_p^2 + \omega_c^2 = \omega_h^2 \tag{4.59}$$

The L wave does not suffer any resonance, as well as the O mode: they suffer instead a cut-off that can be determined by the equations 4.56 and 4.58 when the index of refraction goes to zero. Generally, when the propagation occurs at a given angle with respect to the magnetic field, the modes listed above change continuously into each other. In the following subsections the ECR resonance, will be described more detail in.

4.5.2 The ECR heating: basic principles

From the point of view of the individual electron, the so-called ECR condition takes place when the microwave frequency ν_{MW} equals the Larmor frequency $\nu_c = \omega_c/2\pi = qB/2\pi m_e$: this process was deeply studied by Lieberman and Lichtenberg, who proposed a complicated stochastic heating theory [74, 75]. A simplified way to describe the particle acceleration in presence of the ECR resonance is due to Delcroix [76]: let's suppose for the moment that a sinusoidal electric filed expressed as

$$\mathbf{E} = \mathbf{E}_0 \cos \omega t \tag{4.60}$$

acts on an electron without any velocity component along the magnetic field line ($v_\parallel = 0$). The electron equation of motion is:

$$\mathbf{v} = \frac{q}{m}\mathbf{E}t \tag{4.61}$$

while the Larmor radius is

$$\mathbf{r}_c = \frac{\mathbf{E}}{B}t \tag{4.62}$$

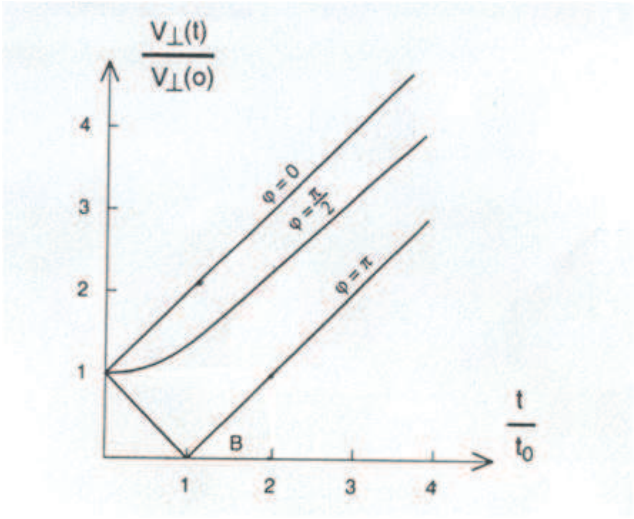

Figure 4.11: Trend of electron's velocity as a function of the time spent at the resonance for different initial phases with respect to the EM field.

It can be seen that both quantities increase linearly with the time and no phase correlations exist between the electron motion and the wave field.
When $v_{\parallel} \neq 0$ the superposition between the Larmor motion and the electric field rotation will depend on the relative phase: it can be demonstrated that the velocity can be expressed as

$$\mathbf{v}_{\perp}(t) = \frac{q}{m}\mathbf{E}t_0\sqrt{\left[1 + \frac{2t}{t_0}\cos\phi + \frac{t^2}{t_0^2}\right]} \tag{4.63}$$

with

$$t_0 = \frac{q}{m}\frac{v_{\perp}(0)}{E} \tag{4.64}$$

Figure 4.11 shows the trend of $v_{\perp}(t)$ versus the time: it is clear that for $\varphi = \pi$, the electron is decelerated first and then accelerated when $t > t_0$; at this time all the electrons are accelerated proportionally to the time and regardless of φ. After some time one has $v_{\perp} \gg v_{\parallel 0}$ and can write:

$$\mathbf{v}_{\perp} = \frac{q}{m}\mathbf{E}t = \mathbf{g}c\omega t \Longrightarrow g = \frac{qE}{mc\omega} \tag{4.65}$$

The Delcroix theory takes into account only the electron acceleration, but it does not provide any result about the electron's energy increase: considering the relativistic effects on the mass the condition for the resonance has to be modified to

$$\omega_{RF} = \frac{eB}{\gamma m_0} = \omega_c \tag{4.66}$$

This effect implies that, as a consequence of the acceleration, the phase between the electron and the wave becomes non synchronous: at that time the electron is

decelerated until the phase condition will be again favourable to the acceleration. If the magnetic field has no gradients this process occurs indefinitely and the maximum attainable energy can be expressed as [45]:

$$W_{max}\,(KeV) = 18.8\left[\frac{E}{B}\right]^{\frac{2}{3}} \propto mc^2 g^{\frac{2}{3}} \tag{4.67}$$

where E is expressed in $[kV/cm]$ and B in $[kGs]$.

4.5.3 ECR heating in presence of a magnetic gradient

A fundamental contribution to the understanding of the ECR resonance in presence of a magnetic field gradient was proposed by Canobbio in 60's [77]: he considered collisionless plasmas and defined some dimensionless quantities that are useful to simplify the treatment. Besides the already seen g, he introduced other two quantities:

$$\delta = \frac{1}{|B_0|}\left[\frac{d\,|B_0|}{dz}\right]; \qquad Z = \frac{\omega_c}{\omega} = \frac{eB}{m\omega} \tag{4.68}$$

The main effects on the ECR dynamics due to the non uniformity of the magnetic field are the following: (a) The electron spends a finite time to cross the ECR region and its final energy will depend on the magnetic gradient; (b) the phase relationship between the gyromotion and the electric field is not fixed for all the times but only for a limited number of gyro-orbits; (c) in case of very low field gradients, because of relativistic effect the electron energy $W_\perp$ may starts oscillating due to the considerations made above.
Generally, in the Canobbio theory the electron is considered to be at rest at the beginning of the resonance: this means that the time needed to go out of phase can be calculated by opportunely solving the equation of motion. It is convenient to distinguish between two situations: one involving a gentle magnetic field gradient, the other one a strong gradient. The gentle gradient regime can be mathematically defined according to the condition $\delta < 3.8g^{2/3}$: the phase between the electron's motion and the wave can be expressed as

$$\phi(\tau) \sim g^2\frac{\tau^3}{3!} \tag{4.69}$$

In this case, it can be demonstrated that the maximum attainable energy can be expressed as:

$$W_{\perp max} \simeq mc^2 g^{\frac{2}{3}} = 2mc^2\left(\frac{eE}{m\omega_0 c}\right)^{\frac{2}{3}} \tag{4.70}$$

or

$$W_{\perp max}(eV) = 1.5\cdot 10^9\left[\frac{E}{\omega_0}\right]^{\frac{2}{3}} \tag{4.71}$$

where E is expressed in $[V/cm]$: it can be seen that $W_{\perp max}$ does not depend on on the magnetic gradient (parameter δ).

The results of the Canobbio theory in case of strong magnetic field gradients are completely different: the strong gradient regime can be expressed with the following relation:

$$\delta > 3.8 g^{\frac{2}{3}} \tag{4.72}$$

After some mathematical calculations it can be demonstrated that acceleration stops (phase $\pi/2$) when $\tau = \tau_R = \omega t_R$: the transit time through the resonance can be expressed as

$$\omega t_R = \tau_R = \left[\frac{\pi}{2} \frac{120}{g^2 \delta^2} \right] \tag{4.73}$$

while the maximum attainable energy is

$$W_\perp \sim 2.9 mc^2 \left(\frac{g^3}{\delta^2} \right)^{\frac{2}{5}} \tag{4.74}$$

where m is the relativistic mass. Differently from the gentle gradient case, now $W_\perp$ depends not only on $g^{\frac{6}{5}}$, but also on the magnetic field gradient $\delta^{-4/5}$: it follows that $W_\perp$ is smaller than the energy obtainable in case of gentle gradients and the electron motion is only weakly relativistic. It is easy to see that to τ_R corresponds a length Z_R which represents a sort of ECR thickness: such thickness, usually in the order of some mm, can be calculated according to relation

$$Z_R \simeq 1.4 \left[\frac{g^2}{\delta^3} \right]^{\frac{1}{5}} \simeq 1.4 \left(\frac{c}{\omega} \right) \left[\frac{\left(\frac{eE}{mc\omega} \right)^2}{\left(\frac{c}{\omega} \right) \left(\frac{\Delta B}{\Delta z} \right) \left(\frac{1}{B_{ECR}} \right)^3} \right]^{\frac{1}{5}} \tag{4.75}$$

The energies attainable in case of strong gradients are about one third of the gentle gradient case: this difference is due to the mirror force $\mu \boldsymbol{\nabla} B$, as the higher is the B gradient the shorter is the time that each electron spends in proximity of the ECR zone. The transit of an electron through the resonance for a finite time τ_R has a twofold positive effect an electron confinement: the first is the fact that the increase of the transversal energy due to the resonance causes an increase of the magnetic force $\mu \boldsymbol{\nabla} B$, with the consequence that the electron is better confined, with a smaller excursion within the magnetic trap. The second is the **ECR mirror plug** effect: it consists basically in those cases when the ECR resonance causes the electron to leave the loss cone due to the increased transversal energy.

4.6 Plasma as a fluid

The picture given by the single particle approach becomes much more complicated when a plasma as a whole is taken into account: the **E** and **B** fields are in fact not prescribed but determined by the positions and motions of the charges themselves. Anyway, to describe the majority of plasma phenomena observed in real experiments it is possible to use fluid mechanics, in which the identity of the individual particle is neglected, and only the motion of fluid elements is taken into account. Such model will be described in the following subsections.

4.6.1 The fluid equation of motion

In the fluid approximation, the plasma is considered as composed of two or more fluids, depending on the number of species: for the sake of simplicity, in the following just electrons and only one species of ion will be taken into account, obtaining two equations of motion. Both fluids will interact with each other even in the absence of collisions because of the **E** and **B** fields they generate. It is useful to derive first an important quantity called the *convective derivative*. By neglecting collisions and thermal motions, all the particles in a fluid element move together and the average velocity **u** in the element is the same as the individual particle velocity **v**: the fluid equation is then given by the relation:

$$mn\frac{d\mathbf{u}}{dt} = qn\left(\mathbf{E} + \mathbf{u} \times \mathbf{B}\right) \tag{4.76}$$

Usually, if $\mathbf{G}(x,t)$ is any property of a fluid in one-dimension, the change of **G** with time in a frame moving with the fluid is the sum of two terms:

$$\frac{d\mathbf{G}(x,t)}{dt} = \frac{\partial \mathbf{G}}{\partial t} + \frac{\partial \mathbf{G}}{\partial x}\frac{dx}{dt} = \frac{\partial \mathbf{G}}{\partial t} + u_x\frac{\partial \mathbf{G}}{\partial x} \tag{4.77}$$

The first term on the right represents the change of **G** at a fixed point in space, and the second term represents the change of **G** as the observer moves with the fluid into a region in which **G** is different. In three dimensions, equation 4.77 generalizes to

$$\frac{d\mathbf{G}}{dt} = \frac{\partial \mathbf{G}}{\partial t} + (\mathbf{u}\cdot\boldsymbol{\nabla})\mathbf{G} \tag{4.78}$$

and is called the convective derivative, sometimes written $D\mathbf{G}/Dt$. In the case of a plasma, we take **G** to be the fluid velocity **u** and write equation 4.76 as

$$mn\left[\frac{\partial \mathbf{u}}{\partial t} + (\mathbf{u}\cdot\boldsymbol{\nabla})\mathbf{u}\right] = qn\left(\mathbf{E} + \mathbf{u} \times \mathbf{B}\right) \tag{4.79}$$

where $\partial\mathbf{u}/\partial t$ is the time derivative in a fixed frame.
If we now introduce the thermal motions a pressure force has to be added to the right-hand side of equation 4.79. Let a fluid element $\Delta x\ \Delta y\ \Delta z$ be centred at $(x_0, 1/2\Delta y, 1/2\Delta z)$ (see figure 4.12):
the total change of momentum at x_0 can be expressed as

$$\frac{\partial}{\partial t}\left(nmu_x\right)\Delta x\Delta y\Delta z = -m\frac{\partial}{\partial x}(n\bar{v_x^2})\Delta x\Delta y\Delta z \tag{4.80}$$

Let's consider the velocity v_x of a particle as decomposed into two parts,

$$v_x = u_r + v_{xr} \qquad u_r = \bar{v_x}$$

where u_x is the fluid velocity and v_{xr} the random thermal velocity. For a one-dimensional Maxwellian distribution we have $v_{xr} = \sqrt{KT/M}$ so that

$$\begin{aligned}\frac{\partial}{\partial t}\left(nmu_x\right) &= -m\frac{\partial}{\partial x}[n(\overline{u_x^2} + 2\overline{uv_{xr}^2} + \overline{v_{xr}^2}] \\ &= -m\frac{\partial}{\partial x}\left[n\left(u_x^2 + \frac{KT}{m}\right)\right]\end{aligned}$$

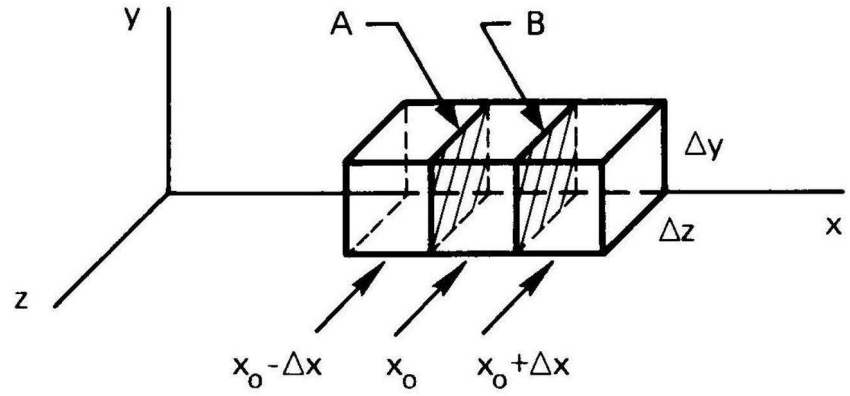

Figure 4.12: Origin of the stress tensor.

After some mathematics and imposing:

$$p \equiv nKT \tag{4.81}$$

we finally have the contribution of thermal motion to momentum change

$$mn\left(\frac{\partial u_x}{\partial t} + u_x\frac{\partial u_x}{\partial x}\right) = -\frac{\partial p}{\partial x} \tag{4.82}$$

The above expression is the pressure-gradient force: by adding the electromagnetic forces and generalizing to three dimensions the complete fluid equation becomes

$$mn\left[\frac{\partial \mathbf{u}}{\partial t} + (\mathbf{u}\cdot\boldsymbol{\nabla})\mathbf{u}\right] = qn(\mathbf{E} + \mathbf{u}\times\mathbf{B}) - \boldsymbol{\nabla}p \tag{4.83}$$

If the plasma is immersed in a magnetic field, it is possible to define two temperatures $KT_\parallel$ and $KT_\perp$ that lead to two pressures $p_\parallel = nkT_\parallel$ and $p_\perp = nkT_\perp$: in this case the pressure is in general represented by a tensor of the form:

$$\mathbf{P} = \begin{pmatrix} p_\perp & 0 & 0 \\ 0 & p_\perp & 0 \\ 0 & 0 & p_\parallel \end{pmatrix} \tag{4.84}$$

4.6.2 Drift perpendicular to B

Since a fluid element is composed of many individual particles, one would expect the fluid to have drifts perpendicular to B if the individual guiding centres have such drifts. However, since the $\boldsymbol{\nabla}p$ term appears only in the fluid equations, there is a drift associated with the pressure gradient that the fluid elements have but the particles do not: for each species, we have an equation of motion

$$mn\left[\frac{\partial \mathbf{v}}{\partial t} + (\mathbf{v}\cdot\boldsymbol{\nabla})\mathbf{v}\right] = qn(\mathbf{E} + \mathbf{v}\times\mathbf{B}) - \boldsymbol{\nabla}p \tag{4.85}$$

By supposing $\partial/\partial t = i\omega$ and considering only the motion perpendicular to $\mathbf{B}$, it can be demonstrated that the ratio between the time derivative on the left hand side of the previous equation and the first term on the right hand side is in the order of ω/ω_c. For drifts slow compared with the time scale of ω_c the former term can be neglected, so as the term $(\mathbf{v}\cdot\boldsymbol{\nabla})\mathbf{v}$.
Let $\mathbf{E}$ and $\mathbf{B}$ be uniform, but let n and p have a gradient. Taking the cross product of equation 4.85 with $\mathbf{B}$ (without the left hand side) and calling $v_\perp$ the component of the velocity perpendicular to the magnetic field we have:

$$\begin{aligned} 0 &= qn\left[\mathbf{E}\times\mathbf{B} + (\mathbf{v}_\perp\times\mathbf{B})\times\mathbf{B}\right] - \boldsymbol{\nabla}\times\mathbf{B} \\ &= qn[\mathbf{E}\times\mathbf{B} + \mathbf{B}(\mathbf{v}_\perp\cdot\mathbf{B}) - \mathbf{v}_\perp B^2] - \boldsymbol{\nabla}\times\mathbf{B} \end{aligned}$$

Therefore

$$\mathbf{v}_\perp = \frac{\mathbf{E}\times\mathbf{B}}{B^2} - \frac{\boldsymbol{\nabla}p\times\mathbf{B}}{qnB^2} \equiv \mathbf{v}_E + \mathbf{v}_D \tag{4.86}$$

where

$$\mathbf{v}_E \equiv \frac{\mathbf{E}\times\mathbf{B}}{B^2} \tag{4.87}$$

$$\mathbf{v}_D \equiv -\frac{\boldsymbol{\nabla}p\times\mathbf{B}}{qnB^2} \tag{4.88}$$

The drift $\mathbf{v}_E$ is the same as for the guiding center, but there is now a new drift $\mathbf{v}_D$, called the diamagnetic drift: since $\mathbf{v}_D$ is perpendicular to the direction of the gradient, our neglect of $(\mathbf{v}\cdot\boldsymbol{\nabla})\mathbf{v}$ is justified if $\mathbf{E}=0$; if $\mathbf{E} = -\boldsymbol{\nabla}\phi \neq 0$, $(\mathbf{v}\cdot\boldsymbol{\nabla})\mathbf{v}$ is still zero if $\nabla\phi$ and ∇p are in the same direction. It can be shown that the diamagnetic drift can be written as

$$\mathbf{v}_D = \pm\frac{\gamma KT}{eB}\frac{\hat{\mathbf{z}}\times\boldsymbol{\nabla}n}{n} \tag{4.89}$$

where γ is given by the relation

$$\gamma = \frac{2+N}{N} \tag{4.90}$$

being N the numbers of degrees of freedom. The physical reason for this drift can be seen from figure 4.13 where the orbit of ions gyrating in a magnetic field are shown: when there is a density gradient toward the left, for any fixed volume element there are more ions moving downward than upward, since the downward-moving ions come from a region of higher density. There is, therefore, a fluid drift perpendicular to $\boldsymbol{\nabla}n$ and $\mathbf{B}$, even though the guiding centres are stationary: since ions and electrons drift in opposite directions, there is a diamagnetic current given by (for $\gamma = Z = 1$)

$$\mathbf{j}_D = ne(\mathbf{v}_{Di} - \mathbf{v}_{De}) = (KT_i + KT_e)\frac{\mathbf{B}\times\boldsymbol{\nabla}n}{B^2} \tag{4.91}$$

In the fluid picture the curvature drift also exists, since the centrifugal force is felt by all the particles in a fluid element as they move along a bend in the magnetic field: a term $\overline{\mathbf{F}}_{cf} = \overline{nmv^2}_\parallel/\mathbf{R}_c = nKT_\parallel/\mathbf{R}_c$ has to be added to the right-hand side of the fluid equation of motion, leading to a drift velocity $\mathbf{v}_g = (m/q)(\mathbf{g}\times\mathbf{B})/B^2$, with $\mathbf{g} = KT_\parallel/;\mathbf{R}_c$.

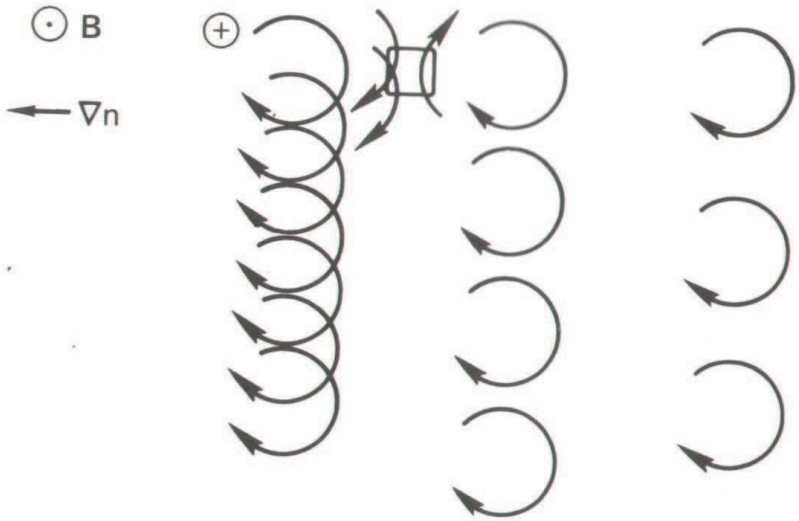

Figure 4.13: Origin of the diamagnetic drift.

4.6.3 Drift parallel to B

The z component of the fluid equation of motion is

$$mn\left[\frac{\partial v_z}{\partial t} + (\mathbf{v}\cdot\boldsymbol{\nabla})v_z\right] = qnE_z - \frac{\partial p}{\partial z} \tag{4.92}$$

The convective term can often be neglected because it is much smaller than the $\partial v_z/\partial t$ term: by choosing the simple case in which v_z is spatially uniform, the equation above can be written as

$$\frac{\partial v_z}{\partial t} = \frac{q}{m}E_z - \frac{\gamma KT}{mn}\frac{\partial n}{\partial z} \tag{4.93}$$

This shows that the fluid is accelerated along **B** under the combined electrostatic and pressure gradient forces. A particularly important result is obtained by applying equation 4.93 to massless electrons: taking the limit $m \to 0$ and specifying $q = e$ and $\mathbf{E} = -\boldsymbol{\nabla}\phi$, we have

$$qE_z = e\frac{\partial \phi}{\partial z} = \frac{\gamma KT_e}{n}\frac{\partial n}{\partial z} \tag{4.94}$$

Integrating, we have $e\phi = KT_e \ln n + C$ or

$$n = n_0 \exp(e\phi/KT) \tag{4.95}$$

called the *Boltzmann relation* for electrons. What this means physically is that electrons, being light, are very mobile and would be accelerated to high energies very quickly if there were a net force on them. Since electrons cannot leave a region without leaving behind a large ion charge, the electrostatic and pressure gradient forces on the electrons must be closely in balance.

4.7 Diffusion

In this section the model of the plasma will become more realistic by considering diffusion and transport phenomena: the problem will be first treated without considering the magnetic field; then will be extended to partially ionized plasmas and finally to fully ionized plasmas.

4.7.1 Diffusion parameters

The fluid equation seen in the previous section can be written, considering collisions but neglecting the magnetic field:

$$mn\frac{d\mathbf{v}}{dt} = mn\left[\frac{\partial \mathbf{v}}{\partial t} + (\mathbf{v}\cdot\boldsymbol{\nabla})\mathbf{v}\right] = \pm en\mathbf{E} - \boldsymbol{\nabla}p - mn\nu\mathbf{v} \tag{4.96}$$

where $\mathbf{v}$ stays for $\mathbf{u}$, e stays for q and the $\pm$ indicates the sign of the charge. We shall consider a steady state in which $\partial\mathbf{v}/\partial t = 0$: if v is sufficiently small (or ν sufficiently large), a fluid element will not move into regions of different $\mathbf{E}$ and $\boldsymbol{\nabla}p$ in a collision time and we will also have $d\mathbf{v}/dt = 0$. If this last condition holds, from equation 4.96 we have:

$$\begin{aligned}\mathbf{v} &= \frac{1}{mn\nu}(\pm en\mathbf{E} - KT\boldsymbol{\nabla}n) \\ &= \pm\frac{e}{m\nu}\mathbf{E} - \frac{KT}{m\nu}\frac{\boldsymbol{\nabla}n}{n}\end{aligned} \tag{4.97}$$

The coefficients in the above equation are called the **mobility** μ and the **diffusion coefficients** D [m^2/s] and can be expressed as:

$$\mu \equiv |q|/m\nu \tag{4.98}$$

$$D \equiv KT/m\nu \tag{4.99}$$

Such coefficients are connected by the known Einstein relation:

$$\mu = |q|D/KT \tag{4.100}$$

and can be used to define the flux $\boldsymbol{\Gamma}_j$ of the j-th species

$$\boldsymbol{\Gamma}_j = n\mathbf{v}_j = \pm\mu_j n\mathbf{E} - D_j\boldsymbol{\nabla}n \tag{4.101}$$

Fick's law of diffusion is a special case of this last equation, occurring when either $\mathbf{E} = 0$ or the particles are uncharged, so that $\mu = 0$:

$$\boldsymbol{\Gamma} = -D\boldsymbol{\nabla}n \tag{4.102}$$

4.7.2 Ambipolar diffusion

Let's describe now how a plasma created in a container decays by diffusion to the walls: once ions and electrons reach the wall, they recombine there and the density in that location is essentially zero. The fluid equations of motion and continuity govern the plasma behaviour but some simplifications can be done: on one hand, if the decay is slow, we are allowed to keep only the time derivative in the continuity equation; on the other hand, the time derivative in the equation of motion 4.96 will be negligible if the collision frequency ν is large. We thus have

$$\frac{\partial n}{\partial t} + \boldsymbol{\nabla} \cdot \boldsymbol{\Gamma}_j = 0 \tag{4.103}$$

with $\boldsymbol{\Gamma}_j$ given by equation 4.101. If the plasma is much larger than a Debye length it must be quasineutral: so it can be expected that the rates of diffusion of ions and electrons would adjust themselves so that the two species leave at the same rate. The electrons, being lighter, have higher thermal velocities and tend to leave the plasma first: a positive charge is left behind and an electric field is set up so as to retard the loss of electrons and accelerate the loss of ions; this is basically the mechanism of formation of the plasma potential. The required $\mathbf{E}$ field is found by setting $\Gamma_i = \Gamma_e = \Gamma$ in equation 4.101

$$\Gamma = \mu_i n \mathbf{E} - D_i \boldsymbol{\nabla} n = -\mu_e n \mathbf{E} - D_e \boldsymbol{\nabla} n \tag{4.104}$$

from which the electric field can be deduced:

$$\mathbf{E} = \frac{D_i - D_e}{\mu_i + \mu_e} \frac{\boldsymbol{\nabla} n}{n} \tag{4.105}$$

The common flux Γ is then given by:

$$\Gamma = \mu_i \frac{D_i - D_e}{\mu_i + \mu_e} \boldsymbol{\nabla} n - D_i \boldsymbol{\nabla} n = -\frac{\mu_i D_e + \mu_e D_i}{\mu_i + \mu_e} \boldsymbol{\nabla} n \tag{4.106}$$

The previous equation is basically the Fick's law with the diffusion coefficient:

$$D_a \equiv \frac{\mu_i D_e + \mu_e D_i}{\mu_i + \mu_e} \tag{4.107}$$

called **ambipolar diffusion coefficient**: if this is constant equation 4.103 becomes simply

$$\partial n / \partial t = D_a \nabla^2 n \tag{4.108}$$

The magnitude of D_a can be estimated if we consider $\mu_e \gg \mu_i$: equations 4.107 and 4.100 then give

$$D_a \approx D_i + \frac{\mu_i}{\mu_e} D_e = D_i + \frac{KT_e}{KT_i} D_i \tag{4.109}$$

that, for $KT_e = KT_i$, becomes

$$D_a \simeq 2 D_i \tag{4.110}$$

Finally, to sustain a plasma against the possible losses, a continuous ionization or injection of particles has to be included: in ECR sources this role is played by the resonance that increases the electron energy and allows ionizations to occur. To calculate the density profile in this case, we must add a source term to the equation of continuity:

$$\frac{\partial n}{\partial t} - D\boldsymbol{\nabla}^2 n = Q(\mathbf{r}) \tag{4.111}$$

The sign is chosen so that when Q is positive, it represents a source and contributes to positive $\partial n/\partial t$; at the steady state $\partial n/\partial t = 0$ and what is left is a Poisson-type equation for $n(\mathbf{r})$.

4.7.3 Diffusion across the magnetic field

A magnetic filed can help in decreasing the rate of plasma losses by diffusion. Let's consider a weakly ionized plasma in a magnetic field: charged particles will move along $\mathbf{B}$ by diffusion and mobility according to what was described in the previous subsection. Thus, we have for each species:

$$\Gamma_z = \pm\mu n E_z - D\frac{\partial n}{\partial z} \tag{4.112}$$

If there were no collisions, particles would not diffuse at all in the perpendicular direction and would be said to be magnetized; there are, of course, particle drifts across $\mathbf{B}$ because of electric fields or gradients in $\mathbf{B}$ (as seen in the single particle approach), but these can be arranged to be parallel to the walls. For example, in a cylindrical plasma the gradients are in radial direction so that the drifts are in azimuthal direction as shown on figure 4.14.

When there are collisions with neutrals, charged particles migrate across $\mathbf{B}$ to the walls along the gradients: as shown in figure 4.15, they undergo a random-walk process, diffusing in the direction opposite to $\boldsymbol{\nabla} n$. The step length of this random walk is no longer the mean free path for collisions λ_m but the magnitude of the Larmor radius r_c: diffusion across $\mathbf{B}$ can therefore be slowed down by decreasing r_c, that is by increasing B. To see how this can be possible the perpendicular component of the fluid equation of motion for either species can be written as:

$$mn\frac{d\mathbf{v}_\perp}{dt} = \pm en(\mathbf{E} + \mathbf{v}_\perp \times \mathbf{B}) - KT\boldsymbol{\nabla} n - mn\nu\mathbf{v}_\perp \tag{4.113}$$

Let's assume that ν is large enough for the $d\mathbf{v}_\perp/dt$ term to be negligible: the x and y components are (supposing $\mathbf{B} = B\hat{z}$)

$$\begin{aligned} mn\nu v_x &= \pm enE_x - KT\frac{\partial n}{\partial x} \pm env_y B \\ mn\nu v_y &= \pm enE_y - KT\frac{\partial n}{\partial y} \mp env_x B \end{aligned} \tag{4.114}$$

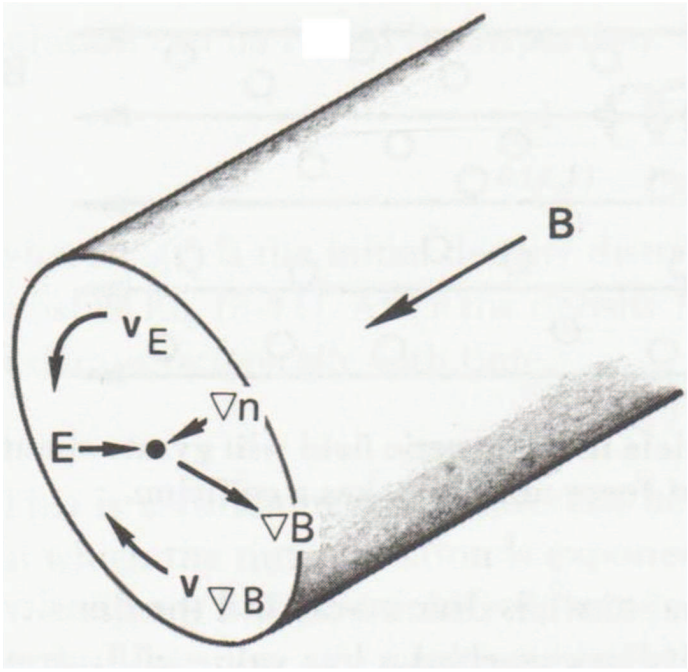

Figure 4.14: Particle drift in a cylindrically symmetric plasma column: it doesn't lead to losses.

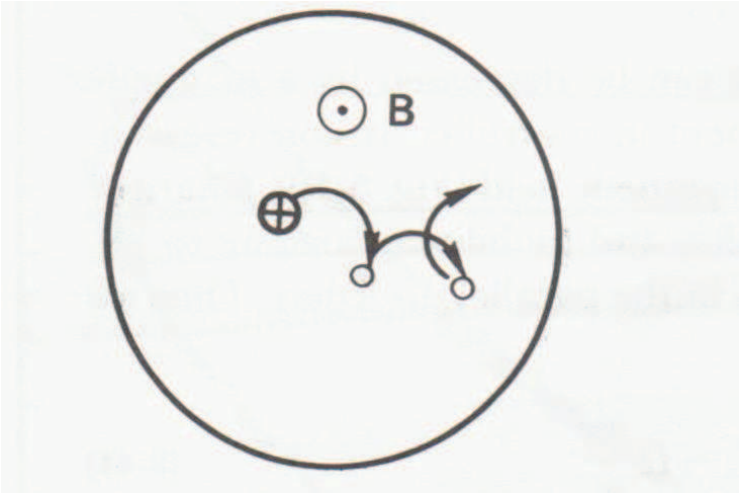

Figure 4.15: Diffusion of plasma particle along ∇B due to collisions.

Using the definitions of μ and D, we have

$$\begin{aligned} v_x &= \pm\mu E_x - \frac{D}{n}\frac{\partial n}{\partial x} \pm \frac{\omega_c}{\nu} v_y \\ v_y &= \pm\mu E_y - \frac{D}{n}\frac{\partial n}{\partial y} \mp \frac{\omega_c}{\nu} v_x \end{aligned} \tag{4.115}$$

Solving the system one founds the usual $\mathbf{E}\times\mathbf{B}$ and diamagnetic drifts and also: the perpendicular mobility and diffusion coefficient

$$\mu_\perp = \frac{\mu}{1+\omega_c^2\tau^2} \qquad D_\perp = \frac{D}{1+\omega_c^2\tau^2} \tag{4.116}$$

where $\tau = \nu^{-1}$. Following the above results it is found that:

$$\mathbf{v}_\perp = \pm\mu_\perp \mathbf{E} - D_\perp \frac{\boldsymbol{\nabla} \boldsymbol{n}}{n} + \frac{\mathbf{v}_E + \mathbf{v}_D}{1+(\nu^2/\omega_c^2)} \tag{4.117}$$

The perpendicular velocity of either species is composed of two parts: first, there are the usual $\mathbf{v}_E$ and $\mathbf{v}_D$ drifts perpendicular to the electric field and density; these drifts are slowed down by collisions with neutrals. Second, there are the mobility and diffusion drifts parallel to the electric field and density: these drifts have the same form as in the $B = 0$ case, but the coefficients μ and D are reduced by the factor $1+\omega_c^2\tau^2$. The product $\omega_c\tau$ is an important quantity in magnetic confinement: when $\omega_c^2\tau^2 \ll 1$ the magnetic field has little effect on diffusion, while when $\omega_c^2\tau^2 \gg 1$ the magnetic field significantly retards the rate of diffusion across $\mathbf{B}$. Considering this last limit we have

$$D_\perp = \frac{KT}{m\nu}\frac{1}{\omega_c^2\tau^2} = \frac{KT\nu}{m\omega_c^2} \tag{4.118}$$

Comparing the last equation with 4.99 we see that the role of the collision frequency ν has been reversed: in diffusion parallel to $\mathbf{B}$, D is proportional to ν^{-1}, since collisions retard the motion; in diffusion perpendicular to $\mathbf{B}$, $D_\perp$ is proportional to ν, since collisions are needed to move transversally to $\mathbf{B}$. The dependence on m has also been reversed: keeping in mind that ν is proportional to $m^{-1/2}$, we see that $D \propto m^{-1/2}$, while $D_\perp \propto m^{1/2}$. In parallel diffusion, electrons move faster than ions because of their higher thermal velocity; in perpendicular diffusion, electrons escape more slowly because of their smaller Larmor radius.

Since the diffusion and mobility coefficients are anisotropic in the presence of a magnetic field, the problem of ambipolar diffusion is not as straightforward as in the $B = 0$ case. Consider the particle fluxes perpendicular to $\mathbf{B}$: normally, since $\Gamma_{e\perp}$ is smaller than $\Gamma_{i\perp}$, a transverse electric field would be set up so as to aid electron diffusion and retard ion diffusion. However the negative charge resulting from $\Gamma_{e\perp} < \Gamma_{i\perp}$ can be dissipated by electrons escaping along the field lines. Although the total diffusion must be ambipolar, the perpendicular part of the losses does not to be ambipolar: the ions can diffuse out primarily radially, while the electrons diffuse out primarily along $\mathbf{B}$.

4.7.4 Diffusion in a fully ionized plasma

Now we can pass to the problem of diffusion in a fully ionized plasma. Since the dissipative term $\mathbf{P}_{ei}$ contains the difference in velocities $\mathbf{v}_i - \mathbf{v}_e$ it is simpler to consider a linear combination of the ion and electron equations and work with $\mathbf{v}_i - \mathbf{v}_e$ instead of $\mathbf{v}_i$ or $\mathbf{v}_e$. Up to now, the plasma have been regarded as composed of two inter penetrating fluid: by using the different linear combination described below the plasma will become a single fluid with a mass density ρ and an electrical conductivity $1/\eta$. What will be obtained are the so called equations of magnetohydrodynamics (MHD).
For a quasineutral plasma with singly charged ions, we can define the mass density ρ, mass velocity $\mathbf{v}$, and current density $\mathbf{j}$ as follows:

$$\rho \equiv n_i M + n_e m \approx n(M+m) \tag{4.119}$$

$$\mathbf{v} \equiv \frac{1}{\rho}(n_i M \mathbf{v}_i + n_e m \mathbf{v}_e) \approx \frac{M\mathbf{v}_i + m\mathbf{v}_e}{M+m} \tag{4.120}$$

$$\mathbf{j} \equiv e(n_i \mathbf{v}_i - n_e \mathbf{v}_e) \approx ne(\mathbf{v}_i - \mathbf{v}_e) \tag{4.121}$$

By adding a term $Mn\mathbf{g}$ representing a gravitational force, the ion and electron equations can be written

$$Mn\frac{\partial \mathbf{v}_i}{\partial t} = en(\mathbf{E} + \mathbf{v}_i \times \mathbf{B}) - \boldsymbol{\nabla} p_i + Mn\mathbf{g} + \mathbf{P}_{ie} \tag{4.122}$$

$$mn\frac{\partial \mathbf{v}_e}{\partial t} = -en(\mathbf{E} + \mathbf{v}_e \times \mathbf{B}) - \boldsymbol{\nabla} p_e + Mn\mathbf{g} + \mathbf{P}_{ei} \tag{4.123}$$

where $\mathbf{P}_{ie} = -textbf{P}_{ei}$ represents the momentum gained by collision of a species with the other. For simplicity the viscosity tensor $\boldsymbol{\pi}$ and the $(\mathbf{v}\cdot\boldsymbol{\nabla})\mathbf{v}$ terms were neglected. By summing equations 4.122 and 4.123 we get :

$$n\frac{\partial}{\partial t}(M\mathbf{v}_i + m\mathbf{v}_e) = en(\mathbf{v}_i - \mathbf{v}_e) \times \mathbf{B} - \boldsymbol{\nabla} p + n(M+m)\mathbf{g} \tag{4.124}$$

where the electric field and the collision terms have cancelled out and $p = p_i + p_e$ is the total pressure. With the help of equations 4.119- 4.121, equation 4.124 can be written simply:

$$\rho\frac{\partial \mathbf{v}}{\partial t} = \mathbf{j} \times \mathbf{B} - \boldsymbol{\nabla} p + \rho\mathbf{g} \tag{4.125}$$

This is the first MHD equation describing the mass flow, where the electric field does not appear explicitly because the fluid is neutral.
To obtain the second MHD equation let's multiply equation 4.122 by m and equation 4.123 by M and subtract the latter from the former: the result is

$$\begin{aligned} Mmn\frac{\partial}{\partial t}(\mathbf{v}_i - \mathbf{v}_e) = {} & en(M+m)\mathbf{E} + en(m\mathbf{v}_i + M\mathbf{v}_e) \times \mathbf{B} \\ & - m\boldsymbol{\nabla} p_i + M\boldsymbol{\nabla} p_e - (M+m)\mathbf{P}_{ei} \end{aligned} \tag{4.126}$$

After some simplification it can be demonstrated that the previous equation becomes:

$$\mathbf{E}+\mathbf{v}\times\mathbf{B}-\eta\mathbf{j}=\frac{1}{e\rho}\left[\frac{Mmn}{e}\frac{\partial}{\partial t}\left(\frac{\mathbf{j}}{n}\right)+(M-m)\mathbf{j}\times\mathbf{B}+m\boldsymbol{\nabla}p_i-M\boldsymbol{\nabla}p_e\right] \quad (4.127)$$

The $\partial/\partial t$ term can be neglected in slow motions, where inertial effects are unimportant. In the limit $m/M\to 0$, equation 4.127 then becomes

$$\mathbf{E}+\mathbf{v}\times\mathbf{B}=\eta\mathbf{j}+\frac{1}{en}(\mathbf{j}\times\mathbf{B}-\boldsymbol{\nabla}p_e) \quad (4.128)$$

where

$$\eta\equiv\frac{\pi e^2 m^{1/2}}{(4\pi\epsilon_0)^2(KT_e)^{3/2}}\ln\Lambda \quad (4.129)$$

This is the second MHD equation, called the generalized Ohm's law: it describes the electrical properties of the conducting fluid. The $\mathbf{j}\times\mathbf{B}$ term is called the Hall current term and it is usually small enough to be neglected, so as the last term of the equation. Ohm's law is then simply

$$\mathbf{E}+\mathbf{v}\times\mathbf{B}=\eta\mathbf{j} \quad (4.130)$$

The last two MHD equations, continuity for mass ρ and charge σ, are easily obtained from the sum and difference of the ion and electron equations of continuity: the complete set of MHD equations is then

$$\begin{aligned}\rho\frac{\partial\mathbf{v}}{\partial t}&=\mathbf{j}\times\mathbf{B}-\boldsymbol{\nabla}p+\rho\mathbf{g}\\ \mathbf{E}+\mathbf{v}\times\mathbf{B}&=\eta\mathbf{j}\\ \frac{\partial\rho}{\partial t}+\boldsymbol{\nabla}\cdot(\rho\mathbf{v})&=0 \quad (4.131)\\ \frac{\partial\sigma}{\partial t}+\boldsymbol{\nabla}\cdot\mathbf{j}&=0 \quad (4.132)\end{aligned}$$

The first two MHD equations can now be used at the steady state in the absence of gravity: they take the form in this case

$$\mathbf{j}\times\mathbf{B}=\boldsymbol{\nabla}p \quad (4.133)$$

$$\mathbf{E}+\mathbf{v}\times\mathbf{B}=\eta\mathbf{j} \quad (4.134)$$

The parallel component of the latter equation is simply the ordinary Ohm's law:

$$E_\parallel=\eta_\parallel j_\parallel \quad (4.135)$$

The perpendicular component is found by taking the cross-product with $\mathbf{B}$:

$$\begin{aligned}\mathbf{E}\times\mathbf{B}+(\mathbf{v}_\perp\times\mathbf{B})\times\mathbf{B}&=\eta_\perp\mathbf{j}\times\mathbf{B}=\eta_\perp\boldsymbol{\nabla}p\\ \mathbf{E}\times\mathbf{B}-\mathbf{v}_\perp B^2&=\eta_\perp\boldsymbol{\nabla}p\\ \mathbf{v}_\perp&=\frac{\mathbf{E}\times\mathbf{B}}{B^2}-\frac{\eta_\perp}{B^2}\boldsymbol{\nabla}p\end{aligned} \quad (4.136)$$

The first term is just the $\mathbf{E} \times \mathbf{B}$ drift of both species together; the second term is the diffusion velocity in the direction of $-\boldsymbol{\nabla} p$. If we suppose a cylindrical plasma with potential and pressure gradients in the radial direction, we could write:

$$v_\theta = -\frac{E_r}{B} \qquad v_r = -\frac{\eta_\perp}{B^2}\frac{\partial p}{\partial r} \tag{4.137}$$

The flux associated with diffusion is:

$$\boldsymbol{\Gamma}_\perp = n\mathbf{v}_\perp = -\frac{\eta_\perp n(KT_i + KT_e)}{B^2}\boldsymbol{\nabla} n \tag{4.138}$$

similar to the Fick's law with the diffusion coefficient given by

$$D_\perp = \frac{\eta_\perp n \sum KT}{B^2} \tag{4.139}$$

The above formula is the so-called "classical" diffusion coefficient for a fully ionized gas: it differs substantially from equation 4.118 for a partially ionized plasma. First of all here $D_\perp$ is not constant but proportional to n; second, since η is proportional to $KT^{-3/2}$, $D_\perp$ decreases with increasing temperature, contrarily to a partially ionized plasma. Finally, diffusion is automatically ambipolar in a fully ionized gas (as long as like-particle collisions are neglected): $D_\perp$ in equation 4.139 is in fact the coefficient for the entire fluid. It is useful to point out that there is no transverse mobility in a fully ionized gas: equation 4.136 for $\mathbf{v}_\perp$ in fact contains no component along $\mathbf{E}$ which depends on $\mathbf{E}$: if a transverse $\mathbf{E}$ field is applied to a uniform plasma both species drift together with the $\mathbf{E} \times \mathbf{B}$ velocity.
The evaluation of the relation between $D_\perp$ and $\mathbf{B}$ in a fully ionized plasma revealed a dependence as B^{-1} rather than B^{-2} and it was found that the absolute value of $D_\perp$ was far larger than that given by equation 4.139: this effect was first noted in 1946 by Bohm, Burhop, and Massey, who were developing a magnetic arc for use in uranium isotope separation. Bohm gave a semiempirical formula for the diffusion coefficient

$$D_\perp = \frac{1}{16}\frac{KT_e}{eB} \equiv D_B \tag{4.140}$$

that agrees with a surprising number of different experiments. Diffusion following this law is called **Bohm diffusion** [78].

4.8 Beam Formation

In general, an ion source consists of two parts: the first is the plasma generator that provides ion and serves as reservoir; the second is the extraction system that accepts ions from the reservoir and forms the ion beam. Both parts of the source may be treated independently as long as the plasma generator provides ions at the required current density and covers the whole area of the extraction system. Considering that the aim of a Charge Breeder is to deliver a usable highly charged ions beam for post-acceleration, it is useful to describe here the process of ions extraction: this is also connected with the proposed three electrodes extraction system for the SPES-CB described in chapter 5.

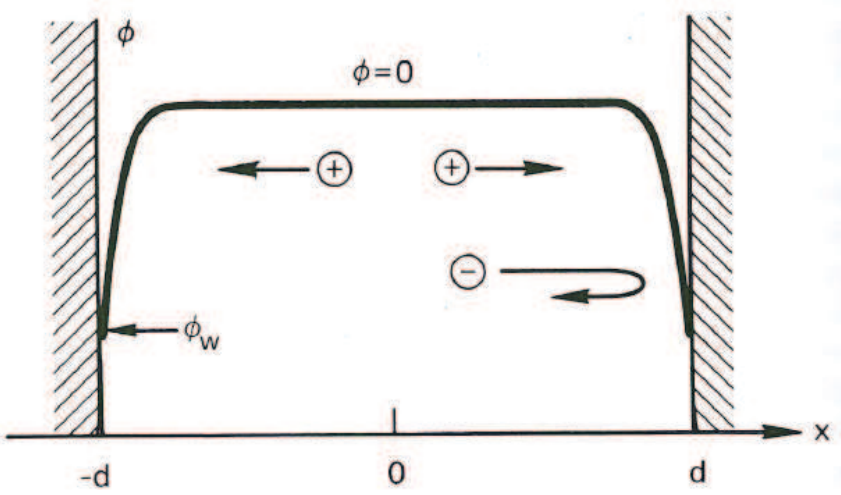

Figure 4.16: Plasma potential profile and sheath formation near the wall of the plasma's container. Potentials adjust so that ions and electrons fluxes reaching the wall are equal.

4.8.1 The sheath formation and the Bohm criterion

Let's suppose that particles are drifting towards the wall of the container, as shown in figure 4.16, and suppose also there is no appreciable electric field inside the plasma, so that we can the let the potential ϕ be zero there. When ions and electrons hit the wall, they recombine and are lost: since electrons have a much higher thermal velocities than ions, they are lost faster and leave the plasma with a net positive potential with respect to the wall (that is the wall potential ϕ_w is negative in this case). The Debye shielding will confine the potential variation to a layer of the order of several Debye lengths in thickness: this layer, which must exist on all walls with which the plasma is in contact, is called **sheath**. The function of a sheath is to form a potential barrier so that the more mobile specie, usually electrons, is confined electrostatically. The height of the barrier adjusts itself so that the flux of electrons that have enough energy to go over the barrier to the wall is just equal to the flux of ions reaching the wall. The situation near one of the walls is zoomed in figure 4.17: at the plane x=0, ions are imagined to enter the sheath region from the main plasma with a drift velocity u_0; for simplicity, we assume $KT_i = 0$, so that all ions have the velocity u_0 at $x = 0$. If $u(x)$ is the ion velocity, conservation of energy requires

$$\frac{1}{2}Mu^2 = \frac{1}{2}Mu_0^2 - e\phi(x) \Longrightarrow u = \left(u_o^2 - \frac{2e\phi}{M}\right)^{1/2} \tag{4.141}$$

The ion equation of continuity then gives the ion density n_i in terms of the density n_0 in the main plasma:

$$n_0 u_0 = n_i(x)u(x) \Longrightarrow n_i(x) = n_0\left(1 - \frac{2e\phi}{Mu_0^2}\right)^{-1/2} \tag{4.142}$$

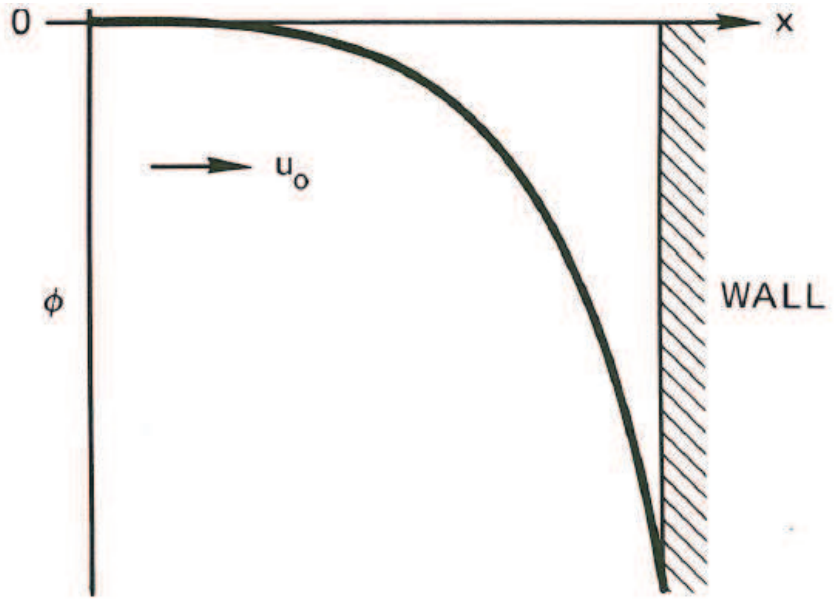

Figure 4.17: Potential ϕ in a planar sheath. Ions are assumed to enter the sheath with a uniform velocity u_0.

In the steady state, the electrons will follow the Boltzmann relation so the Poisson equation is:

$$\epsilon_0 \frac{d^2\phi}{dx^2} = e(n_e - n_i)\left[\exp\left(\frac{e\phi}{KT_e}\right) - \left(1 - \frac{2e\phi}{Mu_0^2}\right)^{-1/2}\right] \tag{4.143}$$

The structure of this equation can be made clearer if we a apply a change in variables as follows:

$$\chi \equiv -\frac{e\phi}{KT_e} \qquad \xi \equiv \frac{x}{\lambda_D} = x\left(\frac{n_0 e^2}{\epsilon_0 KT_e}\right)^{1/2} \qquad \mathscr{V} \equiv \frac{u_0}{(KT_e/M)^{1/2}} \tag{4.144}$$

Then equation 4.143 becomes:

$$\chi'' = \left(1 + \frac{2\chi}{\mathscr{V}}\right)^{-1/2} - e^{-\chi} \tag{4.145}$$

where the prime denote $d/d\xi$. This is the nonlinear equation of a plane sheath and it has an acceptable solution only if $\mathscr{V}$ is large enough, that is if the particles velocity is higher than a given value. Equation 4.145 can be integrated once by multiplying both side by χ' and obtaining:

$$\frac{1}{2}(\chi'^2 - \chi_0'^2) = \mathscr{V}\left[\left(1 + \frac{2\chi}{\mathscr{M}^2}\right)^{1/2} - 1\right] + e^{-\chi} - 1 \tag{4.146}$$

If $\mathbf{E} = 0$ in the plasma, we must set $\chi_0' = 0$ at $\xi = 0$: a second integration to find χ needs a numerical approach but whatever the answer is, the right-hand side of

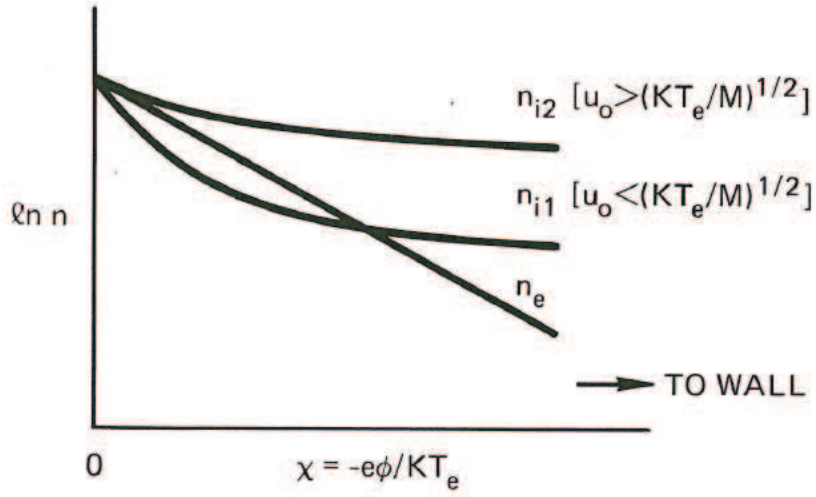

Figure 4.18: Variation of ions and electrons densities Vs potential inside the sheath (log scale): two different ion velocities are supposed (one higher, one lower than u_0.)

equation 4.146 must be positive for all χ. In particular, for $\chi \ll 1$ (that is at the plasma boundary), we can expand the right-hand terms in Taylor series:

$$\begin{aligned} \mathscr{V}^2\left[1+\frac{\chi}{\mathscr{V}^2}-\frac{1}{2}\frac{\chi^2}{\mathscr{V}^4+\cdots-1}\right]+1-\chi+\frac{1}{2}\chi^2+\cdots-1>0 \\ \frac{1}{2}\chi^2\left(-\frac{1}{\mathscr{V}^2}+1\right)>0 \\ \mathscr{V}^2>1 \qquad \text{or} \qquad u_0>(KT_e/M)^{1/2} \end{aligned} \tag{4.147}$$

This inequality is known as the **Bohm criterion** [79]: it says that ions must enter the sheath region with a velocity greater than the acoustic velocity $v_s = \sqrt{KT_e/M}$. To give the ions this directed velocity u_0 there must be a finite electric field in the plasma: this means that the assumption $\chi' = 0$ at $\xi = 0$ is approximate but possible because the scale of the sheath region is usually much smaller than the scale of the main plasma. The value of u_0 is somewhat arbitrary, depending on where we choose to put the boundary $x = 0$ between the plasma and the sheath. Of course, the ion flux n_0u_0 is fixed by the ion production rate, so if u_0 is varied, the value of n_0 at $x = 0$ will vary inversely with u_0. If the ions have finite temperature, the critical drift velocity u_0 will be somewhat lower.

The physical reason for the Bohm criterion is easily seen from a plot of the ion and electron densities versus χ shown in figure 4.18. The electron density n_e falls exponentially with χ, according to the Boltzmann relation; the ion density also falls, since the ions are accelerated by the sheath potential. If the ions start with a large energy, $n_i(\chi)$ falls slowly since the sheath field causes a relatively minor change in the ions velocity. If the ions start with a small energy, $n_i(\chi)$ falls fast and can go below the n_e curve: in that case, $n_e - n_i$ is positive near $\chi = 0$ and equation 4.143 tells us that $\phi(x)$ must curve upward, in contradiction to the requirement that the sheath

must repel electrons. In order for this not to happen, the slope of $n_i(\chi)$ at $\chi = 0$ must be smaller (in absolute value) than that of $n_e(\chi)$; this condition is identical to the condition $\mathscr{V}^2 > 1$.
Since $n_e(\chi)$ falls exponentially with χ, the electron density can be neglected in the region of large χ next to the wall (or any other negative electrode). Poisson's equation is then approximately

$$\chi'' \approx \left(1 + \frac{2\chi}{\mathscr{V}^2}\right)^{-1/2} \approx \frac{\mathscr{V}}{(2\chi)^{1/2}} \tag{4.148}$$

Multiplying by χ' and integrating from $\xi_1 = \xi_s$ to $\xi_1 = \xi$ we have

$$\tfrac{1}{2}(\chi'^2 - \chi_s'^2) = \sqrt{2}\mathscr{V}(\chi^{1/2} - \chi_s^{1/2}) \tag{4.149}$$

where ξ_s is the place where we started neglecting n_e. We can redefine the zero of χ so that $\chi_s = 0$ at $\xi = \xi_s$; the χ_s' term will be also neglected, since the slope of the potential curve can be expected to be much steeper in the $n_e = 0$ region than in the finite-n_e region. Then, equation 4.149 becomes

$$\chi' = 2^{3/4}\mathscr{V}^{1/2}\chi^{1/4} \tag{4.150}$$

or

$$d\chi/\chi^{1/4} = 2^{3/4}\mathscr{V}^{1/2}\, d\xi \tag{4.151}$$

Integrating from $\xi = \xi_s$ to $\xi = \xi_s + \lambda_D = \xi_{wall}$, we have

$$\tfrac{4}{3}\chi_w^{3/4} = 2^{3/4}\mathscr{V} d/\lambda_D \tag{4.152}$$

or

$$\mathscr{V} = \frac{4\sqrt{2}}{9}\frac{\chi_w^{3/2}}{d^2}\lambda_D^2 \tag{4.153}$$

coming back to the variables u_0 and ϕ, and nothing that the ion current density into the walls is $J = en_0u_0$, we then find

$$J = \frac{4}{9}\left(\frac{2e}{M}\right)^{1/2}\frac{\epsilon_0|\phi_w|^{3/2}}{d^2} \tag{4.154}$$

This is just the well-known **Child-Langmuir law** of space charge limited current in a planar diode [80]. The potential variation in a plasma-wall system can be divided into three parts: nearest the wall there is an electron-free region whose thickness d is given by equation 4.154; here J is determined by the ion production rate and ϕ_w is determined by the equality of the electron and ion fluxes. There is also a zone in which n_e is appreciable with a scale length of the Debye length; finally, there is a region with much larger scale length, the *presheath*, in which the ions are accelerated at the required velocity u_0 by a potential drop $|\phi| \geq KT_e/2e$. The potential distribution of course varies smoothly: the above division is made only for convenience and is possible thanks to the disparity in scale lengths of the various zones.

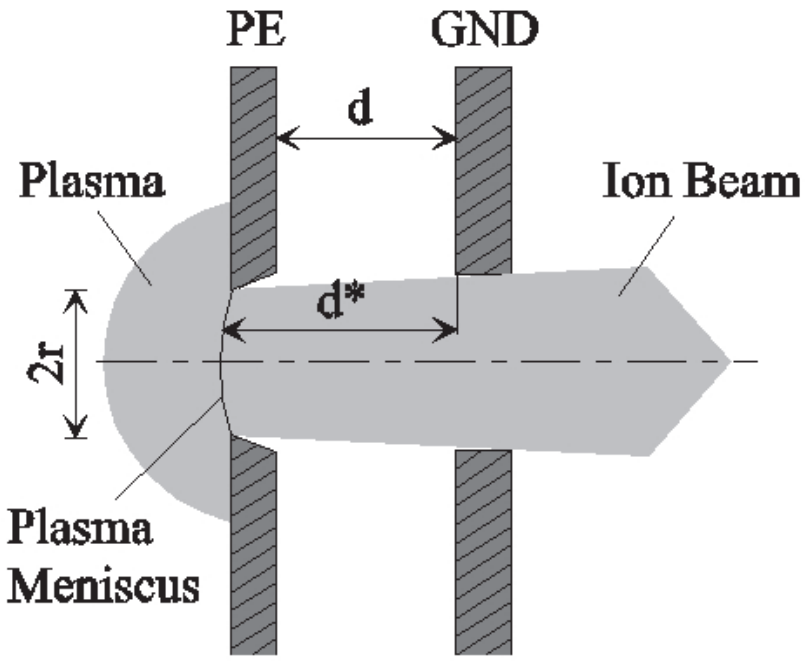

Figure 4.19: Simple diode extraction system: the effective extraction gap $d*$ is given by the distance between the ground electrode and the plasma meniscus.

4.8.2 Ion extraction

The extraction system determines the beam properties such as ion current and beam quality in general: it fulfils the task of adapting the plasma generator to the beam transport line. The simplest type is a single gap, two electrodes system, as the one shown schematically in figure 4.19: the extractor consists of a plasma electrode at positive potential (usually called the plasma electrode) and a grounded electrode. The electric field strength E is given by the voltage V and the distance d between plasma electrode and ground electrode. The emission surface of the ions at the plasma boundary is called the plasma meniscus: the extracted ion beam current is either limited by the plasma itself or by space charge forces. In the first case the current is limited by the amount of charges the plasma can deliver: if we suppose that a magnetic confinement is acting on the plasma, then the extractable current can be calculated by the expression

$$n_{ext}^{+} eS \left\langle v^{+} \right\rangle = j_P S_{ext} \approx \frac{0.5 n_i eV}{\tau_i} = I^{+} \tag{4.155}$$

where n_i is the ion density inside the plasma, n_{ext}^{+} is the one at the plasma boundary ($n_i > n_{ext}^{+}$) and S_{ext} is the plasma section close to the extraction. If the average ion charge is q, being n_q and τ_q its density and confinement time, the maxim extractable current is given by

$$I_q^{+} = j_P S = \frac{0.5 n_q q r^2 L}{\tau_q} \tag{4.156}$$

where r and L are respectively the radius and the length of the plasma.
For the second case the extractable emission current density can be calculated by the Child-Langmuir law previously seen: the emission area is assumed to be planar and infinite and for a generic ion of charge q it can be written (here V stays for $|\phi|_w$ of equation 4.154):

$$j_{CL} = \frac{4}{9}\epsilon_0\sqrt{\frac{2eq}{M}}\frac{1}{d^2}V^{3/2} \tag{4.157}$$

The total ion beam current that can be formed from a cylindrically-symmetric extraction system is then given by the expression

$$I_{CL} = \frac{4}{9}\pi\epsilon_0\sqrt{\frac{2eq}{M}}S^2V^{3/2} \tag{4.158}$$

where $S = r/d$ is the aspect ratio, r is the radius of the hole in the plasma electrode, and $F = \pi r^2$ is the emitting area. The extractable ion beam current is proportional to $V^{3/2}$: the proportionality constant is called the **perveance P of the extraction system**

$$P = \frac{4}{9}\pi\epsilon_0\sqrt{\frac{2eq}{M}}S^2 \tag{4.159}$$

This quantity is usually compared to the **perveance P^* of a given ion beam** defined as:

$$P^* = \frac{I}{V^{3/2}} \tag{4.160}$$

in order to verify if a given extraction system is able to extract the desired current level for a given extraction voltage. The current density given by equation 4.154 depends on the plasma density n_0 at the plasma meniscus: all ions with a small energy component in the z-direction are able to leave the plasma. Therefore, the shape of the plasma meniscus is the results of the condition that the space charge limited current density in equation 4.154 equals the ion current density. The distance d^* (see figure 4.19) between plasma meniscus and ground electrode adjusts in such a way that the electric field strength at the plasma meniscus is zero. For the case of a diode system, electrons that are generated within the beam channel are accelerated towards the plasma and may change the charge state distribution in the emission region. Furthermore, these electrons may not contribute to space charge compensation of the ion beam right behind the ground electrode: without space charge compensation the divergence angles increase rapidly after extraction, making difficult the beam transport. To avoid this inconvenience a third electrode, the so-called puller or suppressor electrode, is placed between the plasma electrode and ground electrode and held at a negative potential, as shown in figure 4.20: this configuration is called triode or accel-decel extraction system due to the fact that, to allow electron reflection, the beam is initially accelerated and then slightly decelerated. In the case of a triode system the absolute value of the negative potential has to be added to the potential used in equation 4.154.

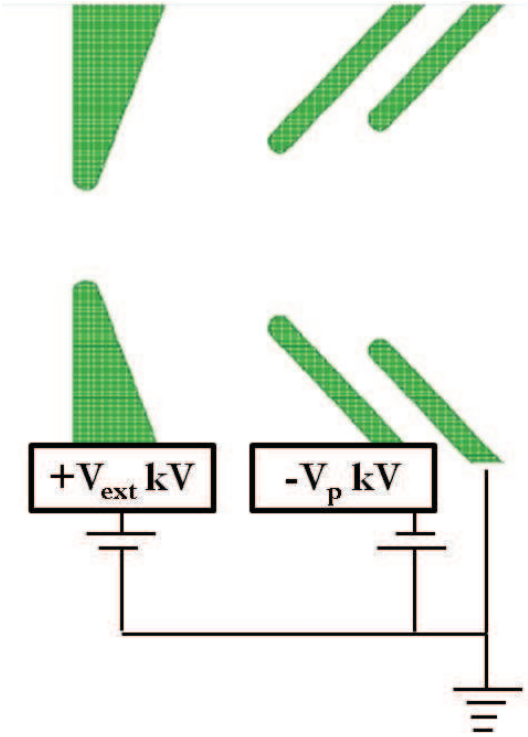

Figure 4.20: Scheme of an accel-decel extraction system.

4.8.3 Beam quality

To characterize an ensemble of particle trajectories a mathematical model is used [81]: this model expresses the trajectories in terms of point in phase space (position Vs momentum). The six-dimensional distribution function can be written as:

$$f = f(x, y, z, p_x, p_y, p_z) \tag{4.161}$$

If the momentum in the z-direction (considered as beam axis) is much greater than in transverse direction, the radial momentum can be replaced by the orbital angle

$$x' = \frac{p_x}{p_z} \qquad y' = \frac{p_y}{p_z} \tag{4.162}$$

In some cases it is possible to divide the six-dimensional distribution function into a two and four dimensional subspaces: the two-dimensional distribution functions f_x^* and f_y^* are obtained by integration over the complementary coordinates x, x' and y, y':

$$f_x^* = \iint_{-\infty}^{\infty} f \; dy \; dy' \qquad f_y^* = \iint_{-\infty}^{\infty} f \; dx \; dx' \tag{4.163}$$

The emittance of an ion beam is defined as the smallest area in the 2-D subspace divided by π,

$$\epsilon_x = \frac{1}{\pi} \iint_{-\infty}^{\infty} dx \; dx' \qquad \epsilon_y = \frac{1}{\pi} \iint_{-\infty}^{\infty} dy \; dy' \tag{4.164}$$

If only conservative forces are present, Liouville's theorem affirms that the density, and therefore the volume in phase space, is constant

$$\frac{df}{dt} = 0 \tag{4.165}$$

The same theorem is also valid in all subspaces of the six-dimensional phase space: this ensures that the emittance in equation 4.164 is a conserved value. Usually the emittance figure is matched to an ellipse

$$\epsilon = \gamma x^2 + 2\alpha x x' + \beta x'^2 \tag{4.166}$$

whose parameters α, β and γ are called the **Twiss parameters**: such parameters are connected together by the relation

$$\beta\gamma - \alpha = 1 \tag{4.167}$$

Knowing the emittance, the Twiss parameters are useful to estimate some beam dimensions thanks to the following relations:

$$\begin{aligned} x_{max} &= \sqrt{\beta\epsilon} \\ x'_{max} &= \sqrt{\gamma\epsilon} \end{aligned} \tag{4.168}$$

Figure 4.21 illustrates the emittance ellipse in xx' phase space: to compare emittances at different beam energies it is necessary to normalize its value with the common relativistic parameters,

$$\epsilon_{x,norm} = \tilde{\beta}\tilde{\gamma}\epsilon_x \tag{4.169}$$

with

$$\tilde{\beta} = \frac{v}{c}, \qquad \tilde{\gamma}\frac{1}{\sqrt{1-\tilde{\beta}^2}} \tag{4.170}$$

being v the speed of ions and c the speed of light. The relativistic parameter β can be calculated by and handy formula:

$$\tilde{\beta} = 1.46 \times 10^{-3}\sqrt{\frac{qV}{A}} \tag{4.171}$$

where q is the charge state of the ion, V the accelerating voltage in kV and A the ion mass in atomic units.
To compare emittances which are based on different distributions the concept of root-mean-square rms emittance is introduced: for the bidimensional subspace it is given by

$$\epsilon_{rms} = \sqrt{\langle x^2\rangle \langle x'^2\rangle - \langle xx'\rangle^2} \tag{4.172}$$

Depending on the kind of distribution, it is said that the whole beam is enclosed within an integer multiple of the rms emittance: this integer if 4 for the so called

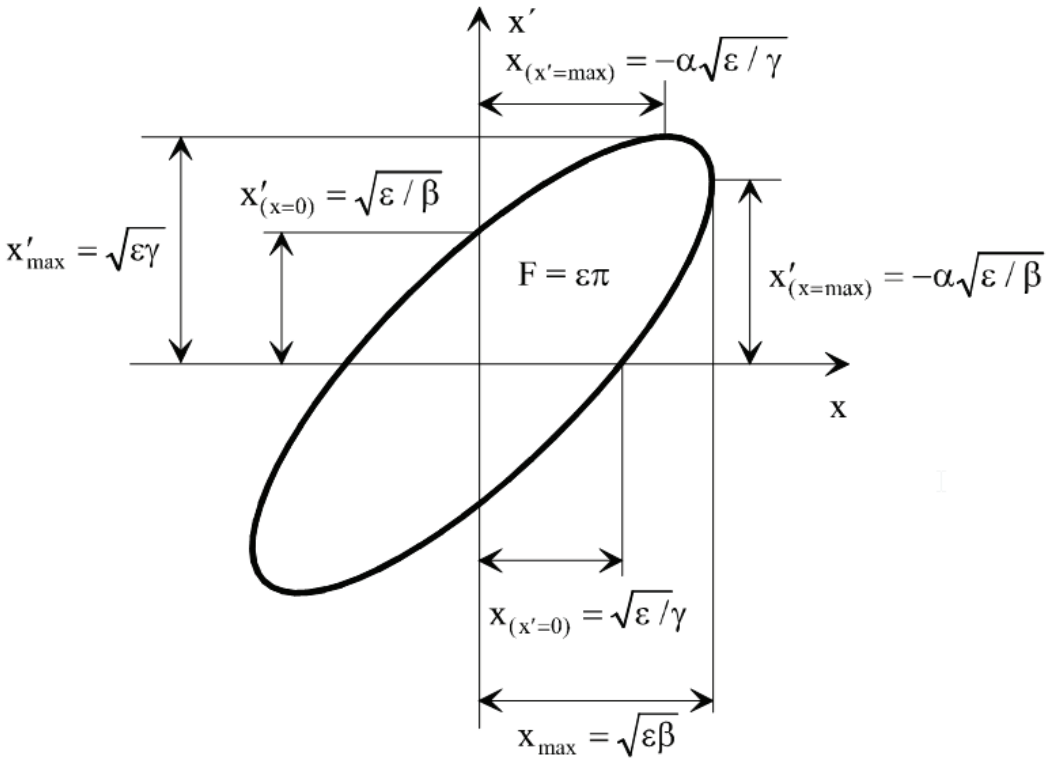

Figure 4.21: Graphic view of the emittance and the Twiss parameters.

Kapchinskij-Vladimirskij (KV) distribution while it is 5 for a Gaussian distribution. Another important parameter is the brightness of an ion beam defined as:

$$B = \frac{I}{\epsilon_x \epsilon_y} \tag{4.173}$$

where I is the ion beam current in Amperes. The brightness indicates the ion beam current normalized by the emittances of the two-dimensional subspaces.

4.8.4 Ion beam extraction from an ECR

The current extracted from ECR ion source were initially low and the extracted beam was easy to be handled, due to the low level of space charge. However, with the dramatic increase in performance over the last decades, modern sources can produce tens of mA of heavy ions, and the extracted ion beams are highly influenced by space-charge [82]. For an ECR extraction system two main contributions to the ion beam emittance have to be considered: (1) the ion temperature, and (2) the decreasing axial magnetic field [83]. The emittance due to ion temperature can be estimated by assuming a Maxwellian temperature distribution inside the plasma [84]:

$$\epsilon^{ion}_{x,norm,rms} = 0.016 r \sqrt{\frac{KT_i}{A/q}} \tag{4.174}$$

where ϵ is the normalized xx' rms emittance in π*mm*mrad, r is the plasm outlet hole radius in mm, KT_i is the ion temperature in eV and A/q is the charge to mass ratio of the considered ion. Assuming an uniform plasma density distribution across the plasma outlet hole, the emittance due to the decreasing magnetic field in the vicinity of the extractor can be described by Busch's theorem:

$$\epsilon^{mag}_{x,norm,rms} = 0.0402 r^2 B_0 \frac{1}{A/q} \tag{4.175}$$

where B_0 is the axial magnetic field strength at the extractor in T. Combining the last two equations, beam rotation due to the decreasing magnetic field becomes the dominating contribution to the ion beam emittance when the following condition is satisfied:

$$B_0 r \geq 0.5 \sqrt{KT_i} \sqrt{M/q} \tag{4.176}$$

4.9 The Charge Breeding process

4.9.1 Generalities

In the previous sections the main mechanisms characterizing an ECR ion source were described: now it is time to underline the peculiarities of an ECR-based Charge Breeder. Roughly speaking, the only mechanical difference between an ECR ion source and an ECR-based Charge Breeder is the modification of the injection side in order to accept a radioactive 1+ beam. Actually such a modification causes a series of limitations on the operation of the Charge Breeder itself: first of all it looses the possibility of using two important tricks typical of ECR ion sources, the biased disk [85] and the gas mixing [66]. The former is sacrificed to allow an easier injection of the 1+ beam; the latter is usually avoided in order to not further complicate the spectra acquired at the exit of the Charge Breeder. Another limitation is connected to the microwave circuit: to properly inject the 1+ beam and to pump efficiently the plasma chamber of the Charge Breeder, the space available for a good design of the microwave injection can be limited, leading to a possible bad coupling of the power with the plasma. This last aspect in not a problem in those models that foresee radial injection through the middle of the plasma chamber, like the Charge Breeder installed at Argonne National Laboratories [57].
The peculiarity of an ECR-based Charge Breeder is that the particles that are extracted as a high charge state ion beam are not fed as neutrals but as an external 1+ beam: a schematic description of the overall process is showed in figure 4.22. The 1+ ion beam at an energy $E = eV$ keV is injected (usually through electrostatic lenses) into the Charge Breeder held at a potential $V_{CB} = +(V - \Delta V)$ kV. As soon as the 1+ ions approach the Charge Breeder their velocity in general decreases due to the increasing V_{CB} and, in particular, to the fringe field of the Charge Breeder's coil that decreases the longitudinal velocity in favour of the transversal one (a kind of trapping effect). By properly tuning the ΔV value, 1+ ions overcome the maximum

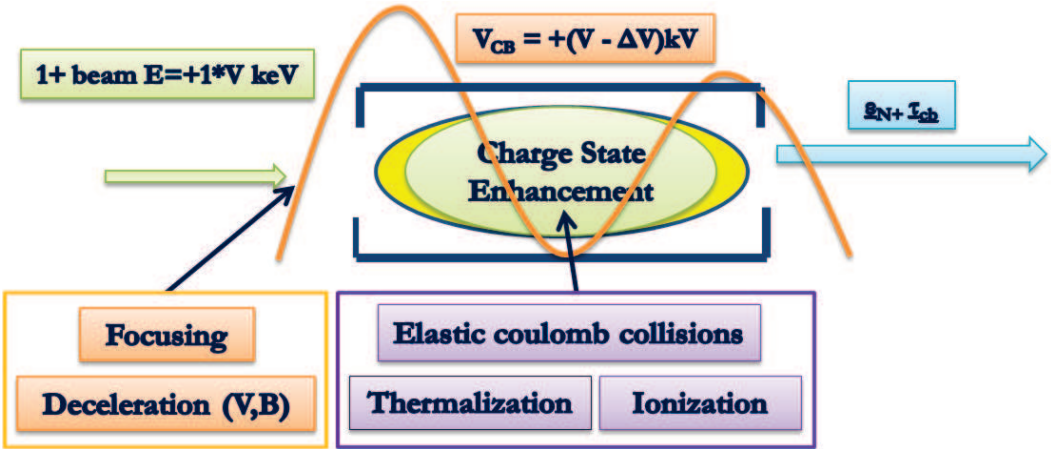

Figure 4.22: Schematic representation of the various stages involved in the charge breeding process: focusing, deceleration, thermalization, ionization and extraction.

of the magnetic field and the plasma potential, penetrating the plasma core: once there, they start to interact with plasma ions mainly through the long range Coulomb collision [86]. The effect of such interaction is twofold: on one hand, there is a general loss of directed velocity, with the mean velocity of the beam particles that starts at a given value v_0 but ends close to zero; on the other hand, there is diffusion in velocity space: the beam particles start with velocities that are very close to each other and end with a distribution of velocities that has the same thermal spread as the background plasma [87]. A picture of this effect is shown in figure 4.23. A very delicate parameter is the injection energy of the 1+ beam, optimized by regulating the value of ΔV: as will be clearer in the following chapter, in order to verify the influence of this parameter it is possible to acquire the so called "ΔV curves" by ramping the value of ΔV, one of which is shown in figure 4.24. From such curve it is evident how carefully the injection energy has to be regulated in order to get the best efficiency: a variation of some volts in the values of ΔV can lead in fact to huge variations in the measured efficiency, especially around the optimum value. It has to be pointed out that due to the fact that inside the charge breeder there is a plasma at a potential V_P (normally higher than V_{CB}) the real injection energy is lower than the product $e\Delta V$.

The collisional slowing down under the influence of an inverse-square force was first treated by Chandrasekhar describing the interaction of the stars in the gravitational field [88, 89]; the mathematical treatment was then used by Spitzer to describe the interaction of charged particles injected inside a plasma [86]. Considering the importance of this process in the functioning of an ECR-based Charge Breeder, the interaction of the so called "test particle" with plasma ions will be described in details in the following sections, deriving all the mathematical expressions for the effects such interaction has on the initial particles' distribution function. As will be described in chapter 6, such mathematical expressions have been used to carry out the most demanding part of this thesis: the development of a Matlab code able to

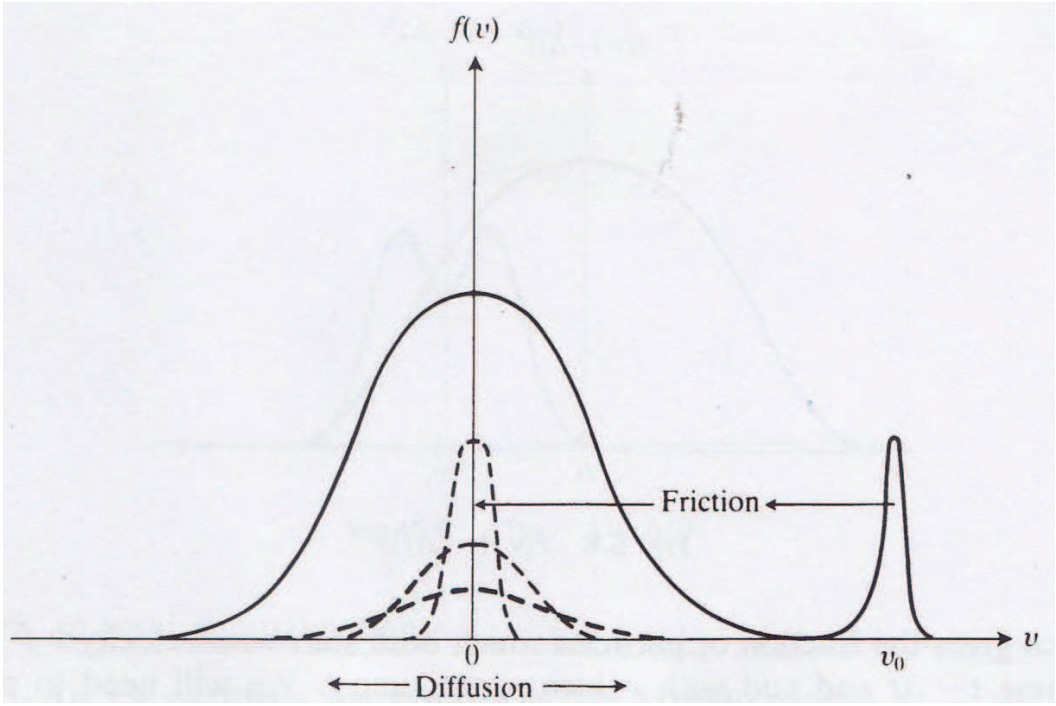

Figure 4.23: Effect of Coulomb Collisions on the distribution function of the particles injected into an ECR-based Charge Breeder.

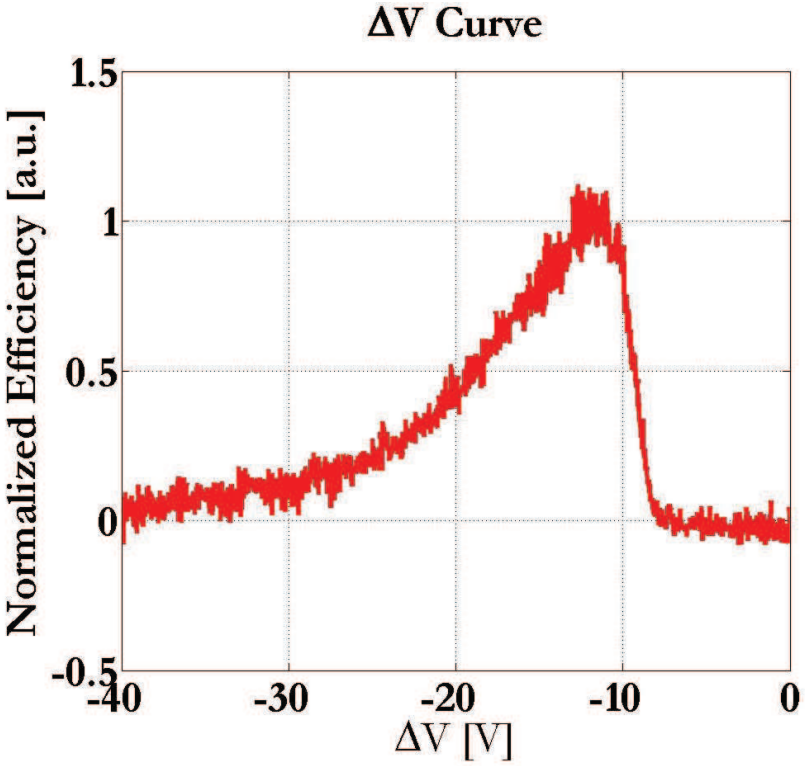

Figure 4.24: Typical ΔV curve acquired during the injection of a metallic beam inside the charge breeder. An optimum value for this parameter is clearly visible.

simulate the Charge Breeding process. In the following, the Rutherford cross-section will be initially derived, then such collisions will be applied to plasma ions with a Maxwell-Boltzmann distribution in order to derive the analytical expressions for the diffusion coefficients in the velocity space. Finally the characteristics times of the process will be obtained.

4.9.2 The Rutherford scattering cross-section

Let's start our analysis from the classical Rutherford formula: consider the relative motion of two particles p_1, p_2 of masses m_1, m_2 and charges Ze, $Z'e$ moving in each other's field of force. Let the particles be at position vectors $\mathbf{r}_1$,$\mathbf{r}_2$ and exert forces $\mathbf{F}$, $-\mathbf{F}$ on each other: then $m_1\ddot{\mathbf{r}}_1 = -\mathbf{F}$,$m_2\ddot{\mathbf{r}}_2 = \mathbf{F}$, so that $m_1m_2(\ddot{\mathbf{r}}_2 - \ddot{\mathbf{r}}_1) = (m_1+m_2)\mathbf{F}$ or

$$M\ddot{\mathbf{r}} = \mathbf{F} \tag{4.177}$$

where $r = r_1 - r_2$ is the relative distance while $M = m_1m_2/(m_1+m_2)$ is the reduced mass. Specifying $\mathbf{r}$ by polar coordinates r, θ in the plane of the orbit, we can write the conservation laws for angular momentum and energy as:

$$\begin{aligned} r^2\dot{\theta} &= cost = gb \\ \frac{1}{2}M(\dot{r}^2 + r^2\dot{\theta}^2) + V &= cost = \frac{1}{2}Mg^2. \end{aligned} \tag{4.178}$$

where b is the impact parameter defined in figure 4.25, g is the constant relative velocity and V is the potential energy (zero at $r = \infty$) of the force $\mathbf{F}$. The force on p_1 due to p_2 is:

$$\mathbf{F} = Z'e\mathbf{E} = \frac{ZZ'e^2\mathbf{r}}{4\pi\epsilon_0 r^3} \tag{4.179}$$

whence

$$V = \frac{ZZ'e^2}{(4\pi\epsilon_0 r)} \tag{4.180}$$

Eliminating θ from equation 4.178,

$$\frac{dr}{dt} = \pm g\Big(1 - \frac{b^2}{r^2} + \frac{2b_0}{r}\Big)^{\frac{1}{2}} \tag{4.181}$$

where the positive (negative) sign applying to the outgoing (incoming) trajectory. The parameter b_0 is the positive number such that

$$b_0 = \frac{|ZZ'|e^2}{4\pi\epsilon_0 Mg^2} \tag{4.182}$$

In deriving the previous expressions it was assumed than Z and Z' have opposite signs (for the other case it is sufficient to change the sign of b_0 in the final expressions).

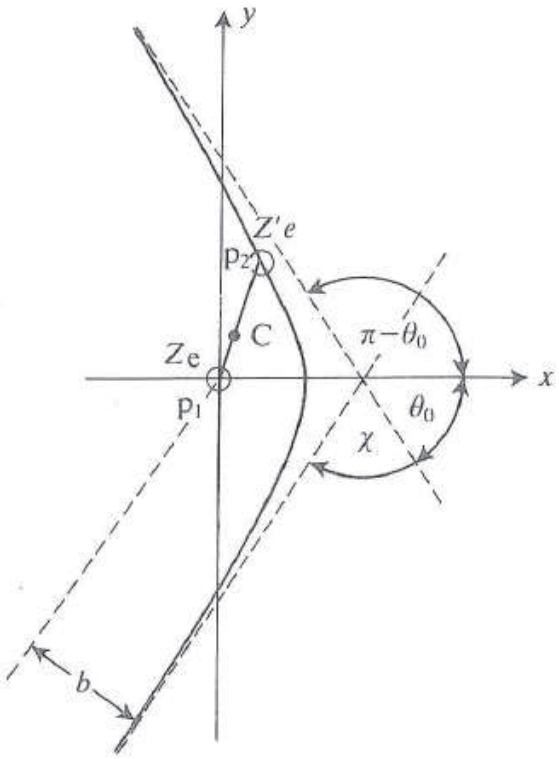

Figure 4.25: Hyperbolic orbit on an electron ($Z' = -1$) in the Coulomb field of an ion.

Using equations 4.178 to remove the time dependence, we get:

$$\frac{d\theta}{dr} = \frac{\pm b dr}{r^2\left(1 - \frac{b^2}{r^2} + \frac{2b_0}{r}\right)} \tag{4.183}$$

Solving the above equation it is found that the trajectory is an hyperbola, as illustrated for the case of an electron being scattered by an ion in figure 4.25. Let θ_0 be the angle between the x axis and the asymptotes of the hyperbola; then for the upper branch of the conic $\theta \longrightarrow \pi - \theta_0$ as $r \longrightarrow \infty$ so

$$\tan\theta_0 = \frac{b}{b_0} \tag{4.184}$$

The scattering angle (see figure 4.25) is given by:

$$\chi = \pi - 2\theta_0 \tag{4.185}$$

so that if $b < b_0$, $\chi > \frac{\pi}{2}$ and we have "close" collisions, while if $b > b_0$, $\chi < \frac{\pi}{2}$ and we have grazing or "distant" collisions.
Now suppose that instead of a precise knowledge of the impact parameter b of p_2, we know only that it is incident on an element of area $bdbd\epsilon$, as shown in figure 4.26. Then, the probability $\sigma d\Omega$ that the particle is deflected into the solid angle $d\Omega = \sin\chi d\chi d\epsilon$ is termed the "differential cross section" for the scattering

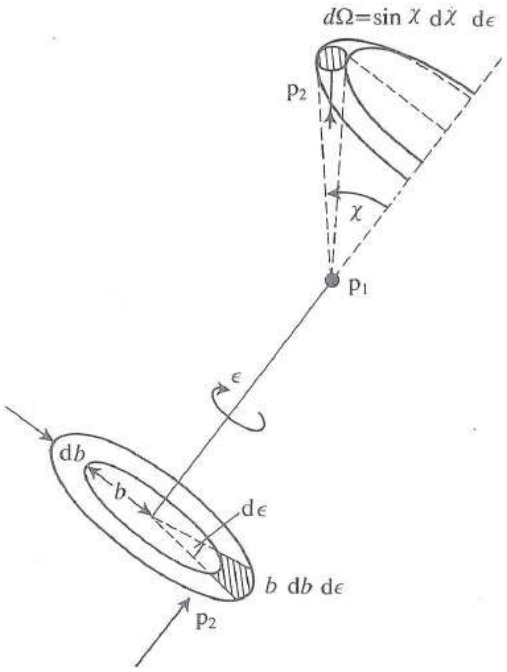

Figure 4.26: The Coulomb Scattering.

collision. Of N incident particles per unit area per second, $|bdbd\epsilon|N$ will be scattered into $d\Omega$: by definition this number also equals $\sigma d\Omega N$, hence $\sigma d\Omega = -bdbd\epsilon$, the negative sign being necessary since $db/d\chi$ is negative. From equation 4.184 and 4.185:

$$b = b_0 \cot\frac{\chi}{2} \qquad b\frac{db}{d\chi} = -\frac{1}{2}b_0^2\frac{\cos\frac{\chi}{2}}{\sin^2\frac{\chi}{2}} \tag{4.186}$$

therefore

$$\sigma(g,\chi) = -\frac{bdb}{\sin\chi d\chi} = \frac{b_0^2}{4sin^4\frac{\chi}{2}} = \Big(\frac{ZZ'e^2}{8\pi\epsilon_0 Mg\sin^2\frac{\chi}{2}}\Big)^2 \tag{4.187}$$

The equation above is the Rutherford scattering cross-section: it is evident from this formula that small angle scattering (distant collisions) are far more probable than large deflections (close collisions) due to the sin^{-4} dependence . This means that the cumulative effects of many small angle deviations can significantly change the direction of motion of the particle.

4.9.3 The Fokker-Plank equation

Let's now consider a given charged particles, called the "test" particle, being part of an ensemble characterized by a velocity distribution $f(\mathbf{r},\mathbf{v},t)$. The long-range Coulomb forces between the test particle p and the "field" particles within a Debye distance will cause p to experience a multiplicity of distant collisions, which as noted above, will be far more numerous than close collisions; consequently, almost all

the changes in direction and speed experienced by p will be small. Let p have an initial velocity $\mathbf{v}$: after a small time-interval Δt, distant collisions will generate a random walk motion in p, characterized by a small cumulative change $\Delta\mathbf{v}$ of the velocity ($|\Delta\mathbf{v}| << |\mathbf{v}|$). Let $P(\mathbf{v}|\Delta\mathbf{v})$ denote the transition probability density that p experiences the change $\Delta\mathbf{v}$ in Δt: then $f(\mathbf{r}, \mathbf{v}-\Delta\mathbf{v}, t-\Delta t) \times P(\mathbf{v}-\Delta\mathbf{v}|\Delta\mathbf{v})d(\Delta\mathbf{v})$ is the number of particles like p that are deflected from $(\mathbf{v}-\Delta\mathbf{v}, \mathbf{v})$ into the element $(\mathbf{v}, \mathbf{v}+d\mathbf{v})$ owing to interactions occurring in $(t-\Delta t, t)$. These particles will contribute to the number $f(\mathbf{r}, \mathbf{v}, t)d\mathbf{v}$, and on the assumption that the process is Markovian (that is, no earlier time-intervals contribute to this number) we obtain the equation:

$$f(\mathbf{r}, \mathbf{v}, t) = \int f(\mathbf{r}, \mathbf{v}-\Delta\mathbf{v}, t-\Delta t)P(\mathbf{v}-\Delta\mathbf{v}|\Delta\mathbf{v})d(\Delta\mathbf{v}) \tag{4.188}$$

where the integration is over all possible changes in the velocity vector. The time Δt must be short enough for $\Delta\mathbf{v}$ to remain quite small compared with $\mathbf{v}$. Expanding the integrand in equation 4.188 in a Taylor series to first order in Δt and to second order in $\Delta\mathbf{v}$, we obtain the approximate form

$$\begin{aligned} f(\mathbf{r}, \mathbf{v}, t) = \int \{(f - \Delta t\mathscr{D}f)P(\mathbf{v}|\Delta\mathbf{v}) - \Delta\mathbf{v} \cdot \frac{\partial}{\partial\mathbf{v}}[fP(\mathbf{v}|\Delta\mathbf{v})] + \\ + \frac{1}{2}\Delta\mathbf{v}\Delta\mathbf{v} : \frac{\partial^2}{\partial\mathbf{v}\partial\mathbf{v}}[fP(\mathbf{v}|\Delta\mathbf{v})]\}d(\Delta\mathbf{v}) \end{aligned} \tag{4.189}$$

where $\mathscr{D}f$ is the rate of change of f following the bunch of particles through phase space, and the terms in the integrand are evaluated at $(\mathbf{r}, \mathbf{v}, t)$. Considering that the probability of a transition of any kind occurring is unity, the leading term in the integral expression for f cancels with the left-hand side: the remaining terms can be arranged as a kinetic equation for f:

$$\mathscr{D}f = \mathbb{C} \tag{4.190}$$

where

$$\mathbb{C} = -\frac{\partial}{\partial\mathbf{v}} \cdot (\mathbf{A}f) + \frac{1}{2}\frac{\partial^2}{\partial\mathbf{v}\partial\mathbf{v}} : (\mathbf{B}f) \tag{4.191}$$

in which

$$\mathbf{A} =< \Delta\mathbf{v} >\equiv \frac{1}{\Delta t}\int \Delta\mathbf{v}P(\mathbf{v}|\Delta\mathbf{v})d(\Delta\mathbf{v}) \tag{4.192}$$

and

$$\mathbf{B} =< \Delta\mathbf{v}\Delta\mathbf{v} >\equiv \frac{1}{\Delta t}\int \Delta\mathbf{v}\Delta\mathbf{v}P(\mathbf{v}|\Delta\mathbf{v})d(\Delta\mathbf{v}) \tag{4.193}$$

The expression in equation 4.191 for the collision term $\mathbb{C}$ is known as the **Fokker-Planck equation**: the averages $\langle\Delta\mathbf{v}\rangle$ and $\langle\Delta\mathbf{v}\Delta\mathbf{v}\rangle$ are termed the friction and diffusion coefficients for reasons that will be clarified below.

To apply equation 4.191 to a plasma we must calculate these averages for the case of Coulomb collisions: we shall start by considering just one type of scatterer and denote its distribution function by $f_s(\mathbf{r}_s, \mathbf{v}_s, t)$. The probability that a single scatterer deflects p into the solid angle $d\Omega = \sin\chi d\chi d\epsilon$ (see figure 4.26) is $\sigma(g, \chi)d\Omega$, where

$g = |\mathbf{v} - \mathbf{v}_s|$ is the relative speed between the interacting particles and $\sigma(g, \chi)$ is the Rutherford scattering cross-section. The corresponding scattering rate is $g\sigma d\Omega$, that is of a group of N incident particles in a time dt, $Ng\sigma d\Omega dt$ will appear in $d\Omega$. The assumption of small scattering angles allows us to linearly superimpose the contributions of all the scatterers lying in the appropriate element $d\mathbf{v}_s$ of velocity space: thus the total probability that p is scattered into $d\Omega$ per second per unit volume is $f_s d\mathbf{v}_s g\sigma(g, \chi)d\Omega$. Hence, the averages in equation 4.192 and 4.193 are equivalent to:

$$< \Delta\mathbf{v} >= \iint \Delta\mathbf{v} g\sigma(g, \chi)d\Omega f_s d\mathbf{v}_s = \int [\Delta\mathbf{v}]_\Omega f_s d\mathbf{v}_s \tag{4.194}$$

$$< \Delta\mathbf{v}\Delta\mathbf{v} >= \iint \Delta\mathbf{v}\Delta\mathbf{v} g\sigma(g, \chi)d\Omega f_s d\mathbf{v}_s = \int [\Delta\mathbf{v}\Delta\mathbf{v}]_\Omega f_s d\mathbf{v}_s \tag{4.195}$$

where (see figure 4.26)

$$[\Delta\mathbf{v}]_\Omega \equiv \int_0^{2\pi} \int_\chi \Delta\mathbf{v} g\sigma(g, \chi) \sin\chi d\chi d\epsilon \tag{4.196}$$

$$[\Delta\mathbf{w}\Delta\mathbf{w}]_\Omega \equiv \int_0^{2\pi} \int_\chi \Delta\mathbf{w}\Delta\mathbf{w} g\sigma(g, \chi) \sin\chi d\chi d\epsilon \tag{4.197}$$

When there are several types of scatterers, equations 4.194 and4.195 have to be considered for all the species and must be summed to give the required averages.

4.9.4 The Superpotentials

Consider a test particle p of mass m undergoing an elastic collision with a scatterer of mass m_s: the velocities before and after the process are, respectively, $\mathbf{v}$, $\mathbf{v}'$ and $\mathbf{v}_s$, $\mathbf{v}'_s$. By indicating with $\mathbf{g} = \mathbf{v} - \mathbf{v}_s$ and $\mathbf{g}' = \mathbf{v}' - \mathbf{v}'_s$ the relative velocities, with $\mathbf{G} = (m\mathbf{v} + m_s\mathbf{v}_s)/(m + m_s)$ and $\mathbf{G}' = (m\mathbf{v}' + m_s\mathbf{v}'_s)/(m + m_s)$ the one of the centre of mass, it is readily shown from the conservation of momentum and energy that:

$$\mathbf{G} = \mathbf{G}' \qquad g = g' \qquad \mathbf{v} = \mathbf{G} + \frac{m}{M} \qquad \left(M \equiv \frac{mm_s}{m + m_s}\right) \tag{4.198}$$

The angle between $\mathbf{g}$ and $\mathbf{g}'$ is the scattering angle χ, and since g is unchanged in magnitude by the collision, $|\Delta\mathbf{g}| = |\mathbf{g}' - \mathbf{g}| = 2g \sin\frac{\chi}{2}$. If, as shown in figure 4.27, we express the vector $\Delta\mathbf{g}$ as the sum of three components, Δg_1 parallel to g and Δg_2, Δg_3 perpendicular to g, we have:

$$\Delta\mathbf{g} = 2g \sin\frac{\chi}{2}\left(-\sin\frac{\chi}{2}, \cos\frac{\chi}{2}\cos\epsilon, \cos\frac{\chi}{2}\sin\epsilon\right) \tag{4.199}$$

By equation 4.198 $\mathbf{v}' - \mathbf{v} = (M/m)(\mathbf{g}' - \mathbf{g})$ and so:

$$\Delta\mathbf{v} = \left(\frac{M}{v}\right)\Delta\mathbf{g} \tag{4.200}$$

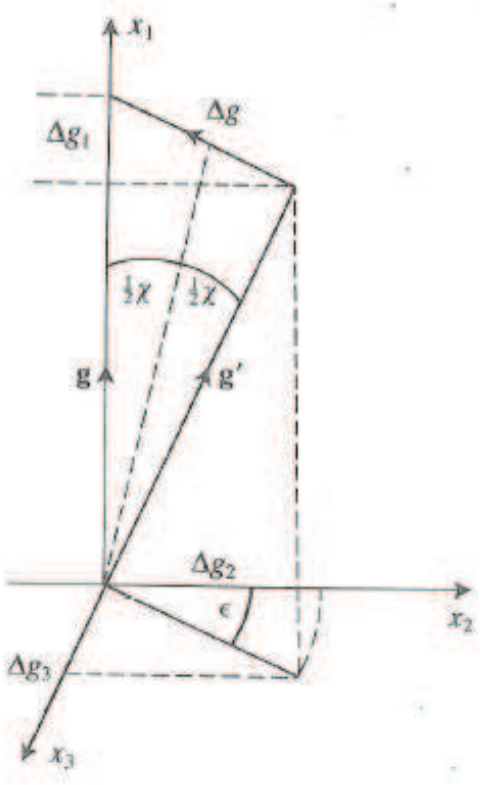

Figure 4.27: Scattering in the velocity space.

The average in equation 4.196 is now calculated using equation 4.187 and 4.199: the integrals containing $\cos\epsilon$ and $\sin\epsilon$ vanish, leaving only a component parallel to the unit vector $\mathbf{g}/g$. Thus, with χ lying in the range $\chi_{min} \leq \chi \leq \chi_{max}$ we get

$$[\Delta\mathbf{v}]_\Omega = -4\pi\frac{M}{m}(b_0 g)^2\left[\ln\sin\frac{\chi}{2}\right]_{\chi_{min}}^{\chi_{max}}\frac{\mathbf{g}}{g} \tag{4.201}$$

As χ is assumed to be small it follows that $\pi/2 \gg \chi_{max} \gg \chi_{min}$; the largest impact parameter b for which the Coulomb force is effective is the Debye length λ_D so a reasonable assumption is that χ_{min} corresponds to $b = \lambda_D$. Then, from equation 4.186 it follows that $\cot(\chi_{min}/2) \sim 2/\chi_{min} = \lambda_D/b_0$ therefore:

$$\left[\ln\sin\frac{\chi}{2}\right]_{\chi_{min}}^{\chi_{max}} \approx (1-\alpha)\ln\Lambda \qquad \left(\alpha \equiv -\frac{\ln\frac{\chi}{2}}{\ln\Lambda}\right) \tag{4.202}$$

where

$$\Lambda \equiv \lambda_D/\bar{b_0} \tag{4.203}$$

To remove the weak dependence of the logarithm on particle's velocity b_0 was replaced by an average value $\bar{b_0}$: the quantity $\ln\Lambda$ is the already seen Coulomb logarithm. Provided $\chi_{max}/2$ is large enough that $\alpha \ll 1$, then it follows from equation 4.180 and 4.201÷ 4.202 that:

$$[\Delta\mathbf{v}]_\Omega = -\frac{\left(ZZ'e^2\right)^2\ln\Lambda}{4\pi\epsilon_0^2 mM}\frac{\mathbf{g}}{g} \tag{4.204}$$

Finally, by integrating over the field particles, we obtain

$$< \Delta \mathbf{v} >= -\Gamma \frac{m}{M} \int f_s(\mathbf{v}_s) \frac{\mathbf{v} - \mathbf{v}_s}{|\mathbf{v} - \mathbf{v}_s|^3} d\mathbf{v}_s \tag{4.205}$$

where

$$\Gamma \equiv \frac{\left(ZZ'e^2\right)^2 \ln \Lambda}{4\pi\epsilon_0^2 m^2} \tag{4.206}$$

Considering that

$$\mathbf{g} \cdot \frac{\partial \mathbf{g}}{\partial \mathbf{v}} = g \frac{\partial g}{\partial \mathbf{v}} = \mathbf{g} \tag{4.207}$$

we can write

$$[\Delta \mathbf{v}]_\Omega = \frac{m}{M} \Gamma \frac{\partial}{\partial \mathbf{v}} \left(\frac{1}{g}\right) \tag{4.208}$$

and therefore

$$< \Delta \mathbf{v} >= \Gamma \frac{\partial \mathscr{H}}{\partial \mathbf{v}} \tag{4.209}$$

where

$$\mathscr{H} \equiv \frac{m}{M} \int \frac{f_s \mathbf{v}_s}{|\mathbf{v} - \mathbf{v}_s|} d\mathbf{v}_s \tag{4.210}$$

This scalar function $\mathscr{H}$ is the **first superpotential**. A similar method is applied to the average $< \Delta \mathbf{v} \Delta \mathbf{v} >$: we first calculate $[\Delta v_i \Delta v_j]_\Omega$, $i, j = 1, 2, 3..$; then integration over ϵ eliminates the terms in which i and j are not equal so it is readily found that

$$[\Delta v_2 \Delta v_2]_\Omega = [\Delta v_3 \Delta v_3]_\Omega = \Gamma / g = [\Delta v_1 \Delta v_1]_\Omega \ln \Lambda \tag{4.211}$$

The above formula can be generalized to give:

$$[\Delta \mathbf{v} \Delta \mathbf{v}]_\Omega = \frac{\Gamma}{g} \left(\mathbb{I} - \frac{\mathbf{gg}}{g^2}\right) \tag{4.212}$$

By the relation

$$\frac{\partial^2 g}{\partial \mathbf{v} \partial \mathbf{v}} = \frac{\partial}{\partial \mathbf{v}} \left(\frac{\mathbf{g}}{g}\right) = \frac{1}{g} \left(\mathbb{I} - \frac{\mathbf{gg}}{g^2}\right) \tag{4.213}$$

equation 4.212 can be expressed

$$[\Delta v_2 \Delta v_2]_\Omega = \Gamma \frac{\partial^2 g}{\partial \mathbf{v} \partial \mathbf{v}} \tag{4.214}$$

Now, introducing the **second superpotential**

$$\mathscr{G} \equiv \int f_s(v_s) |\mathbf{v} - \mathbf{v}_s| d\mathbf{v}_s \tag{4.215}$$

the average of equation 4.214 over the field particles can be written:

$$< \Delta \mathbf{v} \Delta \mathbf{v} >= \Gamma \frac{\partial^2 \mathscr{G}}{\partial \mathbf{v} \partial \mathbf{v}} \tag{4.216}$$

The introduction of the superpotentials is due to Rosenbluth and MacDonald [90]: considering the above calculated averages the Fokker-Planck equation may be expressed as

$$\frac{1}{\Gamma}\mathbb{C} = -\frac{\partial}{\partial \mathbf{v}} \cdot \left(\frac{\partial \mathscr{H}}{\partial \mathbf{v}} \right) + \frac{1}{2} \frac{\partial^2}{\partial \mathbf{v} \partial \mathbf{v}} : \left(f \frac{\partial^2 \mathscr{G}}{\Delta \mathbf{v} \Delta \mathbf{v}} \right) \tag{4.217}$$

In general we should write $\mathscr{H} = \sum_s \mathscr{H}_s$,$\mathscr{G} = \sum_s \mathscr{G}_s$ summing over different types of field particles, and a separate kinetic equation $\mathscr{D} f = \mathbb{C}$ is required for each species. To conclude this subsection it is interesting to report two relations involving $\mathscr{H}$ and $\mathscr{G}$. The first is

$$\frac{m}{M} \nabla^2_{\mathbf{v}} \mathscr{G} = 2\mathscr{H} \tag{4.218}$$

which follows on integrating $\frac{\partial}{\partial \mathbf{w}} \cdot \frac{\partial}{\partial \mathbf{v}} g = \frac{2}{g}$ over the field particles; the second is the Poisson equation

$$\nabla^2_{\mathbf{v}} \mathscr{H} = -4\pi \frac{m}{M} f_s \left(\mathbf{v}_s \right) \tag{4.219}$$

implied by equations 4.205 and 4.209.

4.9.5 The friction and diffusion coefficient with Maxwellian scatterers

The above defined superpotential can be derived in the case of an ECR plasma by considering as field particles ions in thermal equilibrium. Field particles are then distributed following the Maxwell-Boltzmann velocity distribution:

$$f_s dv_s = \frac{4}{\sqrt{\pi}} \frac{n_s}{C_s^3} \exp\left(-v_s^2/c_s^2\right) v_s^2 dv_s \tag{4.220}$$

where

$$C_s \equiv \left(\frac{2KT_s}{m_s} \right)^{1/2} \tag{4.221}$$

is the most probable three dimensional speed. Concerning the first superpotential, the function $\mathscr{H}$ in equation 4.224 is analogous to the gravitational potential due to a symmetrically distributed mass of density mf_s/M, centred on $v_s = 0$: following this analogy it is possible to calculate the increment $d\mathscr{H}$ due to the "mass" in a spherical shell Σ of radius v_s and thickness dv_s. The quantity $d\mathscr{H}$ is zero within Σ while outside is the same as that due to a concentrated mass at the origin. If $v \geq v_s$ the increment can be expressed as:

$$d\mathscr{H} = \frac{m}{M} \left\{ \frac{f_s(v_s)}{v_s} - \frac{f_s(v_s)}{v} \right\} 4\pi v_s^2 dv_s \tag{4.222}$$

while $d\mathscr{H} = 0$ if $v \leq v_s$. By substituting $y = v_s/C_s$ and $x = v/C_s$, $\mathscr{H}$ can be expressed as:

$$\mathscr{H} = \frac{mn_s 4}{MC_s\sqrt{\pi}} \int_0^x \left(\frac{1}{x} - \frac{1}{y} \right) \exp(-y^2) y^2 dy + cost \tag{4.223}$$

After an integration by parts and evaluating the constant of integration it follows that

$$\mathscr{H}(x) = \frac{mn_s}{MC_s}\frac{\Phi(x)}{x} \tag{4.224}$$

where $\Phi(x)$ is the error function; from equation 4.209 the average can be expressed as

$$< \Delta\mathbf{v} >= \Gamma\frac{\partial\mathscr{H}}{\partial\mathbf{v}} = \frac{\Gamma}{C_s}\frac{\partial v}{\partial\mathbf{v}}\frac{\partial\mathscr{H}}{\partial v} = \frac{m}{M}\frac{\Gamma n_s}{C_s^2}\hat{\mathbf{v}}\frac{d}{dx}\left(\frac{\Phi(x)}{x}\right) \tag{4.225}$$

From the equation above the so called **coefficient of dynamical friction** can be derived

$$\hat{\mathbf{v}}\cdot < \Delta\mathbf{v} >=< \Delta\mathbf{v}_{\parallel} >= -\frac{A_D}{C_s^2}\left(1+\frac{m}{m_s}\right)G\left(\frac{v}{C_s}\right) \tag{4.226}$$

where the diffusion constant A_D is defined by

$$A_D \equiv 2\Gamma n_s = \frac{\left(ZZ'\right)^2 e^4 n_s \ln\Lambda}{2\pi\epsilon_0^2 m^2} \tag{4.227}$$

and $G(x)$ is the function

$$G(x) = -\frac{1}{2}\frac{d}{dx}\left(\frac{\Phi(x)}{x}\right) = \frac{\Phi(x) - x\Phi'(x)}{2x^2} \tag{4.228}$$

Considering an ion beam injected into a plasma, this coefficient basically takes into account for the decrease in the average speed of the particles.
The second superpotential con be deduced from equation 4.218 and 4.224: after some mathematics it can be found that

$$\frac{\partial\mathscr{G}}{\partial x} = n_s C_s[\Phi(x) - G(x)] \qquad \frac{\partial^2\mathscr{G}}{\partial x^2} = 2n_s C_s\frac{G(x)}{x} \tag{4.229}$$

Since

$$\frac{\partial\mathscr{G}}{\partial v} = \frac{\partial v}{\partial\mathbf{v}}\frac{1}{C_s}\frac{\partial\mathscr{G}}{\partial x} = \frac{\hat{\mathbf{v}}}{C_s}\frac{\partial\mathscr{G}}{\partial x} \tag{4.230}$$

the expression for $\mathscr{G}$ takes the form:

$$\frac{\partial^2\mathscr{G}}{\partial\mathbf{v}\partial\mathbf{v}} = \frac{1}{C_s v}\left(\mathbb{I} - \hat{\mathbf{v}}\hat{\mathbf{v}}\right) + \frac{1}{C_s^2}\hat{\mathbf{v}}\hat{\mathbf{v}}\frac{\partial^2\mathscr{G}}{\partial x^2} \tag{4.231}$$

From equation 4.231 the so called **parallel and perpendicular diffusion coefficient** can now calculated:

$$\hat{\mathbf{v}}\hat{\mathbf{v}} :< \Delta\mathbf{v}\Delta\mathbf{v} >\equiv< \left(\Delta\mathbf{v}_{\parallel}\right)^2 >= \frac{A_D}{v}G\left(\frac{v}{C_s}\right) \tag{4.232}$$

$$\left(\mathbb{I} - \hat{\mathbf{v}}\hat{\mathbf{v}}\right) :< \Delta\mathbf{v}\Delta\mathbf{v} >\equiv< \left(\Delta\mathbf{v}_{\perp}\right)^2 >= \frac{A_D}{v}\left\{\Phi\left(\frac{v}{C_s}\right)G\left(\frac{v}{C_s}\right)\right\} \tag{4.233}$$

The last coefficient takes into account for the build up of velocity spread in a direction perpendicular to the particle's velocity; the former one instead takes into account for

Table 4.1: Intermediate values for the functions $G(x)$ and $\Phi(x) - G(x)$.

$\boldsymbol{x}$	0	0.2	0.4	0.6	0.8	1.0	1.2	1.4	1.6
$\boldsymbol{G(x)}$	0	0.073	0.137	0.183	0.208	0.214	0.205	0.186	0.163
$\boldsymbol{\Phi(x) - G(x)}$	0	0.149	0.292	0.421	0.534	0.629	0.706	0.766	0.813
$\boldsymbol{x}$	1.8	2.0	2.5	3.0	3.5	4.5	5.0	6.0	8.0
$\boldsymbol{G(x)}$	0.140	0.119	0.08	0.056	0.041	0.031	0.020	0.014	0.008
$\boldsymbol{\Phi(x) - G(x)}$	0.849	0.876	0.920	0.944	0.959	0.969	0.980	0.986	0.992

the build up of a longitudinal velocity spread. It is useful to evaluate the previous expression at the limits 0 and ∞ considering that:

$$\frac{G(x)}{x} \longrightarrow \begin{cases} \frac{2}{\sqrt{\pi}}, & x \to 0 \\ \frac{1}{2x^3}, & x \to \infty \end{cases} \qquad \frac{\Phi(x) - G(x)}{x} \longrightarrow \begin{cases} \frac{4}{3\sqrt{\pi}}, & x \to 0 \\ \frac{1}{x}, & x \to \infty \end{cases} \tag{4.234}$$

It then follows from equation 4.226 and 4.232÷4.234 that if

$$x = 0 \Rightarrow \begin{cases} < \Delta v_{\parallel} >= 0 \\ < \left(\Delta v_{\parallel}\right)^2 >= \frac{1}{2} < (\Delta v_{\perp})^2 >= \frac{2}{3\sqrt{\pi}} \frac{A_D}{C_s} \end{cases} \tag{4.235}$$

or if

$$x \to \infty \Rightarrow \begin{cases} < \Delta v_{\parallel} >= -\frac{A_D}{2} \left(1 + \frac{m}{m_s}\right) \frac{1}{v}^2 \\ < \left(\Delta v_{\parallel}\right)^2 >= \frac{A_D}{2} \frac{C_s^2}{v^3} \\ < (\Delta v_{\perp})^2 >= \frac{A_D}{v} \end{cases} \tag{4.236}$$

Equations 4.235 confirm what is physically evident, namely that stationary test particles experience no friction and that their diffusion is isotropic. On the other hand, equations 4.236 show that quite fast test particles mainly diffuse transversely to their original direction. Finally, it is also important to note that heavy test particles ($m \gg m_s$) tend to be dominated by friction. Table 4.1 shows the above functions evaluated for intermediate values of x while figures 4.28 and 4.29 show the analytic plot of both of them. It is interesting to note that the function G, governing the dynamical friction and the longitudinal diffusion, shows an optimum when $x = 1$, that is when ions are injected with a velocity equal to the plasma thermal speed: the shape of that curve is very similar to the ΔV curves experimentally acquired and showed in figure 4.24. The other function showed in figure 4.29 governs the 90° diffusion and appears to be always increasing, meaning that the higher is the injection energy, the more the particles diffuse transversely. The evaluation of $\langle(\Delta v_{\parallel})^2\rangle$ given above is not valid if $x^2 > \ln \Lambda$, that is roughly $x > 4$: this explains why the two previous plots were limited to $x = 5$. To give a numerical example, by considering ^{85}Rb ions injected in an oxygen plasma with an ion temperature $KT = 0.3$ eV the above limit corresponds to an injection energy around 25 eV: the choice of these

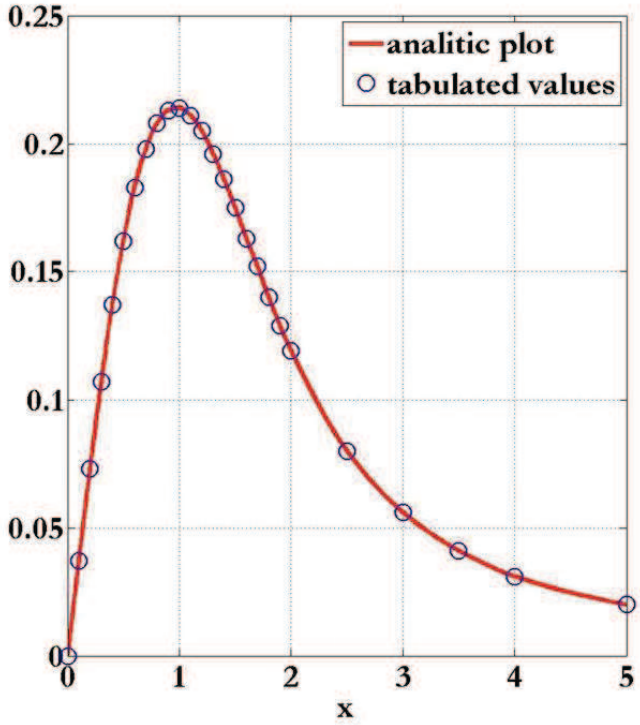

Figure 4.28: Comparison between analytic and tabulated values for the function $G(x)$.

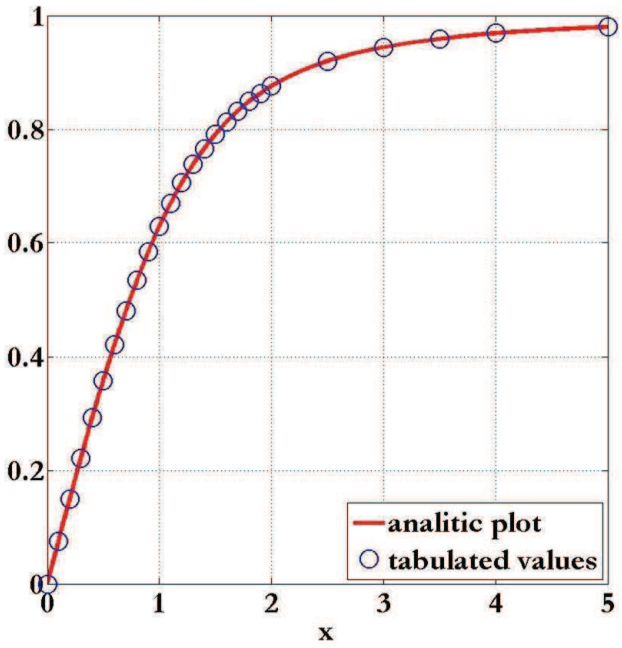

Figure 4.29: Comparison between analytic and tabulated values for the function $\Phi(x) - G(x)$.

particular values will be clearer after the description of the numerical simulations in chapter 6.

4.9.6 Relaxation times

From the coefficient defined above the very useful relaxation times can be derived. In general, a "relaxation time" is the time it takes collisions to effect a substantial change in a given initial velocity or energy distribution: in this particular case they give an idea of the relative importance of the different effects involved in the slowing down of a charged particles beam inside the plasma.
The first is the **Slowing Down Time** defined as:

$$\tau_s \equiv -\frac{v}{<\Delta v_\parallel>} = \frac{vC_s^2}{\left(1+\frac{m}{m_s}\right) A_D G\left(\frac{v}{C_s}\right)} \tag{4.237}$$

If we consider a beam of particles with the same initial velocity v_0, the slowing down time can be seen as the characteristic time of the exponential decay of the average velocity as the particles move through the plasma: if $\langle v\rangle_i$ is the average velocity at a given time t_i, then it follows that

$$\langle v\rangle_j = \langle v\rangle_i \exp -\frac{t_j - t_i}{\tau_s} \tag{4.238}$$

with $t_j > t_i$ and such that $|\langle v\rangle_j - \langle v\rangle_i| \ll \langle v\rangle_i$.
The second is the **Deflection Time**

$$\tau_D \equiv \frac{v^2}{\langle(\Delta v_\perp)^2\rangle} = \frac{v^3}{A_D\left\{\Phi\left(\frac{v}{C_s}\right) - G\left(\frac{v}{C_s}\right)\right\}} \tag{4.239}$$

This is approximately the time it takes collisions to deflect of 90° the test particle velocity: this condition is in fact the one for which the momentum is totally transferred from the longitudinal direction to the transverse one. From another point of view, this time can be thought as the time it takes an initial distribution to becomes isotropic.
The third important characteristic time is the **Energy Exchange Time**:

$$\tau_E = \frac{E^2}{(\Delta E)^2} = \frac{v^3}{4A_D G\left(\frac{v}{C_s}\right)} \tag{4.240}$$

where the second expression follows considering equation 4.232 and the approximation

$$(\Delta E)^2 = \left[\frac{1}{2}m\{(v+\Delta v_\parallel)^2 + (\Delta v_\perp)^2\} - \frac{1}{2}mv^2\right] \approx (mv\Delta v_\parallel)^2 \tag{4.241}$$

This time can be thought as the one a distribution takes to reach thermal equilibrium as a consequence of the Coulomb collisions with plasma ions: at large velocities $\tau_E = v^2x^2/2A_D = (v^2/2C_s^2)\tau_D \gg \tau_D$, showing that the deflection is the dominant

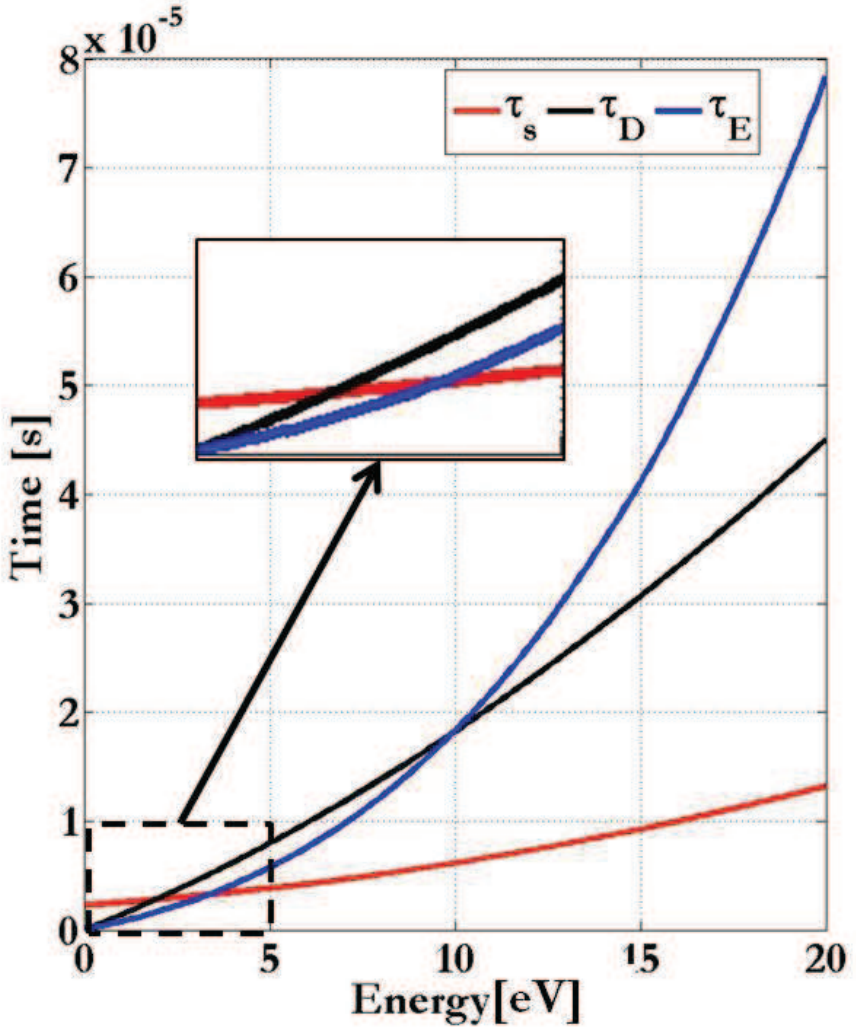

Figure 4.30: Characteristic times Vs energy of a $^{85}Rb^{1+}$ beam supposed injected into an oxygen plasma with a density $n = 2.6 \cdot 10^{+18}$ m^{-3}, $KT = 1$ eV and $\langle z \rangle = 3$.

process. It is interesting to plot in figure 4.30 the above characteristic times as a function of the injection energy considering a $^{85}Rb^{1+}$ beam injected in an oxygen plasma with a density $n = 2.6 \cdot 10^{+18}$ m^{-3}, a temperature $KT = 1$ eV and an average charge $\langle z \rangle = 3$; here again, the reason for this choice will be clear in the following chapter. The energy for which the slowing down (and the energy exchange) is maximum corresponds in this case to slightly more than 5 eV: at lower energies the diffusive processes dominate while at higher energy the fastest process is always the dynamical friction.

When the test and the scatterers are identical and in thermal equilibrium there is no energy exchange: in this case the **Self-collision Time** τ_c can be defined: it basically consists in evaluating τ_D for $v = (3KT/m)^{\frac{1}{2}}$, that is for the root mean square velocity of the distribution. At $x = \sqrt{1.5}$ table 6.1 gives $\Phi - G = 0.714$ and

$G = 0.203$, hence from equation 4.239:

$$\tau_c = \frac{2\pi 3^{\frac{3}{2}}}{0.714}\frac{\epsilon_0^2}{e^4}\frac{(m_p A)^{\frac{1}{2}}}{\ln\Lambda}\frac{(KT)^{\frac{3}{2}}}{Z^4 n} \tag{4.242}$$

where A is the particle mass number ($A_e = 1/1836$) and m_p is the mass of the proton. If the temperature in electron volts unit is expressed as $\tilde{KT}$ and $\tilde{n}$ is the density in number per cubic centimetre units, equation 4.241 reads

$$\tau_c = 1.426 \cdot 10^7 \frac{A^{\frac{1}{2}}}{\ln\Lambda}\frac{\tilde{KT}^{\frac{3}{2}}}{z^4\tilde{n}} \tag{4.243}$$

Let τ_{ee}, τ_{ii} denote the self-collision times for electrons and ions, then in agreement with what has been explained in section 4.3 it follows from equation 4.242 that:

$$\tau_{ee} : \tau_{ii} = 1 : (m_i/m_e)^{\frac{1}{2}} \tag{4.244}$$

meaning that electrons reach thermal equilibrium much faster than ions. The self-collision times are basically the ones introduced in section 4.3 and used to deduce the working regime of the plasma and then the confinement time.
To conclude this section it is interesting to derive the **Equipartition Time**: suppose that two groups of particles are in thermal equilibrium between themselves but at different temperatures KT and KT_s. Then the equipartition time τ_{eq} is defined implicitly by

$$\frac{dKT}{dt} = \frac{KT_s - KT}{\tau_{eq}} \tag{4.245}$$

It can be demonstrated that an expression for τ_{eq}, similar to the one obtained for the self-collision time, is given by the relation

$$\tau_{eq} = 5.89 \cdot 10^6 \frac{AA_s}{n_s Z^2 Z_s^2 \ln\Lambda}\left(\frac{KT}{A} + \frac{KT_s}{A_s}\right)^{\frac{3}{2}} \tag{4.246}$$

where KT is in eV and n is in cm^{-3}.

Chapter 5

A charge breeder for the SPES Project: PHOENIX

As described in chapter 3, the charge breeding technique chosen for the SPES project is the ECR-based one: in particular the device denominated PHOENIX and developed by the LPSC Laboratory [53]. In the 90's the ability of an ECR ions source to charge breed injected ions was proved by the Geller's team in Grenoble: the first experiments of the 1+→q+ conversion technique employing an ECR source were performed with the ISOL-MAFIOS set-up in the framework of the PIAFE project [91]. The results validated the methods and opened the way to its development: to improve the obtained performances, in the late 90's the LPSC Laboratory (ISN at that time) build a new model, the PHOENIX booster [92]. In the following years this device proved its ability to charge breed injected ions at high charge states with reasonable efficiencies and charge breeding times: in particular it was employed during FP6 to compare the two charge breeding techniques, ECR-based and EBIS-based, in the framework of EURISOL [45]. Table 5.1 shows updated breeding efficiencies for this device.

In June 2014 a Research Collaboration Agreement was signed between INFN and CNRS for the delivery to SPES of this charge breeder and ancillary systems by LPSC. The agreement foresees two Scientific Managers, Mr. Thierry Lamy for LPSC and myself for INFN-LNL: since that time I have been following the different stages of construction of the various parts indicating, when necessary, particular technical solutions in collaboration with different colleagues of LNL. The SPES charge breeder (SPES-CB) will be assembled and tested starting from middle March 2015 and will then be delivered to LNL. This chapter will be devoted to the description of the device object of this PhD thesis: first, the technical aspects of the SPES-CB and its installation at LNL will be described, underlining my contribution connected to the design of various parts; a brief description of the experimental activity performed within the EMILIE project [16] will follow, mainly because the obtained results benchmarked the simulations described in the next chapter.

Table 5.1: Updated performances of the PHOENIX charge breeder.

Ion	**q**	**Efficiency [%]**
Cs	27+	9.5
Xe	20+(21+)	10.9(6.2)
Sn	21+	6.0
Sr	14+	3.5
Kr	16+(18+)	12.0(8.5)
Y	14+	3.3
Rb	18+	7.7
Zn	10+	2.8
Ga	11+	2.0
Ar	8+(9+)	16.2(11.5)
Ar	8+(9+)	16.2(11.5)
Na	7+	3.8

5.1 Description of the device

A schematic view of what will be the SPES-CB is shown in figure 5.1: the B-minimum structure is created by three room temperature coils around a permanent magnet hexapole. Microwaves around 14.5 GHz are injected through two standard WR62 rectangular waveguides (one not shown in the picture) and are confined inside the plasma chamber by the extraction electrode from one side and the so called HF blocker from the other. This last element basically consists in an empty aluminium cylinder with the same axis as the plasma chamber and only one base: here a big central hole ($\phi = 28$mm) allows the injection of the 1+ beam, while other small holes ensure a proper pumping. The q+ charge bred ions are extracted through a $\phi = 8$mm hole by means of a three electrodes extraction system.
The SPES-CB can be divided in four main subsystem:

1. The magnetic system.

2. The gas injection system and the DeltaV rack.

3. The microwave injection system and the plasma chamber.

4. The extraction system.

Each of the above subsystem will be described in the following subsections.

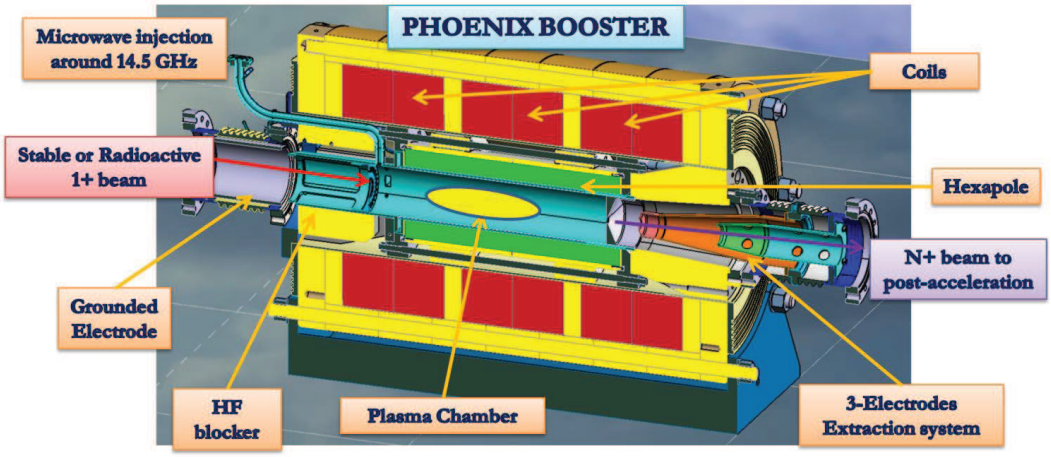

Figure 5.1: Schematic view of the SPES-CB: all the main components are indicated by coloured rectangles.

5.1.1 The magnetic system

The axial magnetic field of the SPES-CB is generated by three main coils (at ground potential) fed with a maximum current of 1300 A. Each main coil consists of two water-cooled coils for a total of six: a schematic view of one of those coils is shown in figure 5.2. Each of them is made of four double pancakes obtained by winding 8x8 mm^2 copper conductors; the conductors have a central 6 mm hole to allow a flow of 10.3 l/m of cooling water with a pressure drop of 6 bar. Figure 5.2 shows also a plot of the magnetic field on axis in the region between the two maxima, that is where the plasma in actually confined: from the values of those maxima a mirror ratio $R = B_{max}/B_{ecr} \sim 2.3$ can be deduced. The red line indicates the value of the magnetic field corresponding to the ECR resonance at 14.52 GHz: the distance between the two resonances on axis, usually taken as the plasma length, takes in this specific case the value $l_p \sim 125$ mm.

The radial field is generated by a FeNdB permanent magnet hexapole: it consists in 24 rows of 4 magnets each forming a cylinder as shown in figure 5.3. The maximum field reached at the plasma chamber wall is around 0.85 T, giving a radial mirror ratio $R = B_{rad}/B_{ecr} \sim 1.5$: figure 5.3 shows also the trend of the radial field as a function of the plasma chamber radius. The permanent magnet hexapole is mounted inside the so called central core: this structure, shown in figure 5.4, is basically mounted inside the coils and completes the magnetic system with two iron plugs (one at injection and one at extraction, see figure 5.4), that help in increasing the magnetic field on axis, and two movable iron rings whose position can be adjusted in order to optimize the magnetic field gradient. The whole central core is put at high voltage during operation so it is insulated with respect to the coils by a 3 mm thickness Erthalene PP cylinder. The central core houses also the plasma chamber that will be described in a following subsection.

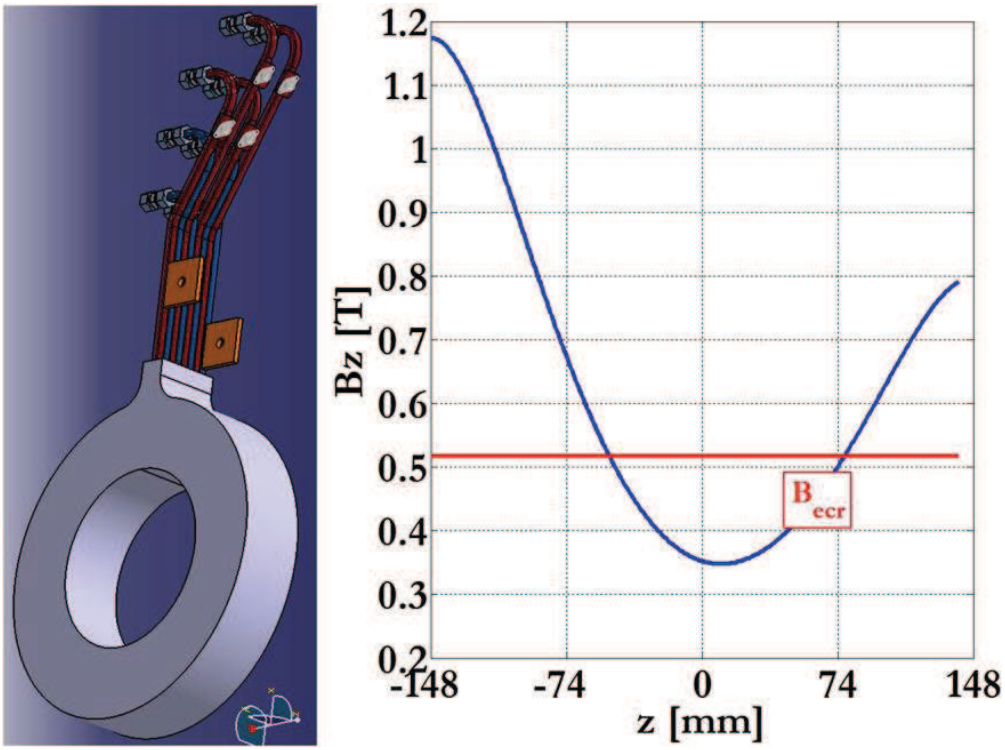

Figure 5.2: Design of one of the six coils generating the axial magnetic field of the SPES-CB (left); typical axial magnetic profile expected for the SPES-CB (right). The field corresponding to the ECR resonance is also shown.

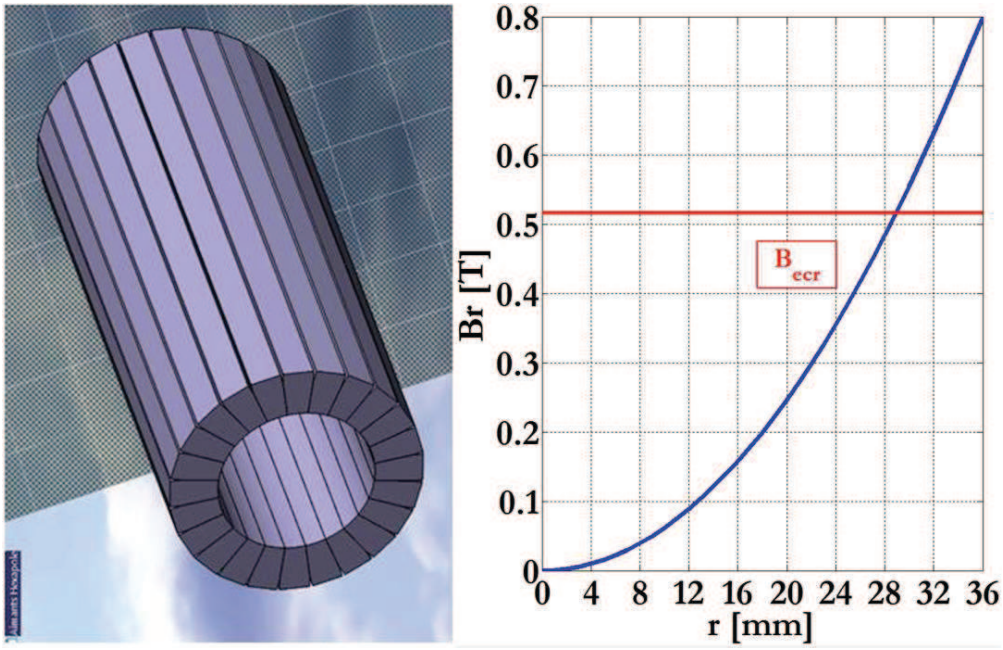

Figure 5.3: Schematic representation of the permanent magnet hexapole that will be mounted on the SPES-CB (left); typical radial profile generated by the hexapole (right). The field corresponding to the ECR resonance is also shown.

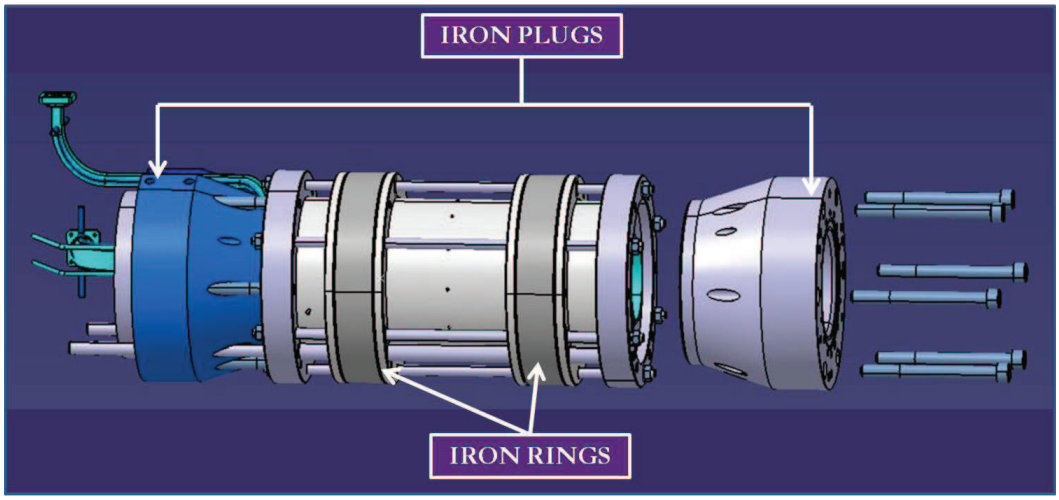

Figure 5.4: The central core of the SPES-CB: it houses the plasma chamber (not shown), the hexapole, two iron plugs and two iron rings to optimize the gradient at the resonance.

5.1.2 The gas injection system and the DeltaV rack

The DeltaV rack is a very important equipment, necessary to regulate the energy of ions injected inside the charge breeder: its electrical scheme is shown in figure 5.5. Basically the high voltage of the 1+ source works also as reference for another power

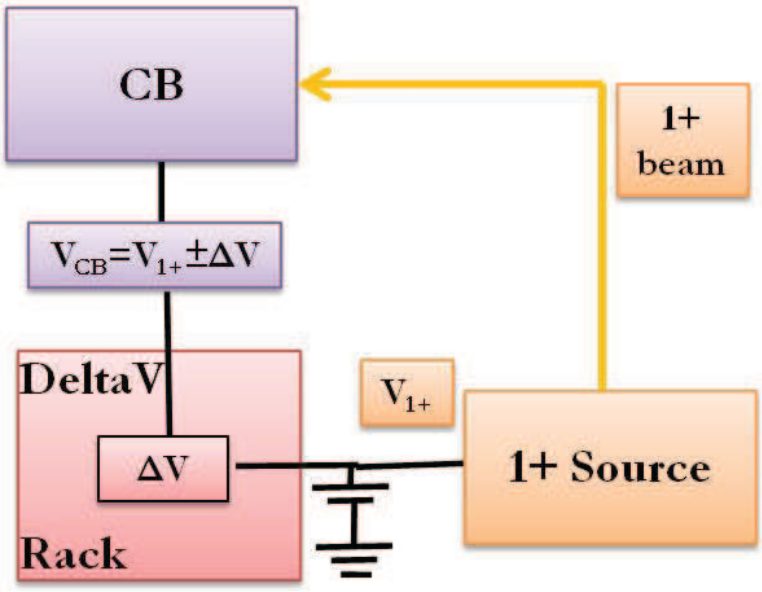

Figure 5.5: Schematic description of the electrical connection of the Delta V rack to optimize the injection of the 1+ beam.

supply mounted on the DeltaV rack and insulated from ground. The output of this last power supply in turns determines the voltage of the Charge Breeder, being less than V_{1+} of a certain amount ΔV so as to allow ions' injection.

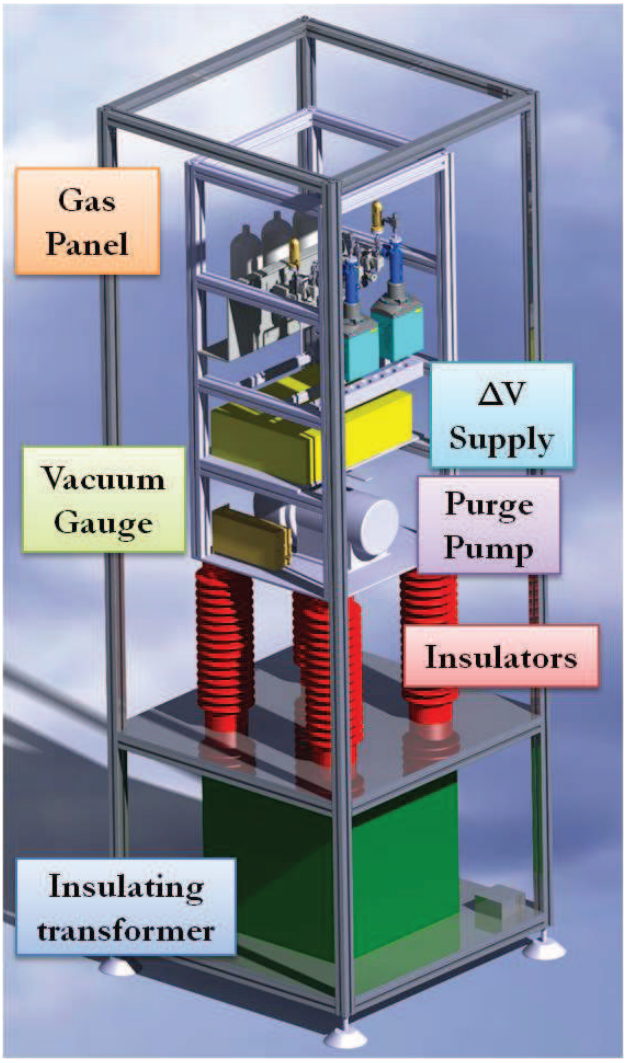

Figure 5.6: Drawing of the DeltaV rack: the gas panel and the leak valves in the upper parts, the electronics necessary to control all the equipments in the middle and at the bottom the purging pump. Insulation in ensured by four 4 kV insulators.

From the description above it comes out that the voltage of the Delta V rack coincides with the voltage of the Charge Breeder: for this reason it houses all the devices that are put at the Charge Breeder potential. For the specific case of the SPES-CB the Delta V rack was designed as shown in figure 5.6: an insulating transformer (60 kV-1 kVA) brings the main to an inner rack insulated from ground by means of four small epoxy columns; inside this rack are placed the ΔV supply (giving the potential to the CB), a complete gas feeding system with vacuum gauge, purging pump and all the necessary electronics to remotely drive the above mentioned equipments.

The gas panel shown in figure 5.7 was designed under my specifications: it consists in two independent branches allowing the possibility to inject two different kinds of gases at the same time; one branch, with only one connection for a gas bottle, will

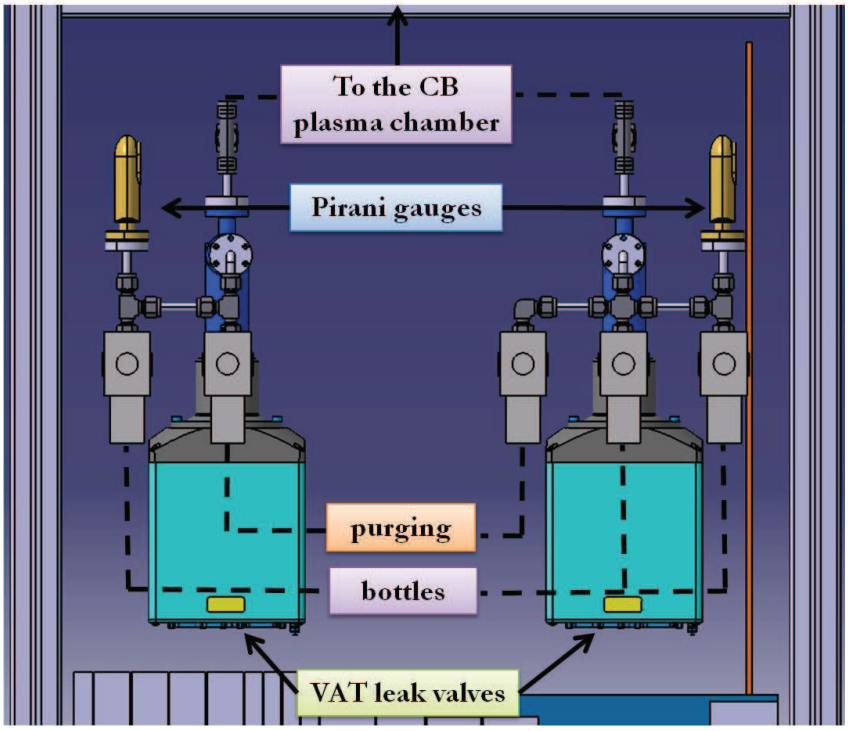

Figure 5.7: Zoom on the gas panel and the leak valves: three different gas connections are foreseen, with automatic switching from one to the other.

be used for noble gases (He and Ar); the second one will mount permanently oxygen and nitrogen gas bottles, being those two gases the ones most commonly used to produce ECR plasmas. The pressure of each branch will be monitored through a Pirani gauge and a purging port will allow cleaning of the entire gas panel. The gas in each branch will be the input for two precision leak valves, the series 59 from the VAT company: those are very precise full metal leak valves, able to adjust a flow rate down to 10^{-10} mbar*l/s; moreover, they are equipped with a system motor+encoder that can be remotely controlled through a serial port.
The Delta V rack will be equipped with a CPU, analogue and digital I/O and serial ports: this will allow to remotely execute any operation with the gas panel (including purging and switching from one gas to the other) and with the ΔV supply. The communication with the Delta V rack will be done through fibre optics: all the hardware was chosen following the standard foreseen for the SPES project, thanks to the support received from the colleague Jesus Vasquez from LNL.

5.1.3 The microwave injection system and the plasma chamber

The SPES-CB will allow the possibility to use two distinct frequencies to sustain the plasma: one around 14 GHz, the other around 18 GHz. The microwave injection system was designed in collaboration with the colleague of LNS: a schematic view of a typical circuit is shown in figure 5.8. A microwave signal will be produced by

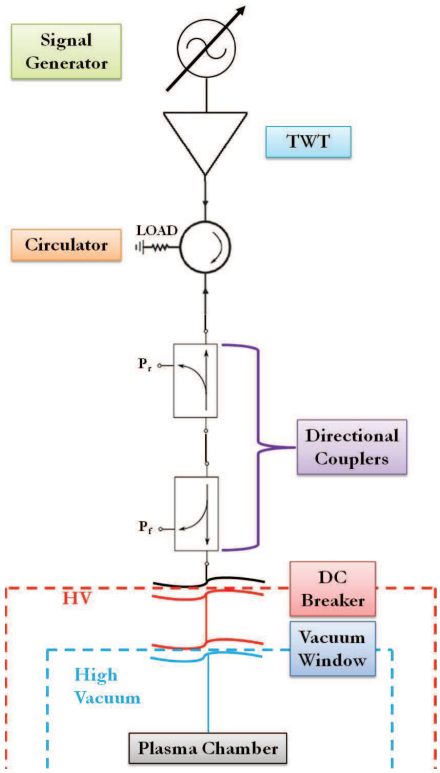

Figure 5.8: Description of one of the two microwave circuits of the SPES-CB.

a wide-band signal generator and amplified by a Travelling Wave Tube amplifier (TWTA); the microwaves will pass through a circulator that will protect the amplifier from the reflected power coming from the charge breeder. By using two directional couplers it will be possible to measure both the forward P_f and the reflected P_r power very close to the charge breeder so as to have a measure of the effective power fed to the plasma. The circuit has a first break that separates the grounded part from the high voltage part: this work is done by the DC breaker that basically consists in two waveguides separated by a given thickness of an insulator (Teflon, quartz); the thickness is big enough to ensure electrical insulation but small enough to avoid microwave losses. Finally, a microwave window from CPI separates the atmospheric pressure part from the high vacuum parts.

Microwaves enter then into the plasma chamber: it basically consists in two stainless steel cylinders, one inserted inside the other and soldered together to form a unique part. A specific path is machined in the space between the two cylinders for letting water cooling flows and keeps cold the plasma chamber. A 3D drawing of this part is shown in figure 5.9. In the picture the structure, of the chamber is clearly visible, with two inputs for gas, two inputs for microwaves and one input and an output for the cooling water. The plasma chamber is delimited by the extraction electrode from one side and the HF blocker from the other, so as to form a resonant cavity for microwaves (see figure 5.1).

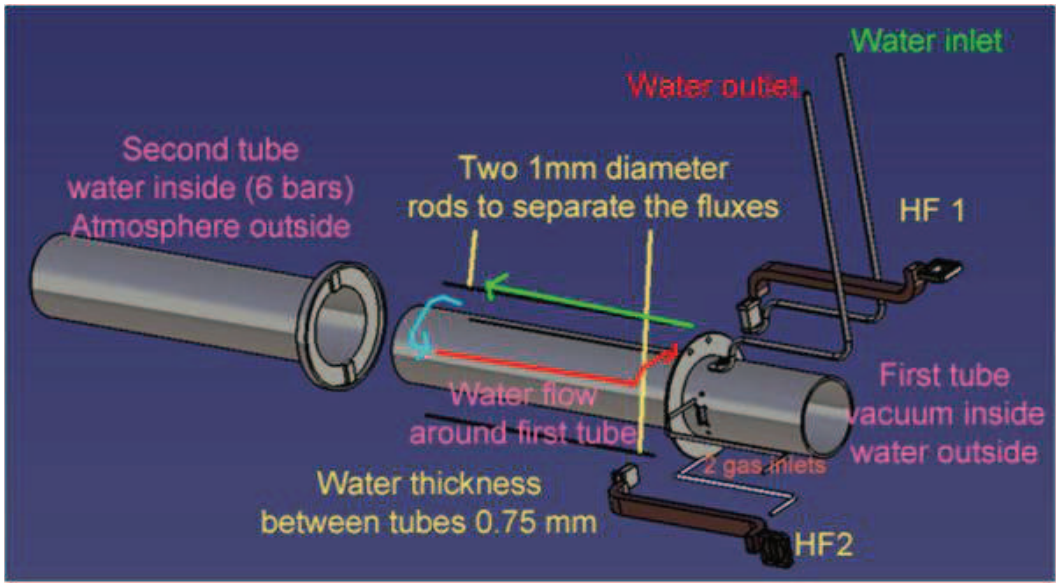

Figure 5.9: Detailed view of the SPES-CB plasma chamber: the path for water cooling is indicated together with gas, water and microwaves connections.

It is widely known that the base vacuum of an ECR-based charge breeder strongly influence its performances [49]; more, this kind of device has the drawback of producing contaminants generated by the surfaces exposed to the plasma: the extracted peaks of such contaminants can be superimposed to the ones of interest of a specific radioactive species, leading to the impossibility to accelerate a given charge state. On the base of these facts, a proper pumping system was designed but, more important, special attention was paid to the choice of the materials and their treatment in order to limit the contamination: in particular, the plasma chamber will be machined in stainless steel AISI 316-LN, whose properties are resistance and easiness of machining with small tolerances even for very thin parts; the parts will be treated with ultrasonic cleaning and thermally at 950° for stress relief both before and after welding, so as to ensure the removal of all the contaminants from the bulk of the material. In this context, the experience of the colleague Carlo Roncolato from LNL was determinant.

5.1.4 The extraction system

The description in chapter 3 and 4 showed that the ECR-based CB produces a typical charge state distribution, with different peaks corresponding to different A/q ratios: the expected values span roughly from 4 to 7 for the species to be charge bred by the SPES-CB. As described in chapter 2, at SPES the selected charge-bred radioactive ion (with a given A/q ratio) will be injected into a room temperature RFQ to allow a pre-acceleration to 727*A keV: this kind of accelerator has the peculiarity to accept ions with a fixed injection energy of 5.7*A keV. Considering the variability of the extracted A/q's, this implies the use of different extraction voltages V_{CB} for the

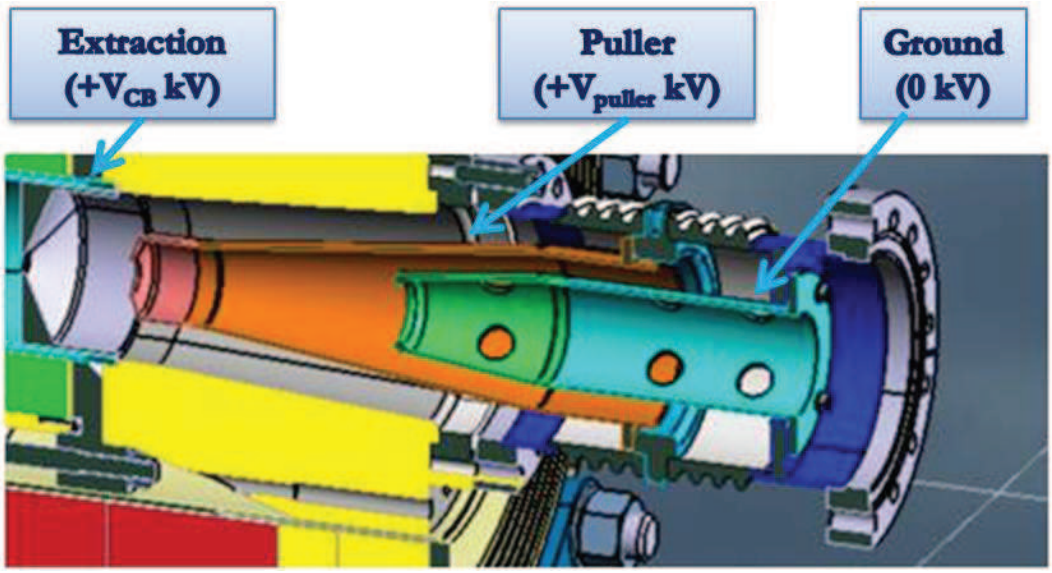

Figure 5.10: The three electrodes extraction system adopted for the SPES-CB.

SPES-CB to meet this condition: in particular, the expected range in A/q's translates in a variable voltage between 20 and 40 kV. From the considerations above the single gap extraction system presently mounted on the PHOENIX charge breeder was judged not enough flexible: starting from a LPSC's design, a more flexible three electrode extraction system, shown in figure 5.10, was proposed instead. For any given value of V_{CB} the voltage V_{puller} will be set so as to keep a constant potential difference of 20 kV in the first gap: this is in fact the zone where the beam is really formed and acquire its characteristics. The configuration of the extraction system in terms of reciprocal distances between the electrodes was optimized by using the numerical code Kobra-3D [93]: this was done keeping in mind the requirement for SPES, that is a normalized emittance lower than 0.1 π*mm*mrad for the accelerated beam.

Kobra-3D is a fully three dimensional finite difference method solver that, for given input parameters that will be described shortly and with proper boundary conditions, calculates the electrostatic potential within a given extraction system, tracing the trajectory of a certain amount of ions extracted from a plasma and including their space charge in a self-consistent calculation. With its post processor, all the calculated quantities can be plotted (potentials, electric and magnetic fields, space charge), as well as beam trajectories and emittance. Ions are supposed to start few millimetres behind the extraction hole at the plasma potential V_p (given as input) and their space charge in the so called plasma sheath is calculated considering the Boltzmann compensation factor due to the electrons [94], with a user defined temperature KT_e: in particular, the values chosen for V_P and KT_e are respectively 20 V and 10 eV. The code accepts as inputs a 3D geometry of the electrodes with the respective potentials and an eventual magnetic map (in the case of extraction from ECR sources). From

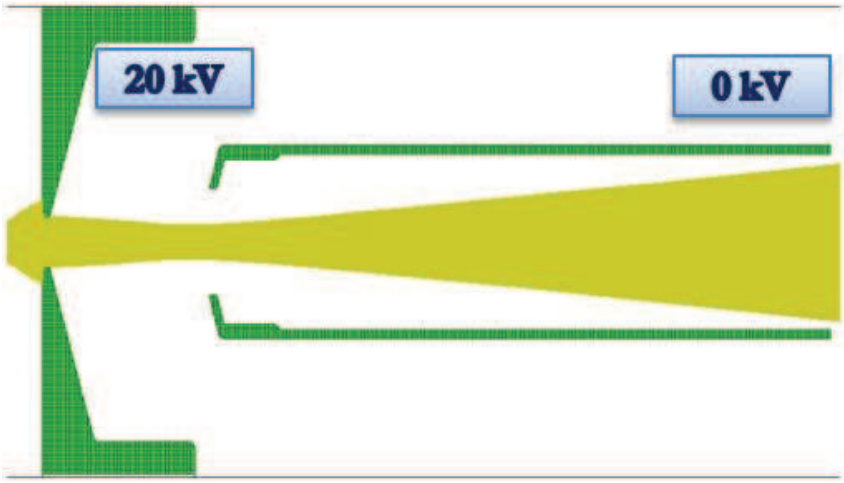

Figure 5.11: Trajectories plot of a 20 keV beam extracted from PHOENIX simulated with Kobra-3D: the risk of beam losses at the end of the grounded electrode is clearly visible.

the experience maturated in using such code, the afore mentioned parameters are usually less important than the proper starting conditions for ions: the code allows for different preset possibilities as well as custom made ones. Considering an oxygen plasma, the total simulated extracted current was 350 μA while the specific charge state distribution was taken from a spectrum acquired at LPSC. Trying to include the characteristics of ions at the plasma boundary, a Matlab script generates the starting conditions, supposing them to start very close to x=0, to be homogeneously distributed within a circle of a given radius (usually slightly bigger than the extraction electrode's radius) and with the transversal velocities generated from a Maxwell-Boltzmann distribution with a temperature KT_i = 0.5 eV. For the longitudinal velocities the Bohm criterion for multiple species is taken into consideration [95].
To validate the starting conditions the actual PHOENIX extraction system at 20 kV was simulated first and the results were compared with experimental measurements [96]. The simulated trajectories are shown in figure 5.11: the first electrode (the plasma electrode) is at 20 kV while the second is grounded. It can be noted that the beam almost touches the electrode in the final part: this means that by extracting higher beam currents beam losses could be observed, as confirmed by the colleagues of LPSC; the simulated values of the normalized emittance agreed within 10% with the experimental ones, confirming the correctness of the input parameters (simulated 0.0532 π*mm*mrad, measured 0.0486 π*mm*mrad).
As a further step the extraction of the same beam was simulated with the new system in order to compare the results with the existing one: in particular, three different couples of values for V_{CB} and V_{puller} were used, that is 40 kV-20 kV, 34 kV-14 kV and 28 kV-8 kV. The values of V_P, KT_e and KT_i were the same as the first simulation: the calculated normalized emittances, shown in table 5.2, are not only well below the SPES requirement but even lower than the one calculated with the actual system. More, it can be noted that all the configurations practically gives

Table 5.2: Simulated emittances of the beam extracted from the SPES-CB for three different extraction voltages.

$\mathbf{V}_{CB}$ [kV]	$\mathbf{V}_{puller}$ [kV]	**norm emittance** π*mm*mrad
40	20	0.0449
34	14	0.0448
28	8	0.0448

the same value for the normalized emittance, meaning that the different voltages do not affect the beam parameters. For the sake of completeness, figure 5.12 and 5.13 show the phase space and trajectories plots obtained for the configuration with the highest value of V_{CB}: considering the promising results, it can be quite confident that the aim of this new system will be accomplished.

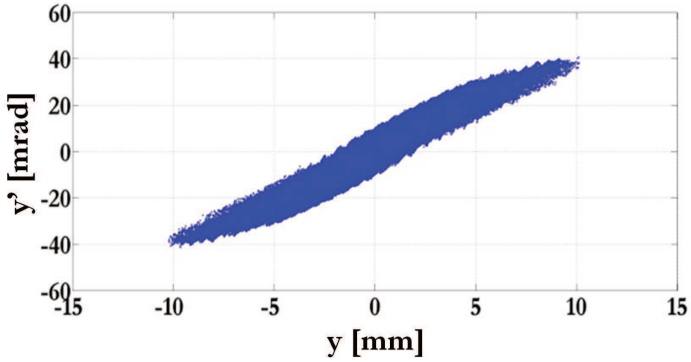

Figure 5.12: Simulated emittance obtained for V_{CB}=40 keV.

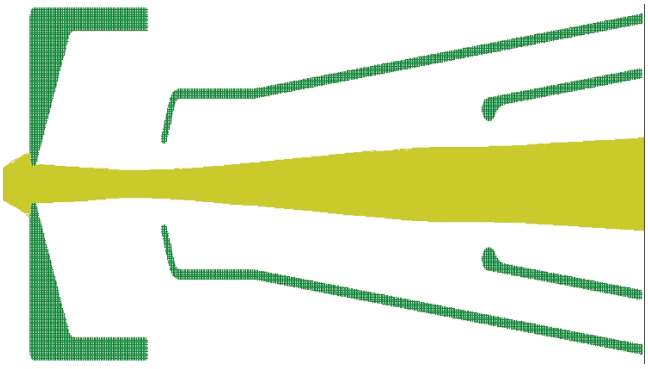

Figure 5.13: Trajectory plot from the new extraction system obtained for V_{CB}=40 keV and V_{puller}=20 keV. An oxygen beam has been simulated

5.2 The Charge Breeder beam line

During this PhD, an important contribution in the definition of various characteristics of the SPES-CB beam line was given, pushing, from the beginning, for the necessity of a complete test bench. Following the experience of different Laboratories, before operating with radioactive beams the Charge Breeder has to be deeply characterized with stable beams, operation impossible without a properly set test bench. The concept of the test bench is correctly described by figure 5.14: first of all it must be equipped with one or more 1+ sources able to produce all the stable counterpart of the radioactive ions will be available at SPES. The use of stable elements can lead to the production of 1+ beams of different isotopes at the same time: a 1+ selection is so necessary in order to select a given ion to be injected inside the charge breeder: the injection of multiple masses in not foreseen for this device while the possibility to select online between different masses is really useful when one wants to check the influence of this parameter on the breeding efficiency. The selected 1+ beam has to be also analysed in order to determine its characteristics (emittances and transversal profiles) and their influence on the performances of the charge breeder: then it can then be injected inside the charge breeder after a proper focusing. After capture and further ionization, a multiple q+ beam is extracted from the charge breeder: a particular A/q ratio is then selected and characterized from the point of view of both beam parameters and breeding performances.

As previously mentioned, a drawback of the ECR-based charge breeder is the risk of unwanted stable contaminations [97] coming from two possible sources: on one hand, the content of the gas bottles used to generate the plasma can consist of small percentage of other gases; on the other hand, neutral particles can be ejected by the surfaces exposed to the plasma, due to the high local heating. This last effect can be limited with a proper treatment of the surfaces and pumping, as pointed out for the plasma chamber in the last section, but this is of course not enough to completely remove the problem. Keeping in mind the possibility of having stable contaminants in the charge breeder's plasma, the attention was focused on the necessary resolution of the q+ selection in order to avoid superposition between stable and radioactive peaks. Considering that we deal with high charge states, the resolution is given in terms of the ratio A/q, that is $R = \Delta(A/q)/(A/q)$. To have a clear picture, the most meaningful species will be produced in SPES [58] (with all their isotopes) have been considered as being ionized in the range A/q=4÷7 and the possible superpositions with the most common stable contaminants have been verified: the list of all the considered species is given in table 5.3; the inclusion of Krypton in the possible contaminants follows from the experience made at KEK [50]. Considering the high number of isotopes and the mass of the stable elements, the possible A/q's obtained cover densely the range of interest. By cross checking the possible superposition of all the above species among each other it has been found that, in order to be confident in always finding a "clean" radioactive peak, the necessary resolution of the q+ selection should have been $R \sim 1/1000$.

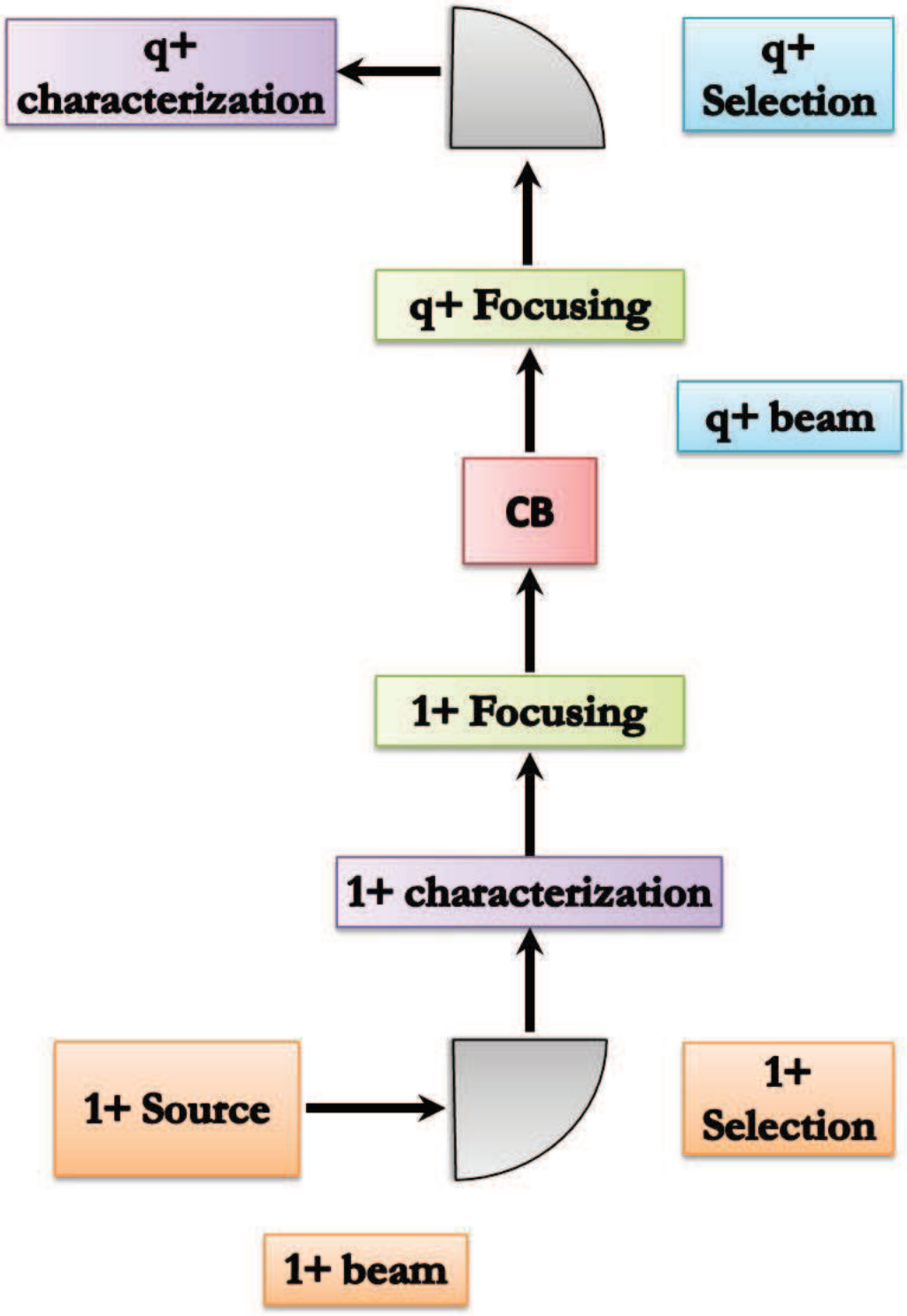

Figure 5.14: Scheme of a typical test bench for charge breeder's optimization.

Table 5.3: Stable and radioactive species considered in estimating the necessary resolution for the q+ spectrometer downstream the SPES-CB.

Element	**A**	**nature**
O	16-18	stable
N	14-15	stable
C	12-13	stable
Ar	36,40	stable
Kr	78,80,82-84,86	stable
Ge	75-80,82-83	radioactive
Rb	88-96	radioactive
Sn	126-133	radioactive
Cs	137-142	radioactive

Unfortunately at LNL there is no space available to allocate exclusively the test bench for the charge breeder, so the management of the project decided to include it in the beam line. Finally, the colleagues of beam dynamics group (Work Unit B7) acknowledged my propositions and produced the final design showed in figure 5.15: the same sources as the ones installed in the Target-Ion-Source system will produce stable beams for charge breeding experiments. The 1+ beam will be extracted and focused by an electrostatic triplet, selected through a 90° dipole and then its current and position will be recorder by a Faraday Cup+Slits system ("1+ DIAG" in figure 5.15). The beam will be again focused, its emittance will be measured and it will then be injected inside the charge breeder through a double electrostatic Einzel lens. From the charge breeder on the beam line change from electrostatic to magnetic: a solenoid and a triplet will initially focus the q+ beam to measure the total current extracted from the charge breeder, in order to verify the overall transmission. The beam will then be injected in the so called Medium Resolution Mass Spectrometer (MRMS) [12]: it will consists in two 90° bending dipole with a multipolar corrector in between and a couple of magnetic quadrupoles both upstream and downstream the two magnets. To increase the resolving power and reach the desired value of 1/1000, the MRMS will be placed in a -160 kV high voltage platform; the emittance of the selected q+ beam will be measured and finally the beam will be ready for post-acceleration at SPES. To validate the expected resolving power before real tests, the beam dynamic group simulated the beam transport with the TraceWin code [98]: in particular, starting from the beam characteristics coming out from the simulations of the new extraction system, they simulated the transport of three beams with a mass difference of 1/1000 and verified that effectively, at the end of the spectrometer, the three beams are correctly resolved as shown in figure 5.16. The SPES facility will be the unique to adopt such a challenging q+ spectrometer.

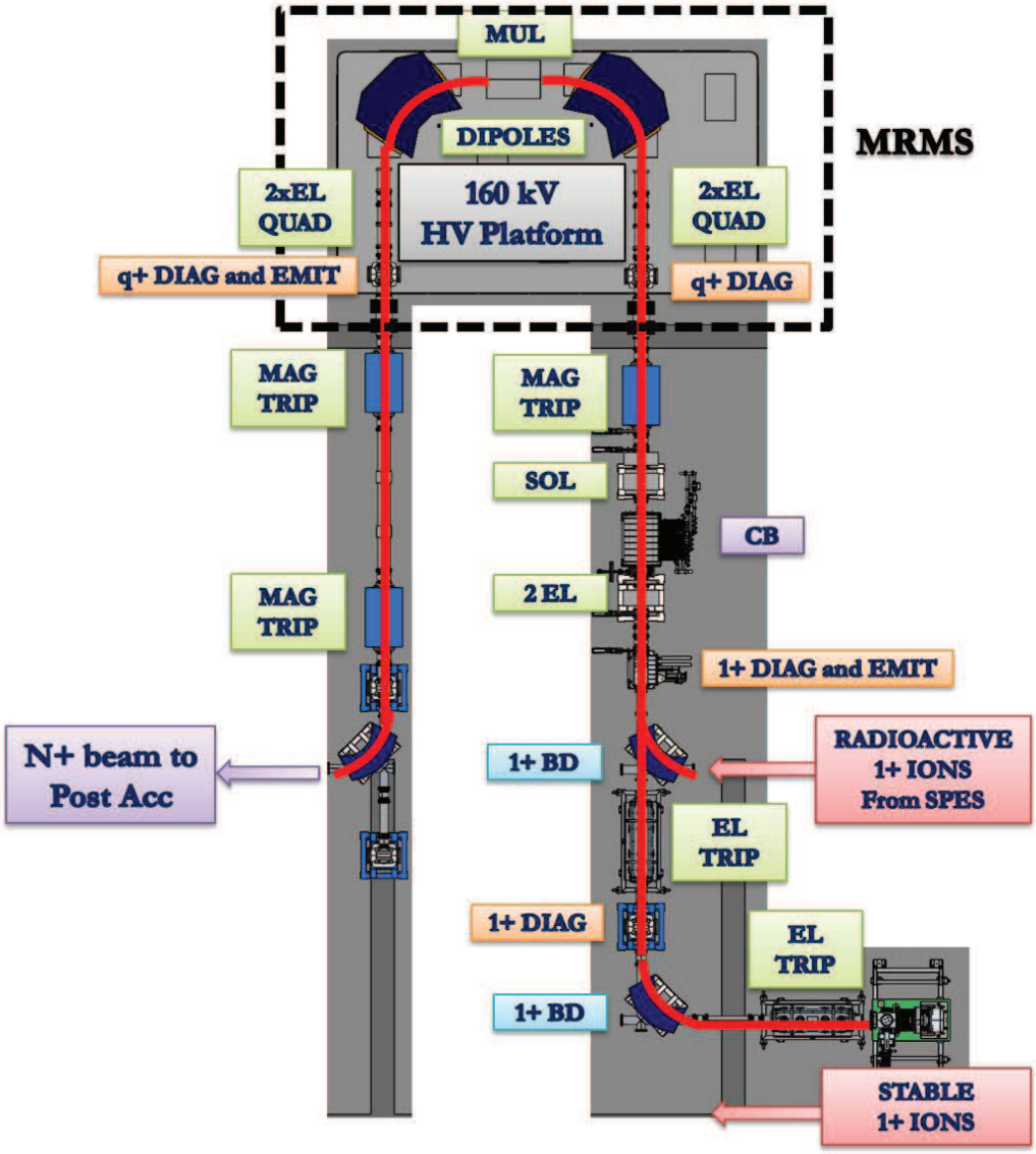

Figure 5.15: Drawing of the future SPES-CB beam line: electrostatic optics is foreseen up to the CB and magnetic before. To optimize the future operation, stable and radioactive injected 1+ beams will share the beam line in proximity of the charge breeder.

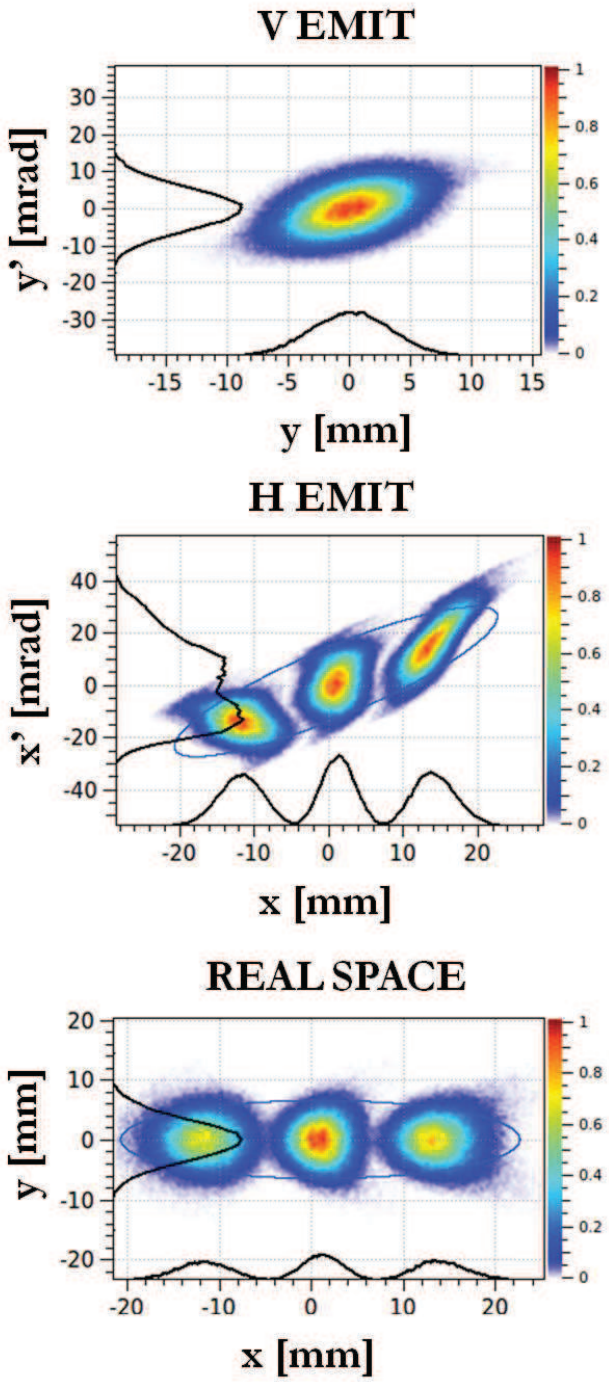

Figure 5.16: Phase space (top and middle) and real space (bottom) plots of three beams with a mass difference of 1/1000 at the exit of the MRMS: the reference beam's parameters come from the numerical simulations.

5.3 Experimental activity at LPSC: the EMILIE project

The work done during this PhD was enriched by an experimental activity with the PHOENIX charge breeder at LPSC; this experience will be very useful during the commissioning and operation of the SPES-CB. Since 2012 I have been in fact involved as Deputy Coordinator in the European project Enhanced Multi-ionization of short-Lived Isotopes at EURISOL (EMILIE) [16, 17], approved by the NuPNET in 2011 [99]: aim of the project is the optimization of both EBIS and ECRIS charge breeding techniques in view of the unprecedented intensities expected for EURISOL. Within the project I have been leading the Work Package WP3 whose aim is the optimization of the performances of the PHOENIX charge breeder by different approaches: numerical, experimental and technical. In particular, one task is devoted to the numerical simulations of the charge breeding process described in the next chapter; another one, led by the Laboratory JYFL (Finland), is devoted to experimental activities with the PHOENIX charge breeder at LPSC: are involved in this task LPSC, JYFL, INFN-LNL and LNS, GANIL (France) and HIL (Poland). To have a complete picture of the experience made, a brief description of this activity will be given in this section, mainly because it benchmarks the numerical simulations described in the next chapter.

The LPSC test bench is equipped alternatively with two different 1+ sources: the COMIC source [100] for gaseous species and a surface ionization source for alkali metals: both ion sources revealed to produce intensities higher than needed with a very low emittance (around 2-4 π*mm*mrad rms at 20 kV). The 1+ beam, extracted at a given voltage V_{1+}, is focused, magnetically selected and then injected inside the PHOENIX charge breeder through a double Einzel lens; in this part of the beam line magnetic steerers allow to correct eventual misalignments. The high voltage of the charge breeder V_{CB} is lowered with respect to V_{1+} of a given quantity ΔV (through the ΔV supply) in order to optimize the injection: the charge bred ions are extracted through a single-gap extraction system and focused by an Einzel lens; finally a 105° bending dipole select a given charge state. The selected beam is then characterized in terms of charge breeding performances and (eventually) emittance. Turbomolecular pumps connected in various points of the beam line allow the pumping to high vacuum: close to the charge breeder the base vacuum is in the high 10^{-8} mbar range and increases to around $3{\cdot}10^{-7}$ mbar during operations. For all the tests described below the PHOENIX charge breeder generated an oxygen plasma by feeding microwave at 14.521 GHz produced by a fixed-frequency Klystron. During a typical test, a pulsed X^{1+} beam (more or less 1 s on 1 s off) is injected inside the charge breeder with its downstream beamline optimized for a given charge state X^{q+}. The q+ signal is used to check the optimization of the charge breeder: it includes the injection optics, the value of the ΔV and the typical parameter of an ion source (gas feeding rate and microwave power) in a "self-consistent" way. Finally, from the difference ΔI in the X^{q+} current between injection and no injection the breeding efficiency is calculated as $\eta = \Delta I(X^{q+})/q + \cdot I(X^{1+})$; the global efficiency

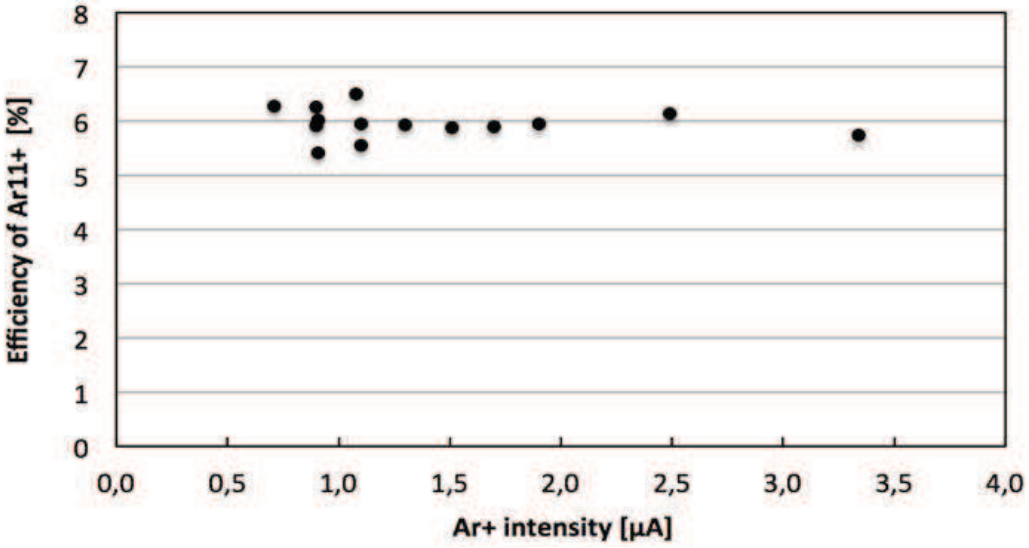

Figure 5.17: Efficiency of Ar^{11+} as a function of the Ar^{1+} injected current. No remarkable differences are observed.

is obtained by measuring the ΔI for each charge state q+. To measure the charge breeding time the q+ signal is connected to a fast oscilloscope: the track is acquired as a function of time and the charge breeding time can be determined off-line. To check the breeding efficiency as a function of the injection energy a ΔV curve is usually acquired: keeping unchanged the q+ beam line, the ΔV supply is ramped and, at the same time, the X^{q+} is recorder on the Faraday Cup. The picture obtained is like the one already shown in chapter 4.

The first tests were performed on May 2013 with Argon and Krypton beams produced by the COMIC source. First of all, the capability of the ECR-based charge breeder to capture very high intensities was verified with an Argon beam: figure 5.17 shows the Ar^{11+} efficiency as a function of the Ar^{1+} intensity. It can be seen that no remarkable variations are observed up to 3.5 μA of injected current, proving as an ECR-based charge breeder is the best choice for high intensity RIBs facilities; in the considered case, the charge breeder was first optimized for the best efficiency at the lowest injected current. With the same Argon beam we verified also the effect of the so called "frequency tuning" proposed by the colleagues from LNS [101]: to inject microwave with a variable frequency a TWTA amplifier in the range 11-16 GHz was employed. Due to a limitation of this amplifier, the injected power was fixed at 250 W: the efficiency of Ar^{11+} was recorder in the entire frequency range and compared with value obtained with the Klystron for the same setting of the booster, as shown in figure 5.18. It is important to point out that in this case the charge breeder did not show its best performances but the data are anyway useful to deduce the influence of the frequency. We can see from the picture that for particular frequencies the efficiency was actually twice the one obtained with the Klystron (defined by the red line) but this is not the most important information: several negative efficiencies

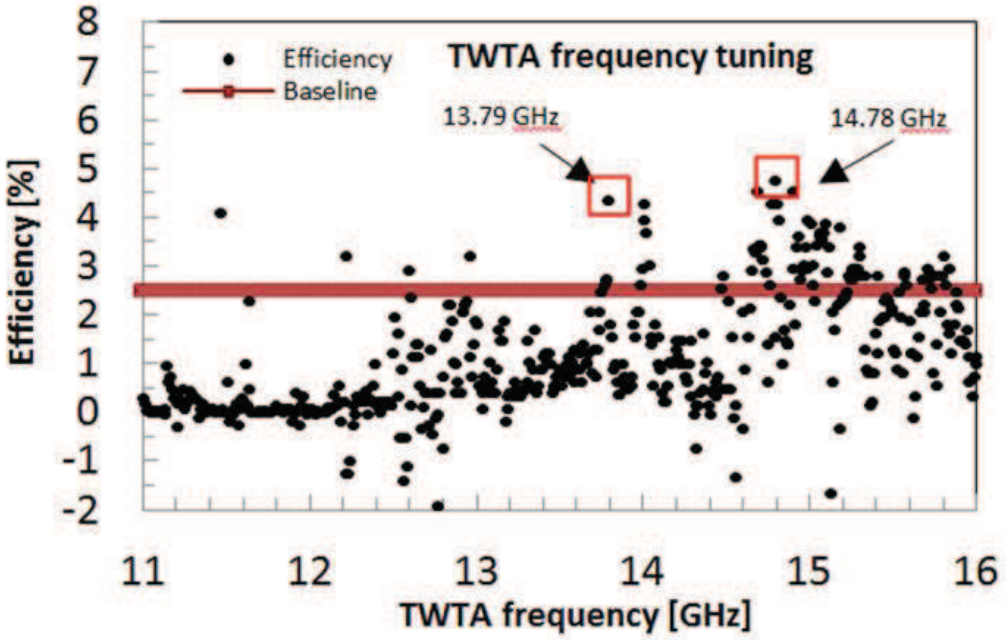

Figure 5.18: Efficiency of Ar^{11+} as a function of the operational frequency by using a TWTA: the red line gives value corresponding to Klystron.

appeared, for which an explanation is needed. When the 1+ source is operated with gases part of the neutral particles flow to the charge breeder and a X^{q+} current is recorded even without injecting the X^{1+} beam. The measure of negative efficiencies is an indication that the injection of few (compared to the plasma density) X^{1+} particles can negatively influence the charge breeder's performance, including the ionization of the previously present X^{q+} ions; this effect was already observed at LPSC on oxygen high charge states.

In a following session of experiments we verified the effect of the two-frequency heating on Krypton's efficiencies: to do this we used both the two microwave injection ports of the PHOENIX's plasma chamber, one connected to the Klystron and the other to the above mentioned TWTA. In this case the total power was fixed at around 600 W: first of all the charge breeder was optimized for the best Kr^{17+} efficiency by using the Klystron alone; then the global efficiency was also recorded. After verifying different values of frequency and power for the TWTA we chose 14.270 GHz and 140 W: in this case, as in the previous one, values up to 80% for the total capture were recorded. The comparison of the two "efficiency spectra" with and without the two frequency heating is shown in figure 5.19: we actually see that by a proper choice of the second heating frequency the overall performances of the charge breeder improve, recording higher efficiencies for the higher charge states. The same picture shows also a kind of anomaly: an unusual high intensity of very low charge states ($1+ \div 3+$) was recorded ,almost separated from the conventional "bell" of high charge states usually extracted from ECR ion sources. This effect was found to be interesting and

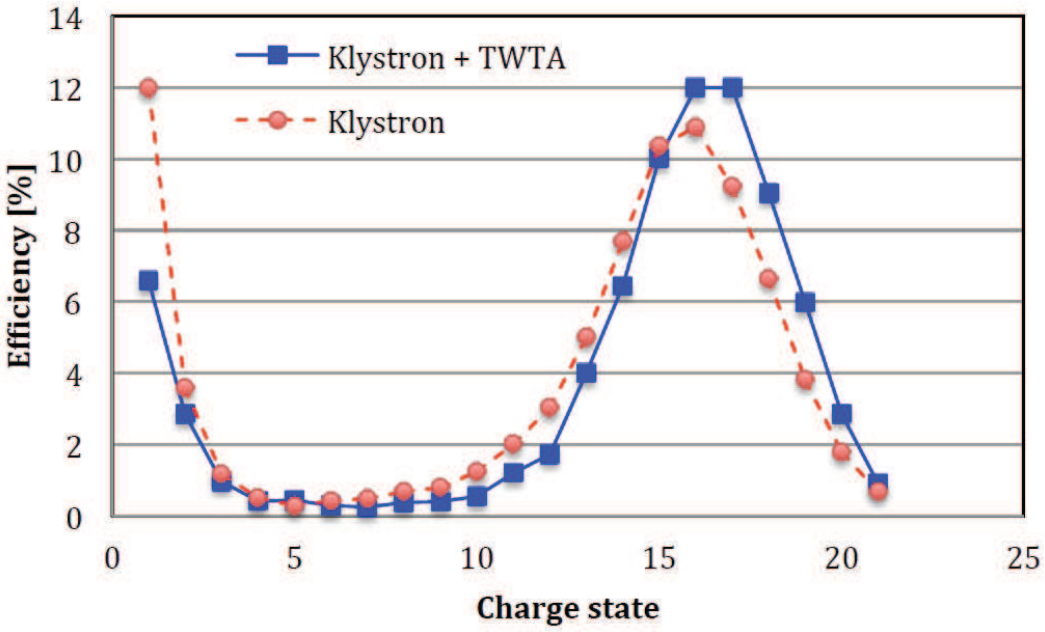

Figure 5.19: Comparison of the efficiency distributions for Kr between single and double frequency heating: the total microwave power is ∼ 600 W; the secondary frequency used is 14.27 GHz at 140 W.

a dedicated experiments with Rubidium was planned for November 2013. All the information obtained up to now revealed the positive effect of the two investigated techniques: anyway both need to be further optimized in order to become a "knob" to be used with radioactive beams. The above shown results have been object of a joint publication on a peer review journal [102].

The dedicated experiment performed with Rubidium to investigate the charge breeding of low charge states revealed very interesting results: the big amount of data is presently being analysed in order to be submitted for a joint publication; for this reason these information given in this thesis will be limited to the ones necessary to correctly understand the description of the numerical simulations in the next chapter. Around 350 nA of Rb^{1+} ions were extracted from a surface ionization source: during the experiments the efficiency of different high charge states was optimized with a microwave power below 500 W. In this occasion record efficiencies were measured for this element: in particular 3% for Rb^{15+}, 8% for Rb^{18+} and 5% for Rb^{20+}. We moved then our attention to the lowest charge state, that is the Rb^{1+} ions coming out from the charge breeder. First of all we acquired a ΔV curve compared in figure 5.20 with the one obtained for Rb^{20+}: the curve of the higher charge state shows the typical optimum ΔV value, in the specific case around 12 V, while the curve of Rb^{1+} shows a completely different trend. No efficiency is recorded until the ΔV value reach more or less its optimum for Rb^{20+}, then the efficiency rapidly increases up to more or less ΔV=-25 V where a kind of saturation starts. Other curves at different power level were acquired showing basically the same trend, except for the fact that the

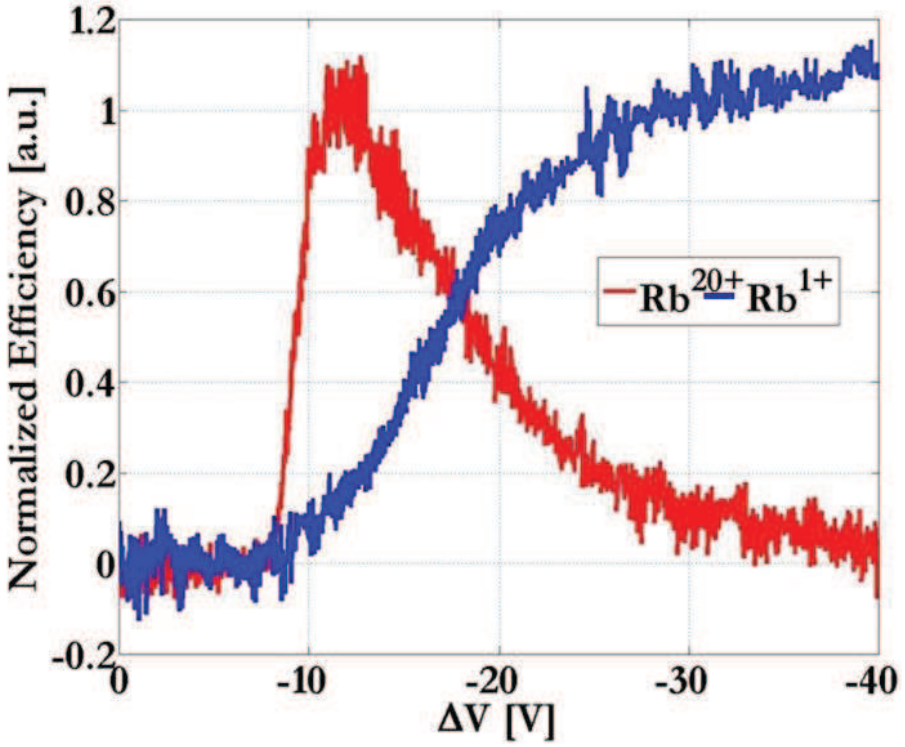

Figure 5.20: Comparison of the DeltaV curves obtained for high (Rb^{20+}) and low (Rb^{1+}): in this last case the optimum ΔV is absent.

onset of Rb^{1+} efficiency appears at lower ΔV values and the maximum increases by decreasing the microwave power: figure 5.21 shows the comparison between the one obtained at 470 W and another at 250 W. In interpreting the results the suspect was that the recorded Rb^{1+} ions were basically injected particles that weakly interacted with the plasma, without being finally really captured. To have a first indication of the correctness of our interpretation we focused our attention on the charge breeding time of Rb^{1+} measuring it at the optimum ΔV for high charge states; then, we repeated the measurement for the same ΔV but without igniting the plasma: the two plots obtained are compared in figure 5.22. Following the definition of CB time, the time it takes for the two signals to reach the 90% of the maximum was measured and found to be around 500μs in both cases: this discover was a strong support of our hypothesis that was deeply investigated with further measurements. We will come back to the Rb^{1+} ΔV curves in the following chapter.

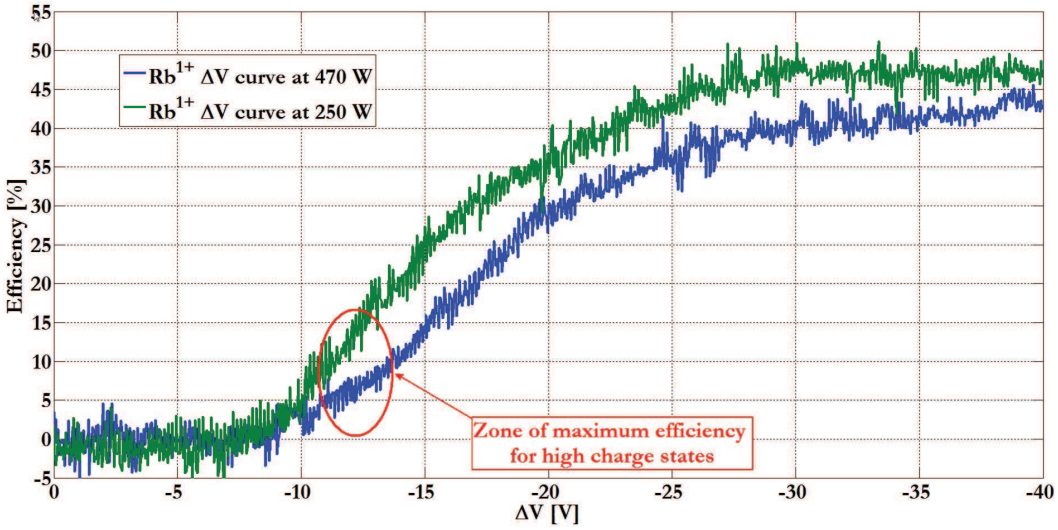

Figure 5.21: Rb^{1+} DeltaV curves for two different microwave powers.

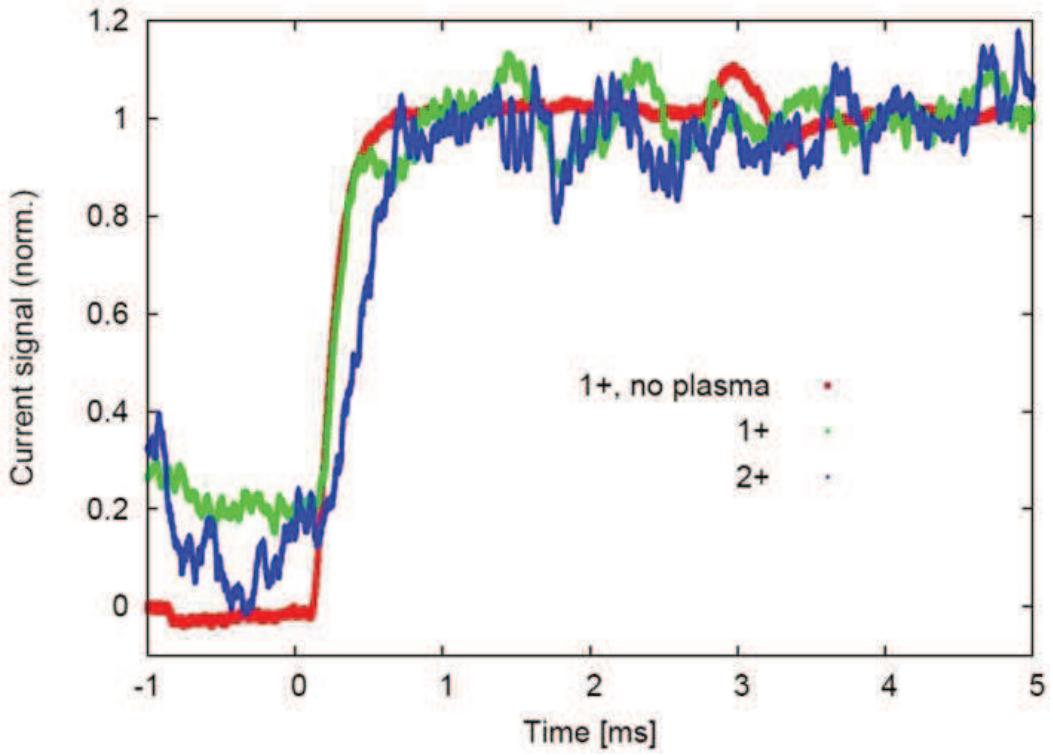

Figure 5.22: Charge breeding times measured on the LPSC test bench: Rb^{1+} (blue curve), Rb^{2+} (green curve) and Rb^{1+} without plasma (red curve). This last one is in perfect agreement with the first one.

Chapter 6

Charge Breeding simulations

6.1 General consideration

6.1.1 Introduction

As anticipated in the previous chapter, I have been involved in the European Project EMILIE since 2012: in the framework of this project the core of this PhD thesis has been carried out. In fact, besides being Deputy Coordinator of the project and INFN Representative, I have been leading a task regarding numerical simulation of the slowing down and capture of monocharged ions by the plasma of the charge breeder. To this scope, a MATLAB code [103] has been developed, with the fundamental support of my external tutor Dr. Eng. Luigi Celona from INFN-LNS and two colleagues from the same lab, Dr. David Mascali and Dr. Lorenzo Neri.
A reliable numerical simulation can be helpful in better understanding the base physical mechanisms behind the charge breeding process. It could be possibly also used in predicting the behaviour of this device following the variation of the usual "source" parameters (density, electron and ion temperature, magnetic field) or depending on the radioactive ion injected. This aspect is very important for two main reasons. First of all, the experimental results in terms of efficiencies revealed a discrepancy between charge breeding of gaseous or metallic ions. Considering what is usually quoted, that is the global efficiency (sum of the efficiencies of all the charge bred ions) and the peak efficiency (the charge state having the highest efficiency), gaseous ions give respectively values up to 80% and more than 10%; for metallic ions those values go down to 50% and more than 5% [104]. Is it widely accepted that this is due to the fact that 1+ gaseous ions, if not captured by the plasma, can recombine at the chamber wall and come back into the plasma as neutrals, so increasing the probability to be highly ionized and extracted. A better understanding of the parameters affecting the breeding efficiency can lead to an optimization of the capture process and so an improvement of the performances with metallic ions.
The second reason is connected with the operation of the charge breeder itself. In spite of the high intensities expected to be produced in SPES, radioactive ion beams are orders of magnitude (depending on the specie) less intense than the stable ones

and can be hardly measured on a common Faraday Cup. This means that with such beams it is not possible to perform a real tuning of the charge breeder because the main diagnostics (the beam intensity) is missing. What can be done is to tune the charge breeder by injecting a stable element first and then to consider it to be optimized for the radioactive ion as well: this is quite often called "blind tuning" [36]. The numerical simulation can help in choosing the way to tune the booster, by verifying if is more convenient to choose an element with similar mass or one of the stable isotopes of the same element. In the first case, the injection optics is surely optimized (same mass) but the charge state distribution could not due to the difference in the electronic configuration between the two elements. In the second case, the optics could not be optimized due to the difference in mass but we can expect the two elements could be equivalent from the point of view of ionization, so the charge state distribution obtained. It is helpful in this context to do a practical example. Let's suppose we want to inject and charge breed radioactive $^{132}Sn^{1+}$ ions: thanks to numerical simulations we could be able to foresee if it better to set up the charge breeder with a $^{132}Xe^{1+}$ beam or with one of the stable tin isotopes, let's say $^{120}Sn^{1+}$.

The main mechanism a numerical simulation has to implement in order to reproduce the charge breeding process are the elastic Coulomb collisions between injected ions and plasma ions. This problem is quite diffuse in the field of Computational Physics because has many applications, from Astrophysics to Inertial Confinement Fusion [105÷108]. As we saw in the chapter regarding the theoretical description of the charge breeding process, Coulomb collisions are a collective effect that can be described by a cross section and from which we can deduce some relaxation times: usually a kinetic approach is used by studying the evolution of the particle distribution function considering the Fokker-Plank equation with the diffusion coefficient found in the previous chapter. For this code it has been decided to follow a single particle approach by solving the ions equation of motion under the influence of external magnetic field taking into account the presence of a plasma with a given structure, density and temperature. This approach has some advantages: first of all the possibility to store and track particles' trajectories so as to verify ions dynamics. This could be helpful in identifying the areas where particles are lost, becoming points where radioactivity accumulates leading to possible radiation protection issues. More, it is possible to implement various kind of collisions predicting average behaviour for particles motion and lifetime. By adopting the single particle calculation it will be also possible to determine the energy loss of the injected ions: this point could be helpful in explaining what was experimentally observed, that is the destruction of high charge states of an oxygen plasma due to the injection of a low quantity of 1+ ions. A further aspect is that single particle approach allows the creation of a 3D density map, that can help in determining how injected ions are distributed before and after the capture process. As will be clear in the description that follows, in approaching the problem I proceeded through several steps of complexity, starting from a benchmark, passing through some failures to arrive then to reproduce some

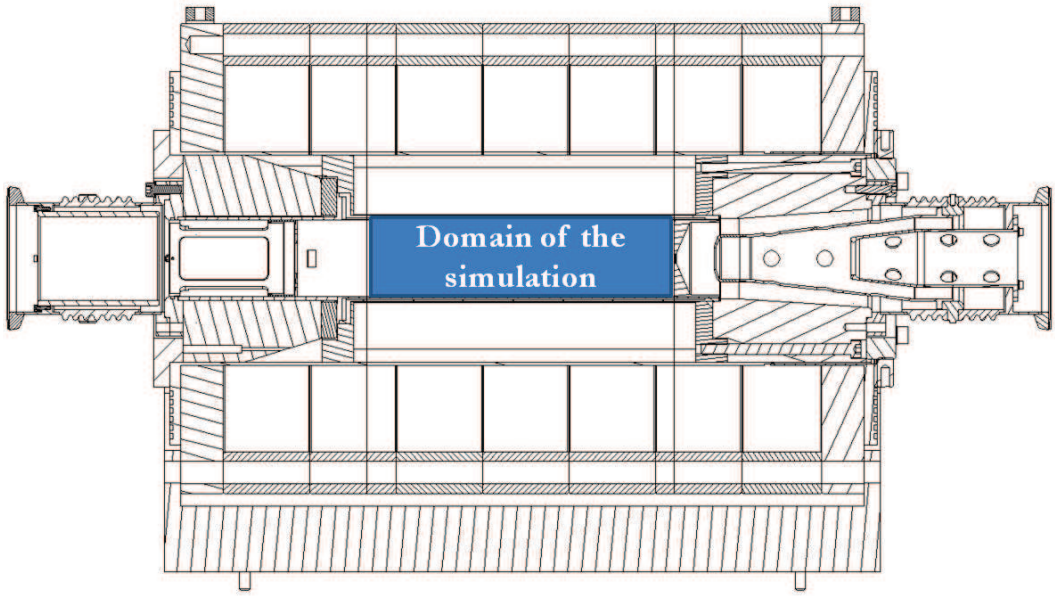

Figure 6.1: Cut view drawing of the SPES Charge Breeder: the coloured rectangle indicates the domain of the simulation, going from the maximum of the magnetic field at injection to the extraction hole.

experimental evidences like the injection of $^{85}Rb^{1+}$ ions at the LPSC test bench within the EMILIE project. Some interesting physical aspects coming out from the simulations will be also underlined.

6.1.2 The domain of the simulation

Before going into details on the numerical approach let's describe the geometry of the problem. Figure 6.1 shows the physical boundaries of the domain of the simulations: basically it is a cylinder with the same radius as the plasma chamber (0.036 m) and a length extending from the maximum of the magnetic field at injection to the extraction hole (0.248 m). In this region a minimum-B geometry is created by three coils and a permanent magnet hexapole: figure 6.2 shows the z component of the magnetic field along the axis of the charge breeder. The maximum at injection is B_{inj} = 1.177 T, at extraction B_{ext} = 0.793 T while the minimum is B_{min} = 0.352 T; the field generated by the hexapole gives a $B_{rad} \sim 0.8$ T on the plasma chamber walls. Considering the operating frequency of 14.521 GHz, the corresponding resonant field of $B_{ECR} \sim 0.518$ T is shown also together with the two points where the ECR resonance takes place, z=-0.049 m e z=0.076 m. The traps has mirror ratios of:

$$\begin{aligned} R_{inj} &= B_{inj}/B_{ECR} \sim 2.3 \\ R_{ext} \simeq R_{rad} &= B_{rad}/B_{ECR} \sim 1.5 \end{aligned} \tag{6.1}$$

As can be seen from figure 6.2, by taking as the origin the middle of the central coil the longitudinal magnetic field is very well interpolated by the following 6th order

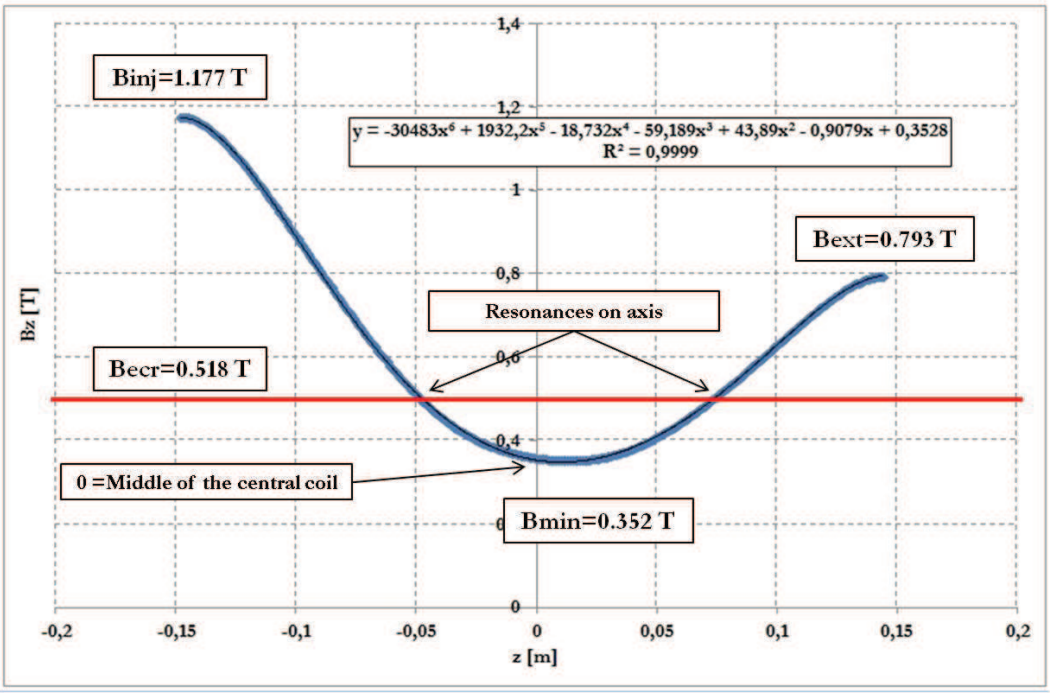

Figure 6.2: Plot of the longitudinal magnetic field on the axis of the charge breeder. The graph is perfectly interpolated by a 6th order polynomial.

polynomial in z:

$$\begin{aligned} B_z = &- 30483z^6 + 1932.2z^5 - 18.732z^4 - 59.189z^3 \\ &+ 43.89z^2 - 0.9079z + 0,3528 \end{aligned} \tag{6.2}$$

its values being in T with z in m. This allowed the implementation of a very precise magnetic map by using analytical formulas for all the magnetic field components: in fact the x and y components of the axial field off-axis can be expressed as

$$\begin{aligned} B_x = -\frac{x}{2}\frac{dB_z}{dz} = &- \frac{x}{2}(-30483 * 6z^5 + 1932.2 * 5z^4 - 18.732 * 4z^3 \\ &- 59.189 * 3z^2 + 43.89 * 2z + 0.9079) \end{aligned} \tag{6.3}$$

$$\begin{aligned} B_y = -\frac{y}{2}\frac{dB_z}{dz} = &- \frac{y}{2}(-30483 * 6z^5 + 1932.2 * 5z^4 - 18.732 * 4z^3 \\ &- 59.189 * 3z^2 + 43.89 * 2z + 0.9079) \end{aligned} \tag{6.4}$$

while the x and y component of the radial field have the form

$$B_{x,rad} = 2\text{hex}\ x \cdot y \tag{6.5}$$

$$B_{y,rad} = \text{hex}(x^2 - y^2) \tag{6.6}$$

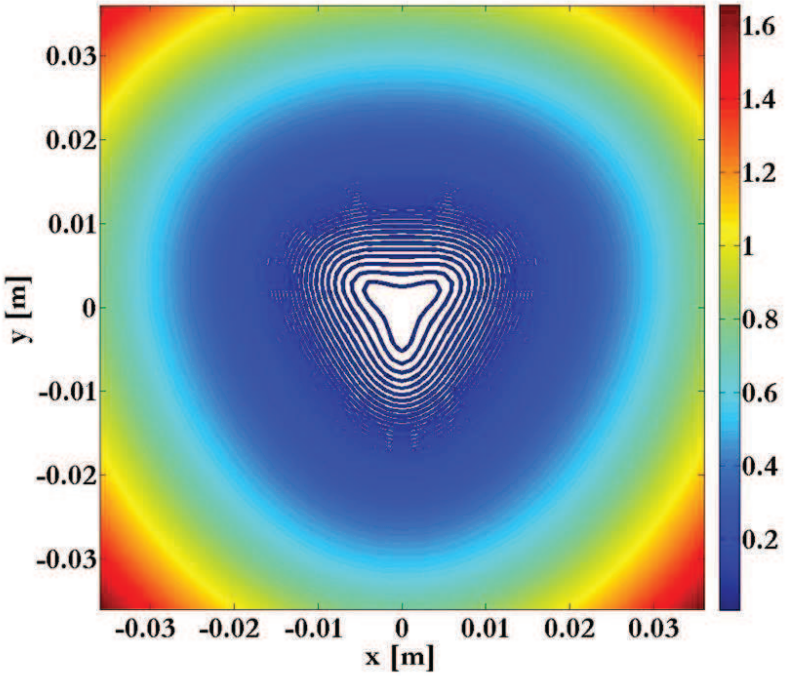

Figure 6.3: Magnetic field distribution [T] on a plane perpendicular to the plasma chamber axis at extraction.

with x, y, z in m and hex = 617.28 T/m^2. To better understand the topology of the magnetic trap figure 6.3 shows a contour plot of the magnetic field in the xy plane at the extraction. The surface with constant magnetic field are usually "egg-shaped": figure 6.4 shows a 3D plot of two such surfaces, the closed one with the highest **B** value and the one corresponding to the resonance at the operating frequency.

6.1.3 Time scale of the involved processes

As previously said, the code aims at integrating the ions' equation of motion inside the charge breeder's plasma taking into account the interaction with ions: as a consequence, the first parameter to be determined is the integration step of the simulation (T_{step}). To do this all the characteristics times of the processes involved in the calculation has to be estimated and taken into account. The predominant motion is due to the magnetic field and is characterized by the ion cyclotron frequency that can be expressed (in MHz) by the following handy formula:

$$\nu_{ci} = 0.152 \frac{z}{A} B \tag{6.7}$$

where the magnetic field is in T. By considering the highest possible magnetic field intensity inside the chamber (∼1.2 T) and a reasonably high value of the charge aver mass ratio $z/A = 0.25$, the above formula gives a cyclotron frequency of around 4.5 MHz, to which corresponds a period of $\tau_{ci} = 2.2 \cdot 10^{-7}$ s. The characteristic times

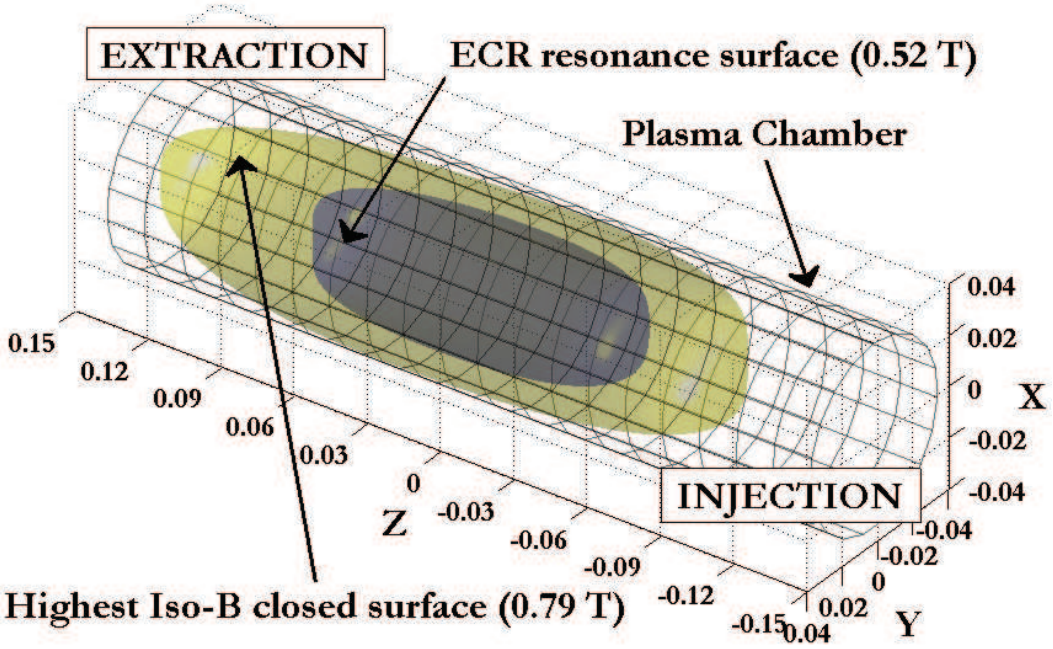

Figure 6.4: 3D view of the highest Iso-B magnetic field surface together with the one corresponding to the ECR resonance. The plasma chamber is also indicated in the picture.

involved in the calculation are the ones connected with the Coulomb collision: from the theory described in the previous chapter, four characteristic times can be derived whose expressions are here recalled

$$\begin{aligned}
&\textbf{Slowing Down Time} && \tau_s \equiv -\frac{v}{<\Delta v_{\parallel}>} = \frac{vC_s^2}{\left(1+\frac{m}{m_s}\right) A_D G\left(\frac{v}{C_s}\right)} \\
&\textbf{90°Diffusion Time} && \tau_D \equiv \frac{v^2}{<(\Delta v_{\perp})^2>} = \frac{v^3}{A_D\left\{\Phi\left(\frac{v}{C_s}\right) - G\left(\frac{v}{C_s}\right)\right\}} \\
&\textbf{Longitudinal Diffusion Time} && \tau_L \equiv \frac{v^2}{<\left(\Delta v_{\parallel}\right)^2>} = \frac{v^3}{A_D G(\frac{v}{C_s})} \\
&\textbf{Energy Exchange Time} && \tau_E = \frac{E^2}{<(\Delta E)^2>} = \frac{v^3}{4A_D G\left(\frac{v}{C_s}\right)}
\end{aligned} \tag{6.8}$$

Tabulated values of the functions describing the previous equations are given in table 6.1: to obtain points in between, the previous data have been interpolated through a Matlab routine called "interp1", using the "cubic" method. Then, in order to validate the interpolation, the analytic formulas showed in the following equations

$$G(x) = \frac{\Phi(x) - x\Phi'(x)}{2x^2} \tag{6.9}$$

$$\Phi(x) - G(x) = -\frac{x\Phi'(x)}{2x^2} \tag{6.10}$$

Table 6.1: Intermediate values for the functions $G(x)$ and $\Phi(x) - G(x)$

x	0	0.2	0.4	0.6	0.8	1.0	1.2	1.4	1.6
G(x)	0	0.073	0.137	0.183	0.208	0.214	0.205	0.186	0.163
Φ(x) − G(x)	0	0.149	0.292	0.421	0.534	0.629	0.706	0.766	0.813
x	1.8	2.0	2.5	3.0	3.5	4.5	5.0	6.0	8.0
G(x)	0.140	0.119	0.08	0.056	0.041	0.031	0.020	0.014	0.008
Φ(x) − G(x)	0.849	0.876	0.920	0.944	0.959	0.969	0.980	0.986	0.992

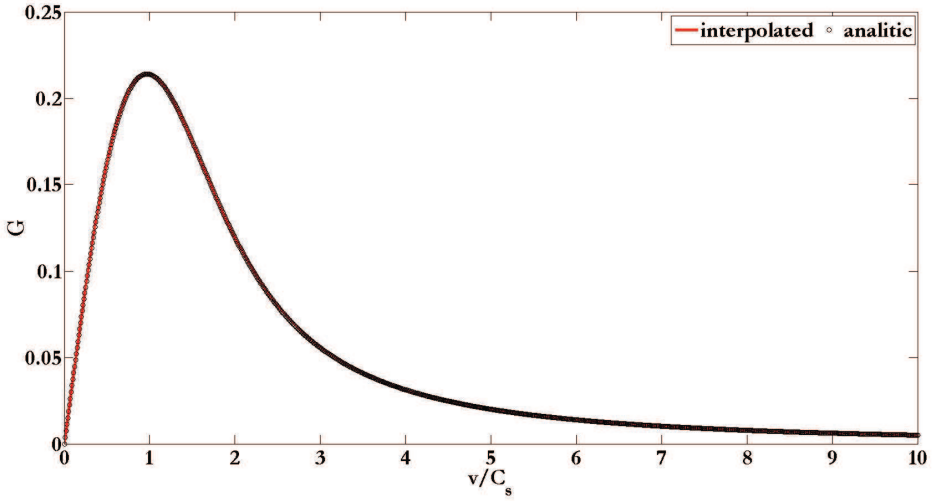

Figure 6.5: Comparison between interpolated and analytic data for the function $G(x)$

have been used to calculate the functions G and Φ - G (it has to be reminded the the function $\Phi(x)$ is the error function) and compared them with the interpolated data. As can be seen from figures 6.5 and 6.6 the interpolation method used gives reliable values for the two functions. It is useful now to give some numerical values for those characteristic times by considering two possible radioactive ions produced at SPES, that is $^{132}Sn^{1+}$ and $^{90}Rb^{1+}$: let's suppose that those ions are injected with a very low energy ($\sim$ 2 eV) and interact with a oxygen plasma with an electron density $n_e = 2.47{\cdot}10^{18}$ m^{-3} (roughly the cut-off density at 14 GHz, the common operating frequency of second generation ECRIS), an average charge $\langle z \rangle = 3.55$ (calculated from a spectrum given by the colleagues of LPSC) and a temperature KT = 1 eV. The choice of those particular parameters expresses the aim to consider the worst possible case (lowest characteristic times) : in evaluating τ_D and τ_s two further charge states for each ion were also considered, 10+ and 17+ for ^{90}Rb and 14+ and 21+ for ^{132}Sn, even if the simulation time will not allow the formation of those charge states (for a reason that will be clearer later). The calculated values are shown in tables 6.2: as can be seen, the friction is always faster than the other two processes and randomization and energy equipartition take roughly the same

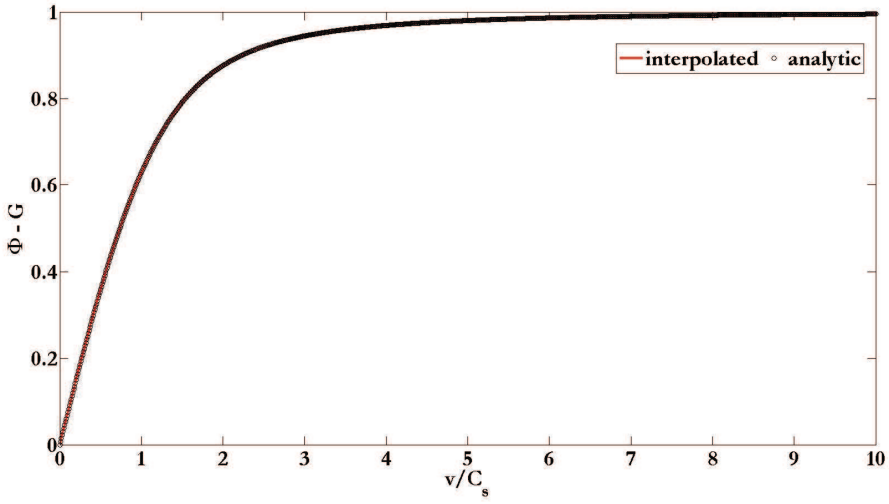

Figure 6.6: Comparison between interpolated and analytic data for the function Φ-G

Table 6.2: Characteristic times evaluated for different ^{90}Rb and ^{132}Sn ions. The slowing down time is evaluated only for 1+ ions because an higher ionization implies particles to be slowed down already.

Time [s]	$^{90}Rb^{1+}$	$^{90}Rb^{10+}$	$^{90}Rb^{17+}$	$^{132}Sn^{1+}$	$^{132}Sn^{14+}$	$^{132}Sn^{21+}$
τ_s	$6.17{\cdot}10^{-6}$	-	-	$9.51{\cdot}10^{-6}$	-	-
τ_D	$1.96{\cdot}10^{-5}$	$1.96 \cdot 10^{-7}$	$6.78{\cdot}10^{-8}$	$4.22{\cdot}10^{-5}$	$2.15{\cdot}10^{-7}$	$9.56{\cdot}10^{-8}$
τ_L	$8.18{\cdot}10^{-5}$	$8.18{\cdot}10^{-7}$	$2.83{\cdot}10^{-7}$	$1.76{\cdot}10^{-4}$	$8.98{\cdot}10^{-7}$	$3.99{\cdot}10^{-7}$
τ_E	$2.04{\cdot}10^{-5}$	$2.04{\cdot}10^{-7}$	$7.08{\cdot}10^{-8}$	$4.40{\cdot}10^{-5}$	$2.24{\cdot}10^{-7}$	$9.98{\cdot}10^{-8}$

time to be reached. The last time involved is the one for ionizations to take place as a stepwise process: to evaluate it, the Lotz formula described in chapter 4 have been used, and reported in the following for the sake of clearness

$$\left(\tau_{ion}^{(i\to i+1)} n_e\right)^{-1} = 6.7 \cdot 10^{-7} \sum_{j=1}^{N} \frac{a_{ij} q_{ij}}{T_e^{3/2}} \left\{ \frac{1}{P_{ij}/T_e} E_1(P_{ij}/T_e) - \frac{b_{ij} \exp c_{ij}}{P_{ij}/T_e + c_{ij}} E_1(P_{ij}/T_e + c_{ij}) \right\} \tag{6.11}$$

By considering again electrons with density $n_e = 2.47{\cdot}10^{18}$ m^{-3} and in thermal equilibrium at a temperature $KT_e = 1$ keV (value suited for ionization to high charge states) we obtain for ^{90}Rb the ionization times shown in table 6.3 for the charge states from 1+ to 6+ .

From the considerations written above it comes out that the times involved can be low down to 10^{-8} s: for this reason and following the experience of the colleagues from LNS in simulating plasma dynamics [109], I opted for an integration step of

Table 6.3: Characteristic times for ionization of Rubidium up to charge state 6+.

Ionization	Time [s]
$0 \rightarrow 1$	$2.62{\cdot}10^{-6}$
$1 \rightarrow 2$	$8.07{\cdot}10^{-6}$
$2 \rightarrow 3$	$1.48{\cdot}10^{-5}$
$3 \rightarrow 4$	$1.49{\cdot}10^{-5}$
$4 \rightarrow 5$	$2.14{\cdot}10^{-5}$
$5 \rightarrow 6$	$2.42{\cdot}10^{-5}$

10^{-10} s. Now that the basic ingredients of the code have been introduced I will describe in the next section the first step toward the final results, that is a benchmark to test the correct implementation of the Coulomb collisions.

6.2 A first benchmark of the slowing down process

The main problem encountered in developing the code was the proper implementation of the Coulomb collisions in the integration of the equation of motion. To validate the methods a very simplified model has been implemented: it consists in an oxygen plasma generated at 14 GHz ($B_{ecr} = 0.5$ T) with an average ion charge $\langle z \rangle = 3.55$ and an ion temperature $KT_i = 1$ eV . The plasma has been modelled according to the "plasmoid-halo" scheme, proposed by theoretical papers [109, 110] and then verified by experimental results. In this particular case the plasmoid, that is the region inside the resonance surface ($B \leq B_{ecr}$), has a density $n_e = 2.47{\cdot}10^{18}$ m^{-3}, while the halo ($B > B_{ecr}$) a density $n_e = 2.47{\cdot}10^{16}$ m^{-3}. Considering that the ion density $n_i = n_e/\langle z \rangle$ is included in the formula of the constant A_D, the evaluation of the diffusion coefficients (and then of the characteristic times) depends on the position of the particle with respect to the magnetic field.
Following the theory, whatever the initial velocity distribution of some externally injected ions, Coulomb collisions lead to thermal equilibrium with plasma ions: after a time in the order of the characteristic times defined in equations 6.8, external ions will be indistinguishable from plasma ions and exhibit a Maxwell-Boltzmann distribution of velocities with

$$v_{rms} = \sqrt{\frac{KT_i}{M_{inj}}} \tag{6.12}$$

being M_{inj} their mass.
As a benchmark it has been tried to reproduce the slowing down and thermalization of a monochromatic ^{132}Sn ion beam in the above described plasma, being this element of interest for SPES. The injected ions have a total energy of about 15 eV and an

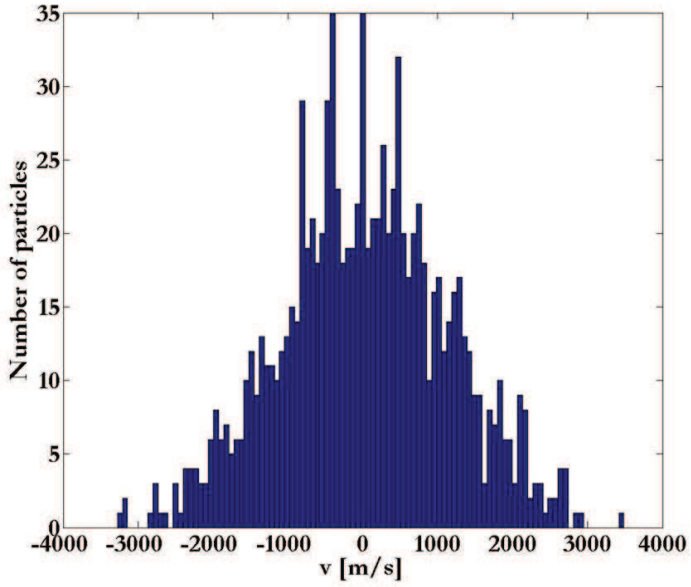

Figure 6.7: 1D Maxwell-Boltzmann distribution of ^{132}Sn ions for KT=1 eV.

initial velocity distribution such that:

$$v_x^{Sn}(t=0) = v_y^{Sn}(t=0) = 0 \qquad v_z^{Sn}(t=0) \simeq 4 \cdot v_{rms}^{Sn} = 3.4 \cdot 10^{+3} \text{ m/s} \qquad (6.13)$$

where v_{rms}^{Sn} corresponds to equation 6.12 evaluated for the ion considered (v_{rms}^{Sn} = 851.3 m/s) and z is the direction of the axial magnetic field. This condition corresponds to a value close to one for the variable v/C_s, that is to a maximum of the friction coefficient as can be seen from figure 6.5. To have enough statistics the number of simulated particles was fixed to 1000: what was expected at the end of the simulation was particles acquiring, for each spatial direction, the velocity distribution shown in figure 6.7 as a consequence of the Coulomb collisions. The initial longitudinal position of the particles corresponds to the maximum of the magnetic field at injection (z = -0.148 m) while the transversal coordinates are randomly generated within a circle of radius 0.005 m, as shown in figure 6.8.
In order to properly reproduce a given process by a numerical simulation, the integration time (T_{span}) should be longer than the highest characteristic time involved in the calculation: considering the number of particles and the computational resources available, the injected ions were assumed to be charged to 4+ to keep reasonably low the time necessary for a single simulation. This translated in the following values for the characteristic times of the Coulomb collisions:

$$\tau_s = 3.6 \cdot 10^{-7} \text{ s}; \quad \tau_D = 1.1 \cdot 10^{-6} \text{ s}; \quad \tau_L = 3.2 \cdot 10^{-6} \text{ s}; \quad \tau_E = 8.0 \cdot 10^{-7} \text{ s} \quad (6.14)$$

from which the integration time was fixed to $4.8 \cdot 10^{-5}$ s, corresponding to 480001 integration steps. Table 6.4 summarizes the starting conditions and some parameters of the simulation.

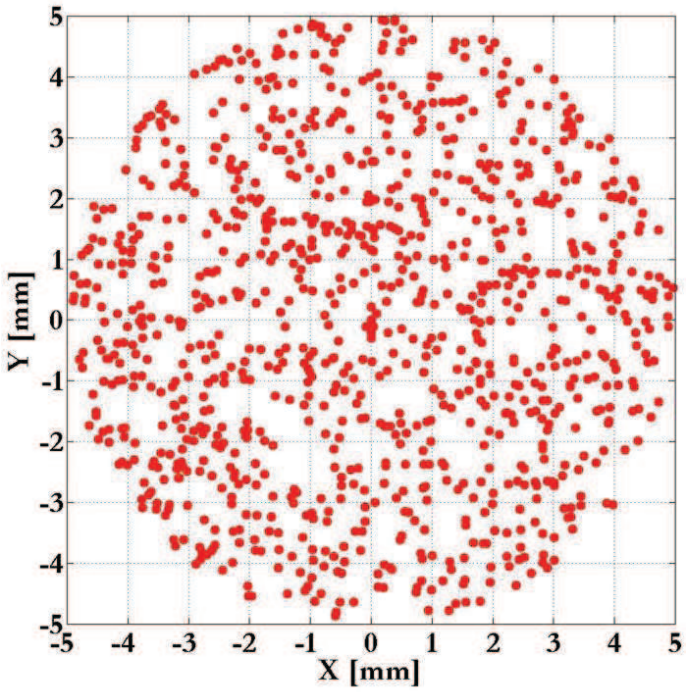

Figure 6.8: Transversal distribution of $^{132}Sn^{4+}$ ions at the beginning of the simulations.

Table 6.4: Initial conditions and parameters of the simulations.

Number of simulated particles	1000
$T_{step}[s]$	10^{-10}
$T_{span}[s]$	$4.8{\cdot}10^{-5}$
v_x(t=0) [m/s]	0
v_y(t=0) [m/s]	0
v_z(t=0) [m/s]	$3.4{\cdot}10^{-3}$
x(t=0) [m] y(t=0) [m]	Randomly distributed within a circle of radius 0.005
z(t=0) [m]	-0.148
Charge	4+

Let's go now to the description of the first version of the code: it basically solves, for the given starting conditions, the following differential equations for the x coordinate

$$\frac{dv_x}{dt} = \frac{F_x}{m} = a_x \tag{6.15}$$

$$\frac{dx}{dt} = v_x \tag{6.16}$$

and the same for y and z. Considering the very small integration step, the above equations can be approximated by the following expressions

$$\frac{\Delta v_x}{T_{step}} = a_x \tag{6.17}$$

$$\frac{\Delta x}{T_{step}} = v_x \tag{6.18}$$

and then integrated at each time step to give

$$v_x(t) = v_x(t-1) + a_x(t)T_{step} \tag{6.19}$$

$$x(t) = x(t-1) + v_x(t)T_{step} \tag{6.20}$$

The above equations, solved for each particle at the same time, become the starting conditions for the next iteration to be executed within a *for* loop; the calculation ends when the number of cycles is equal to 48001. The simulated ions are not interacting so the only contribution to the term a_x in the equation 6.17 comes from the Coulomb collisions. Those collisions were supposed to have on the particles' distribution function three different effects:

- **Exponential decrease** of the particle's speed, consequence of the dynamical friction and characterized by a frequency $\nu_s = \tau_s^{-1}$.
- **Random rotation of 90°** of the velocity vector, consequence of the transversal diffusion and characterized by the time τ_D.
- **Addition** to the velocity vector **of a random kick** chosen within a normal distribution with sigma given by equation 6.12, a consequence of the longitudinal diffusion and characterized by the time τ_L.

At each time step, the code first of all calculates the magnetic field at each particle's position by equations 6.2 - 6.6, in order to collocate them in one of the two densities zone the plasma is divided (the magnetic field is not included in the equation of motion). It then calculates the modulus of the velocity vector that, together with the previous variable and the charge z of the ions, is given as input argument to a self-made external Matlab function that finally gives as output the corresponding collision frequency ν_s and the two characteristic times τ_D and τ_L. What basically the function does for each particle is do determine the plasma density by the value of the magnetic field and use it, together with the charge z, to calculate the constant

A_D; it then uses the modulus of the velocity vector to deduce the variable v/C_s and then evaluate the functions G and Φ - G. Finally, from equations 6.8 the expected outputs are obtained.
The way the effect of Coulomb collisions have been implemented is the following: basically the dynamical friction was included in the equation of motion, by writing the term a_x, and the corresponding for the y and z axes, as given by a friction force

$$\begin{aligned} a_x &= -\nu_s v_x \\ a_y &= -\nu_s v_y \\ a_z &= -\nu_s v_z \end{aligned} \tag{6.21}$$

In this way the equations 6.19 and 6.20, for each spatial coordinate at each time step, become:

$$\begin{aligned} v_x(t) &= v_x(t-1) - v_x(t-1)\nu_s T_{step} = v_x(t-1)\cdot(1-\nu_s T_{step}) \\ v_y(t) &= v_y(t-1) - v_y(t-1)\nu_s T_{step} = v_y(t-1)\cdot(1-\nu_s T_{step}) \\ v_z(t) &= v_z(t-1) - v_z(t-1)\nu_s T_{step} = v_z(t-1)\cdot(1-\nu_s T_{step}) \end{aligned} \tag{6.22}$$

$$\begin{aligned} x(t) &= x(t-1) + v_x(t)T_{step} = x(t-1) + v_x(t-1)\cdot(1-\nu_s T_{step})T_{step} \\ y(t) &= y(t-1) + v_y(t)T_{step} = y(t-1) + v_y(t-1)\cdot(1-\nu_s T_{step})T_{step} \\ z(t) &= z(t-1) + v_z(t)T_{step} = z(t-1) + v_z(t-1)\cdot(1-\nu_s T_{step})T_{step} \end{aligned} \tag{6.23}$$

and can be calculated.
Then, the diffusive effects were considered as two independent random events characterized, at each time step, by the probabilities:

$$\begin{aligned} P_D &= 1 - \exp\frac{T_{step}}{\tau_D} \\ P_L &= 1 - \exp\frac{T_{step}}{\tau_L} \end{aligned} \tag{6.24}$$

The code calculates for each particle the above probabilities and compare them with randomly extracted numbers *rnd* through a Monte Carlo technique [111].
It then acts as follow:

- **For those particle for which *rnd* $\leq$ P_D** the code calls another external function written by the colleague of LNS that accept a velocity vector and gives back a new one $\mathbf{v}^{rot} \equiv [v_x^{rot}, v_t^{rot}, v_z^{rot}]$ rotated of 90°. The code then verifies the conservation of energy for the new velocity and updates the already calculated values of equations 6.22 as follows:

$$\begin{aligned} v_x(t) &= v_x^{rot} \\ v_y(t) &= v_y^{rot} \\ v_z(t) &= v_z^{rot} \end{aligned} \tag{6.25}$$

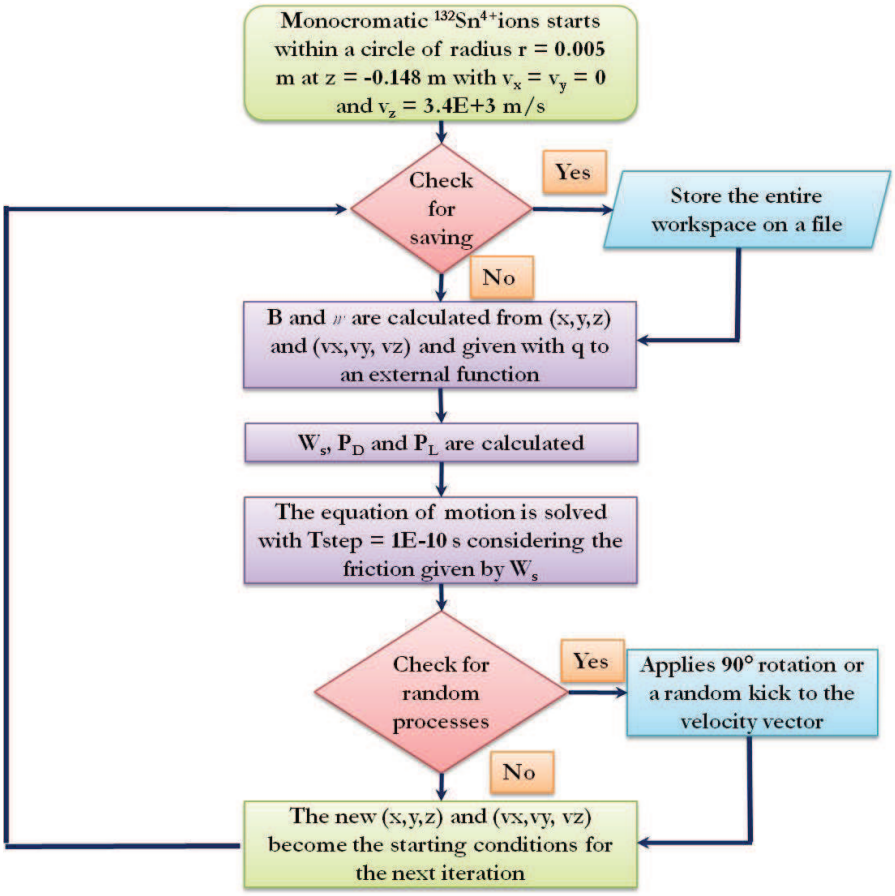

Figure 6.9: Flow diagram of the calculation made by the code for each iteration of the *for* loop.

- **For those particles for which $P_D < rnd < P_D + P_L$** the code extracts three velocities from a normal distribution with sigma given by equation 6.12 and consider them as components of a random vector $\mathbf{v}^{rand} \equiv [v_x^{rand}, v_y^{rand}, v_z^{rand}]$. It then considers this vector as a random velocity kick and adds it to the equations 6.22 that become:

$$\begin{aligned} v_x(t) &= v_x(t-1) \cdot (1 - \nu_s T_{step}) + v_x^{rand} \\ v_y(t) &= v_y(t-1) \cdot (1 - \nu_s T_{step}) + v_y^{rand} \\ v_z(t) &= v_z(t-1) \cdot (1 - \nu_s T_{step}) + v_z^{rand} \end{aligned} \tag{6.26}$$

The calculations for the given time step are then concluded and the velocity and position vectors become the starting conditions for the next iteration of the *for* loop; each 1.5 μs the code saves all the work space of the simulation to post process the data. The flow diagram shown in figure 6.9 summarizes the steps followed by the code during the calculation: unfortunately, figures 6.10 shows that the results obtained did not satisfy the expectations. The final velocity distribution is in fact not Maxwellian at all because too many particles show a velocity very close to 0, as

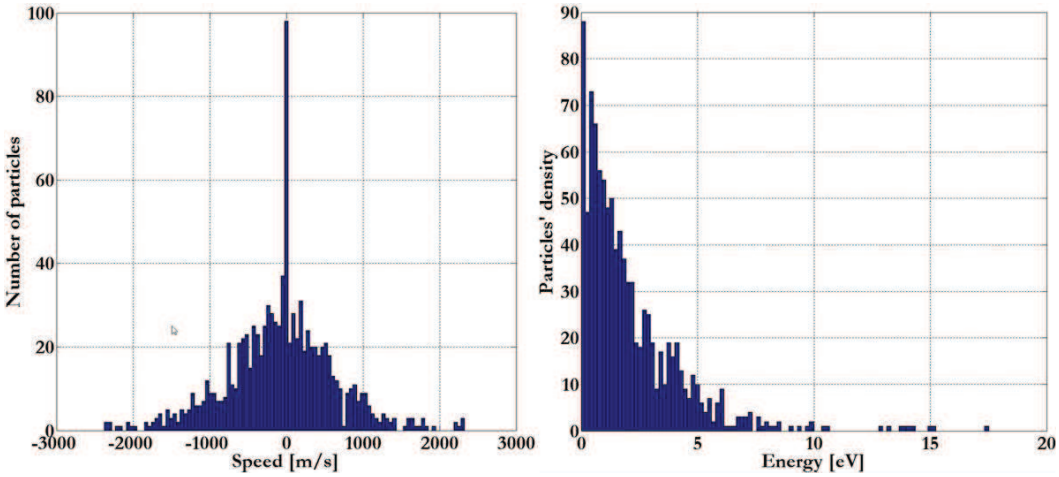

Figure 6.10: Final particles' velocity and energy distributions. An "over-damping" effect is evident.

having suffered an "over-damping" in interacting with the plasma. Probably, the random effects on the particle's velocity, selected through the Monte Carlo technique, are not effective enough to counteract the deterministic friction applied at each time step; the final effect is that the velocity drops too much.

After the first, failure I searched for a possible solution in the literature of computational physics, where I found a confirmation to the interpretation of the bad results obtained. The use of a Monte Carlo technique to describe collisions is suited for weakly ionized plasmas, where collisions between charged particles are dominated by e-neutral and i-neutral collisions: these latter are in fact characterized by a fast interaction that takes place only when the particles come close to each other and no interaction is observed otherwise. The same technique is suited to treat Coulomb collisions in fully ionized plasmas for particles already in thermal equilibrium: the effect of the interaction can be in fact reduced to the simple 90° deflection because no energy is exchanged between them. This is the reason why, in describing the Spitzer collisions in chapter 4, they were characterized only by the effect of deflecting the particle's trajectory of 90°. In this scenario it makes sense to treat this kind of collisions by a Monte Carlo technique because, basically, these processes can be translated in a certain effect happening in a very short time, with a given probability determined by the corresponding cross section. When an ions beam is injected into a fully ionized plasmas, as in the case of the ECR-based charge breeders, collisions between charged particles not in thermal equilibrium dominate and the Monte Carlo approach fails in reproducing these long range "continuous" small interactions that are always present.

Fortunately, a solution was found by adopting a formulation used by different authors in representing Coulomb collisions in PIC simulations: the application of the Langevin equation [112]. Before going into details in the implementation of this formalism I will briefly describe this equation in the next section.

6.3 The Langevin equation and the Brownian motion

In statistical physics, a Langevin equation is a stochastic differential equation describing the time evolution of a subset of the degrees of freedom: the original one describes the Brownian motion, the apparently random movement of a particle in a fluid due to collisions with the molecules of the fluid itself. Reasoning for simplicity in one dimension, two forces act on a particle of mass m: a viscous friction force $-m\nu_s(dx/dt)$, characterized by the friction coefficient $\nu_s > 0$, and a fluctuating force $F(t)$, representing the unceasing impacts of the fluid's molecules on the particle. This last one is assumed to be independent of the particle's velocity and considered as an external force, called the **Langevin force**. In the absence of a potential, the Brownian particle is said to be "free": its equation of motion, the **Langevin equation**, reads

$$m\frac{d^2x}{dt^2} = -m\nu_s\frac{dx}{dt} + F(t) \tag{6.27}$$

or

$$m\frac{dv_x}{dt} = -m\nu_s v_x + F(t), \qquad v_x = \frac{dx}{dt} \tag{6.28}$$

This is historically the first example of a stochastic differential equation, that is, a differential equation involving a random term $F(t)$. In the Langevin model, the friction force $-m\nu_s v_x$ and the fluctuating force $F(t)$ represent two consequences of the same physical phenomenon. To fully define the model, we have to characterize the statistical properties of the random force. The fluid is supposed to be in a stationary state: the fluctuating force acting on the Brownian particle is conveniently described by a stationary random process, having as a consequence that the one-time average $\langle F(t)\rangle$ does not depend on t and the two-time average $\langle F(t)F(t')\rangle$ depends only on the time difference $t - t'$. Besides these minimal characteristics, the Langevin model requires some supplementary hypotheses about the random force:

I It is assumed that the average value of the Langevin force vanishes:

$$\langle F(t)\rangle = 0 \tag{6.29}$$

This hypothesis is necessary to have the average value of the Brownian particle's velocity vanishing at equilibrium (as it should, since there is no applied external force).

II The autocorrelation function of the random force

$$g(\tau) = \langle F(t)F(t+\tau)\rangle \tag{6.30}$$

is an even function of τ , decreasing over a characteristic time τ_c (correlation time). Such time is of the order of the mean time interval separating two successive collisions of the fluid's molecules on the Brownian particle: if this time is much shorter than the other characteristic times, such as for instance the relaxation time of the average velocity from a well-defined initial value, we can

assimilate $g(\tau)$ to a delta function (the signification of the following parameter $\mathcal{D}$ will be made precise later):

$$g(\tau) = 2\mathcal{D}m^2\delta(\tau) \tag{6.31}$$

III Most often, it is also assumed for convenience that $F(t)$ is a Gaussian process. All the statistical properties of the Langevin force are then calculable given only its average and its autocorrelation function.

Let's assume now that there is no applied external force, and that at time $t = 0$ the Brownian particle's velocity has a well-defined value denoted by $v_0 = v(0)$: the solution of equation 6.28 reads

$$v(t) = v_0 e^{-\nu_s t} + \frac{1}{m}\int_0^t F(t')e^{-\nu_s(t-t')}\,dt', \qquad t > 0 \tag{6.32}$$

It is possible now to compute the average value and the variance of $v(t)$ at any time $t > 0$: since the fluctuating force vanishes on average we obtain from equation 6.32

$$\langle v(t)\rangle = v_0 e^{-\nu_s t} \tag{6.33}$$

that is, the average velocity relaxes exponentially towards zero with a relaxation time $\tau_s = \nu_s^{-1}$. The variance of the velocity is defined for instance by the formula:

$$\sigma_v^2(t) = \left\langle [v(t) - \langle v(t)\rangle]^2 \right\rangle \tag{6.34}$$

that can be expressed as

$$\sigma_v^2(t) = \frac{1}{m^2}\int_0^t dt' \int_0^t dt'' \left\langle F(t')F(t'')\right\rangle e^{-\nu_s(t-t')}e^{-\nu_s(t-t'')} \tag{6.35}$$

When the autocorrelation function of the Langevin force is given by the simplified equation 6.31 we obtain:

$$\sigma_v^2(t) = 2\mathcal{D}\int_0^t e^{-2\nu_s(t-t')}\,dt' \tag{6.36}$$

that is

$$\sigma_v^2(t) = \frac{\mathcal{D}}{\nu_s}\left(1 - e^{-2\nu_s t}\right), \qquad t > 0 \tag{6.37}$$

At time t = 0 the variance of the velocity vanishes because the initial velocity is determined: under the effect of the Langevin force, velocity fluctuations arise and the variance $\sigma_v^2(t)$ increases with time. At first, this increase is linear:

$$\sigma_v^2(t) \simeq 2\mathcal{D}t, \qquad t \ll \tau_s \tag{6.38}$$

and can interpret the above equation as describing a phenomenon of diffusion in the velocity space. The parameter $\mathcal{D}$, which has been introduced in the definition of $g(\tau)$ takes the meaning of a diffusion coefficient in the velocity space: the variance of the

velocity does not however increase indefinitely, but ends up saturating at the value $\mathcal{D}/\nu_s$. The variance of the velocity can be also written in the form:

$$\sigma_v^2(t) = \left\langle v^2(t) \right\rangle - \langle v(t) \rangle^2 \tag{6.39}$$

For $t \gg \tau_s$, the average velocity tends towards zero from equation 6.33: $\left\langle v^2(t) \right\rangle$ then tends towards a limit value $\mathcal{D}/\nu_s$ independent of v_0; the average energy $\langle E \rangle = m \left\langle v^2(t) \right\rangle /2$ tends towards the corresponding limit $\langle E \rangle = m\mathcal{D}/2\nu_s$: in this condition the Brownian particle is in equilibrium with the bath. If the bath is itself in thermodynamic equilibrium at temperature KT, the average energy of the particle in equilibrium with it takes its equipartition value $\langle E \rangle = kT/2$: by comparing both expressions for $\langle E \rangle$, we get a relation between the diffusion coefficient $\mathcal{D}$ in the velocity space and the friction coefficient:

$$\nu_s = \frac{m}{KT}\mathcal{D} \tag{6.40}$$

It can be demonstrated that the previous equation can be written in the form:

$$\nu_s = \frac{1}{2mKT} \int_{-\infty}^{\infty} \langle F(t)F(t+\tau) \rangle \tag{6.41}$$

Equation 6.41 relates the friction coefficient to the autocorrelation function of the Langevin force and it is known as the **fluctuation-dissipation theorem**: it expresses here the fact that the friction force and the fluctuating force represent two aspects of the same physical phenomenon.

6.4 The correct numerical implementation of Coulomb collisions

The correct description of Coulomb collisions has an important implication in determining the Electron Energy Distribution Function (EEDF), even in those discharges where 90° scattering is dominated by e-neutral collisions. In many of them, in fact, the energy input is primarily into the thermal part of the EEDF and the high-energy tail is populated mainly by energy up-scattering due to e-e collisions. The high-energy tail is then depleted by excitation and ionization processes, that in turn determine many of the properties crucial for processing applications. Those inelastic processes have basically an effect opposite to e-e collisions in populating the tail of the EEDF and for this reason both have to be modelled accurately. The problem of using the Monte Carlo approach in describing e-e collisions is that they consist in many almost continuous very small angle scatterings: to treat them as a succession of random effects it should be necessary to use a numerically unmanageable integration step.
An alternative approach which has been emphasized in the analytical development of plasma kinetic theory is to represent Coulomb scattering through a Fokker–Planck equation: direct numerical solutions of the Fokker–Planck equation are often performed, but there is no obvious way to combine this procedure with a PIC or single

particle simulation. However, it is possible to construct a Langevin equation (comprising a deterministic friction and a random diffusive scattering) which is entirely equivalent to any given Fokker–Planck equation. Differently from what was stated in the previous section, the dynamical friction and the diffusion coefficients are here velocity-dependent quantities: by using the Langevin formalism, the variation of velocity vector $\mathbf{v}$ of a test particle due to Coulomb collisions with a background plasma can be expressed at each time step as

$$\Delta\mathbf{v} = \mathbf{v}(t+1) - \mathbf{v}(t) = \mathbf{a}(t)T_{step} + \mathbf{v}^{rand} \tag{6.42}$$

where $\mathbf{a}$ is the dynamical friction directed along the original velocity and corresponding to the vectorial form of equation 6.21, that is

$$\mathbf{a}(t) = -\nu_s \mathbf{v}(t) \tag{6.43}$$

while the term $\mathbf{v}^{rand}$ is a random velocity vector whose components are chosen from the distributions

$$\phi(\mathbf{v}^{rand}) = \frac{1}{(2\pi T_{step})^{3/2} D_\perp D_\parallel^{1/2}} \exp\left(-\frac{v_3^2}{2D_\parallel T_{step}} - \frac{v_1^2 + v_2^2}{2D_\perp T_{step}}\right) \tag{6.44}$$

where $D_\perp$ and $D_\parallel$ are the perpendicular and parallel diffusion coefficients of the Fokker-Plank equation (see section 4.9). Here perpendicular and parallel are referred to the particle's direction of motion: v_3 lies along the original velocity while the components v_1 and v_2 are oriented in two directions perpendicular between each other and to v_3. Equation 6.44 basically describes three normal distributions with mean 0: the two associated with the perpendicular directions have the same width given by the relation

$$\sigma_\perp = \sqrt{D_\perp T_{step}} \tag{6.45}$$

while for the longitudinal part

$$\sigma_\parallel = \sqrt{D_\parallel T_{step}} \tag{6.46}$$

If the background plasma is in thermal equilibrium, the above coefficient can be traced back to the expressions found in section 4.9:

$$\begin{aligned} D_\perp =& \frac{1}{2}\langle(\Delta v_\perp)^2\rangle = \frac{1}{2}\frac{A_D}{v}\left[\Phi\left(\frac{v}{C_s}\right) - G\left(\frac{v}{C_s}\right)\right] \\ D_\parallel =& \langle(\Delta v_\parallel)^2\rangle = \frac{A_D}{v} G\left(\frac{v}{C_s}\right) \end{aligned} \tag{6.47}$$

Considering that $D_\perp \neq D_\parallel$ if follows from equations 6.45 and 6.46 that the distribution of equation 6.44 is not isotropic.

Let's go now to the implementation of this formalism in the code: the goal was to calculate, at each time step, the necessary variables to construct an equation like 6.42 for each of the simulated particles. With respect to the version of section 6.2, the

Table 6.5: Initial conditions and parameters of the simulations.

Number of simulated particles	10000
$T_{step}[s]$	10^{-10}
$T_{span}[s]$	$1.4{\cdot}10^{-4}$
v_x(t=0) [m/s]	0
v_y(t=0) [m/s]	0
v_z(t=0) [m/s]	$3.4{\cdot}10^{3}$
x(t=0) [m] y(t=0) [m]	Randomly distributed within a circle of radius 0.005
z(t=0) [m]	-0.148
Charge	6+

parameters of the simulation have been slightly modified: first of all, the number of ^{132}Sn ions was increased to 10000, in order to have more statistics, and the particles were considered charged 6+ instead of 4+. More, a homogeneous plasma was considered this time, with a density $n_e = 2.47{\cdot}10^{16}$ m^{-3}. Keeping the same initial velocity, all these modifications translated in the following values for the characteristic times

$$\tau_s = 1.58 \cdot 10^{-5} \text{ s} \qquad \tau_D = 4.88 \cdot 10^{-5} \text{ s} \qquad \tau_L = 1.42 \cdot 10^{-4} \text{ s} \qquad \tau_E = 3.55 \cdot 10^{-5} \text{ s}$$

The magnetic field was totally excluded from the calculation and one of the two external functions was integrated in the body of the script. The integration step T_{step} was maintained at 10^{-10} s while the integration time T_{span} was preventively increased to $2.88{\cdot}10^{-4}$ s (corresponding to $2.88{\cdot}10^{6}$ integrations) so as to be much longer than all the characteristic times; table 6.5 summarizes the simulation's parameters. Figure 6.11 shows a flow diagram of the code: as before, after loading the starting conditions it verifies if a multiple of 1.5 μs is elapsed so as to save the entire workspace; the code then calculates the value of v/C_s for each particle and evaluates ν_s and the diffusion coefficients $\langle(\Delta v_{\parallel})^2\rangle$ and $\langle(\Delta v_{\perp})^2\rangle$ using the interpolation method mentioned in section 6.2. At this point the work is almost done: the quantity ν_s can be directly used to determine $\mathbf{a}$ in equation 6.42 and only the vector $\mathbf{v}^{rand}$ has still to be defined from the two diffusion coefficients. In a reference frame xyz the components v_1, v_2 and v_3 of $\mathbf{v}^{rand}$ become three orthogonal vectors $\mathbf{v}_{orto1}, \mathbf{v}_{orto2}$ and $\mathbf{v}_{long}$ individuating three spatial directions. Unfortunately the nature of the interaction is such that the particle's velocity changes continuously so that the above direction are not univocally determined for each time step: the code solves this problem in two steps, creating first three orthogonal directions, of which one always coincides with the particle velocity, and then associating to the above directions three vectors from three normal

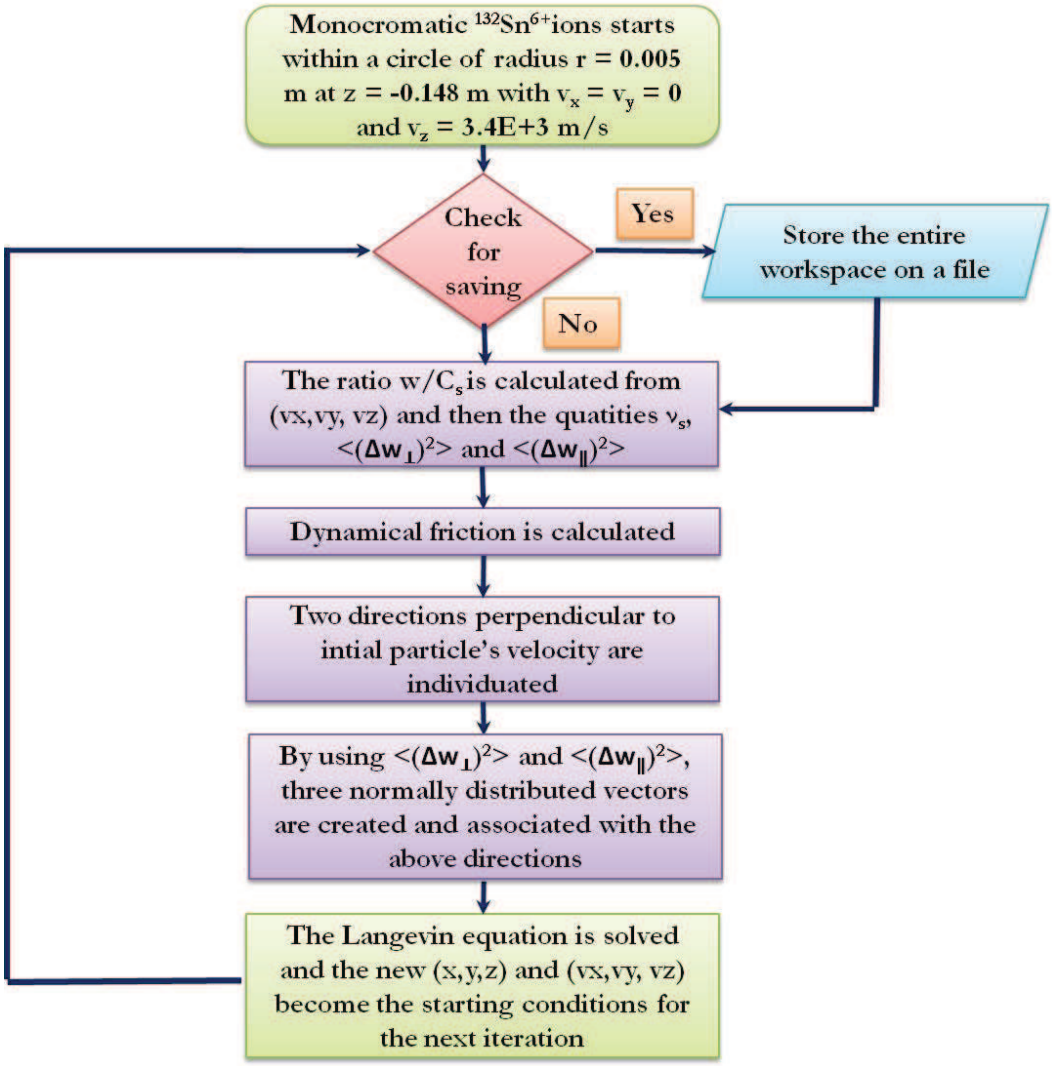

Figure 6.11: Flow diagram of the revised version of the code.

distributions with standard deviations calculated through equations 6.45÷6.47. To identify the three directions the code uses the direction cosines: considering a generic vector $\mathbf{v} \equiv (v_x, v_y, v_z)$ these quantities correspond to the angle it forms with the coordinate axis

$$\begin{aligned} \cos(\hat{vx}) &= \frac{v_x}{\sqrt{v_x^2 + v_y^2 + v_z^2}} \\ \cos(\hat{vy}) &= \frac{v_y}{\sqrt{v_x^2 + v_y^2 + v_z^2}} \\ \cos(\hat{vz}) &= \frac{v_z}{\sqrt{v_x^2 + v_y^2 + v_z^2}} \end{aligned} \tag{6.48}$$

At the same time, it can be said that the above equation identifies the direction of $\mathbf{v}$ if one considers the directions cosines as the cartesian component of a unit vector

parallel to $\mathbf{v}$. Every other vector $\mathbf{v}' \equiv (v'_x, v'_y, v'_z)$ parallel to $\mathbf{v}$ can be expressed in cartesian components as:

$$\begin{aligned} v'_x &= v' \cdot \cos(\hat{vx}) \\ v'_y &= v' \cdot \cos(\hat{vy}) \\ v'_z &= v' \cdot \cos(\hat{vz}) \end{aligned} \tag{6.49}$$

being v' the modulus of the new vector. Following this reasoning, the code identifies the direction parallel to $\mathbf{v}_{long}$ with the results of equation 6.48 considering $\mathbf{v} = \mathbf{v}(t)$. To identify one of the orthogonal directions the code first creates a vector $\mathbf{v}_{\perp 1}$ rotated by 90° with respect to $\mathbf{v}(t)$ (by calling the external function mentioned in section 6.2) and then calculates the corresponding direction cosines:

$$\begin{aligned} \cos(\hat{v_{\perp 1}x}) &= \frac{v_{\perp 1x}}{\sqrt{v^2_{\perp 1x} + v^2_{\perp 1y} + v^2_{\perp 1z}}} \\ \cos(\hat{v_{\perp 1}y}) &= \frac{v_{\perp 1y}}{\sqrt{v^2_{\perp 1x} + v^2_{\perp 1y} + v^2_{\perp 1z}}} \\ \cos(\hat{v_{\perp 1}z}) &= \frac{v_{\perp 1z}}{\sqrt{v^2_{\perp 1x} + v^2_{\perp 1y} + v^2_{\perp 1z}}} \end{aligned} \tag{6.50}$$

The above direction cosines are associated with the direction of the vector $\mathbf{v}_{orto1}$ corresponding to v_1. For the direction associated with v_2 it calculates the cross product between $\mathbf{v}$ and $\mathbf{v}_{\perp 1}$ to obtain a third vector $\mathbf{v}_{\perp 2}$ orthogonal to both the previous ones. The direction cosines of this vector are given by a relation similar to 6.50, and are associated to the vector $\mathbf{v}_{orto2}$. Finally the code extracts the amplitudes v_{long}, v_{orto1} end v_{orto2} of the vectors $\mathbf{v}_{long}, \mathbf{v}_{orto1}$ and $\mathbf{v}_{orto2}$ from three normal distribution, two having standard deviations given by equation 6.45 and one given by equation 6.46: we talk about amplitude and not modulus because for the way they are created those quantities could be in principle also negative; this does not invalidate the calculation because a negative value means direction cosines opposite with respect to a positive one, but lying always along the same direction. At this point the code solves the equation 6.42 that becomes for each component:

$$\begin{aligned} v_x(t+1) - v_x(t) = &- \nu_s \cdot v_x(t) \cdot T_{step} + v_{orto1} \cdot \cos(\hat{v_{\perp 1}x}) + v_{orto2} \cdot \cos(\hat{v_{\perp 2}x}) \\ &+ v_{long} \cdot \cos(\hat{vx}) \\ v_y(t+1) - v_y(t) = &- \nu_s \cdot v_y(t) \cdot T_{step} + v_{orto1} \cdot \cos(\hat{v_{\perp 1}y}) + v_{orto2} \cdot \cos(\hat{v_{\perp 2}y}) \\ &+ v_{long} \cdot \cos(\hat{vy}) \\ v_z(t+1) - v_z(t) = &- \nu_s \cdot v_z(t) \cdot T_{step} + v_{orto1} \cdot \cos(\hat{v_{\perp 1}z}) + v_{orto2} \cdot \cos(\hat{v_{\perp 2}z}) \\ &+ v_{long} \cdot \cos(\hat{vz}) \end{aligned} \tag{6.51}$$

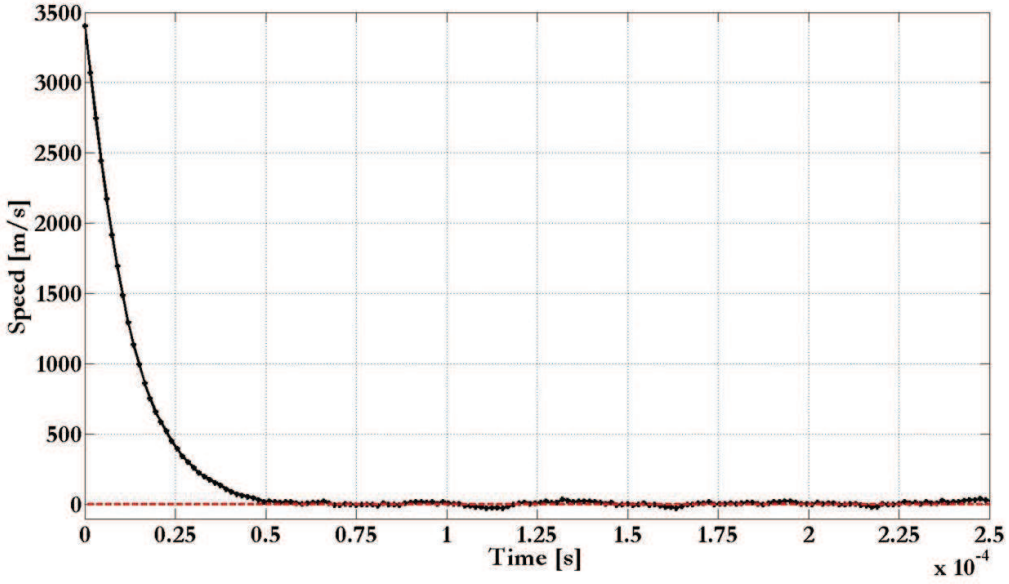

Figure 6.12: Evolution of the particles' average velocity.

As a final step the new spatial coordinates are calculated:

$$\begin{aligned} x(t+1) &= x(t) + v_x(t+1) \cdot T_{step} \\ y(t+1) &= y(t) + v_y(t+1) \cdot T_{step} \\ z(t+1) &= z(t) + v_z(t+1) \cdot T_{step} \end{aligned} \tag{6.52}$$

and together with the equation 6.51 become the starting conditions for the following iteration.

6.4.1 First results

The modifications adopted led this time to the expected results: figure 6.12 shows the evolution with time of the average particles' velocity. The velocity drops to 0 in around 50-60 μs and stably stays around this value until the end of the simulation: the average velocity reaches 1/e its initial value after about 13 μs, in very good agreement with the estimate of the characteristic time $\tau_s = 15.8\ \mu s$. The theory foresees that the particles reach a Maxwell Boltzmann distribution with temperature KT: this implies that for each degree of freedom the average energy should tend to

$$\langle E_x \rangle = \frac{1}{2} M_{inj} \langle v_x^2 \rangle = \langle E_y \rangle = \langle E_z \rangle = \frac{KT}{2} = 0.5 \text{ eV} \tag{6.53}$$

while the average total energy to

$$\langle E \rangle = \frac{1}{2} M_{inj} \langle v_x^2 + v_y^2 + v_z^2 \rangle = \frac{3}{2} KT = 1.5 \text{ eV} \tag{6.54}$$

As can be seen from figure 6.13 this is exactly what happens: the average energy tends to the expected value $KT/2$ for all the degrees of freedom: those values are reached

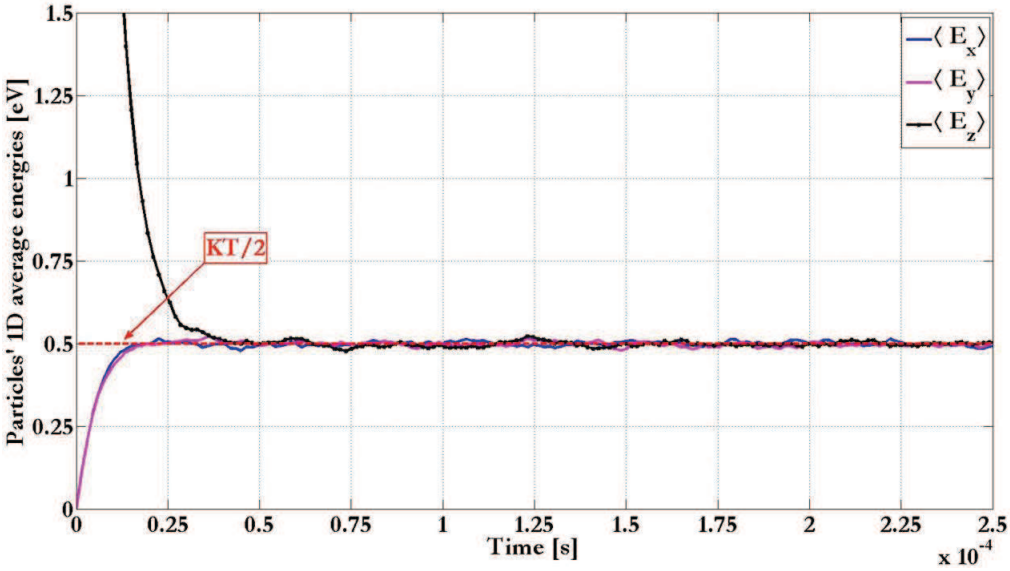

Figure 6.13: Evolution of the particles' average velocities. The expected value of $KT/2$ is also indicated. The vertical axis is reduced for the sake of clearness

quite before the end of the simulation but they are stably maintained, showing that the solution represents a steady state. The equipartition of energy is faster along the x and y axis and is completed after about 40 μs, to be compared with the expected value of $\tau_E = 35.5\ \mu s$. It is interesting also to see how the system tends to be isotropic by looking at the evolution of the standard deviation for each spatial direction shown in figure 6.14: after some tens of μs the three standard deviation starts to oscillate around the expected value, in perfect agreement with the theoretical estimates.

For the sake of completeness, the final particles' velocities, along a single direction, and the total energy distribution functions are showed in figure 6.15: it is evident that a Maxwell-Boltzmann distribution is reached; as a further proof of this fact I used the Matlab routine "normplot": if a given variable is supposed to be distributed as a Maxwell-Boltzmann then by plotting its values through normplot the points should lie on a straight line. To have a comparison, the effect of this routine was verified on 10000 numbers extracted from a normal distribution with mean 0 and σ = 851.3: the results, compared with the obtained distribution along z in figure 6.16, evidence that, in both cases, the most of the values lie on the straight line except for the high-energy tail that deviates a little bit.

As a further characterization of this benchmark, two parameters of the simulations were modified. First of all, to proof the value of T_{step} to be appropriate, a simulation was performed by decreasing it at 10^{-11} s: to reduce the computational time, the calculation was limited to 51 μs. Fortunately the results showed that the chosen value was adequate to properly simulate the problem: the plots of the average velocity and the average total energy in figure 6.17 show in fact that no remarkable differences can be found between the two integration steps.

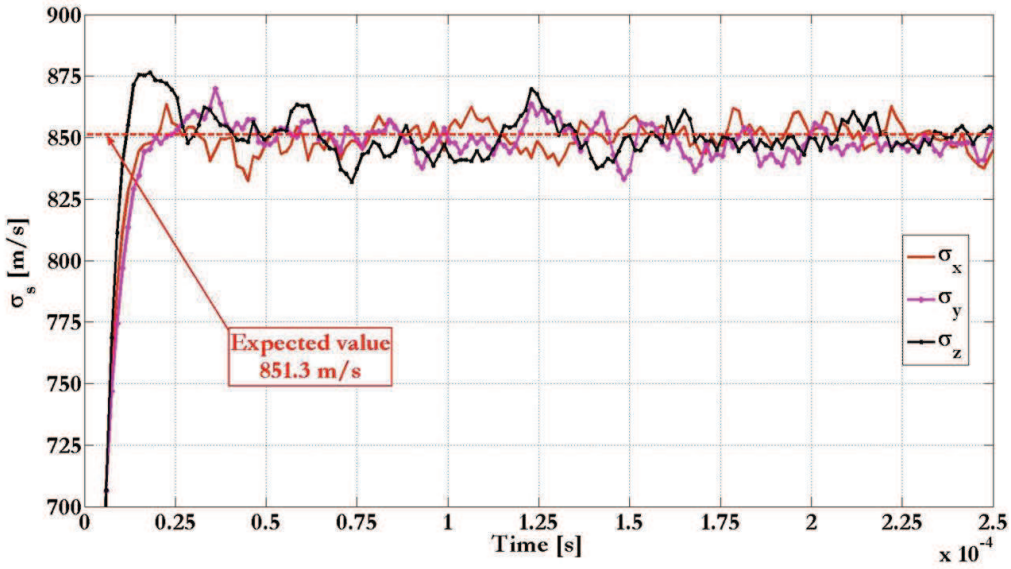

Figure 6.14: Evolution of the σ_s of the particles' distribution function. The expected value of 851.3 m/s is shown for comparison. The vertical axis is reduced for the sake of clearness.

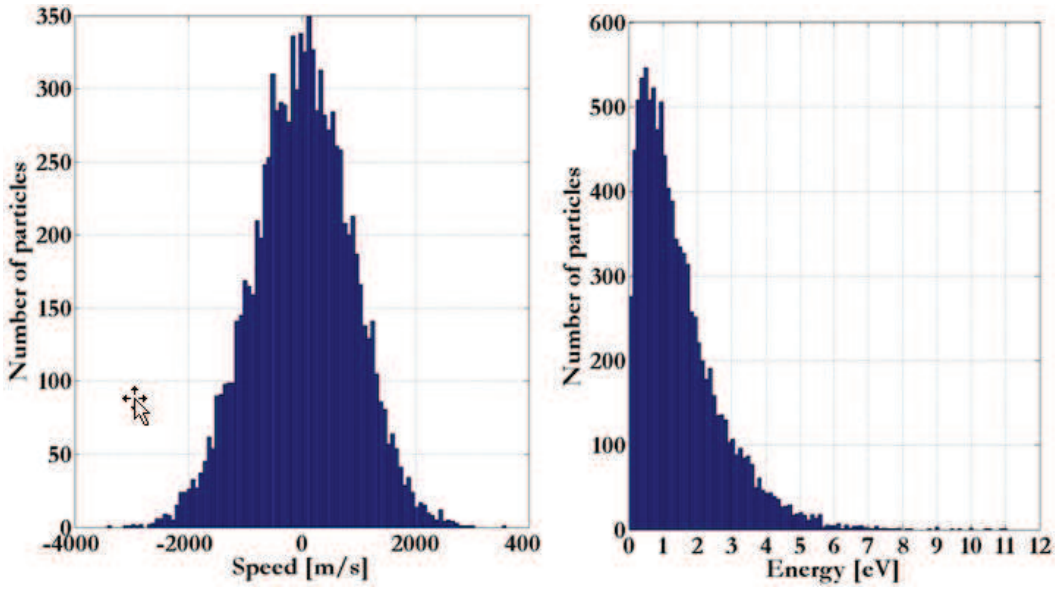

Figure 6.15: Final particles velocity and energy distribution along z.

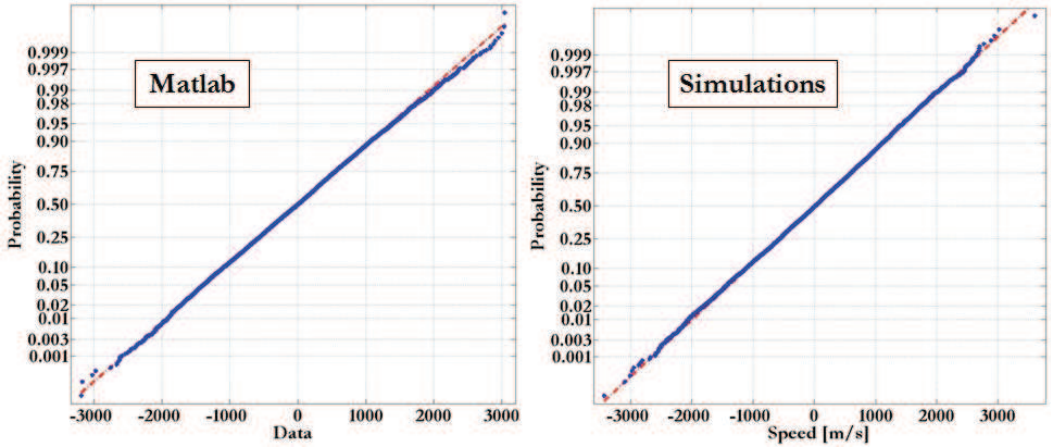

Figure 6.16: Normplot of the final velocity distribution along z

.

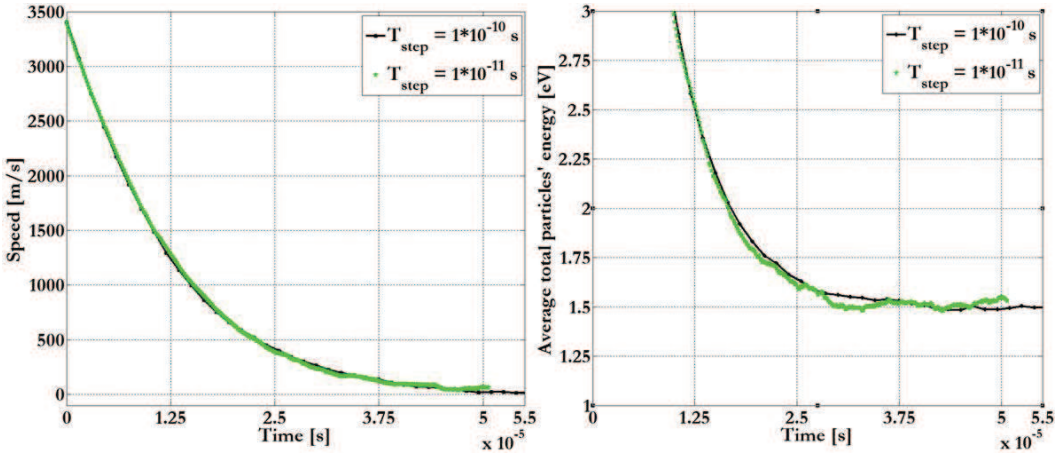

Figure 6.17: Comparison between the average velocities obtained for two different T_{step}.

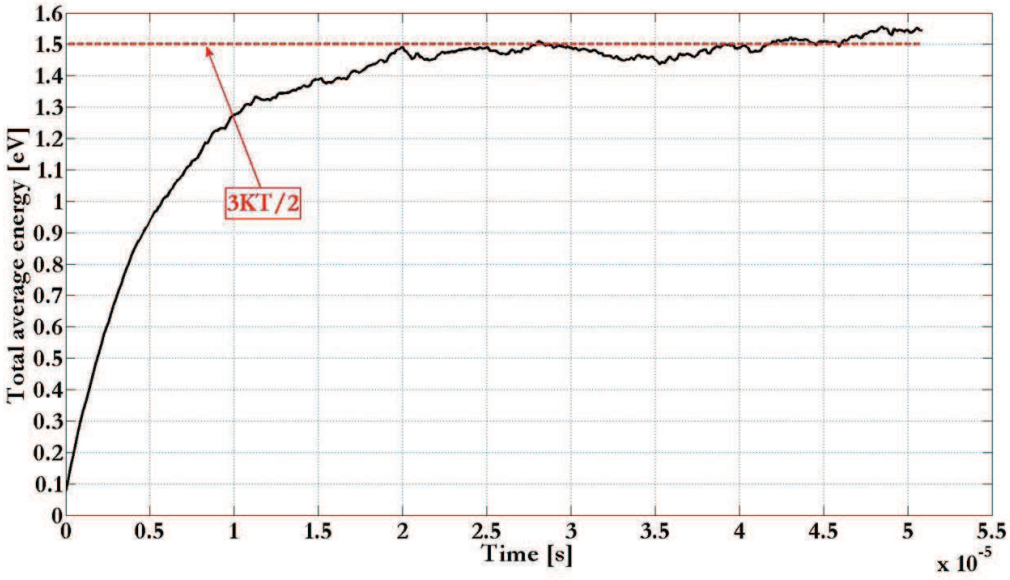

Figure 6.18: Evolution of the total energy of slow particles: the heating effect of Coulomb collisions is evident.

The second modification regarded the starting velocity of ions: the situation considered up to now was one in which the simulated beam cools down as a consequence of Coulomb collision. It was found interesting to verify also a situation in which particles are heated instead: to this scope, a simulation was executed by keeping the lowered value of $T_{step} = 10^{-11}$ s but letting the ions start with 1/10th of the velocity they had in the previous calculation ($\sim$ 340 m/s). In this case, the characteristic times take the values:

$$\tau_s = 9.31 \cdot 10^{-6} \text{ s} \qquad \tau_D = 4.11 \cdot 10^{-7} \text{ s} \qquad \tau_L = 8.34 \cdot 10^{-7} \text{ s} \qquad \tau_E = 2.09 \cdot 10^{-7} \text{ s}$$

As it can be seen from figure 6.18, effectively slow particles are heated by interacting with plasma and the average energy increases up to the expected value.

6.4.2 Preliminary conclusions

The benchmark revealed that the code properly reproduces the effects of Coulomb collisions: following the Langevin formalism, it solves the equation 6.42 by applying a "deterministic" (that is, not random) dynamical friction and creating the vector $\mathbf{v}^{rand}$, consequence of the diffusive part of the interaction. The thermalization is well reproduced and a steady state is confirmed by the fact that the solution stays stable for a time longer than the characteristic times. Both the effects of ions cooling and heating were successfully reproduced with the average energy tending to the expected value $3KT/2$ in both cases. Finally, a comparison lowering T_{step} down to 10^{-11} s revealed that the former value was adequate to simulate the problem and was used for the following calculations.

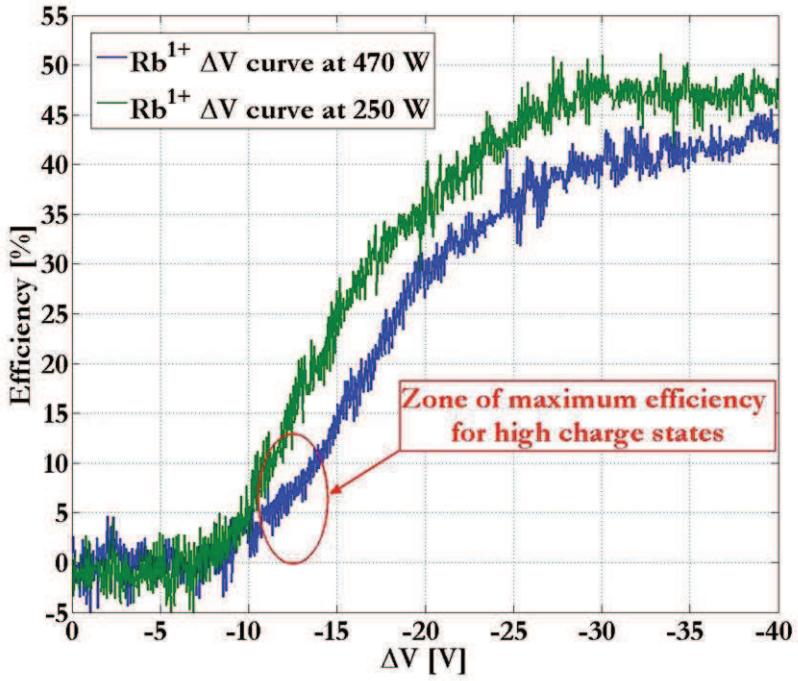

Figure 6.19: ΔV curves for $^{85}Rb^{1+}$ acquired at two different power levels during an EMILIE experiment.

Once implemented correctly the Coulomb collision mechanism, it was possible to proceed simulating the capture process of 1+ ions by the breeding plasma, as described in the following sections.

6.5 Towards simulating the capture process

Before proceeding in refining the code it was thought that having some experimental results to be reproduced could have been a proof of its validity. The simulation of the breeding efficiency of a given $q+$ ion would have been the best choice but the charge breeding time takes usually 10-15 ms*q, too long to be simulated with the available computational resources. The answer arrived from the experiments performed at LPSC within the EMILIE project: as described in the previous chapter, the spectra acquired at the extraction of the PHOENIX charge breeder revealed the presence of an unusually high intensity of very low charged ions. From a dedicated experiment, executed on November 2013 with 20 keV $^{85}Rb^{1+}$ ions, it came out that these very low charges were basically ions weakly or not interacting at all with the plasma. By optimizing the charge breeder for the highest efficiency of $^{85}Rb^{20+}$, the so called ΔV curves were acquired for both $^{85}Rb^{1+}$ and $^{85}Rb^{2+}$ in different operating conditions: figure 6.19 shows the results for $^{85}Rb^{1+}$ at two different power levels. At the ΔV value corresponding to the maximum efficiency of the charge state 20+ the $^{85}Rb^{1+}$'s charge breeding time was measured and compared with the one acquired without

Table 6.6: Measured parameters of the 20 keV $^{85}Rb^{1+}$ ion beam.

ϵ_{rms} [π*mm*mrad]	2
α	2.14
β [mm/mrad]	0.56
γ [mrad/mm]	9.96

plasma. Both values were found to be in the order of 500 μs confirming that the 1+ ions extracted from the booster weakly interact with the plasma.
The reproduction of the trend shown in figure 6.19 was the perfect test bench for the code: anyway, before implementing the model, realistic starting conditions were needed. At the LPSC's test bench the transversal emittance of the 20 keV $^{85}Rb^{1+}$ ion beam used for the experiments was already measured, showing the results of table 6.6. At the same time, the geometry of LPSC's beam line from the beam diagnostic box to the plasma chamber of the charge breeder was implemented in a tracking particle code called SIMION [113], as shown in figure 6.20. To obtain realistic input parameters for the Matlab code, the SIMION's geometry has been used to simulate the injections of $^{85}Rb^{1+}$ inside the charge breeder, starting from the beam diagnostic box and considering the fringe field. To take into account the deceleration due to the plasma potential, the geometry was slightly modified: considering that the plasma is supposed to be contained within the two maxima of the magnetic field, it was allowed for the possibility to impose a given potential to an area extending from the maximum at injection till the end of the geometry; this explain the red area indicated as "PLASMA" in figure 6.20. The only limitation of this assumption is that the plasma is seen as a fixed equipotential surface without considering the presence of the sheath.
To obtain proper starting conditions for SIMION, a Matlab script was written, able to generate particles' positions and velocities from the measured emittance: it revealed to be necessary because the program is not able to create this kind of input. From the rms-emittance and supposing the two transversal planes to be identical, it is possible to calculate the rms values of positions and angles for the particles distribution [81]:

$$\begin{aligned} x_{rms} &= y_{rms} = \sqrt{\epsilon_{rms} \cdot \beta} \\ x'_{rms} &= y'_{rms} = \sqrt{\epsilon_{rms} \cdot \gamma} \end{aligned} \tag{6.55}$$

By supposing the above distributions to be Gaussian it can be said that almost 100% of the beam is contained within three times the values given by equation 6.55: this means that if a particle is part of the beam, its transversal coordinates (x, x') and (y, y') have to satisfy the following relations at the same time

$$\begin{aligned} \gamma \cdot x^2 + 2\alpha \cdot x \cdot x' + \beta x'^2 &\leq 9 \cdot \epsilon_{rms} \\ \gamma \cdot y^2 + 2\alpha \cdot y \cdot y' + \beta y'^2 &\leq 9 \cdot \epsilon_{rms} \end{aligned} \tag{6.56}$$

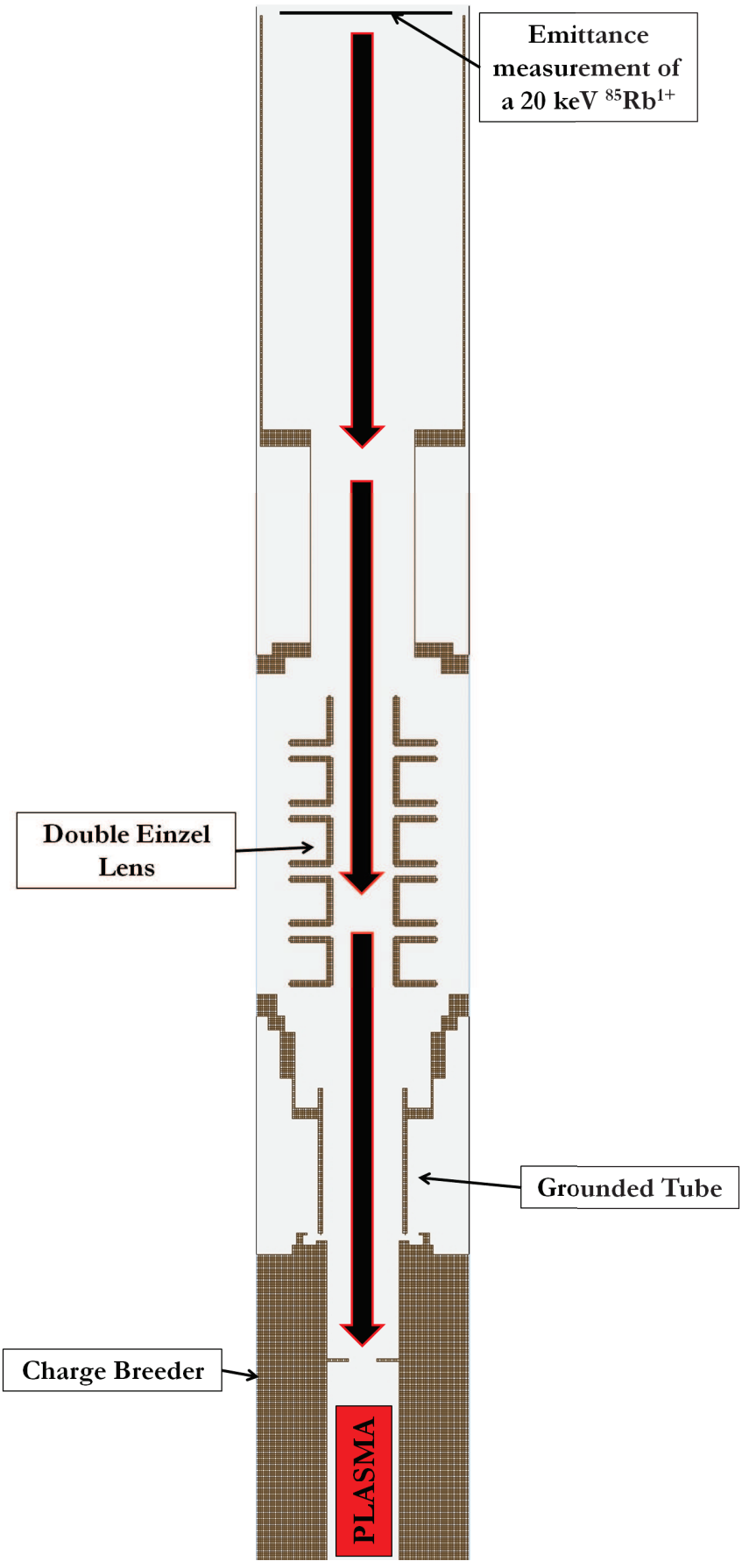

Figure 6.20: Sketch of the geometry of the LPSC beam line implemented in SIMION: the 1+ beam is injected into the charge breeder through a double Einzel lens. The red rectangle represents the plasma, supposed at a positive potential with respect to the charge breeder.

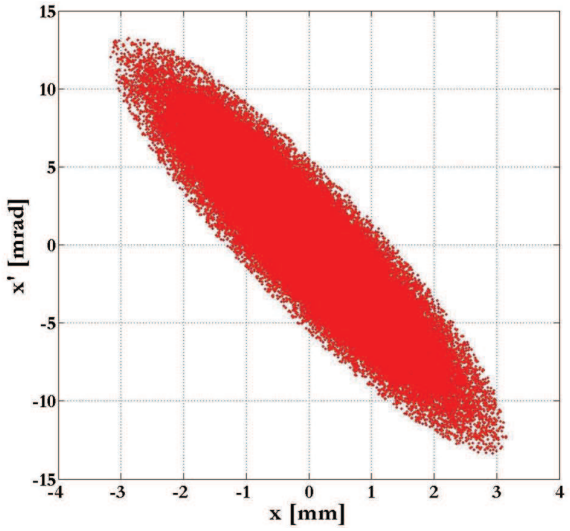

Figure 6.21: Reproduction by the Matlab script of the $^{85}Rb^{1+}$ measured emittance.

The script initially selected the quantities x, x', y, y' from Gaussian distributions with the parameters of equation 6.55 and then imposed the beam radius to not be higher than 3 times x_{rms} by letting:

$$r = \sqrt{x^2 + y^2} \leq 3 \cdot x_{rms} \tag{6.57}$$

Finally it imposed that the four extracted quantities satisfy equations 6.56. This way of generating particles revealed to be correct as long as the beam has a waist, that is $\alpha = 0$: when $\alpha \neq 0$ in fact the distribution of x and x' are not independent but correlated, meaning that the joint distribution of x and x' is not simply the product of two Gaussian but has a term due to correlation. The real distribution function for the two variables is then [114]:

$$f(x, x') = \frac{1}{2\pi x_{rms} x'_{rms} \sqrt{1 - r^2}} \exp\left\{ -\frac{1}{2(1 - r^2)} \left[\frac{x^2}{x_{rms}^2} + \frac{x'^2}{x'^2_{rms}} - \frac{2rxx'}{x_{rms} x'_{rms}} \right] \right\} \tag{6.58}$$

where

$$r = -\alpha \frac{\epsilon_{rms}}{x_{rms} x'_{rms}} \tag{6.59}$$

is the correlation. Matlab allows to extract variables within a multivariate distribution by calling the routine "mvnrnd": in this way it was possible to properly select x and x' within the desired ellipse, as proved by figure 6.21; of course the same picture is obtained for the (y, y') space. At this point the information on x' and y' had to be translated in a three dimensional velocity vector for each particle: from the definition of the afore mentioned variables, the transversal components of the velocity vector can be expressed as

$$\begin{aligned} v_x &= x' \cdot v \simeq x' \cdot v_z \\ v_y &= y' \cdot v \simeq y' \cdot v_z \end{aligned} \tag{6.60}$$

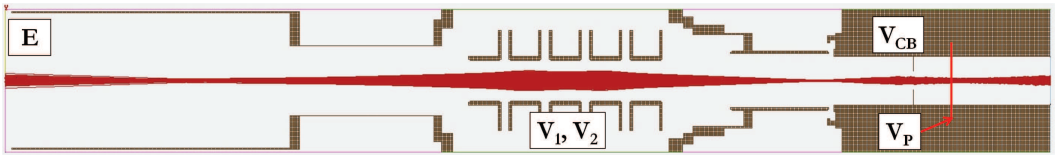

Figure 6.22: Scheme of the injection of a 20 keV $^{85}Rb^{1+}$ ion beam into the charge breeder, with $E = 20$ keV, $V_1 = V_2 = 10400$ V and $V_{CB} < V_P$. The final beam energy is $E - 1 \cdot V_P$.

where v is the modulus of the velocity. With the aid of the above equations the kinetic energy of a particle of mass m can be written:

$$\begin{aligned} E = \frac{1}{2}m\left(v_x^2 + v_y^2 + v_z^2\right) &= \frac{1}{2}m\left((x' \cdot v_z)^2 + (y' \cdot v_z)^2 + v_z^2\right) \\ &= \frac{1}{2}mv_z^2\left(1 + x'^2 + y'^2\right) \end{aligned} \tag{6.61}$$

By fixing the kinetic energy E and having already determined x' and y' it is possible to deduce v_z from equation 6.61 and then v_x and v_y by using equations 6.60. In this way, the two transversal coordinates and the three spatial velocities to be used as starting condition in SIMION were obtained, the starting position along the axis being fixed; the script allows also the possibility to give the particles an energy spread by letting E be chosen within a normal distribution of given mean and sigma.

The starting conditions were ready so the colleagues from LPSC created from them an input file suited for SIMION. They then gave me back the new input file together with the entire geometry in order to let me make all simulations I needed: I am very thankful for this availability, especially to Julien Angot and Thierry Lamy. The typical injection scheme used is shown in figure 6.22: 10000 $^{85}Rb^{1+}$ ions, with characteristics given by table 6.6, are injected through a double Einzel lens (V_1, V_2) into the charge breeder at a potential V_{CB}, with the plasma being at a potential V_P with respect to ground. Particles positions and velocities are then saved at the plane corresponding to the red line and become the starting conditions for the Matlab code. For the double Einzel lens, the values $V_1 = V_2 =$10400 V coming from the experiments were used, while $V_{CB} \leq V_P$ always. The curves like figure 6.19 are basically efficiencies as a function of V_{CB} but actually what really determines the injection energy is the value of the plasma potential V_P. To prove this, the injection of a 20 keV Rubidium beam was simulated in three different conditions: plasma and charge breeder at the same given potential ($V_{CB} = V_P = 19998$ V); the plasma potential being 10 V higher than V_{CB} ($V_{CB} = 19988$ $V, V_P = 19998$ V); the plasma potential being 5 V higher than V_{CB} ($V_{CB} = 19993$ $V, V_P = 19998$ V). The obtained energy distributions showed in fact they are not affected at all by the value of V_{CB} but are determined only by V_P. For this reason, only the value of the real injection energy $E_{inj} = E - q \cdot V_P$ will be used to identify a given starting condition for the Matlab code.

6.6 The capture of a $^{85}Rb^{1+}$ ion beam by the PHOENIX charge breeder.

The scope of this Matlab code was to reproduce the dynamics of the capture process benchmarked by the curves of figure 6.19: such curves are basically $^{85}Rb^{1+}$ efficiencies as a function of the difference between the injected beam's energy (fixed) and V_{CB}. The simulated curves will be function of the difference between the injected beam's energy (fixed) and V_P: considering that usually $V_P \geq V_{CB}$, the curves were expected to coincide with those in figure 6.19 or be shifted towards the left. The curves of figure 6.19 were acquired with the PHOENIX charge breeder optimized for the best $^{85}Rb^{20+}$: the optimum ΔV value revealed to be -12.3 V with an efficiency of ∼2.4% for the charge state 20+ and ∼6% for 1+. In these conditions the recorder global efficiency was slightly lower than 50% so a value of at least 40% was sought for the results to be considered valid. Just to summarize, to be validate the results had to satisfy the following conditions:

- **The plots of $^{85}Rb^{1+}$'s efficiency for different values of V_P should coincide with figure 6.19 or to be shifted to its left, never to its right**. This last condition would imply in fact V_P to be lower than V_{CB}.
- **For those energies for which the efficiency of $^{85}Rb^{1+}$ is a few percent the global capture should be at least 40%**.

By using SIMION, different starting conditions for the Matlab code were created, corresponding to different values of V_P down to 19978 V, that is $E_{inj} = 22$ eV at the plasma boundary. The first real modification to the code regarded the implementation of the conditions for ion losses: by considering the reference frame of figure 6.2 the code checks at each interaction if the particles' coordinates (x, y, z) satisfy the following conditions at the same time

$$\begin{aligned} \sqrt{x^2 + y^2} = r \leq r_{max} &= 0.036\text{m} \\ z \leq z_{max} &= 0.140\text{m} \\ z \geq z_{min} &= -0.148\text{m} \end{aligned} \tag{6.62}$$

where r_{max} is the radius of the plasma chamber, z_{min} the position of the maximum at injection and z_{max} the position of the extraction hole. If not, particles are considered to be lost and removed from the calculation: their positions and velocity components are stored in a matrix in order to analyse the zones of the chamber interested by ion losses and also their energy content. To obtain the final results I basically proceeded through three steps of complexity:

1. Implementation of a **two-zones plasma immersed in the magnetic field** of equations 6.2 - 6.6.
2. Implementation of a two-zones plasma immersed in the magnetic field of equations 6.2 - 6.6 including the **negative potential dip** for ion confinement.

3. Implementation of a two-zones plasma immersed in the magnetic field of equations 6.2 - 6.6 including the negative potential dip for ion confinement and **ionizations**.

The above mentioned three steps will be described in the following subsections.

6.6.1 A simplified plasma model

As a first step we came back to the very first version of the plasma: it consists in an oxygen plasma with an average ion charge $\langle z \rangle = 2.5$ and an ion temperature $KT =$ 1 eV divided in two different zones, one with an electron density $n = n_{ins}$ representing the plasmoid, and another with a density $n = n_{out} = n_{ins}/100$ representing the halo; the ion density is then calculated as $n_{ion} = n/\langle z \rangle$. The total number of simulated particles was still 10000: the only differences were in the starting conditions (now generated with SIMION) and that rubidium and not tin ions were considered this time. Even if the model is not so accurate, the results with this very simplified plasma were expected to give useful information on its ability to slow down charged particles.
As described in section 6.4, after loading the starting conditions the code calculates the magnetic field from the particles' spatial coordinates and collocates them in one of the two zones: this time it is included in the equation of motion 6.51 that becomes

$$\Delta \mathbf{v} = \mathbf{v}(t+1) - \mathbf{v}(t) = -\nu_s \cdot \mathbf{v}(t) \cdot T_{step} + \mathbf{v}^{rand} + \frac{q}{m}(\mathbf{v} \times \mathbf{B}) \cdot T_{step} \tag{6.63}$$

To solve the part of this equation due to the Lorentz force (even with $\mathbf{E} \neq 0$) it is not possible to use the simple approach of the "forward difference" method as it was showed before: it is known in fact that to solve the equation

$$m\frac{d\mathbf{v}}{dt} = q(\mathbf{E} + \mathbf{v} \times \mathbf{B}) \tag{6.64}$$

by simply writing

$$\begin{gathered} \Delta \mathbf{v} = \mathbf{v}(t+1) - \mathbf{v}(t) = \tfrac{q}{m}(\mathbf{E} + \mathbf{v} \times \mathbf{B}) \cdot \Delta t \\ \Delta \mathbf{x} = \mathbf{x}(t+1) - \mathbf{x}(t) = \mathbf{v}(t+1) \cdot \Delta t \end{gathered} \tag{6.65}$$

leads to numerical instabilities and a continuous energy gain by the particle. To overcome this problem, the so called **Boris method** is used [115]: by applying this method equations 6.65 assume the form

$$\begin{gathered} \mathbf{x}_{Boris}(t+1) = \mathbf{x}_{Boris}(t) + \mathbf{v}_{Boris}(t+\tfrac{1}{2}) \cdot T_{step} \\ \mathbf{v}_{Boris}(t+\tfrac{1}{2}) = \mathbf{u}' + q'\mathbf{E}_t \end{gathered} \tag{6.66}$$

In the equations above, positions and velocities are shifted by a half of the time step as in the Leapfrog method; $\mathbf{E}_t$ represent the value of the static electric field at the

time t while the two quantities $\mathbf{u}'$ and q' are given by the expressions:

$$\begin{aligned} \mathbf{u}' &= \mathbf{u} + (\mathbf{u} + (\mathbf{u} \times \mathbf{h})) \times \mathbf{s} \\ \mathbf{u} &= \mathbf{v}_{Boris}(t - \tfrac{1}{2}) + q'\mathbf{E}_t \\ \mathbf{h} &= q'\mathbf{B}_t \\ \mathbf{s} &= 2\mathbf{h}/(1 + h^2) \end{aligned} \tag{6.67}$$

$$q' = \frac{q}{2m} \cdot T_{step} \tag{6.68}$$

being $\mathbf{B}_t$ the magnetic field value at time t. By using the above relations equation 6.63 becomes:

$$\mathbf{v}(t + \tfrac{1}{2}) = (1 - \nu_s T_{step})\,\mathbf{v}(t - \tfrac{1}{2}) + \mathbf{v}^{rand} + \mathbf{v}_{Boris} \tag{6.69}$$

and is solved by the code constructing the new vector $\mathbf{v}_{Boris}$ (equations 6.66 - 6.68) and the other two contributions due to Coulomb collisions as described in section 6.4; the new positions are in turn calculated through the relation:

$$\mathbf{x}(t + 1) = \mathbf{x}(t) + \mathbf{v}(t + \tfrac{1}{2})T_{step} \tag{6.70}$$

The code then checks for particles losses, eventually remove them from calculations and stores their final positions in a matrix. Positions and velocities vectors are finally updated and become the starting conditions for the next iteration.
For the first set of simulations I considered different values of the plasma density starting from $n_{ins} = 2.6 \cdot 10^{+18}$ m$^{-3} \simeq n_{co}$ and going down to $n_{ins} = 0.1 * n_{co}$, where n_{co} is the cut-off density at the operating frequency of the PHOENIX charge breeder (14.521 GHz). Rb^{1+} ions are injected at different values of the plasma potential, from 19998 V to 19978 V at steps of 5 V: considering that the measured charge breeding time of those ions was found to be around 500 μs this value was used as T_{span}; keeping $T_{step} = 1 \cdot 10^{-10}$ s this translated in a total of five millions iterations. The results for those simulations are summarized in table 6.7: it shows, for every injection energy, the percentage of particles losses , distinguishing between injection, radial and extraction; the percentage of captured particles is then deduced. The last column represents the percentage of 1+ ions coming out from the extraction hole: belong to this column those particles that do not fulfil the second condition of equation 6.62 and fulfil $\sqrt{x^2 + y^2} = r \leq r_{ext} = 0.004$ m, where r_{ext} is the extraction hole.
This first set of simulations revealed a high loss rate of the injected ions that seems to be independent from the plasma density and the injection energy: the only variation is on the specific distribution of the losses between injection, radial and extraction. The picture is clearer looking at figure 6.23: particle losses are around 90% down to $n = 0.3 * n_{co}$ and almost independent from the injection energy; at very low densities, where the interaction with the plasma is weaker, the influence of the

Table 6.7: Results of the injection of $^{85}Rb^{1+}$ ions into an oxygen plasma with KT=1 eV for different values of the injection energy and plasma density. Here $n_{co} = 2.6 \cdot 10^{+18}$ m^{-3}.

$\boldsymbol{n = n_{co}}$						
$\mathbf{E}_{inj}$ [eV]	**Losses** [%]				**Captured** [%]	$\boldsymbol{\epsilon}_{1+}$ [%]
	Inj	**Rad**	**Ext**	**Tot**		
2	40.73	41.72	0.09	82.54	17.46	0.01
7	28.78	60.12	0.14	89.04	10.96	0
12	16.88	74.12	0.3	91.30	8.70	0.06
17	8.96	82.44	0.73	92.13	7.87	0.1
22	4.25	86.88	0.35	91.48	8.52	0.35
$\boldsymbol{n = 0.6 * n_{co}}$						
$\mathbf{E}_{inj}$ [eV]	**Losses** [%]				**Captured** [%]	$\boldsymbol{\epsilon}_{1+}$ [%]
	Inj	Rad	Ext	Tot		
2	34.51	47.82	0.49	82.82	17.18	0.13
7	20.93	66.64	0.97	88.54	11.46	0.13
12	10.33	79.02	1.88	91.23	8.77	0.39
17	4.61	82.35	5.42	92.38	7.62	1.15
22	1.96	75.85	14.94	92.75	7.25	3.68
$\boldsymbol{n = 0.3 * n_{co}}$						
$\mathbf{E}_{inj}$ [eV]	**Losses** [%]				**Captured** [%]	$\boldsymbol{\epsilon}_{1+}$ [%]
	Inj	Rad	Ext	Tot		
2	25.6	53.46	2.72	81.78	18.22	0.73
7	13.20	68.05	6.30	87.55	12.45	1.81
12	4.60	72.52	13.58	90.70	9.30	3.94
17	2.20	52.83	37.14	92.17	7.83	13.43
22	0.81	27.79	67.46	96.06	3.94	28.14
$\boldsymbol{n = 0.1 * n_{co}}$						
$\mathbf{E}_{inj}$ [eV]	**Losses** [%]				**Captured** [%]	$\boldsymbol{\epsilon}_{1+}$ [%]
	Inj	Rad	Ext	Tot		
2	14.94	48.00	12.89	75.83	24.17	5.23
7	6.24	43.32	36.75	86.31	13.69	17.34
12	1.73	38.66	56.11	96.50	3.50	28.13
17	0.52	12.06	87.01	99.59	0.41	49.37
22	0.08	3.58	96.34	100	0	61.96

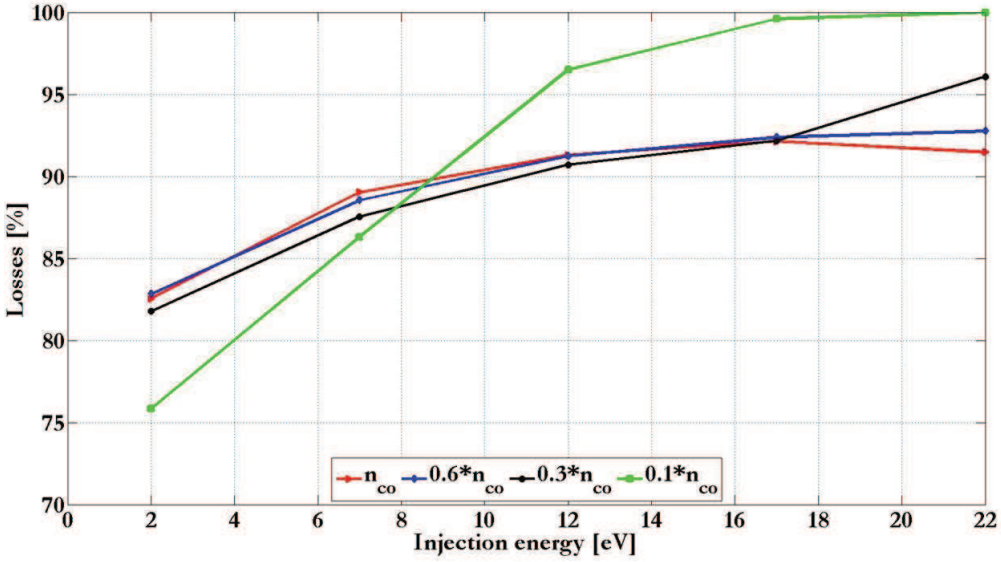

Figure 6.23: Percentage of Rb^{1+} losses as a function of the injection energy for different plasma densities. The total simulation time is 500 μs.

injection energy is clearer even if the percentage of the losses stays comparable. The simulations revealed also that, except for the lowest density, injected ions reach thermal equilibrium.

To evaluate the residence time of the injected particles in thermal equilibrium in a magnetized plasma it is necessary to compare the Coulomb collision frequency ν_{coll} with their Larmor frequency ω_c [67]: in those cases where $\nu_{coll} > \omega_c$ the plasma is said to be in a collisional regime; vice versa the plasma is said to be magnetized. Thermalized ions do not exchange energy with the plasma so the only process to be considered in determining ν_{coll} is the 90° diffusion expressed by τ_D in equation 6.8: to evaluate it in this case it is necessary to substitute $v = \sqrt{3KT/M_{Rb}}$. Considering that the collision frequency depends on the plasma density and that the distribution of the plasma density depends on the magnetic field (like the Larmor frequency), the above quantities can be plotted as a function of the position along the axis, as shown in figure 6.24: it can be seen that for any value of the plasma density and in any point along the axis the condition $\omega_c \geq \nu_{coll}$ holds so the particles are magnetized; the confinement time can be estimated from the relation already seen in chapter 4

$$\tau_{mag} = \frac{Rl}{v_T} \tag{6.71}$$

where R is the mirror ratio, l the length of the plasma and v_T^2 is the one dimensional thermal velocity. The previous relation perfectly explains the results of the simulation: for a given magnetic trap and plasma length, the ion confinement time does not depend on the plasma density, in agreement with what has been found. More, it has been said that particles reach thermal equilibrium (except for the lowest density) so the value of v_T^2 does not change for a given value of KT and injected ion, explaining

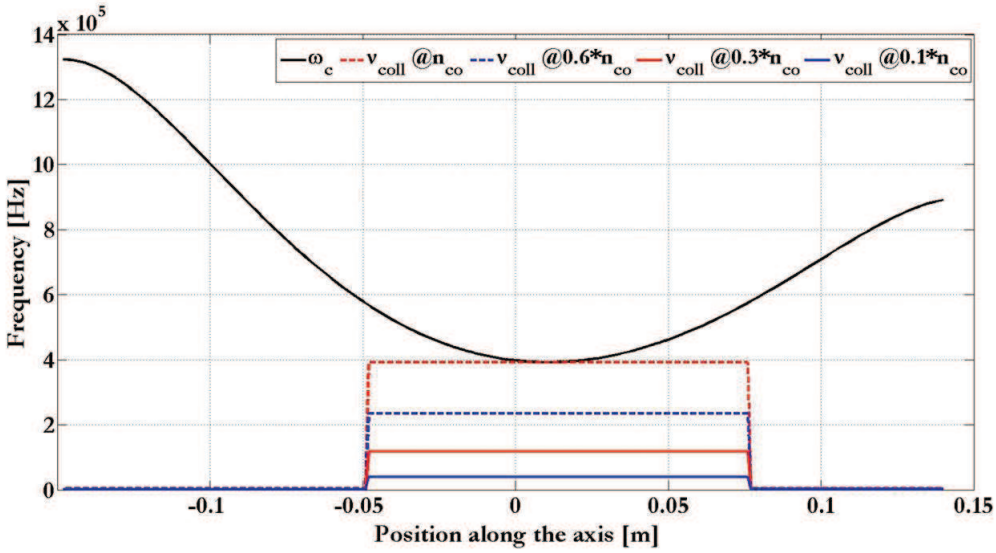

Figure 6.24: Comparison between the Larmor frequency ω_c and the collision frequency ν_{coll} for different plasma densities for KT=1 eV. The quantities are plotted as a function of the position along the axis of the plasma chamber.

the constancy of the losses with respect of the injection energy. Evaluating the confinement time for the PHOENIX charge breeder ($R = 1.5 - 2.3$, $l = 0.288$ m distance between the two maxima) it was found to be between 407 μs and 624 μs: those values well agree with the percentage of simulated particles still present inside the plasma chamber after 500 μs.

After obtaining these very interesting information from the first set of simulations, the influence of the ion temperature was investigated by decreasing KT down to 0.376 eV: a higher influence of the plasma, due to the higher Coulomb collision frequency ν_{coll}, and in general a better confinement, due to the fact that v_T decreases was expected. The results of this second set are summarized in table 6.8, while figure 6.25 shows the comparison between the collision frequencies and the Larmor frequency. As expected, the confinement in general increased: now we observe lower values and different trend for the ion losses, depending on the plasma density and the injection energy; looking at figure 6.25, we see now that by increasing the density the plasma passes from a state where it is magnetized (up to $n = 0.3 * n_{co}$) to a collisional regime (for the highest densities). In this last case the plasma behaves like a viscous medium: its ability to trap particles is due to the "zig-zag" path it imposes to them as a consequence of the frequent collisions; charged particles practically do not feel the influence of the magnetic field. A handy formula to evaluate the confinement time of an ion of charge q in a plasma in the collisional case is given by the following equation (see chapter 4):

$$\tau_q \simeq 7.1 \cdot 10^{-20} \left(\frac{l}{2}\right)^2 \ln\Lambda \frac{q^2}{KT^{5/2}} n\sqrt{A}\langle z\rangle \tag{6.72}$$

Table 6.8: Results of the injection of $^{85}Rb^{1+}$ ions into an oxygen plasma with KT=0.376 eV for different values of the injection energy and plasma density.

$\boldsymbol{n = n_{co}}$						
$\mathbf{E}_{inj}$ [eV]	**Losses** [%]				**Captured** [%]	ϵ_{1+} [%]
	Inj	**Rad**	**Ext**	**Tot**		
2	444.9	8.50	0.00	53.40	46.60	0.0
7	30.60	21.30	0.00	51.90	48.10	0.00
12	13.80	35.00	0.00	48.80	51.20	0.00
17	3.39	42.37	0.00	45.76	54.24	0.00
22	0.50	45.00	0.00	45.50	54.50	0.00
27	0.00	49.50	0.00	49.50	50.50	0.00
$\boldsymbol{n = 0.6 * n_{co}}$						
$\mathbf{E}_{inj}$ [eV]	**Losses** [%]				**Captured** [%]	ϵ_{1+} [%]
	Inj	Rad	Ext	Tot		
2	45.60	14.10	0.00	59.70	40.3	0.00
7	29.10	31.70	0.00	60.80	39.20	0.00
12	7.40	50.60	0.00	58.00	42.00	0.00
17	2.00	57.80	0.00	59.80	40.20	0.00
22	0.00	59.60	0.00	59.60	40.40	0.00
27	0.00	61.30	6.00	67.30	32.70	0.00
$\boldsymbol{n = 0.3 * n_{co}}$						
$\mathbf{E}_{inj}$ [eV]	**Losses** [%]				**Captured** [%]	ϵ_{1+} [%]
	Inj	Rad	Ext	Tot		
2	36.88	24.08	0.00	60.90	39.04	0.00
7	16.16	46.12	0.00	62.28	37.72	0.00
12	2.75	63.96	0.11	66.82	33.18	0.02
17	0.18	63.12	4.01	67.31	32.69	0.99
22	0.00	36.66	43.11	79.77	20.23	16.55
27	0.00	21.38	76.53	97.91	2.09	30.91
$\boldsymbol{n = 0.1 * n_{co}}$						
$\mathbf{E}_{inj}$ [eV]	**Losses** [%]				**Captured** [%]	ϵ_{1+} [%]
	Inj	Rad	Ext	Tot		
2	24.33	33.26	0.38	57.97	42.03	0.09
7	5.09	53.33	4.03	62.45	37.55	1.14
12	0.17	45.41636.51	82.09	17.91	16.60	
17	0.14	13.04	85.35	98.53	1.47	49.22
22	0.06	3.80	96.14	100.00	0.00	60.22
27	0.01	12.09	87.9	100.00	0.00	49.71

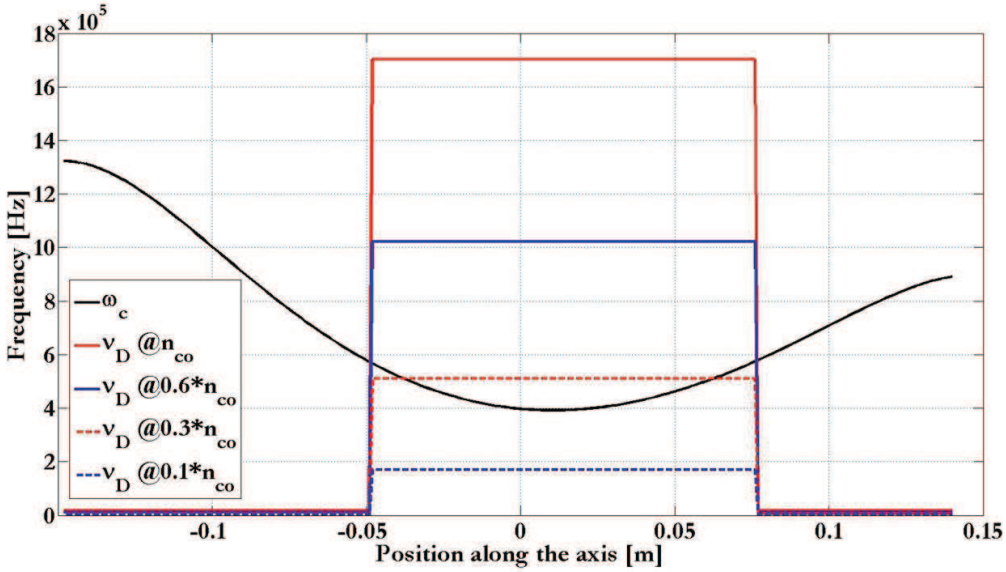

Figure 6.25: Comparison between the Larmor frequency ω_c and the collision frequency ν_{coll} for different plasma densities for KT=0.376 eV. The quantities are plotted as a function of the position along the axis of the plasma chamber.

where l is the hot plasma length in cm, $\ln\Lambda \sim 15$, A is the plasma mass number, $\langle z \rangle$ is its average charge, n the density in cm^{-3} and KT is in eV. Considering as plasma length the distance between the two resonances on axis ($l = 0.125$ m), the above formula gives very high confinement times for the simulated plasma, in the order of tens of ms. Usually this formula is applied to determine the confinement time of high charge states in ECR plasmas at the steady state: in the case of Rubidium normally the charge state distribution does not show peaks of 1+ ions (because it is shifted towards higher charges) so it is difficult to apply equation 6.72 in this particular case. What can be expected is that after 500 μs a consistent number of particles are still inside the plasma chamber and this is what happens for the highest simulated densities. To analyse the interaction of the injected particles with a collisional plasma it is interesting to plot the percentage of captured particles for the two highest density and compare them with the previous case, as shown in figure 6.26. The number of confined particles is now much higher and closer to the experimental results about the total capture of ions inside the PHOENIX charge breeder; for those last cases, to find the point where the capture starts to decrease (so as to have a more complete picture) a further injection energy has been simulated (27 eV). For both densities, but more pronounced for the highest one, a kind of optimum injection energy appears in agreement with what is experimentally observed in the ΔV curves. Going down to the magnetized state at the lowest densities the trend of captured particles changes as shown in figure 6.27: in the same picture the values obtained for $KT = 1$ are also shown for comparison. At $n = 0.3 * n_{co}$ the percentage of captured ions varies very slightly by varying the injection energy (as in all the

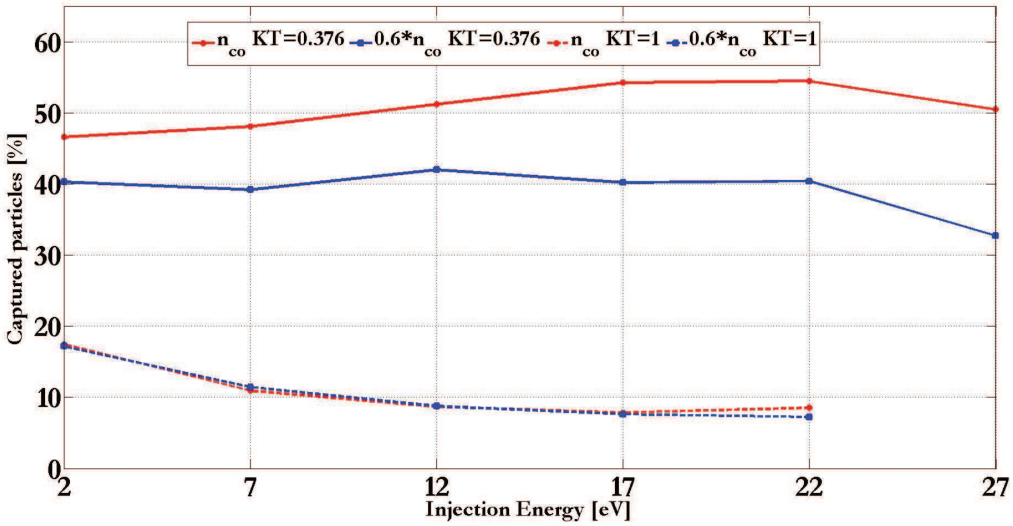

Figure 6.26: Percentage of captured particles as a function of the injection energy for KT=0.376 eV and the two highest densities. The values obtained for KT=1 are also shown as reference.

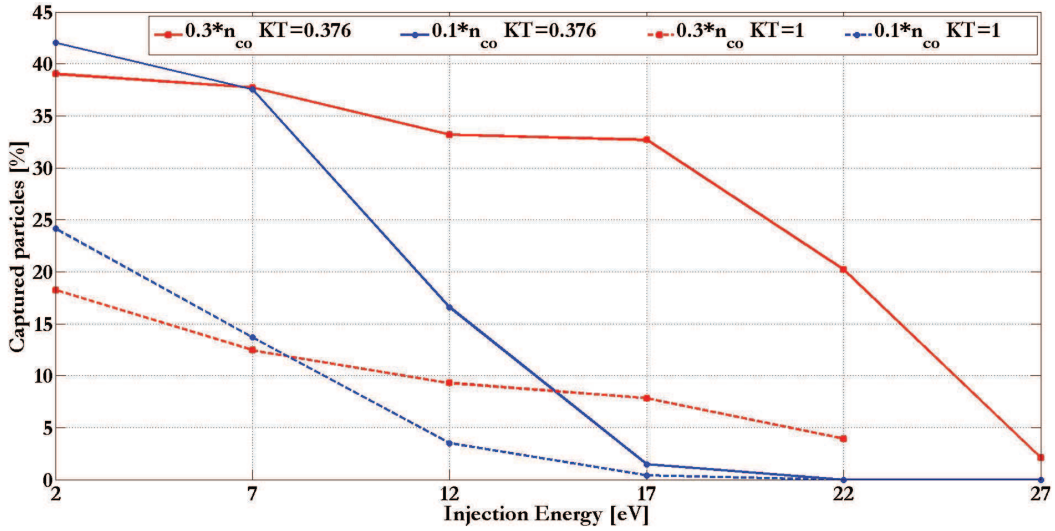

Figure 6.27: Percentage of captured particles as a function of the injection energy for KT=0.376 eV and the two lowest densities. The values obtained for KT=1 are also shown as reference.

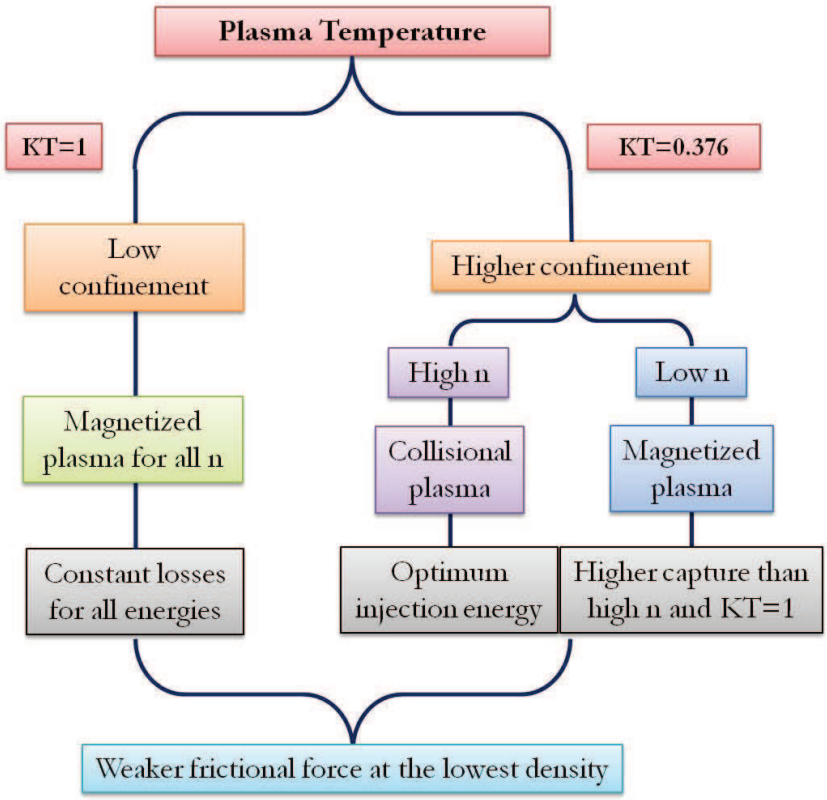

Figure 6.28: Schematic summary of the outcomes of the simulations

previous cases at higher temperature), except for very high values. Here again, at the lowest density the interaction with the plasma is so weak that the capture process is controlled by the injection energy. The magnetic confinement time evaluated for this low temperature case ranges from 0.664 to 1.000 ms, justifying the values of the total capture observed in figure 6.27 and the differences with respect to the previous case. The results obtained from the previous first two sets of simulations are schematically summarized in figure 6.28: in the high temperature regime the confinement is very poor and the losses are almost independent from n and the injection energy; in the low temperature regime the confinement is in general better: the plasma changes to a collisional regime by increasing the density with a clear effect on the confinement of particles.

From the point of view of the comparison with the experimental results of figure 6.19, a common aspect for both plasma temperatures comes out from table 6.7 and table 6.8: in order to extract 1+ ions, the plasma density has to be low, the 1+ current being in fact absent until the density decreases to $n = 0.3 * n_{co}$. Figures 6.29 and 6.30 compares the measured $^{85}Rb^{1+}$ efficiencies with the results of the simulations for the lowest densities: depending on the density and the temperature, the calculated data have similar trend with respect to the experimental ones at both microwave powers. Anyway, for all the cases the total capture at the ΔV (injection energy) corresponding to the maximum efficiency of Rubidium high charge states is quite

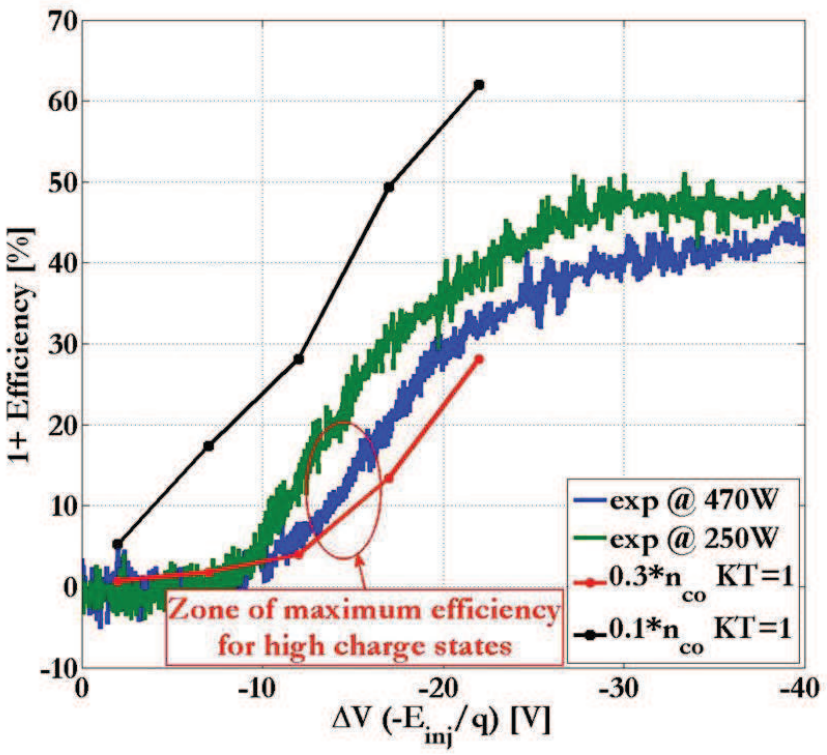

Figure 6.29: Comparison between the simulated Rb^{1+} efficiency at the lowest densities and the experiments for KT=1 eV.

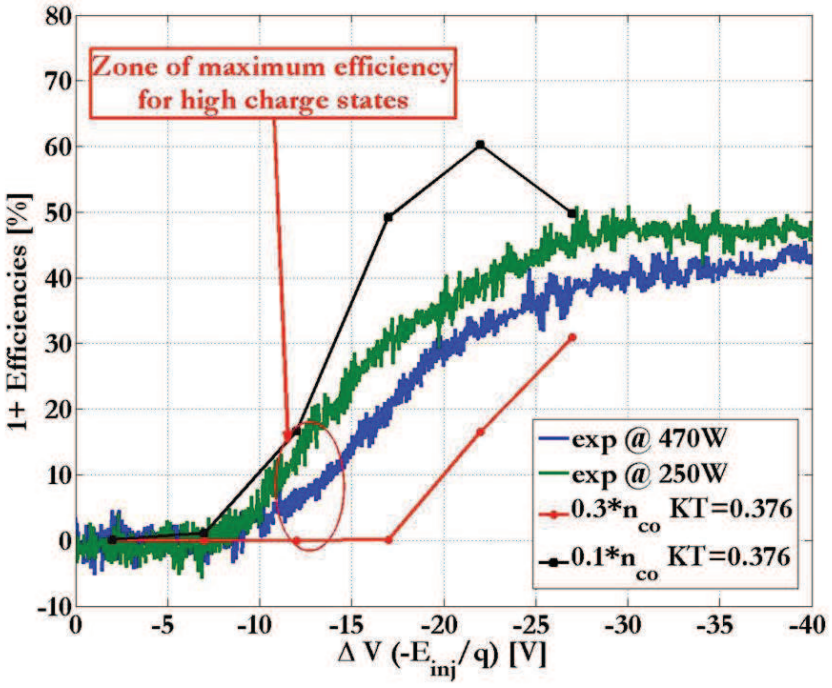

Figure 6.30: Comparison between the simulated Rb^{1+} efficiency at the lowest densities and the experiments for KT=0.376 eV.

lower than the measured one. To conclude this subsection it can be said that this very simplified model revealed the importance of ion temperature in the capture process: if the temperature is high, particles' motion is controlled by the magnetic field and the confinement times are not consistent with the formation of high charge states trough step by step ionizations. By lowering the temperature, the overall confinement improves: for the higher densities the plasma changes to a collisional regime and the total capture reaches values comparable with the experimental ones, even if no Rb^{1+} ions are extracted at the end of the simulation. On the other hand, at lower densities Rb^{1+} efficiency curves can be found, whose shape is very similar to the experimental ones, but the number of confined particles is too low. This apparent contradiction was an indication that the model of the simulated plasma should have to be improved, as will be described in the following subsections.

6.6.2 The implementation of the potential dip

As described in chapter 4, the confinement of highly charged ions is improved by the presence of a negative potential dip in the plasma core. Its origin is still controversial: during the years the effect was attributed to the collisionless hot electrons component that is adiabatically confined by the magnetic field and forms a negative charge cloud. In a magnetized regime, the confinement time of an ion of charge q due to such potential dip $\Delta\phi$ can be obtained by multiplying equation 6.71 for an exponential factor, that is [66]:

$$\tau_{\mathrm{Rb}}^{q} \simeq \frac{Rl}{v_T} \exp\left(\frac{|qe\Delta\phi|}{KT}\right) \tag{6.73}$$

For the collisional case equation 6.72 still holds. Interesting numerical studies recently carried out at LNS on the plasma of the ECR source SERSE put in crisis the accepted origin of the potential dip [67]. They showed in fact that it is due to the formation of a so called "double layer" at the edge of the plasma core (that is around $B = B_{ecr}$), consisting in a negative charges excess on the inner part and a positive charge excess in the outer part: this effect is showed in figure 6.31; the depth of the potential dip can be heuristically estimated to be $\Delta\phi \sim -0.5KT/e$. Following this interpretation, the ion confinement time in the collisional case become:

$$\tau = \tau_{coll} * \exp\left(\frac{|qe\Delta\phi|}{KT}\right) + \tau_{mag} \tag{6.74}$$

In order to implement the real potential map in the code it would have been necessary to calculate the electron and the ion dynamics in the electromagnetic field of the charge breeder. Unfortunately there was no time enough to perform all such huge calculations within the duration of the PhD: discussing with the colleagues of LNS we found a solution by using a scaled potential map obtained from their calculations. The spatial potential map already obtained for the ECR ion source SERSE was stored as a function of the ratio B/B_{ecr} and applied to the magnetic configuration of the PHOENIX charge breeder.

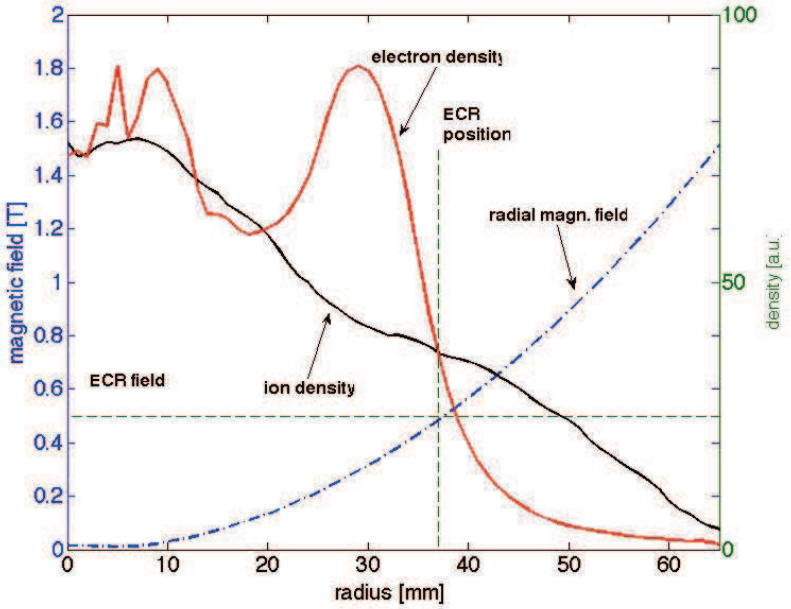

Figure 6.31: Charged particles excesses leading to the formation of a double layer responsible for the negative potential dip coming out from LNS calculations.

Figure 6.32 and 6.33 show two plots of the map obtained for $KT = 1$ eV: the first is the transversal section in the middle of the charge breeder while the second is a section on the plane $y = 0$. To obtain a 3D map the potential values were calculated and stored on a matrix: it represents the spatial 3D mesh of the domain of the simulation, whose points are spaced of 1 mm. From the matrix of the potential map Matlab generates the ones corresponding to the three components (E_x, E_y, E_z) of the related electric field $\mathbf{E}$ that will be used to solve the equation of motion. As an example, figure 6.34 shows the modulus of the electric field generated by the above potential in the plane $y = 0$.

Going now to the first refinement of the model, the only difference with respect to the previous subsection is the implementation of the electric filed related to the potential map and the use of 1000 particles to speed up the calculations. This time the code uses the particles spatial coordinates in two ways: the usual, to collocate the particles in one of the two zones of the plasma by means of the magnetic field; a new one, to associate to the particles' components (x, y, z) an element of each matrix representing the components of the electric field. This is done by rounding the vectors (x, y, z) to the nearest integer and associating to the tern of indexes obtained the corresponding position in the matrices of the electric field. The three values obtained are used to solve the equations 6.66 - 6.67 and then the complete equation 6.69 in the already described way.

In order to have a precise comparison with the results obtained with the previous model, the same set of simulations was repeated: the new results are showed in

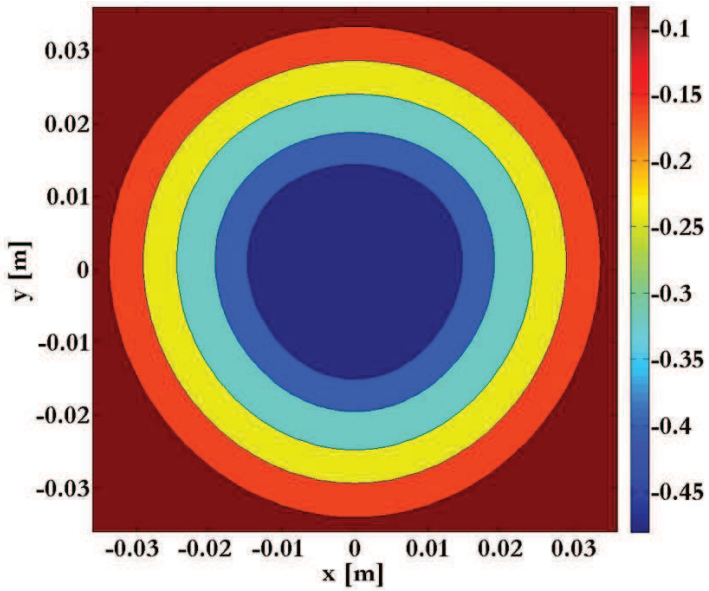

Figure 6.32: Plot of the scaled potential [V] for the SPES charge breeder obtained for KT=1 eV on the plane $z = 0$.

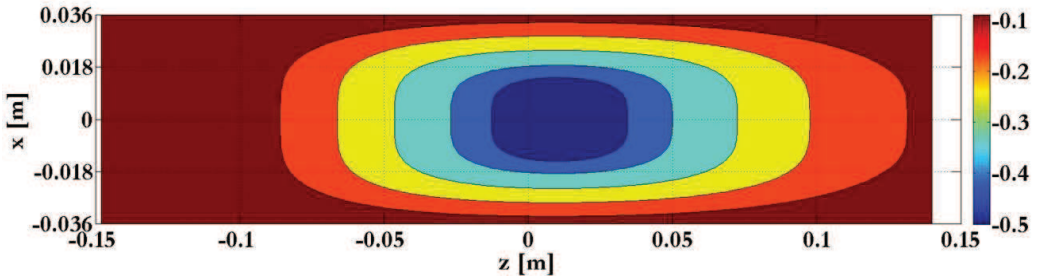

Figure 6.33: The scaled potential dip [V] for the SPES charge breeder obtained for KT=1 eV on the plane $y = 0$.

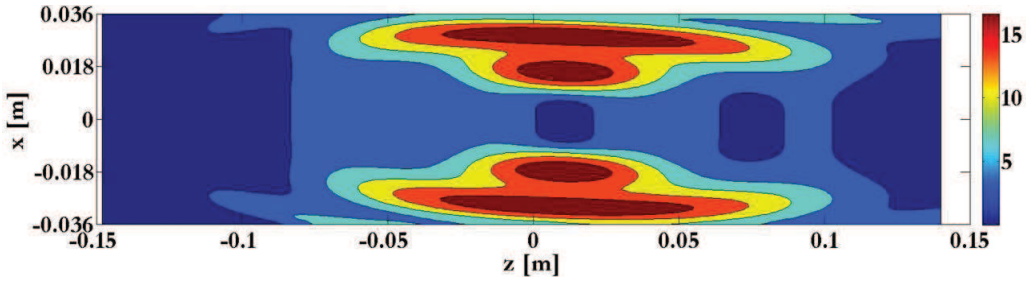

Figure 6.34: The modulus of the electric field [V/m] related to the above potential in the plane $y = 0$.

tables 6.9 and 6.10. As it can be seen, no real differences were found on the total capture after this refinement: except for a couples of data point difficult to be explained, the numbers of captured particles are in fact almost the same as the previous simulations. To find an explanation it is necessary to analyse the effect of the potential dip: it in fact acts on the particles motion like a barrier that prevents them from leaving the plasma. Of course the effectiveness of the barrier depends on the particle energy: considering a 3D Maxwell-Boltzmann distribution with a temperature KT ($\langle E_{tot} \rangle = 3KT/2$) and a potential dip in the order of $KT/2$ it can be calculated that the 80% of the particles have enough energy to overcome the barrier (no matter the temperature) and leave the plasma. The barrier is more effective for higher charge states: the percentage of particles leaving the plasma decreases to 57% for $q = 2$, to 39% for $q = 3$ and so on. In the next subsection ionization will be taken into account, so the effect of the potential dip will be clearer.

6.6.3 The complete model: implementation of ionizations

The final step of modelling the charge breeder's plasma consisted in implementing the ionization process: the formula used to calculate the ionization times is equation 6.11, with the Rubidium's data and the coefficients necessary to evaluate the equation kindly provided by Dr. Marco Cavenago from LNL [116]. The only imposed parameters are the temperature KT_e and density n_{ioniz} of the hot electron component: in this model those variables have the same spatial distribution as the total density. The plasmoid is characterized by a temperature $KT_e = KT_e^{core} = 1$ keV, a total density n_{ins} and a hot density $n_{ioniz} = n_{ins}/10 = n_{core}$; the halo by a temperature $KT_e = KT_e^{halo} = KT_e^{core}/10 = 100$ eV, a total density n_{out} and a hot density $n_{ioniz} = n_{out}/10 = n_{halo}$. Temperatures' values are average estimates for ECR sources [117] while the ratio between the total and hot electron densities was estimated experimentally at GSI [118]. A schematic description of the simulated plasma is given in figure 6.35: thanks to the simplified distribution of the above parameters, it was possible to implement the ionization as tabulated probabilities for all the possible charge states. A Matlab script was written, that uses the two couples of variables (n_{core}, KT_e^{core}) and (n_{halo}, KT_e^{halo}) to calculate, through equation 6.11, all the stepwise ionization times $\tau_{ioniz}^{q,q+1}$ from 1+ to 37+ for Rubidium. What is obtained are two tables for all the $\tau_{ioniz}^{q,q+1}$, one for the core and one for the halo: table 6.11 shows the calculated values for ionization up to 6+ considering $n = n_{co}$. The data in the two column differ roughly of two order of magnitude, exactly the ratio of the densities: this means that from the point of view of ionization of the first charge states the hot electrons temperature has the same influence inside and outside the plasma. The ionization times are then translated in ionization probability through the already seen relation

$$P_{ioniz} = 1 - \exp \frac{T_{step}}{\tau_{ioniz}^{q,q+1}} \tag{6.75}$$

Table 6.9: Results of the injection of $^{85}Rb^{1+}$ ions into an oxygen plasma with KT=1 eV for different values of the injection energy and plasma density by implementing the potential dip.

$\boldsymbol{n = n_{co}}$						
$\mathbf{E}_{inj}$ [eV]	**Losses** [%]				**Captured** [%]	ϵ_{1+} [%]
	Inj	**Rad**	**Ext**	**Tot**		
2	35.40	51.00	0.10	86.50	13.50	0.00
7	25.2	62.9	0.1	88.2	11.8	0.00
12	12.96	76.82	0.00	89.75	10.25	0.00
17	8.37	82.75	0.60	91.72	8.28	0.10
22	3.50	86.70	0.50	90.70	9.30	0.50
$\boldsymbol{n = 0.6 * n_{co}}$						
$\mathbf{E}_{inj}$ [eV]	**Losses** [%]				**Captured** [%]	ϵ_{1+} [%]
	Inj	Rad	Ext	Tot		
2	27.50	56.00	0.60	84.10	15.90	0.20
7	16.60	71.70	1.30	89.60	10.40	0.20
12	8.00	84.50	1.20	93.70	6.30	0.00
17	3.79	84.05	3.34	91.18	8.82	0.80
22	0.90	76.57	14.56	92.03	7.97	3.79
$\boldsymbol{n = 0.3 * n_{co}}$						
$\mathbf{E}_{inj}$ [eV]	**Losses** [%]				**Captured** [%]	ϵ_{1+} [%]
	Inj	Rad	Ext	Tot		
2	23.00	57.99	2.496	83.48	16.52	0.64
7	10.68	70.74	5.62	87.04	12.96	1.39
12	3.29	75.47	11.36	90.12	9.88	4.29
17	1.49	60.72	30.91	93.12	6.88	10.87
22	0.50	30.41	64.61	95.52	4.48	26.02
$\boldsymbol{n = 0.1 * n_{co}}$						
$\mathbf{E}_{inj}$ [eV]	**Losses** [%]				**Captured** [%]	ϵ_{1+} [%]
	Inj	Rad	Ext	Tot		
2	11.36	56.33	12.36	80.05	19.95	4.06
7	5.68	45.46	35.39	86.53	13.47	17.55
12	1.39	40.58	54.83	96.80	3.20	25.52
17	0.20	27.20	72.50	99.90	0.10	39.70
22	0.00	3.60	84.40	88.00	12.00	60.70

Table 6.10: Results of the injection of $^{85}Rb^{1+}$ ions into an oxygen plasma with KT=0.376 eV for different values of the injection energy and plasma density by implementing the potential dip.

$\boldsymbol{n = n_{co}}$						
$\mathbf{E}_{inj}$ [eV]	**Losses** [%]				**Captured** [%]	$\boldsymbol{\epsilon}_{1+}$ [%]
	Inj	**Rad**	**Ext**	**Tot**		
2	39.50	10.20	0.00	49.70	50.30	0.00
7	27.70	21.50	0.00	49.20	50.80	0.00
12	12.80	38.20	0.00	51.00	49.00	0.00
17	2.89	43.57	0.00	46.46	53.54	0.00
22	0.50	47.36	0.00	47.86	52.14	0.00
$\boldsymbol{n = 0.6 * n_{co}}$						
$\mathbf{E}_{inj}$ [eV]	**Losses** [%]				**Captured** [%]	$\boldsymbol{\epsilon}_{1+}$ [%]
	Inj	Rad	Ext	Tot		
2	39.00	13.20	0.00	52.20	47.80	0.00
7	22.93	33.20	0.00	56.13	43.87	0.00
12	5.48	52.54	000	58.02	41.98	0.00
17	1.30	58.22	0.00	59.52	40.48	0.00
22	0.10	59.22	0.30	59.62	40.38	0.00
$\boldsymbol{n = 0.3 * n_{co}}$						
$\mathbf{E}_{inj}$ [eV]	**Losses** [%]				**Captured** [%]	$\boldsymbol{\epsilon}_{1+}$ [%]
	Inj	Rad	Ext	Tot		
2	37.09	23.83	0.00	60.92	39.08	0.00
7	15.35	47.66	0.00	63.01	36.99	0.00
12	2.49	62.51	0.00	65.00	35.00	0.00
17	0.20	67.60	3.89	71.69	28.31	1.10
22	0.00	40.68	39.18	79.86	20.14	15.15
$\boldsymbol{n = 0.1 * n_{co}}$						
$\mathbf{E}_{inj}$ [eV]	**Losses** [%]				**Captured** [%]	$\boldsymbol{\epsilon}_{1+}$ [%]
	Inj	Rad	Ext	Tot		
2	24.43	32.10	0.30	56.83	43.17	0.10
7	5.08	52.64	3.99	61.71	38.29	1.30
12	0.10	46.06	33.00	79.16	20.84	15.95
17	0.00	27.92	71.09	99.01	0.99	37.39
22	0.00	4.70	95.10	99.80	0.20	60.00

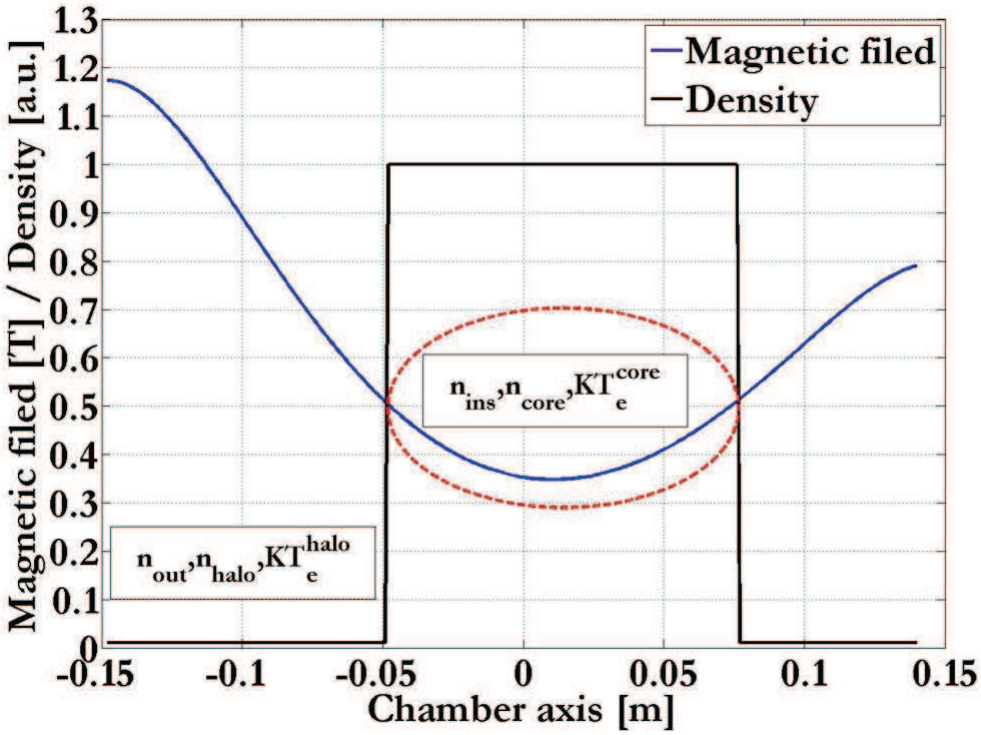

Figure 6.35: Stepwise density distribution along the z axis: higher values of density and temperature are supposed for the plasma core ($B \leq B_{ECR}$) with respect to the halo. The plot of magnetic field is also shown.

Table 6.11: Calculated Ionization times for Rubidium charge states from 1+ to 6+. Values are given inside and outside the plasma.

Ionization	τ_{ins} [s]	τ_{out} [s]
$0 \rightarrow 1$	$2.14{\cdot}10^{-5}$	$1.61{\cdot}10^{-3}$
$1 \rightarrow 2$	$6.24{\cdot}10^{-5}$	$7.92{\cdot}10^{-3}$
$2 \rightarrow 3$	$1.17{\cdot}10^{-4}$	$2.17{\cdot}10^{-2}$
$3 \rightarrow 4$	$1.20{\cdot}10^{-4}$	$2.6{\cdot}10^{-2}$
$4 \rightarrow 5$	$1.74{\cdot}10^{-4}$	$5.10{\cdot}10^{-2}$
$5 \rightarrow 6$	$2.45{\cdot}10^{-4}$	$9.83{\cdot}10^{-2}$

and stored in two tables. The way those tables are used in the main code will be described shortly.

For the sake of clearness, it is useful to summarize all the steps the complete code follows, showing its flow diagram in figure 6.36: at the beginning the code loads the problem's constants and positions and velocities from the output of SIMION. Then it checks if the total integration time is a multiple of 5 μs and eventually stores the entire workspace on a file. For the integration step T_{step} and time T_{span} the previous values were used, that is 10^{-10} s and $5{\cdot}10^{-4}$ s respectively. Particles are localized inside the chamber by calculating the magnetic field corresponding to their positions: in this way one of the two terns of values $(n_{ins}, n_{core}, KT_e^{core})$ or $(n_{out}, n_{halo}, KT_e^{halo})$ is associated to each of them. The code then starts building all the necessary terms to solve the Langevin equation: it applies the Boris method taking into account the electric field generated by the potential map; after that calculates the friction and diffusion coefficients and then generates the vector $\mathbf{v}^{rand}$; finally it solves the Langevin equation 6.42 and in turn updates all the position vectors. All the particles are verified to be inside the plasma chamber, otherwise are removed from the calculation. At this point the ionization process is implemented by a Monte Carlo technique: depending on its position and its charge q, to each simulated charged particles is associated the probability $P(q \rightarrow q+1)$ for the ionization $q \rightarrow q+1$ to occur. Such probabilities are compared with randomly extracted numbers n_{rand}: for those particles for which $n_{rand} < P(q \rightarrow q+1)$ the charge q is increased of one unity keeping unchanged position and velocity. Finally the next iteration starts.

With this final model I simulated first the highest density with $KT = 1$ in order to verify the combined effect of the ionizations and the potential dip: the percentages of captured particles are now higher compared to the previous case, as figure 6.37 shows. By implementing the ionization process the multiply charged ions produced have less chances to overcome the potential dip, especially when $q \geq 3$ as estimated at the end of the previous subsection. By increasing the injection energy, the difference with the previous results is more evident but is anyway limited, meaning that particles are lost faster than being ionized. As an example, the charge state distribution obtained at the end of simulation with $E_{inj} = 2$ eV is shown in figure 6.38 (26% of the total particles): the maximum charge observed is 4+ with a peak on 2+, in agreement with the ionization times that give a minimum of 320 μs to create a 4+ ion through step wise ionizations. Unfortunately no 1+ ions are extracted, meaning that the simulated plasma parameters do not reflect the experimental conditions leading to figure 6.19.

As put in evidence by the previous results, in order to obtain Rb^{1+} ions coming out from the extraction hole and a reasonable total capture, both the plasma density and temperature have to be low. It was decided then to focus the attention on the comparison with experimental results: in particular, the variation of the plasma parameters was done in order to reproduce the curve of figure 6.19 corresponding to the highest power. This because in those conditions not only the information about the Rb^{1+} efficiency is available but also the one about the total capture. It

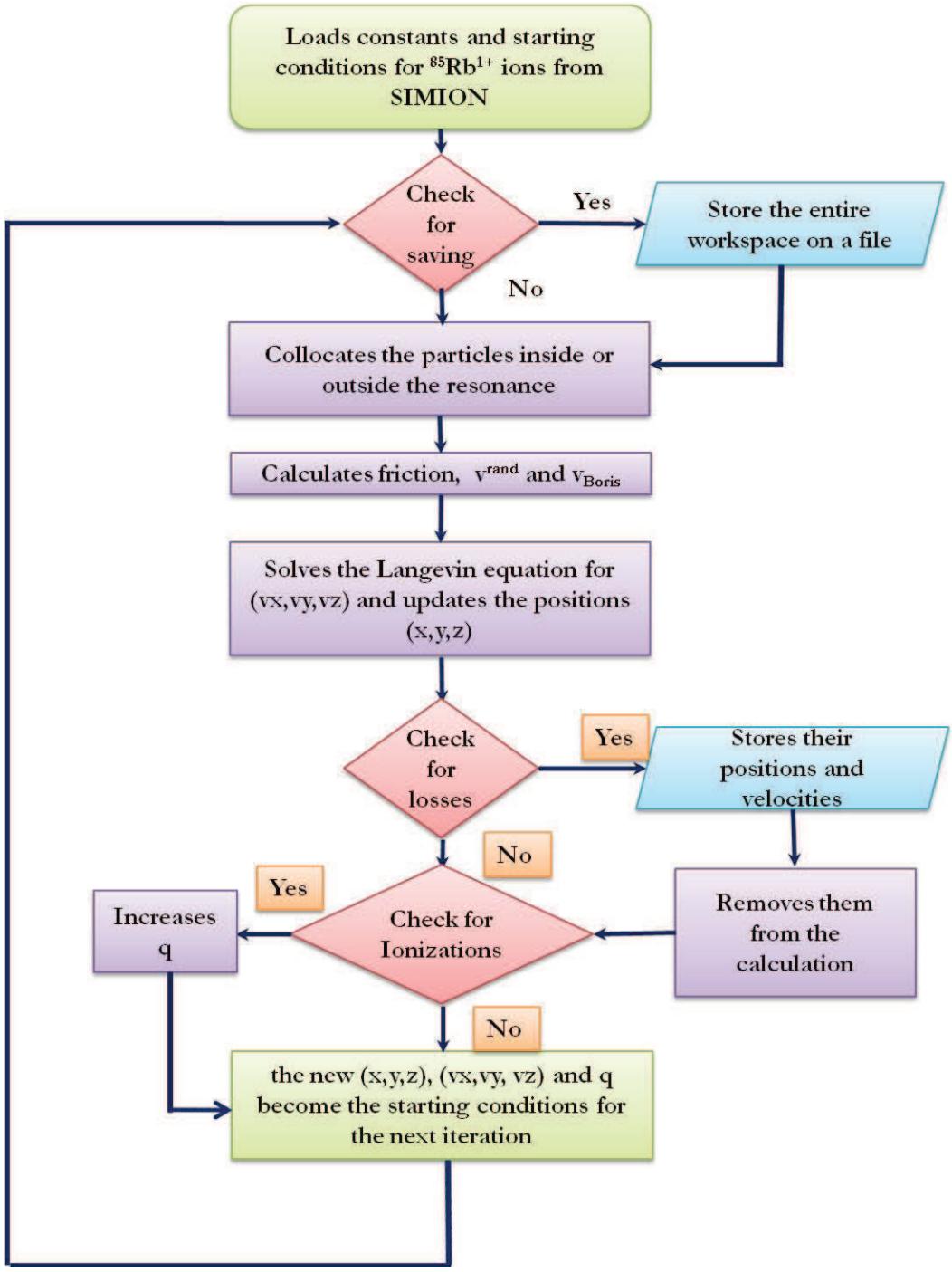

Figure 6.36: Flow diagram of the complete code.

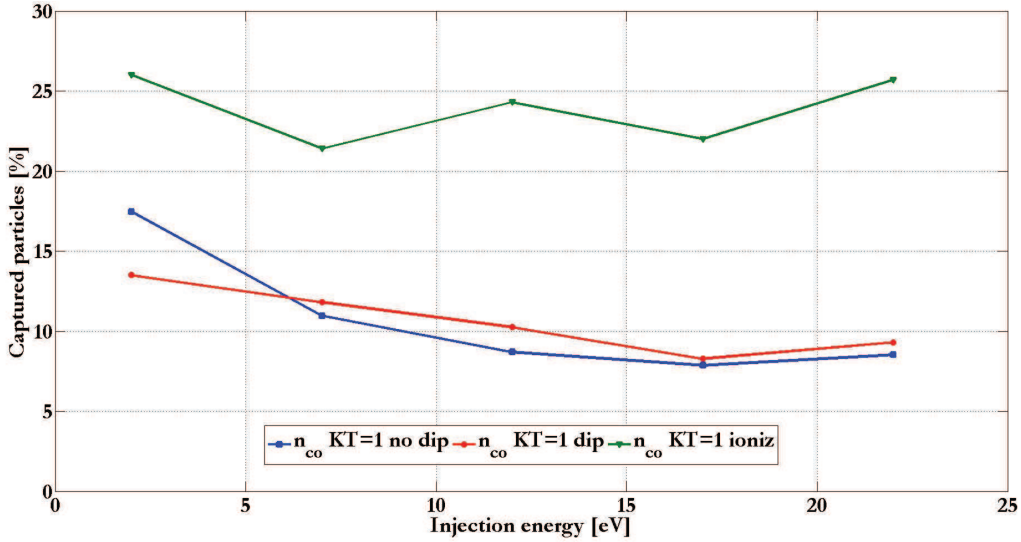

Figure 6.37: Comparison of the calculated percentages of captured particles as a function of the injection energy for KT=1 eV and $n = n_{co}$ by employing the three plasma models.

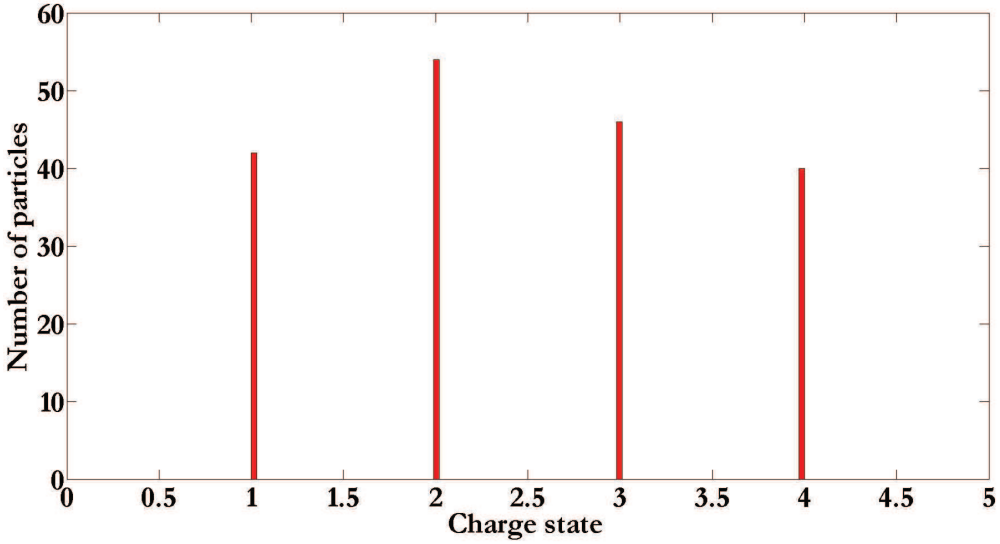

Figure 6.38: Rubidium charge states distribution obtained at the end of the simulation for $E_{inj} =$ 2 eV, $n = n_{co}$ and KT=1 eV.

Table 6.12: Results of the injection of $^{85}Rb^{1+}$ ions into an oxygen plasma with KT=0.376 eV and $n = 0.3 * n_{co}$ for different injection energies.

$\mathbf{E}_{inj}$ [eV]	**Losses** [%]				**Captured** [%]	ϵ_{1+} [%]
	Rad	Inj	Ext	Tot		
2	31.34	33.53	0.00	64.87	35.13	0.00
7	49.50	13.47	0.00	62.97	37.03	0.00
12	64.10	2.50	0.30	66.90	33.10	0.10
17	63.67	0.50	7.00	71.17	28.83	0.72
22	38.72	0.00	42.41	81.13	18.87	11.04

has to be reminded that the experimental curves are plotted as a function of the difference $(V_{CB} - V_{1+})$ between the 1+ source extraction voltage V_{1+} that is fixed (1+ beam energy) and the variable charge breeder extraction voltage V_{CB}. The simulated curves are instead basically function of the difference $(V_P - V_{1+})$, where the plasma potential V_P is usually higher than V_{CB}. Considering this, in comparing experimental and simulated curves the latter were allowed to be shifted towards lower (negative) ΔV values in order to find the best agreement with the former: this could be a measure of the plasma potential with respect to the charge breeder but the verification of this parameter is not the aim of this code. The experimental curves have been recorded on the LPSC test bench having an estimated beam line transmission of 80%: for this reason a factor 0.8 was taken into account in evaluating the simulated efficiencies. For the sake of clearness, the criteria used in judging a simulation are here repeated: the obtained Rb^{1+} efficiency has to be in the order of some percent for the injection energy (plasma potential) corresponding to the peak of high charge states efficiencies (ΔV around -12 V); at the same energy, the total particles capture should be at least 40%.

On the basis of what showed in tables 6.7 ÷ 6.10, we proceeded simulating a plasma with $n_{ins} = 0.3 * n_{co}$ and $KT =$ 0.376 eV, while for n_{ioniz} and KT_e the considerations made above hold. The results are showed in table 6.12: it can be seen that both the total capture and the Rb^{1+} efficiency are too low in comparison with experimental results. The plasma density was then lowered to $n_{ins} = 0.1 * n_{co}$, in order to try to have more extracted 1+ ions, and intermediate values of the injection energy (5 and 10 eV) were added, in order to have a more precise curve in the low energy region. The results are showed in table 6.13: it is interesting to note that now the simulated Rb^{1+} efficiencies start to agree with the experimental curves as figure 6.39 shows; the two trends in fact coincide considering a shifting of the simulated values of -2.5 V but the evaluated total efficiency is still too low compared to experiment. To let the approach be closer to reality I modified in sequence two input parameters: first, I precisely calculated the average charge of the plasma using an oxygen spectrum

Table 6.13: Results of the injection of $^{85}Rb^{1+}$ ions into an oxygen plasma with KT=0.376 eV and $n = 0.1 * n_{co}$ for different injection energies.

$\mathbf{E}_{inj}$ [eV]	**Losses** [%]				**Captured** [%]	ϵ_{1+} [%]
	Rad	Inj	Ext	Tot		
2	32.03	22.95	0.40	55.38	44.62	0.16
5	47.40	10.88	0.90	59.18	40.82	0.16
7	53.19	3.79	3.00	60.07	39.93	0.64
10	52.09	0.60	17.00	69.56	30.44	5.44
12	48.20	0.60	32.50	81.30	18.70	11.68
17	27.94	0.10	68.76	96.80	3.20	27.76
22	5.40	0.00	94.20	99.60	0.40	44.72

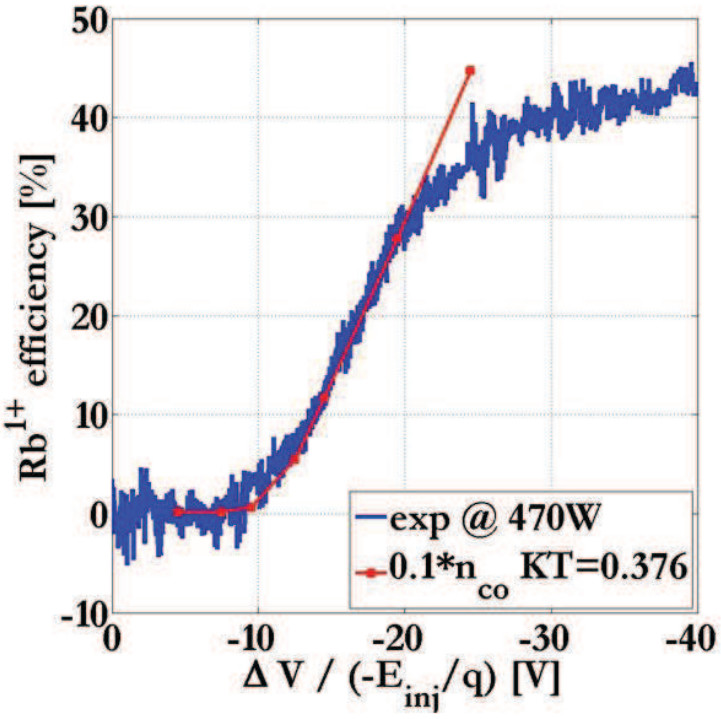

Figure 6.39: Comparison between experimental and simulated efficiency for the complete model using $n = 0.1 * n_{co}$ and $KT = 0.376$ eV. The beam line transmission is taken into account.

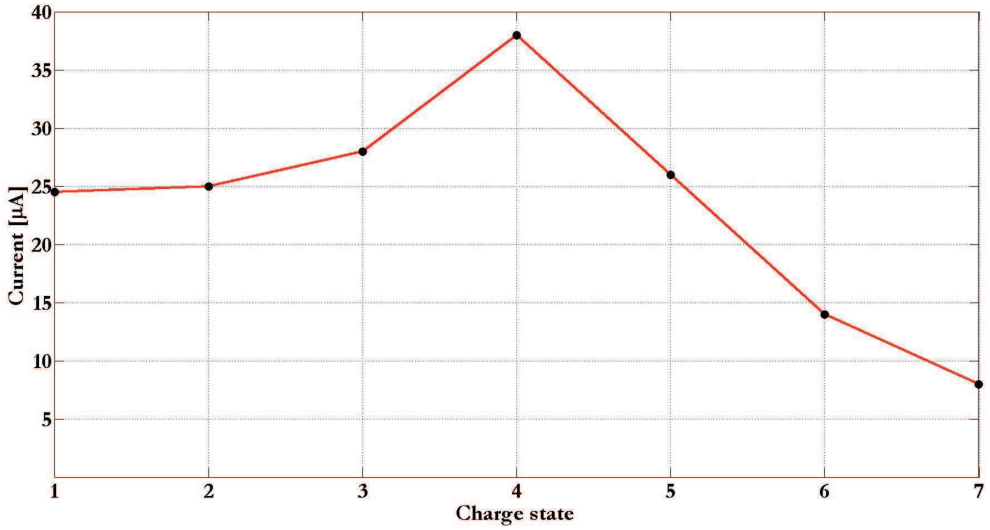

Figure 6.40: Oxygen charge state distribution obtained on the LPSC's test bench.

Table 6.14: Results of the injection of $^{85}Rb^{1+}$ ions into an oxygen plasma with KT=0.376 eV, $\langle z \rangle$=3 and $n = 0.1 * n_{co}$for different injection energies.

$\mathbf{E}_{inj}$ [eV]	**Losses** [%]				**Captured** [%]	ϵ_{1+} [%]
	Rad	Inj	Ext	Tot		
2	31.24	24.75	0.00	55.99	44.01	0.00
5	46.81	11.08	0.20	58.09	41.91	0.08
7	54.69	5.79	1.20	61.68	38.32	.0.08
10	53.09	1.00	9.40	63.47	36.53	2.56
12	52.60	0.20	21.30	74.10	25.90	6.48
17	31.54	0.10	63.67	95.31	5.469	23.60
22	6.29	0.15	92.51	98.95	1.05	42.32

obtained at LSPC's test bench [119] and shown in figure 6.40; a value of around 3 was found and then considered for the following simulation. More, considering that experimentally Rb^{1+} are produced with a surface ionization source, new starting conditions were generated, taking into account an initial energy spread of 2 eV for the 1+ beam. The new results obtained after the above modifications are showed in tables 6.14 and 6.15 while in figure 6.41 the obtained 1+ efficiencies are compared with the experimental results. In particular the blue curve is shifted of -1 V while the red curve of -1.5 V. The agreement with the experiment is now better: it can be seen that the curve obtained considering both modifications has the same "S" shape as the experimental results. Looking at the data in tables 6.13, 6.14 and 6.15 it can be noted that the above modification did not affect the total capture but influenced just the shape of the 1+ efficiency obtained at the end of the simulation. Again as

Table 6.15: Results of the injection of $^{85}Rb^{1+}$ ions into an oxygen plasma with KT=0.376 eV,⟨z⟩=3 and $n = 0.1 * n_{co}$for different injection energies considering an energy spread of 2 eV.

$\mathbf{E}_{inj}$ [eV]	**Losses** [%]				**Captured** [%]	ϵ_{1+} [%]
	Rad	Inj	Ext	Tot		
2	34.43	24.35	0.00	58.78	41.22	0.00
5	45.61	11.38	0.70	57.59	42.31	0.16
7	51.79	7.58	2.30	61.67	38.33	0.64
10	50.50	2.29	11.90	64.67	35.33	2.72
12	54.10	0.50	21.70	76.30	23.70	7.28
17	20.96	0.00	72.95	93.91	6.09	29.44
22	8.08	0.20	89.52	97.80	2.20	38.72

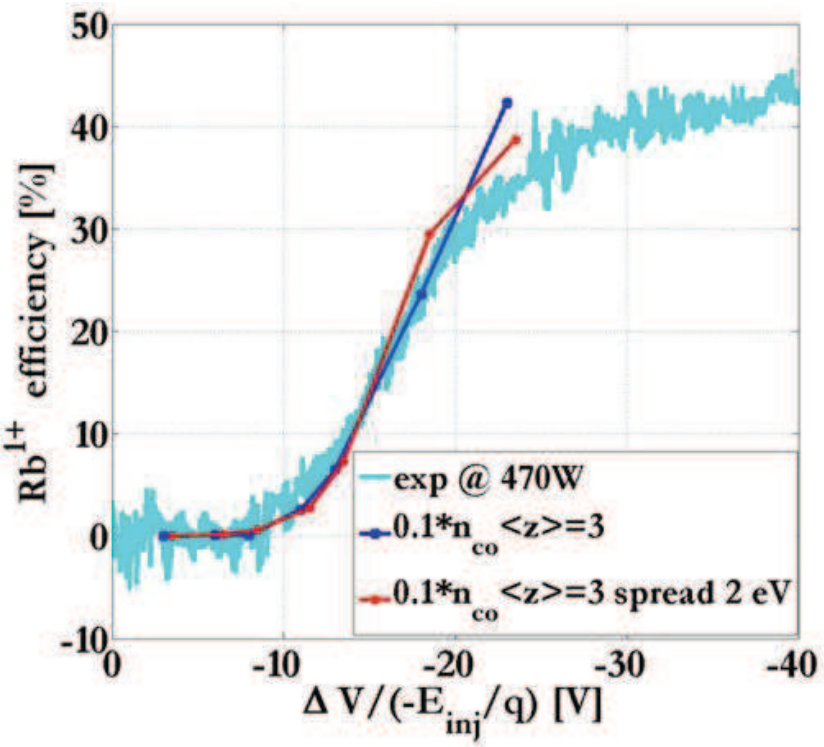

Figure 6.41: Comparison between experimental and simulated efficiency for the complete model using $n = 0.1 * n_{co}$, ⟨z⟩=3, $KT = 0.376$ eV (blue curve) and considering also an energy spread of 2 eV (red curve). The beam line transmission is taken into account.

Table 6.16: Results of the injection of $^{85}Rb^{1+}$ ions into an oxygen plasma with KT=0.3 eV,⟨z⟩=3 and $n = 0.1 * n_{co}$for different injection energies considering an energy spread of 2 eV. In bold the injection energy satisfying the requirements expressed in section 6.6.

$\mathbf{E}_{inj}$ [eV]	**Losses** [%]				**Captured** [%]	ϵ_{1+} [%]
	Rad	Inj	Ext	Tot		
2	25.84	22.75	0.00	48.59	51.41	0.00
5	40.12	12.87	0.20	53.19	46.81	0.00
7	45.01	5.29	0.30	50.60	49.40	0.00
10	47.11	0.90	7.30	55.29	**44.71**	**2.16**
12	47.00	0.40	21.20	68.60	31.40	7.44
15	36.40	0.00	46.60	83.00	17.00	16.56
17	21.26	0.00	68.96	90.22	9.78	29.68
22	6.89	0.00	90.87	97.76	2.24	36.32

before, the total capture in the region around $\Delta V = -12V$ is below the desired value of 40%. Considering the beneficial effect of ion temperature on the overall confinement, I decided then to lower it at 0.3 eV: this in order to try to keep the same 1+ efficiency and increase a little bit the total capture. As shown in table 6.16 this last modification gave the desired results: it can be seen that for an injection energy of 10 eV the 1+ efficiency is 2.16 % while the total capture is 44.71 %, that is the basic requirements were satisfied. From the point of view of the evolution of the 1+ efficiency with the ΔV it can be seen in figure 6.42 that the agreement with the experimental results is very good by shifting the data of -1.5 V. It is interesting to note, in the calculated data, that the onset of the 1+ current at the extraction always happens when the losses at injection are almost zero.

At this point I found a set of plasma parameters ($n_{ins} = 0.1 * n_{co}, KT = 0.3$ eV, $\langle z \rangle = 3, KT_e^{core} = 1$keV) and a characteristic of the injected beam (energy spread of 2 eV) that showed a very good agreement with the experimental results from both the point of view of the Rb^{1+} efficiency and the total capture. Anyway, a further modification was tried, aiming at keeping constant the shape of 1+ curve and the total capture but letting the onset of the 1+ current appears at lower energy: this in order to try to let experimental and simulated curves coincide with a bigger shift in ΔV, closer to the usual estimates of the plasma potential. To try to fulfil the above conditions, the plasma density was decreased to $n_{ins} = 0.075 * n_{co} \sim 2 \cdot 10^{+17}$ m^{-3}, while the other parameters were left unchanged: from the results showed in table 6.17 it can be seen that the condition of validity for a simulation are still satisfied, as evidenced in bold in the same table. The only effect was the one expected: figure 6.43 shows that the agreement with the experiments is still very good and that the necessary shift to superimpose the two curves is now -4 V, value much closer the the usual estimate of the plasma potential (in the order of the cold electrons temperature). The small

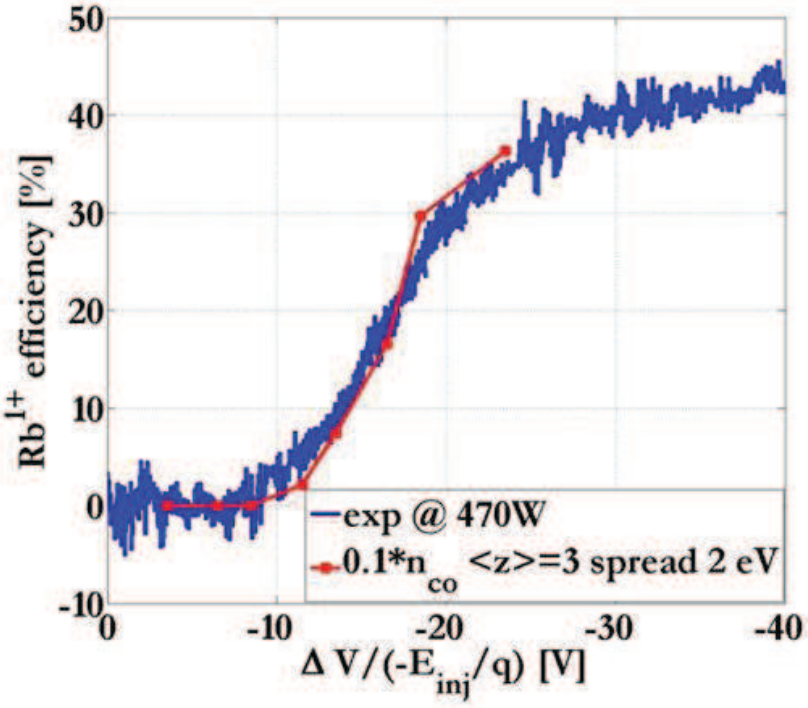

Figure 6.42: Comparison between experimental and simulated efficiency for the complete model using $n = 0.1 * n_{co}$, $\langle z \rangle$=3, $KT = 0.3$ eV and considering also an energy spread of 2 eV. The beam line transmission is taken into account.

Table 6.17: Results of the injection of $^{85}Rb^{1+}$ ions into an oxygen plasma with KT=0.3 eV,$\langle z \rangle$=3 and $n = 0.075 * n_{co}$for different injection energies considering an energy spread of 2 eV. In bold the injection energies satisfying the requirements expressed in section 6.6.

$\mathbf{E}_{inj}$ [eV]	**Losses** [%]				**Captured** [%]	ϵ_{1+} [%]
	Rad	Inj	Ext	Tot		
2	28.71	20.94	0.20	49.85	50.15	0.00
5	40.98	11.86	1.10	53.84	46.16	0.40
7	44.78	4.58	3.00	52.36	**47.64**	**0.80**
10	38.20	0.50	22.00	60.49	**39.51**	**9.28**
12	40.90	0.20	37.20	78.30	21.70	14.40
15	30.70	0.00	62.30	93.00	7.00	26.72
17	14.26	0.10	82.75	97.11	2.89	37.52
20	6.50	0.00	92.60	99.10	0.90	42.40
22	4.80	0.00	95.00	99.80	0.20	44.72

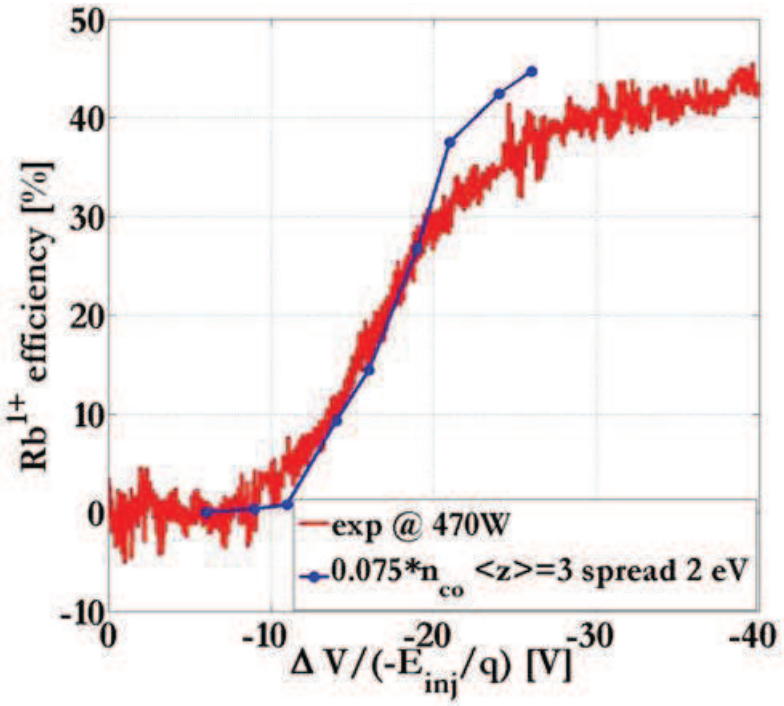

Figure 6.43: Comparison between experimental and simulated efficiency for the complete model using $n = 0.075 * n_{co}$, $\langle z \rangle$=3, $KT = 0.3$ eV and considering also an energy spread of 2 eV. The beam line transmission is taken into account.

discrepancy at high energies can be justified by the fact that the considered equations come close to their limit of validity in this range, as expressed in section 4.9; it could be also explained from the point of view of beam optics: very fast ions loose in fact a small amount of the injection energy, as figure 6.44 shows, in the case of Rb^{1+} injected at 20 eV and then extracted through the extraction hole. The 1+ current is experimentally recorded after a 105° bending dipole: if the injected 1+ ions maintain a certain amount of the injection energy once they are extracted, it can happen that the trajectories they follow inside the bending dipole are such that some of them are not recorded on the downstream Faraday Cup. The simulated data are instead equivalent to measure the efficiency before any bending dipole so cannot be influenced by this phenomenon.

As described above, it was possible to find a set of plasma parameters and characteristic of the injected 1+ beam that gave a very good agreement with the measured values, as table 6.17 and figure 6.43 show. In obtaining these results different parameters were modified (plasma density, temperature, energy distribution of the injected particles) except an important one, the temperature of the hot electrons component. For the sake of completeness, other two set of simulations were executed, considering an hot electron temperature KT_e^{core} inside the plasma of, respectively, 5 keV and 10 keV; the ratio between the temperatures KT_e^{core} and KT_e^{halo} was kept the same. The results of those further simulations are showed in table 6.18 and compared with

Table 6.18: Results of the injection of $^{85}Rb^{1+}$ ions into an oxygen plasma with KT=0.3 eV, $\langle z \rangle$=3 and $n = 0.075 * n_{co}$for different plasma temperatures, injection energies and considering an energy spread of 2 eV.

$\mathbf{KT}_e^{core}$=5 keV						
$\mathbf{E}_{inj}$ [eV]		**Losses** [%]			**Captured** [%]	$\boldsymbol{\epsilon}_{1+}$ [%]
	Rad	Inj	Ext	Tot		
2	29.80	18.00	0.20	48.00	52.00	0.00
5	39.20	9.50	1.50	50.20	49.80	0.08
7	44.50	4.10	4.00	52.10	**47.90**	**1.04**
10	41.57	0.70	21.00	63.31	**36.69**	**7.04**
12	42.67	0.20	34.60	77.47	22.53	12.96
15	32.90	0.10	60.30	93.32	6.68	23.52
17	13.26	0.00	84.10	97.31	2.69	39.44
20	5.88	0.10	92.20	98.20	1.80	44.56
22	5.78	0.10	93.20	99.10	0.90	45.76
$\mathbf{KT}_e^{core}$=10 keV						
$\mathbf{E}_{inj}$ [eV]		**Losses** [%]			**Captured** [%]	$\boldsymbol{\epsilon}_{1+}$ [%]
	Rad	Inj	Ext	Tot		
2	29.10	18.80	0.10	48.00	52.00	0.00
5	38.60	9.60	0.90	49.10	50.90	0.16
7	48.70	3.40	4.00	56.30	**43.70**	**1.36**
10	40.18	0.70	23.00	63.81	**36.19**	**8.16**
12	39.98	0.10	36.50	76.57	23.43	13.44
15	31.60	0.10	60.30	92.02	7.98	24.72
17	14.96	0.10	82.60	97.61	2.39	36.40
20	6.18	0.10	92.70	99.00	1.00	44.80
22	5.48	0.10	93.40	99.00	1.00	44.80

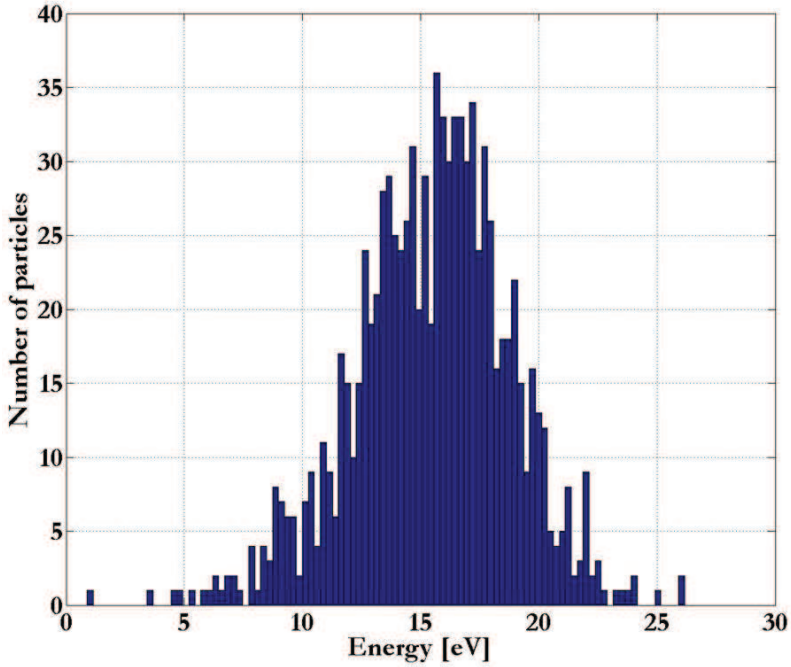

Figure 6.44: Energy distribution of Rb^{1+} ions extracted at the end of the simulation for $n = 0.075 * n_{co}$, $\langle z \rangle$=3, $KT = 0.3$ eV. The injection energy was 20 eV with 2 eV of energy spread.

the usual case with $KT_e^{core} = 1$ keV in figure 6.45: as it can be seen, the variation of the temperature does not affect significantly neither the total capture nor the 1+ efficiency. The three curves are in fact quite similar in values and trend, even if the first one obtained for $KT_e^{core} = 1$ keV seems to have a slightly better agreement with the experiments. The explanation for this small influence can be found considering that during the time span of the simulation (500 μs) only the first ionizations can occur: the ionization potentials of the corresponding ions are so small that the three temperatures above lead roughly to the same ionization times, as table 6.19 shows for the first six ionizations.
Now it is interesting to analyse more in details the final simulations, after having post-processed the saved data for the injection energy closer to the optimum experimental value for high charge states, that is 7 eV: taking into account the necessary shift to let the experimental and simulated curves coincide (-4 V), this is equivalent in fact to consider a ΔV of -11 V. Let's start with the evaluation of the characteristic times for this particular case: if we consider a Rb^{1+} beam with an average energy of 7 eV and an energy spread of 2 eV, interacting with a plasma characterized by a density $n_{ins} = 1.95 \cdot 10^{+17}$ m^{-3}, an ion temperature $KT = 0.3$ eV and a hot electron temperature $KT_e^{core} = 1$ keV, the characteristic times take the values:

$$\tau_s = 35\ \mu s \qquad \tau_D = 121\ \mu s \qquad \tau_E = 243\ \mu s \tag{6.76}$$

As it can be seen, the friction is very fast but the integration time (500 μs) is

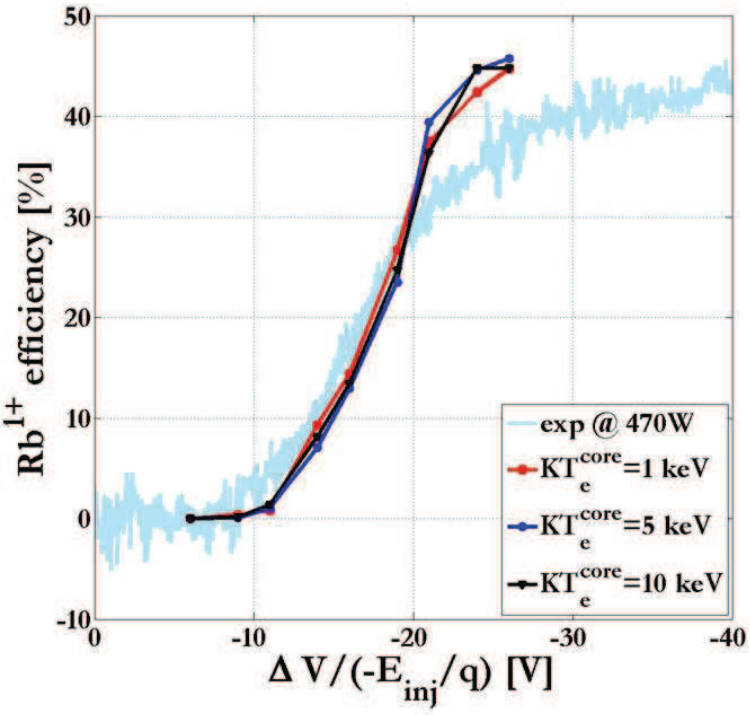

Figure 6.45: Comparison between experimental and simulated efficiency for the complete model using $n = 0.075 * n_{co}$, $\langle z \rangle = 3$, $KT = 0.3$ eV, an energy spread of 2 eV and different hot electrons temperatures. The beam line transmission is taken into account.

Table 6.19: Calculated Ionization times inside the plasma for Rubidium charge states from 1+ to 6+ considering different hot electron temperatures.

Ionization	τ_{ins} [s]		
	$KT_e^{core} = 1$ keV	$KT_e^{core} = 5$ keV	$KT_e^{core} = 10$ keV
$0 \rightarrow 1$	$2.85{\cdot}10^{-4}$	$4.42{\cdot}10^{-4}$	$5.32{\cdot}10^{-4}$
$1 \rightarrow 2$	$8.31{\cdot}10^{-4}$	$1.14{\cdot}10^{-3}$	$1.38{\cdot}10^{-3}$
$2 \rightarrow 3$	$1.56{\cdot}10^{-3}$	$1.96{\cdot}10^{-3}$	$2.33{\cdot}10^{-3}$
$3 \rightarrow 4$	$1.60{\cdot}10^{-3}$	$1.93{\cdot}10^{-3}$	$2.26{\cdot}10^{-3}$
$4 \rightarrow 5$	$2.32{\cdot}10^{-3}$	$2.65{\cdot}10^{-3}$	$3.06{\cdot}10^{-3}$
$5 \rightarrow 6$	$3.26{\cdot}10^{-3}$	$3.51{\cdot}10^{-3}$	$4.01{\cdot}10^{-3}$

now of the same order of magnitude of the characteristic times for 90° diffusion and energy equipartition. The velocity distribution of the captured Rubidium ions should tend to a Maxwell Boltzmann distribution with $\sigma = \sqrt{KT/M_{inj}} = 581.04$ m/s: figure 6.46 shows the distributions obtained along the three axis. Looking at the data, it came out that the widths of the distributions along x and y are very close to the theoretical one while the distribution along z should "shrink" a bit more. By inspecting the distributions with the "normplot" routine, it came out that all the three are Maxwellian, except for few particles in the very high velocity region along y and z: this is not surprising because it is known from the literature that the high energy tail of the Maxwell Boltzmann distribution takes usually more time to be populated by Coulomb collision then the core of the distribution [90]. Figure 6.47 shows two important results of the calculation: in the upper part, the spatial distribution of the captured particles at the end of the simulations is showed, with the surface corresponding to $B = B_{ecr}$ in yellow; we can note that the most of them are trapped inside the plasmoid, while a few stay in the halo. The lower picture is basically obtained by superimposing the Rubidium's density maps calculated from the saved data. It can be seen as the density map at the steady state for a continuous beam injection: particles spend in fact more time (and so the density is higher) along the path during injection, because the deceleration due to friction dominates on lateral diffusion, and inside the resonance surface (this time coloured in blue) due to trapping of the particles. No density is observed in the rest of the domain of the simulation, indicating that once left the plasma, particles are lost quite fast without coming back inside. This is consistent with what is experimentally observed and mentioned before, that is the discrepancy between charge breeding gaseous and condensible, the last ones do not taking advantage of wall recycling. Even if the plasma density is low, some ionization take place, as the charge states distribution in figure 6.48 shows. Looking at table 6.17 it can be seen that the particle losses are mainly in radial direction: figure 6.49 shows the distribution of the particles lost on the plasma chamber surface. In agreement with the theory, charged particles are lost in particular zones where the magnetic field is lower: such zones are within the two poles of the hexapole and in fact spaced of 60° one from each other. As a very final step, it was searched for a possible agreement even with the second curve in figure 6.19: the two curves have been obtained just varying the microwave power and leaving the other parameters unchanged, without calculating the total capture. The higher loss rate of Rb^{1+} ions observed at 250 W can be traced back to a lower plasma density, with a reduced frictional force. To verify this effect, another simulation was executed by just lowering the density to $n = 0.05 * n_{co} = 1.3 \cdot 10^{+17}$: very happily, the agreement continues to persist as figure 6.50 shows; it is important to note that the curves have been superimposed by using the same shift of the numerical data used before (-4 V). For the discrepancy observed at high velocities hold the considerations made above.

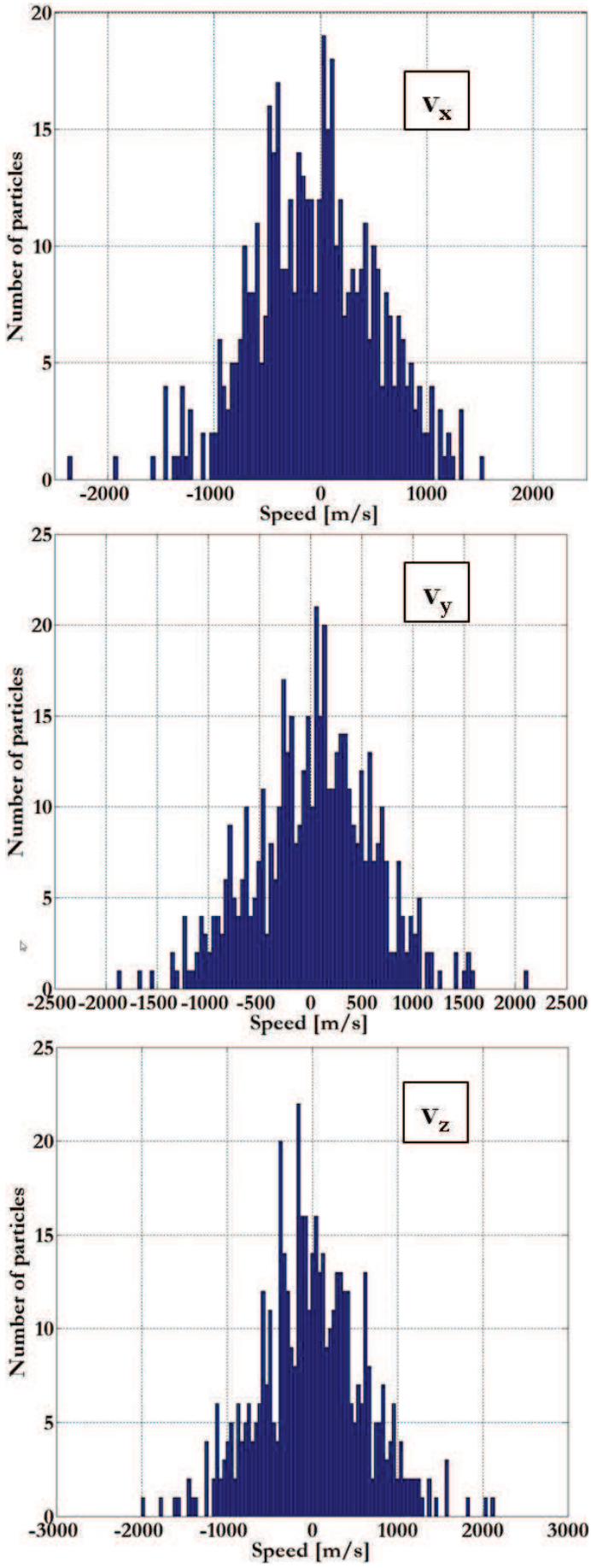

Figure 6.46: Particles' velocities distributions obtained at the of the simulation for the complete model using $n = 0.075 * n_{co}$, $\langle z \rangle = 3$, $KT = 0.3$ eV, an energy spread of 2 eV.

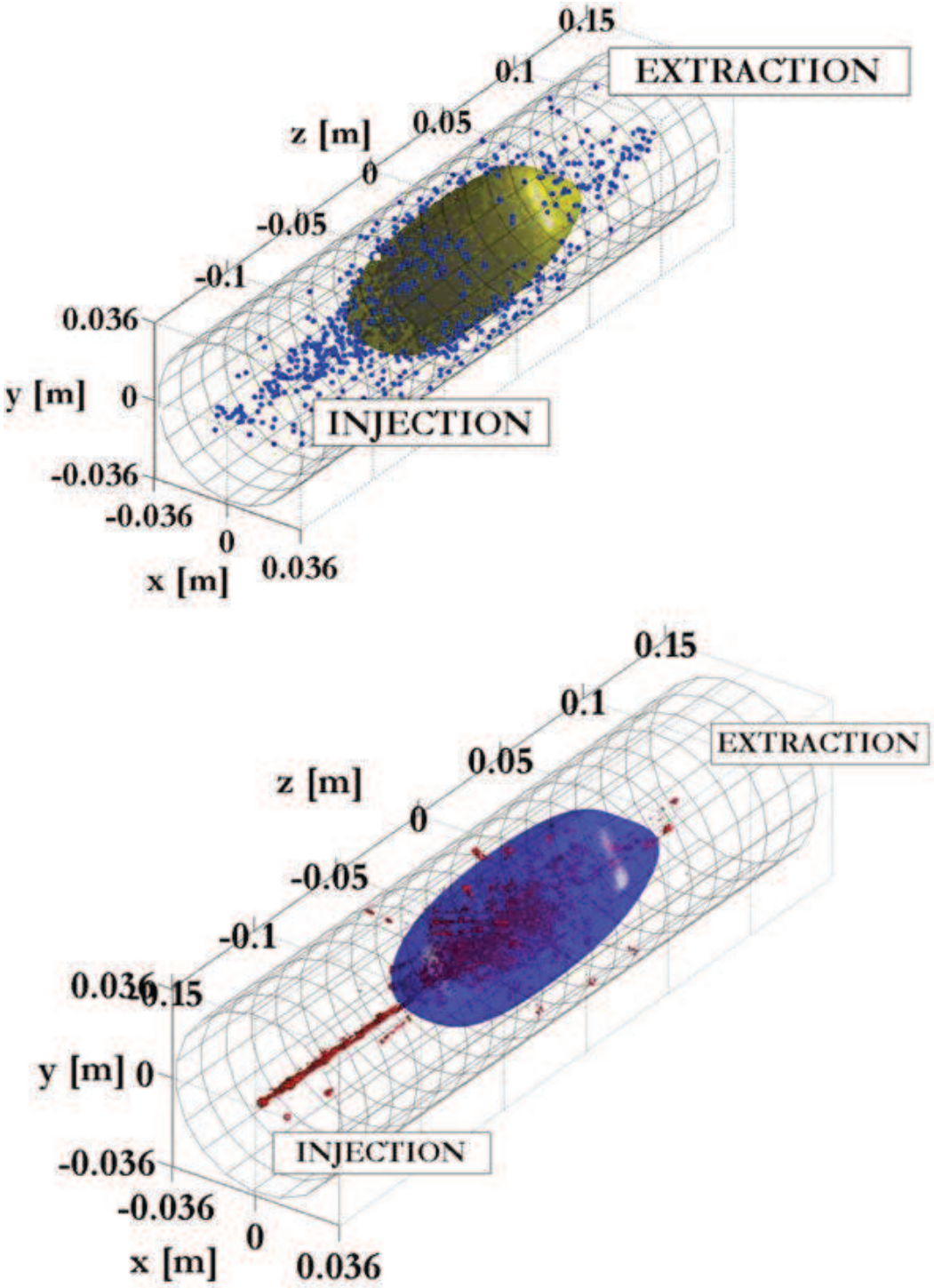

Figure 6.47: Spatial distribution of the captured particles at the end of the simulations (upper part): the most of them are contained inside the resonance surface (in yellow); density map of the injected particles at the steady state (lower part): captured particles are localized on the injection path and inside the resonance surface (in blue).

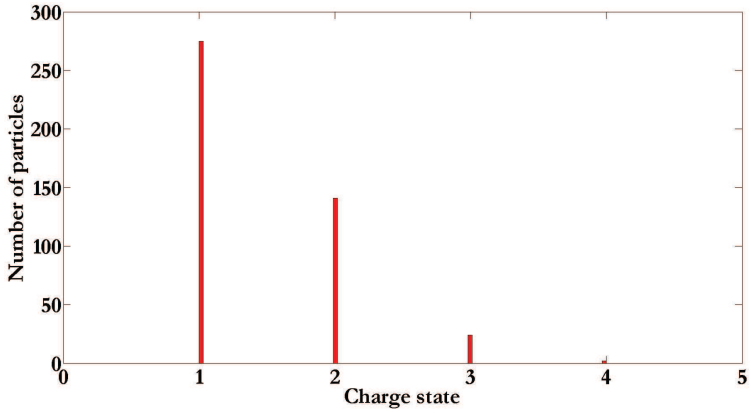

Figure 6.48: Final charge state distribution at the end of the simulation for $n = 0.075 * n_{co}$, <z>=3, $KT = 0.3$ eV, $E_{inj} = 7$ eV and an energy spread of 2 eV.

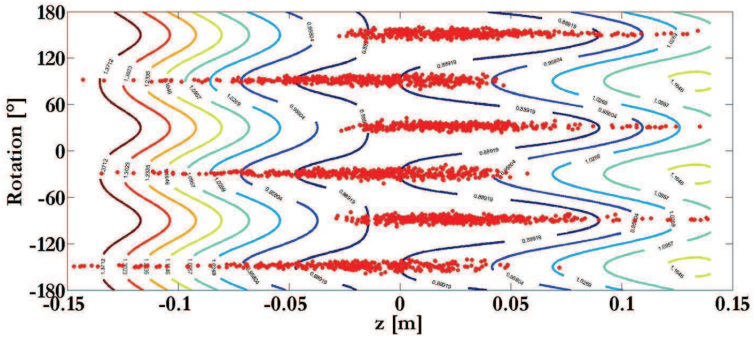

Figure 6.49: Distribution of particles lost on the plasma chamber's surface for $E_{inj} = 7$ eV: losses are localized zones of low magnetic field that follow the hexapole's symmetry.

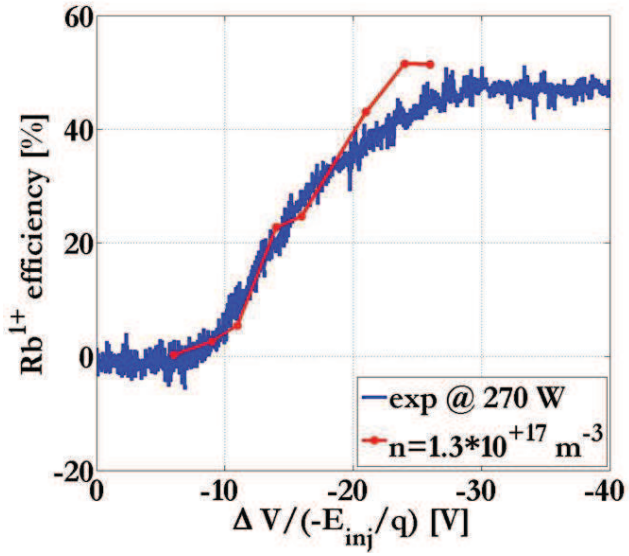

Figure 6.50: Comparison between experimental and simulated efficiency for the complete model using $n = 0.05 * n_{co}$, ⟨z⟩=3, $KT = 0.3$ eV and considering also an energy spread of 2 eV. The beam line transmission is taken into account.

6.7 Summary and Perspectives

A new physical description of the charge breeding process of injected ions into Electron Cyclotron Resonance plasmas has been proposed and benchmarked by experimental results: its theoretical investigation revealed the importance of the many small angle Coulomb collisions, suffered by the injected ions, that lead to thermal equilibrium with plasma ions. For those interactions, three characteristic times can de deduced, that together give an idea for the time it takes thermalization to be reached: the slowing down time (the time it takes for the average velocity to go to zero), the 90° diffusion time (the time it takes for the initial distribution to be isotropic) and finally the energy equipartition time (whose name is self explaining). The correct implementation of the above theory on a particle tracking code revealed to be not easy: after an extensive research in the literature of Computational Physics, a solution was found by employing the Langevin formalism. The physics of the simulated model has been progressively improved by adding more and more sophisticated hypothesis:

I **Isotropic/homogeneous plasma** with a given temperature and density;

II Effect of the **B filed**;

III Implementation of the **plasmoid/halo** plasma model;

IV Implementation of a **potential dip** structure as mechanism for ion confinement;

V Implementation of the **ionization** process;

A numerical code, based on the MATLAB platform, has been implemented, thus performing a wide campaign of simulations for each of the steps listed above: in particular, from step I to step IV the results were asked to agree with the theoretical prediction on ion confinement and dynamics, while the last step was benchmarked by experimental results obtained on the LPSC test bench. The simulations evidenced the most critical input parameters, listed in order of importance in the following:

1. Plasma **ion temperature**;
2. Plasma **ion** (electron) **density**;
3. Injected **beam energy**;
4. Injected **beam energy spread**;
5. **Electron temperature**;

When exploring the multi-dimensional space of parameters, the simulations revealed to be a powerful tool for explaining the physics of the capture, thermalization and multi-ionization of the charge bred ions: in particular, simulations showed that only a precise combination of the above mentioned parameters (extremely critical was the

ion temperature) matches the experimental results, in terms of both 1+ efficiency and global capture. In detail, the final parameters that nicely reproduce the experimental results, obtained at LPSC within the EMILIE project, can be summarized as follows: $n_e \sim 2 \cdot 10^{17}$ m^{-3}, KT_e= 1 keV, KT_i= 0.3 eV, $\Delta\phi = KT_i/2$.
In this perspectives, the activity carried out opens now to very interesting scenarios:

- From one side, the code is now able to run as a **predictive tool** for the charge breeding experiments, with a lot of advantages for the future operation within the SPES facility. As an example, simulations revealed in fact that, at the optimum injection energy for the 1+ beam, particle losses are mainly concentrated on the plasma chamber wall and through the extraction hole. This is an important information from the point of view of radiation-protection: it foresees in fact that the contamination of the injection and extraction parts of the charge breeder will be absent or, at least, very limited, with a positive impact on the safety of the maintenance operations and the time they will take to be completed. Moreover, to have identified the ion temperature as a fundamental parameter in determining the charge breeder performances, provides a useful goal for an R&D program aiming at optimizing this plasma characteristic.

- From another side, the strategy followed so far has permitted also the benchmarking of model assumptions, with a lot of **consequences on plasma physics** studies that could be carried out, if the path traced by the present work would be explored.

Concerning this last point, the obtained results are in agreement with a view of the plasma based on a plasmoid/halo scheme, with a self-generated potential dip whose strength has been evaluated on the basis of a "Double-Layer" assumption.
The very good agreement between the experiments and the simulations encourages us to proceed towards a further optimization of the model. It is worth mentioning that several experimental data feature a critical sensitivity of ECRIS (and so charge breeder) plasma to the electromagnetic field established inside the plasma chamber: the two main effects are the "two frequency heating" and the "frequency tuning", whose consequences on the charge breeder performances are still controversial. The beneficial effect of the latter on ECRIS performances, and the fruitful application of the former at Argonne National Laboratories on the ECR-based charge breeder suggest, as a natural evolution of the work carried out in this thesis, the necessity of the **improvement of the plasma model when taking into account the self-consistent interaction with the microwave field**. The support of LNS team (a paper concerning preliminary self-consistent results, obtained through a Maxwell-kinetic loop as simulation strategy, has been recently published [120]) will provide the "plasma-target model" under different excitation frequencies.
Finally, another advancement will concern the **perturbation of the Ion Energy Distribution Function** induced by the injected beam: this study may explain some

still unexplored issues concerning the drop down of the highly charged ions of the buffer plasma when the charge breeding takes place, as experimentally observed at LPSC. The strict interplay of the capture tool with the plasma kinetics simulations will be fundamental in this frame.

References

[1] J. Al-Khalili, E. Roeckl, *The European Lectures on Physics with Exotic Beams*, vol. 1, Springer, Berlin, 2006.

[2] B. Harss, R. C. Pardo, K. E. Rehm, F. Borasi, J. P. Greene, R. V. F. Janssens, C. L. Jiang, J. Nolen, M. Paul, J. P. Schiffer, R. E. Segel, J. Specht, T. F. Wang, P. Wilt and B. Zabransky, *Production of radioactive ion beams using the in-flight technique*, Rev. Sci. Instrum. 71 (2000), pagg 380-387.

[3] J. Al-Khalili, E. Roeckl, *The European Lectures on Physics with Exotic Beams*, vol. 2, Springer, Berlin, 2006.

[4] G. Prete, A. Andrighetto, M. Manzolaro, S. Corradetti, D. Scarpa, M. Rossignoli, A. Monetti, M. Lollo, M. Calderolla, J. Vasquez, D. Zafiropoulos, L. Sarchiapone, D. Benini, P. Favaron, M. Rigato, R. Pegoraro, D. Maniero, L. Calabretta, M. Comunian, M. Maggiore, A. Lombardi, L. Piazza, A.M. Porcellato, C. Roncolato, G. Bisoffi, A. Pisent, A. Galata', M. Giacchini, G. Bassato, S. Canella, F. Gramegna, J. Valiente, J. Bermudez, P.F. Mastinu, J.Esposito, J. Wyss, S. Zanella, *The SPES project at the INFN- Laboratori Nazionali di Legnaro*, EPJ Web Conferences 66, 11030 (2014).

[5] https://web.infn.it/spes/index.php/component/content/article/133-spes-phases/192-gamma.

[6] https://web.infn.it/spes/index.php/component/content/article/133-spes-phases/195-delta.

[7] http://www.bestcyclotron.com/products.html.

[8] https://web2.infn.it/spes/.

[9] M. Manzolaro, *Engineering of the INFN SPES Target – Ion Source System*, LAP LAMBERT Academic Publishing, 2012, Saarbrucken, Germany.

[10] M. Maggiore, M. Cavenago, M. Comunian, F. Chirulotto, A. Galata', M. De Lazzari, A. M. Porcellato, C. Roncolato, S. Stark, A. Caruso, A. Longhitano, F. Cavaliere, G. Maero, B. Paroli, R. Pozzoli and M. Romé, *Plasma-beam traps and radiofrequency quadrupole beam coolers*, Rev. Sci. Instrum. 85, 02B909 (2014).

[11] SPES technical design report 2008.

[12] A. Galata', M. Comunian, M. Maggiore, M. Manzolaro, J. Angot and T. Lamy, *The charge breeder beam line for the selective production of exotic species project at INFN-Legnaro National Laboratories*, Rev. Sci. Instrum. 85, 02B905 (2014).

[13] M. Comunian, A. Palmieri, A. Pisent, C. Roncolato, *The new RFQ as RIB injector of the ALPI LINAC* , Proceedings of IPAC2013, Shanghai, China.

[14] G. Bisoffi, G. Bassato, A. Battistella, J. Bermudez, D. Bortolato, S. Canella, B. Chalykh, M. Comunian, A. Facco, E. Fagotti, A. Galata', M. Giacchini, F. Gramegna, T. Lamy, P. Modanese, A. Palmieri, R. Pengo, A. Pisent, M. Poggi, A. Porcellato, C. Roncolato and D. Scarpa, *ALPI setup as the SPES accelerator of exotic beams*, EPJ Web Conferences 66, 11003 (2014).

[15] J. Angot, T. Lamy, M. Marie-Jeanne, P. Sortais, T. Thuillier, *LPSC PHOENIX ECR charge breeder beam optics and efficiencies*, Proceedings of ECRIS2012, Sydney, Australia.

[16] P. Delahaye, A. Galata', J. Angot, G. Ban, L. Celona, J. Choinski, P. Gmaj, A. Jakubowski, P. Jardin, T. Kalvas, H. Koivisto, V. Kolhinen, T. Lamy, D. Lunney, L. Maunoury, A. M. Porcellato, G. F. Prete, O. Steckiewicz, P. Sortais, T. Thuillier, O. Tarvainen, E. Traykov, F. Varenne and F. Wenander, *Prospects for advanced electron cyclotron resonance and electron beam ion source charge breeding methods for EURISOL*, Rev. Sci. Instrum. 83, 02A906 (2012).

[17] http://www.eurisol.org/site02/index.php.

[18] A. Herlert, Y. Kadi, *The HIE-ISOLDE Project*, J. Phys. Conf. Ser. 312 052010 (2011).

[19] S. Gales, *GANIL-SPIRAL2: a new era*, AIP Conf. Proc. 1355, 36 (2011).

[20] A.M. Stefanini, L. Corradi, G. Maron, A. Pisent, M. Trotta, A.M. Vinodkumar, S. Beghini, G. Montagnoli, F. Scarlassara, G.F. Segato, A. De Rosa, G. Inglima, D. Pierroutsakou, M. Romoli, M. Sandoli, G. Pollarolo, A. Latina, *The heavy-ion magnetic spectrometer PRISMA*, Nuclear Physics A 701 (2002) 217-221.

[21] C. A. Ur, *Perspectives for the gamma-ray spectroscopy at LNL: the GALILEO project*, Journal of Physics 366 (2012) 012044.

[22] E. Farnea, F. Recchia, D. Bazzacco, T. Kroll, Z. Podolyak, B. Quintana, A. Gadea, *The AGATA Collaboration* , Nucl. Instr. and Meth. A 621, 331-343 (2010).

[23] G. Jaworski, M. Palacz, J. Nyberg, G. de Angelis, G. de France, A. di Nitto, J. Egea, M.N. Erduran, S. Erturk, E. Farnea, A. Gadea, V. González, A. Gottardo, T. Huyuk, J. Kownacki, A. Pipidis, B. Roeder, P. A. Soderström, E.

Sanchis, R. Tarnowski, A. Triossi, et al, *Monte Carlo simulation of a single detector unit for the neutron detector array NEDA*, Nucl. Instr. and Meth. A 673, 64-72 (2012).

[24] A. Maj et al, *The PARIS Project*, Acta Phys. Pol. B40 (2009).

[25] http://fazia.in2p3.fr/Fazia/fazia.htm

[26] J. J. Livingood. *Cyclic Particle Accelerators*, D.Van Nostrand Company Inc.

[27] Fred Samson Grillet, Bruce Forrest Milton, Darcy Montgomery, *Magnetic Field Mapping of the Best 70 MeV Cyclotron*, Proceedings of Cyclotrons 2013, Vancouver, Canada.

[28] A. Andrighetto, S. Cevolani, C. Petrovich, *Fission fragment production from uranium carbide disc targets*, European Physical Journal A, 25, 1 (2005)41-47.

[29] M. Manzolaro, A. Andrighetto, G. Meneghetti, M. Rossignoli, S. Corradetti, L. Biasetto, D. Scarpa, A. Monetti, S. Carturan, G. Maggioni, *Ionization efficiency estimations for the SPES surface ion source*, Nucl. Instr. and Meth. B 317 (2013) 446-449.

[30] D. Scarpa, J. Vasquez, A. Tomaselli, D. Grassi, L. Biasetto, A. Cavazza, S. Corradetti, M. Manzolaro, J. Montano, A. Andrighetto and G. Prete, *Studies for aluminium photo ionization in hot cavity for the Selective Production of Exotic Species project*, Rev. Sci. Instrum. 83, 02B317 (2012).

[31] M. Manzolaro, A. Andrighetto,G. Meneghetti, A. Monetti, D. Scarpa, M. Rossignoli, J. Vasquez, S. Corradetti, M. Calderolla and G. Prete, *Ongoing characterization of the forced electron beam induced arc discharge ion source for the Selective Production of Exotic Species facility*, Rev. Sci. Instrum. 85, 02B918 (2014).

[32] A. Pisent et al, Proc. HB 2014, East Lansing , MI (in course of publication).

[33] G. Savard, R. Pardo, S. Baker, C. Davids, A. Levand, D. Peterson, D. Phillips, T. Sun, R. Vondrasek, B. Zabransky, G. Zinkann, *Hyperfine Interactions*, vol. 199 Issue 1-3, (2011) 301.

[34] M. Maggiore, A. M. Porcellato, S. Stark, F. Chiurlotto, A. Galata', A. Dainelli, M. De Lazzari, A. Caruso, A. Longhitano, *Status of the RFQ beam cooler for the SPES project at LNL*, EPJ Web Conferences 66, 11024 (2014).

[35] F. G. Major and H. G. Delmet, *Exchange-Collision Technique for the rf Spectroscopy of Stored Ions*,Phys. Rev. 170 (1968) 91.

[36] T. Lamy, J. Angot and T. Thuillier, *European research activities on charge state breeding related to radioactive ion beam facilities*, Rev. Sci. Instrum. 79 02A909 (2008).

[37] G. Fortuna et al, *The ALPI Project at the Laboratori Nazionali di Legnaro*, Nucl. Instr. and Meth. A 287 (1990) 253.

[38] G. Bisoffi, P. Favaron, A. Lombardi, A. Pisent, R. Tovo, *The positive Ion Injector for ALPI*, Nucl. Instr. and Meth. A 382 (1996) p. 245.

[39] R. Corra', *Fasci instabili per esperimenti di fisica nucleare: sviluppo e test di primi apparati*, degree thesis.

[40] G. F. Grinyer, J. C. Thomas, B. Blank, H. Bouzomita, R. A. E. Austin, G. C. Ball, F. Bucaille, P. Delahaye, P. Finlay, G. Frémont, J. Gibelin, J. Giovinazzo, J. Grinyer, T. Kurtukian-Nieto, A. T. Laffoley, K. G. Leach, A. Lefèvre, F. Legruel, G. Lescalié, D. Perez-Loureiro, *Upgrade of the SPIRAL identification station for high-precision measurements of nuclear β decay*, Nucl. Instr. and Meth. A 741(2014)18-25.

[41] E. D. Donets, *Historical review of electron beam ion sources*, Rev. Sci. Instrum. 69 (1998) 614.

[42] R. Geller, *Electron Cyclotron Resonance Ion Source and ECR plasmas*, IOP, Bristol, UK, 1996.

[43] G. Schiwietz and P.L. Grande, *Improved charge-state formula*, Nucl. Instr. and Meth. B 175-177 (2001) 125-131.

[44] M. Toulemonde, *Irradiation by swift heavy ions: Influence of the non-equilibrium projectile charge state for near surface experiments*, Nucl. Instrum. and Meth. B 250 (2006) 263-268.

[45] P. Delahaye, O. Kester, C. Barton, T. Lamy, M. Marie-Jeanne and F. Wenander, *Evaluation of charge breeding options for EURISOL*, Eur. Phys. J. A 46, 421–433 (2010).

[46] F. Ames, G. Bollen, P. Delahaye, O. Forstner, G. Huber, O. Kester, K. Reisinger, P. Schmidt, *Cooling of radioactive ions with the Penning trap REXTRAP*, Nucl. Instrum. Meth. A 538 (2005) 17.

[47] F. Wenander, P. Delahaye, R. Scrivens, R, Savreux, *The REX-ISOLDE charge breeder as an operational machine*, Rev. Sci. Instr. 77 (2006) 03B104.

[48] T. Lamy, R. Geller, P. Sortais, and T. Thuillier, *Status of charge breeding with electron cyclotron resonance ion sources*, Rev. Sci. Instr. 77, 03B101 (2006).

[49] R. Vondrasek, R. Scott, J. Carr, R. Pardo, *Initial results of the ECR Charge Breeder for the ^{252}Cf fission source project (CARIBU) at ATLAS*, Proceedings of HIAT09, Venice, Italy.

[50] N. Imai, S. C. Jeong, M. Oyaizu, S. Arai, Y. Fuchi, Y. Hirayama, H. Ishiyama, H.Miyatake, M. H. Tanaka, M. Okada, and Y. X. Watanabe S. Ichikawa, H. Kabumoto, A. Osa, Y. Otokawa, and T. K. Sato, *KEK-CB electron cyclotron resonance charge breeder at TRIAC*, Rev. Sci. Instr. 79, 02A906 (2008).

[51] R. Geller, C. Tamburella, J. L. Belmont, *The ISOL-MAFIOS Source*, Rev. Sci. Instrum. 68 (1997) 2319-232.

[52] J. L. Bouly, J. F. Bruandet, N. Chauvin, J. C. Curdy, R. Geller, T. Lamy, P. Sole, P. Sortais, J. L. Vieux-Rochaz, *Ion charge state increase* $1+ \rightarrow N+$ *for the acceleration of alkali and metallic radioactive ions*, Proc Int. Workshop on the Physics and techniques of secondary nuclear beams, Dourdan France, 23-25 March 1992, pag. 407.

[53] T. Lamy, R. Geller, J.L. Bouly, N. Chauvin, J.C. Curdy, A. Lacoste, P. Sole, P. Sortais, T. Thuillier, J.L. Vieux-Rochaz, *The Development Of An ECRIS Charge-State Breeder For Generating RIBs*, AIP Conf. Proc. 576, 281 (2001).

[54] P. Delahaye, C. J. Barton, K. Connell, T. Fritioff, O. Kester et al, *Recent results with the PHOENIX booster at ISOLDE*, Rev. Sci. Instrum. 77, 03B105 (2006).

[55] S.C. Jeong, N. Imai, M. Oyaizu, S. Arai, Y. Fuchi, Y. Hirayama, H. Ishiyama, H. Miyatake, M. Okada, M. H. Tanaka, Y. X. Watanabe, S. Ichikawa, A. Osa, T. K. Sato, H. Kabumoto, *KEKCB-18 GHz ECR charge breeder at TRIAC*, Nucl. Instr. and Meth. B 266 (2008) 4411-4414.

[56] F. Ames, R. Baartman, P. Bricault, K. Jayamanna, A. Mjos, *Operation of an ECRIS charge state breeder at TRIUMF,* Proceedings of ECRIS2012, Sydney, Australia.

[57] R. Vondrasek, S. Baker, P. Bertone, S. Caldwell, J. Clark, C. Davids, D. Lascar, A. Levand, K. Lister, R. Pardo, D. Peterson, D. Phillips, G. Savard, M. Sternberg, T. Sun, J. Van Schelt, B. Zabransky, *Commissioning experience with CARIBU* ,Proceedings of HIAT 2012, Chicago, IL USA.

[58] A. Monetti, M. Manzolaro, S. Corradetti, D. Scarpa, J. Vasquez, M. Rossignoli, M. Calderolla, F. Rossetto, R. Silingardi, A. Mozzi, C. Gobbi, F. Borgn, A. Andrighetto, G. Prete, F. Martinez, C. Petrovich and G. Meneghetti, *The RIB production target for the SPES project*, to be submitted to EPJ A.

[59] S. Gammino and G. Ciavola, *The role of microwave frequency on the high charge states build-up in the ECR ion sources.* Plasma Source Sci. Technol., May 1996. 5, 19-27.

[60] R. Geller, F. Bourg, P. Briand, J. Debernardi, M. Delaunay, B. Jacquot, P. Ludwig, R. Pauthenet, M. Pontonnier, and P. Sortais, *The Grenoble ECRIS*

status 1987 and proposal for ECRIS scaling, Proc. 8th Int. Workshop ECR Ion Sources, East Lansing, 1, 1987, p. 22, report MSUCP-47.

[61] D. Leitner, C. M. Lyneis, *High intensity high charge states ECR ion sources*, Proc of PAC 2005, Knoxville, Tennessee.

[62] S. Gammino and G. Ciavola, *The contribution of the INFN-LNS to the development of electron cyclotron resonance ion sources*, Rev. Sci. Instrum. 71 , 631 (2000).

[63] M. S. Ioffe, *Mirror Traps*, Plasma Physics, 1965.

[64] L. Spitzer, R. Harm, *Transport Phenomena in a Completely Ionized Gas*, Phys. Rev. 89, 977-81 (1953).

[65] P. Debye, W. Huckel, Phys. Z. 24 183, 305 (1923).

[66] G. Melin, A. G. Drentje, A. Girard and D. Hitz, *Ion behaviour and gas mixing in electron cyclotron resonance plasmas as sources of highly charged ions*, J. Appl. Phys. 86 (9), 4772-4779, (1999).

[67] D. Mascali, L. Neri, L. Celona, G. Castro, G. Torrisi, S. Gammino, G. Sorbello, and G. Ciavola, *A double-layer based model of ion confinement in electron cyclotron resonance ion source*, Rev. Sci. Instrum. 85, 02A511 (2014).

[68] W. Lotz, *Electron-Impact Ionization cross-sections and Ionization rate coefficients of Ar atoms And Ions*, NASA Astrophysics Data System.

[69] W. Lotz, *An Empirical Formula for the Electron-Impact Ionization Cross-Section*, Zeitschrift ftir Physik 206, 205–211 (1967).

[70] K. S. Golovanivsky, *Instruments and experimental techniques*, vol. 28 no. 5 part 1 pag 989, New York: Plenum.

[71] R. W. P. MacWhirter, *Plasma diagnostics techniques*, New York: academic.

[72] A. Muller, E. Salzborn, *Scaling of cross sections for multiple electron transfer to highly charged ions colliding with atoms and molecules*, Phys. Lett. 62 A 391, 1977.

[73] S. Barbarino, *Appunti di campi elettromagnetici*, 2006.

[74] F. Jeager, A. J. Lichtenberg, and M. A. Lieberman, *Theory of electron cyclotron resonance heating I. Short time and adiabatic effects*, Plasma Phys., Dec. 1972. vol. 14, no. 12, pp. 1073-1100.

[75] F. Jeager, A. J. Lichtenberg, and M. A. Lieberman, *Theory of electron cyclotron resonance heating II. Long time and stochastic effects*, Plasma Phys., Feb. 1973. vol. 15, no. 2, pp. 125-150.

[76] J. L. Delcroix, *Introduction to the Theory of Ionized Gases*, New York, Wiley Interscience.

[77] E. Canobbio, *Gyroresonant particle acceleration in a non-uniform magnetostatic field*, Nucl. Fusion, 1969. vol. 9, p. 27.

[78] D. Bohm, *Electrical Discharges In A Magnetic Field*, A. Guthrie and R. K. Wakerling (New York: MGram Hill).

[79] K-U Riemann, *The Bohm criterion and the sheath formation*, J. Phys. D: Appl. Phys. 24 (1991) 493-518.

[80] C. D. Child, *Discharge from hot cathode*, Phys. Rev. (Ser. I) 32 492-511.

[81] S. Humphries Jr., *Charged Particles beams*, J. Wiley and Sons.

[82] P. Spaedtke, *The role of space charge compensation for ion beam extraction and ion beam transport*, Rev. Sci. Instrum. 85 , 02A744 (2014).

[83] I. G. Brown, *The Physics and Technology of Ion Sources*, (Wiley, New York, 1989).

[84] A. Septier, *Focusing of Charged Particles*, vol. 2, Academic Press, New York, 1967.

[85] S. Gammino, J. Sijbring and A. G. Drentje, *Experiment with a biased disk at the K.V.I. ECRIS*, Rev. Sci. Instrum. 63 , 2872 (1992).

[86] L. Spitzer Jr., *Physics of fully ionized gases*, Dover Publications Inc.

[87] O. Dendy, *Plasma Physics*, Oxford Science Publication.

[88] S. Chandrasekhar,*Dynamical Friction I. General Considerations: The Coefficient of Dynamical Friction*,The Astrophysics Journal 97. 255-262.

[89] S. Chandrasekhar, *The time of relaxation of stellar system*, Astrophysics journal 93, 285-304.

[90] W.M. MacDonald, M.N. Rosenbluth, *Relaxation of a system of particles with coulomb interactions*, Phys. Rev. vol 107, 2 (1957).

[91] J. L. Belmont at al, *The PIAFE project at Grenoble: beam transport and acceleration*, Proc. 13th Int Conf. on Cyclotron and their applications, Vancouver, July 6-10, 1992.

[92] N. Chauvin et al, *The 1+→ N+ charge breeding method for the production of radioactive and stable continuous/pulsed multi-charged ion beams*, Proceedings of the 14th international workshop on ECR sources, CERN, Genève, Suisse (1999).

[93] P. Spaedtke, *Model for the description of ion beam extraction from electron cyclotron resonance ion source*, Rev. Sci. Instrum. 81 , 02B725 (2010).

[94] S. A. Self, *Exact solution of the collisionless plasma-sheath equation*, Phys. of Fluids vol. 6, no. 12 (1963).

[95] R. N. Franklin, *Plasma with more than one species of positive ion and the Bohm criterion*, J. Phys. D: Appl. Phys. 33 3186-3189 (2000).

[96] T. Lamy, J. Angot, private communication.

[97] F. Ames, R. Baartman, P. Bricault, K. Jayamanna, T. Lamy and M. McDonald, *Charge state breeding for the acceleration of radioactive ions at TRIUMF*, Rev. Sci. Instrum. 81, 02A903 (2010).

[98] http://irfu.cea.fr/Sacm/logiciels/index3.php

[99] http://www.nupnet-eu.org/wps/portal/index.html

[100] P. Sortais, T. Lamy, J. Médard, J. Angot, L. Latrasse and T. Thuillier, *Ultra-compact/ultralow power electron cyclotron resonance ion source for multipurpose applications*, Rev. Sci. Instrum. 81 , 02B314 (2010).

[101] G. Ciavola, S. Gammino, L. Celona, F. Maimone, A. Galata', M. Pullia, R. Monferrato, C. Bieth, W. Bougy, G. Gaubert, O. Tasset, A.C.C. Villari, *Commissioning of the ECR ion sources at CNAO facility*, Proceedings of EPAC08, Genoa, Italy.

[102] H. Koivisto, O. Tarvainen, V. Toivanen, J. Komppula, R. Kronholm, T. Lamy, J. Angot, P. Delahaye, L. Maunoury, A. Galata', G. Patti, L. Standylo, O. Steczkiewicz and J. Choinski, *Ionization efficiency studies with charge breeder and conventional electron cyclotron resonance ion source*, Rev. Sci. Instrum. 85 , 02B917 (2014).

[103] http://it.mathworks.com/products/matlab/

[104] T. Lamy, J. Angot, C. Fourel *Latest developments in ECR charge breeders*, Proceedings of HIAT09, Venice, Italy.

[105] S. Manservisi and V. G. Molinari, *Charged-Particle Distribution in Velocity, Angle and Time by Fokker-Planck Equation*, Nuovo Cimento, 14, 9 (1992).

[106] S. Manservisi and V. G. Molinari, *Slowing-Down Time of Fast Electrons in Plasmas via the Fokker-Planck Equation*, Nucl. Sci. Eng., 112, 296 (1992).

[107] M. E. Jones, D. S. Lemons, R. J. Mason, V. A. Thomas and D. Winske, *A Grid-Based Coulomb Collision Model for PIC Codes*, Journal of Comp. Phys. 123, 169-181 (1996).

[108] C. K. Birdsall, *Particle-in-cell charged particle simulations, plus montecarlo collisions with neutral atoms*, IEEE Trans. of Plasma Science vol 19 no. 2 1991.

[109] D. Mascali, S. Gammino, L. Celona and G. Ciavola, *Towards a better comprehension of plasma formation and heating in high performances electron cyclotron resonance ion sources*, Rev. Sci. Instrum. 83 , 02A336 (2012).

[110] A. A. Ivanov, K. Wiesemann, *Ion confinement in electron cyclotron resonance ion sources (ECRIS): importance of nonlinear plasma-wave interaction*, IEEE Trans. Pl. Sci. vol. 33, issue 6, pagg. 1743-1762 (2005).

[111] http://it.wikipedia.org/wiki/Metodo_Monte_Carlo

[112] W. M. Manheimer, M. Lampe, G. Joyce, *Langevin representation of Coulomb collisions in PIC simulations*, Journal of Comp. Phys. 138, 563–584 (1997).

[113] http://simion.com/

[114] http://en.wikipedia.org/wiki/Multivariate_normal_distribution

[115] https://www.particleincell.com/2011/vxb-rotation/

[116] M. T. Marchetti and M. Cavenago F. Pegoraro, *Models of many-element electron cyclotron resonance plasmas*, Rev. Sci. Instrum. 69, no. 2, 1123.

[117] V. Toivanen, V. Aho, P. Jones, J. Kauppinen, H. Koivisto, P. Peura, T. Ropponen, O. Tarvainen, L. Celona, G. Ciavola, S. Gammino D. Mascali A. Galata', *Effects of microwave frequency fine tuning on the performance of JYFL 14 GHz ECRIS*, Proceedings of ECRIS10, Grenoble, France.

[118] D. Mascali, L. Celona, F. Maimone, J. Maeder, G. Castro, F. P. Romano, A. Musumarra, C. Altana, C. Caliri, G. Torrisi, L. Neri,S. Gammino, K. Tinschert, K. P. Spaedtke, J. Rossbach, R. Lang and G. Ciavola, *X-ray spectroscopy of warm and hot electron components in the CAPRICE source plasma at EIS test bench at GSI*, Rev. Sci Instrum. 85, 02A956 (2014).

[119] J. Angot, private communication.

[120] D. Mascali, G. Torrisi, L. Neri, G. Sorbello, G. Castro, L. Celona, S. Gammino, *3D-full wave and kinetics numerical modelling of electron cyclotron resonance ion sources plasma: step towards self-consistency*, Eur. Phys. J. D (2015) 69: 27.